



8-2009

## Analytical, Computational and Experimental Studies of Capillary Flow in Complex Geometries

Yongqing Peng  
*Western Michigan University*

Follow this and additional works at: <https://scholarworks.wmich.edu/dissertations>



Part of the Mechanical Engineering Commons

---

### Recommended Citation

Peng, Yongqing, "Analytical, Computational and Experimental Studies of Capillary Flow in Complex Geometries" (2009). *Dissertations*. 706.

<https://scholarworks.wmich.edu/dissertations/706>

This Dissertation-Open Access is brought to you for free and open access by the Graduate College at ScholarWorks at WMU. It has been accepted for inclusion in Dissertations by an authorized administrator of ScholarWorks at WMU. For more information, please contact [wmu-scholarworks@wmich.edu](mailto:wmu-scholarworks@wmich.edu).



ANALYTICAL, COMPUTATIONAL AND EXPERIMENTAL STUDIES OF  
CAPILLARY FLOW IN COMPLEX GEOMETRIES

by

Yongqing Peng

A Dissertation  
Submitted to the  
Faculty of The Graduate College  
in partial fulfillment of the  
requirements for the  
Degree of Doctor of Philosophy  
Department of Mechanical and Aeronautical Engineering  
Advisors: William W. Liou, Ph.D. and Peter Parker, Ph.D.

Western Michigan University  
Kalamazoo, Michigan  
August 2009

ANALYTICAL, COMPUTATIONAL AND EXPERIMENTAL STUDIES OF  
CAPILLARY FLOW IN COMPLEX GEOMETRIES

Yongqing Peng, Ph.D.

Western Michigan University, 2009

The dynamic processes of capillary flow in complex geometries have been studied analytically, computationally and experimentally in this research. A general approach for modeling the capillary flow in arbitrary irregular geometries with straight axis of symmetry is proposed. Using this approach, the governing equation to describe the dynamic capillary rising motion in capillaries with nonuniform elliptical cross-section is first derived under the assumptions of parabolic distribution of the axial velocity and constant contact angle. The calculation results for the capillary flow in different tubes with irregular wall show that, in comparison with existing models that have been tested, the present model can improve the underestimation of the nonuniformity effects.

Using the perturbation method, an asymptotic solution of the flow field in nonuniform circular tubes is obtained and is shown to be superior to the traditional

Hagen-Poiseuille solutions in comparison to the numerical FLUENT results. A new DCA (dynamic contact angle) model, combining the current velocity-dependent model based on molecular-kinetic theory and empirical time-dependent model based on experiments, is proposed to describe the dynamic transition process of the gas-liquid interface. The applicable scope of the new DCA model is extended to the entire process from the initial state to the equilibrium state. The capillary flow model is further developed by using the new velocity distribution and the DCA model. The proposed theoretical models are validated by a series of experiments of capillary flow in complex geometries.

The industrial application of the research was explored by adopting the proposed model to describe the water flow through a multi-layer porous medium that is used in Procter & Gamble's dewatering device for the paper making industry. Comparing with the experimental data, the proposed model has good predictions on the dewatering performance of the device, and hence, can potentially be used as an industrial design optimization tool.

Copyright by  
Yongqing Peng  
2009

UMI Number: 3376935

### INFORMATION TO USERS

The quality of this reproduction is dependent upon the quality of the copy submitted. Broken or indistinct print, colored or poor quality illustrations and photographs, print bleed-through, substandard margins, and improper alignment can adversely affect reproduction.

In the unlikely event that the author did not send a complete manuscript and there are missing pages, these will be noted. Also, if unauthorized copyright material had to be removed, a note will indicate the deletion.

UMI<sup>®</sup>

---

UMI Microform 3376935  
Copyright 2009 by ProQuest LLC  
All rights reserved. This microform edition is protected against  
unauthorized copying under Title 17, United States Code.

---

ProQuest LLC  
789 East Eisenhower Parkway  
P.O. Box 1346  
Ann Arbor, MI 48106-1346

## ACKNOWLEDGMENTS

I would like to express appreciations to my academic advisors, Dr. William W. Liou and Dr. Peter Parker, who provided me with professional assistance and thoughtful guidance throughout the completion of my dissertation. My sincere gratitude should also go to the members of my committee, Dr. Parviz Merati and Dr. Tianshu Liu, who gave me very valuable suggestions on my research work and spent their precious time reviewing my dissertation. Special thanks to Dr. Iskender Sahin who once served on the committee.

My most profound gratitude goes to my parents and parents-in-law for all the support and love throughout the whole time during my dream of pursuing the doctoral degree.

Finally, I would like to thank my lovely wife, Yan Zhou, and my daughter, Ariane, who always understand me, encourage me and love me. This dissertation is dedicated to you for your love.

Yongqing Peng

## TABLE OF CONTENTS

ACKNOWLEDGMENTS .....	ii
LIST OF TABLES .....	vi
LIST OF FIGURES .....	vii
NOMENCLATURE .....	xiv
CHAPTER	
1. INTRODUCTION .....	1
1.1 Capillary Interface and Capillary Pressure .....	1
1.2 Experimental Studies on Dynamic Contact Angle .....	4
1.3 Theoretical Studies on Dynamic Contact Angle .....	9
Hydrodynamic Models .....	9
Molecular Kinetic Models .....	16
Combined Molecular Hydrodynamics Models .....	24
Shikhmurzaev Model .....	27
1.4 Dynamics of Capillary Flow .....	36
Capillary Flow in Circular Uniform Tubes .....	40
Capillary Flow in Noncircular Uniform Tubes .....	44
Capillary Flow in Nonuniform Tubes .....	51
1.5 Objectives of the Research .....	52
2. MODELING OF CAPILLARY FLOW OF CONSTANT CONTACT ANGLE IN TUBES OF NONUNIFORM ELLIPTICAL CROSS SECTION .....	58

## Table of Contents-continued

CHAPTER		
2.1	Model Equation .....	59
	Derivation of the Governing Equation.....	60
	Characteristics Analysis.....	69
2.2	Model Validation .....	72
	Circular Cylindrical Capillary.....	73
	Rectangular Cylindrical Capillary.....	76
	Circular Convergent-Divergent (C-D) and Divergent- Convergent (D-C) Capillary.....	77
2.3	Results of Nonuniform Capillaries .....	80
	Parabolic Nonuniform Capillary.....	81
	Sinusoidal Varying Wall Capillary.....	90
	Divergent Sinusoidal Wall Capillary.....	105
2.4	Conclusions .....	111
3.	MODELING OF CAPILLARY FLOW WITH DYNAMIC CONTACT ANGLE IN TUBES OF NONUNIFORM CIRCULAR CROSS SECTION .....	113
3.1	Asymptotic Series Solution of Flow Field.....	113
	Zeroth-order Stream Function Solution.....	119
	First-order Stream Function Solution.....	120
	Second-order Stream Function Solution.....	122
3.2	New Derivation of Governing Equation of Capillary Flow ...	140
3.3	Dynamic Contact Angle Model of Capillary Flow in Non- uniform Tubes .....	147
3.4	Validation of Capillary Flow in Circular Cylindrical Tubes .....	151
3.5	Validation of Capillary Flow in Nonuniform Tubes .....	162

## Table of Contents-continued

CHAPTER		
	Experimental Details .....	163
	Theoretical Governing Equation .....	165
	Results and Discussion .....	170
	3.6 Conclusions .....	188
4.	MODELING OF CAPILLARY FLOW IN MULTI-LAYER POROUS MEDIUM .....	190
4.1	Background .....	191
	Introduction of Paper Making Machine .....	191
	RCP Dewatering Process .....	195
	RCP Porous Medium .....	202
4.2	Experimental Study of the Dewatering of RCP Medium .....	210
	Flow Rate Test of RCP Medium .....	210
	Pilot Plant Dewatering Test of RCP Medium .....	217
4.3	Theoretical Studies of Capillary Flow in Multi-layer Porous Media .....	224
	Derivation of the Governing Equation .....	224
	Results and Discussion .....	232
4.4	Conclusions .....	246
5.	CONCLUSIONS AND DISCUSSION .....	248
	BIBLIOGRAPHY .....	252

## LIST OF TABLES

1.1 Values of parameters obtained by applying the molecular-kinetic theory to experimental data for various system .....	20
3.1 Values of $\alpha_i$ for circular tubes .....	145
3.2 Fluid properties .....	152
4.1 Geometry summary of the RCP porous medium .....	206
4.2 Results of the RCP dewatering experiment .....	219
4.3 The critical pulp pore size under different vacuum pressure .....	238

## LIST OF FIGURES

1.1 Capillary interface in circular tube .....	3
1.2 Velocity-dependence of the contact angle for a partially wetting liquid .....	7
1.3 Viscous bending on the mesoscale for and advancing interface .....	10
1.4 Dynamic wetting according to the molecular kinetic theory .....	17
2.1 Schematic of a nonuniform tube with elliptical cross-section .....	61
2.2 Velocity contour and velocity vector for sinusoidal tube .....	63
2.3 Comparison of the present model solution with the FEM solution for the capillary rise in a 100- $\mu$ m-diameter capillary tube .....	73
2.4 Effects of fluid inertia on the capillary rise in circular cylindrical tubes of different radius .....	74
2.5 Comparison of capillary rises for rectangular cylindrical tubes .....	76
2.6 Convergent-divergent and divergent-convergent capillary geometries .....	78
2.7 Convergent-divergent and divergent-convergent capillary geometries .....	79
2.8 Sketch of capillary with parabolic wall .....	81
2.9 Capillary rise for parabolic circular tube with $R_k = 10$ .....	84

## List of Figures-continued

2.10	Comparison of capillary rise for parabolic circular tube with $R_k = 10$ .....	85
2.11	Capillary rise for parabolic circular tube with $R_k = 100$ .....	86
2.12	Comparison of capillary rise for parabolic circular tube with $R_k = 100$ .....	87
2.13	Viscous effect for parabolic circular tubes ...	89
2.14	Sinusoidal geometry .....	90
2.15	Comparison of capillary rise for sinusoidal circular tubes with $L=2$ and $A=0.3$ .....	92
2.16	Comparison of capillary rise for sinusoidal circular tubes with $L=2$ and $A=0.6$ .....	93
2.17	Comparison of capillary rise for sinusoidal circular tubes with $L=4$ and $A=0.3$ .....	94
2.18	Comparison of capillary rise for sinusoidal circular tubes with $L=4$ and $A=0.6$ . .....	95
2.19	Comparison of capillary rise velocity for sinusoidal circular tubes with $L=2$ and $A=0.3$ . .	97
2.20	Comparison of capillary rise velocity for sinusoidal circular tubes with $L=2$ and $A=0.6$ . .	98
2.21	Comparison of capillary rise velocity for sinusoidal circular tubes with $L=4$ and $A=0.3$ . .	99
2.22	Comparison of capillary rise velocity for sinusoidal circular tubes with $L=4$ and $A=0.6$ . .	100
2.23	Viscous effect for sinusoidal tubes. ....	101
2.24	Force function $F(h)$ and equilibrium heights for $L=2$ and $A=0.3$ .....	104

## List of Figures-continued

2.25 Sketch of sinusoidal divergent tube .....	106
2.26 Capillary rise velocity for sinusoidal divergent tubes .....	108
2.27 Nonuniformity effect in viscous terms .....	110
3.1 Schematic of geometry setting in FLUENT .....	127
3.2 Stream line in sinusoidal tube. Solid line: Equation (3.56); Dash line: Equation (3.55); Discrete points: FLUENT Results .....	128
3.3 Velocity distribution in the cross section plane at $z=0$ of a sinusoidal tube .....	131
3.4 Velocity distribution in the cross section plane at $z=-L/8$ of a sinusoidal tube .....	132
3.5 Velocity distribution in the cross section plane at $z=L/8$ of a sinusoidal tube .....	133
3.6 Velocity distribution in the cross section plane at $z=3L/8$ of a sinusoidal tube .....	134
3.7 Velocity distribution in the cross section plane at $z=4L/8$ of a sinusoidal tube .....	135
3.8 Velocity distribution in the cross section plane at $z=5L/8$ of a sinusoidal tube .....	136
3.9 Pressure drop in axial direction of a sinu- soidal tube .....	140
3.10 Convection parameter in a sinusoidal tube ....	147
3.11 Transition of $\theta_m$ in capillary rise problems...	150
3.12 The capillary rise of water in a circular cylindrical tube with $\zeta=0.45$ , $t_c=0.15$ and $M_p$ $=20$ .....	154

## List of Figures-continued

3.13 The capillary rise of ethanol in a circular cylindrical tube with $\zeta=0.04$ , $t_c=0.15$ and $M_p=20$ .....	155
3.14 The capillary rise of water-ethanol mixture in a circular cylindrical tube with $\zeta=0.14$ , $t_c=0.08$ and $M_p=40$ .....	156
3.15 The capillary rise of SF 0.65 in a circular cylindrical tube with $t_c=0.08$ , $M_p=40$ and $\zeta=0.02$ for $h_i=10$ mm, $\zeta=0.015$ for $h_i=50$ mm.....	160
3.16 The capillary rise of SF 1.00 in a circular cylindrical tube with $t_c=0.02$ , $M_p=80$ and $\zeta=0.05$ for $h_i=10$ mm, $\zeta=0.06$ for $h_i=50$ mm.....	161
3.17 The capillary rise of FC-77 in a circular cylindrical tube with $t_c=0.02$ , $M_p=80$ and $\zeta=0.08$ for $h_i=10$ mm, $\zeta=0.1$ for $h_i=50$ mm.....	162
3.18 The experimental set-up .....	164
3.19 Surface tension-driven flow into a circular cylindrical tube .....	170
3.20 Surface tension-driven flow into the A-type nonuniform tube .....	171
3.21 Surface tension-driven flow into the B-type nonuniform tube .....	172
3.22 The capillary rise of distilled water in a circular cylindrical tube with $t_c=0.5$ , $M_p=40$ , $A_d=0.922$ , $B_d=1.004$ and $\zeta=0.3$ .....	174
3.23 Time-dependent variations of dynamic contact angle .....	176
3.24 Geometry of Type-A nonuniform tube .....	177

## List of Figures-continued

3.25	The capillary rise of distilled water in Type-A nonuniform tube with $t_c=0.5$ , $M_p=40$ , $A_d=0.922$ , $B_d=1.004$ and $\zeta=0.2$ .....	179
3.26	Time-dependent variations of dynamic contact angle for Type-A nonuniform tube .....	180
3.27	Geometry of Type-B nonuniform tube .....	182
3.28	The capillary rise of distilled water in a sinusoidal tube with $t_c=0.1$ , $M_p=40$ , $A_d=0.99$ , $B_d=1.0025$ and $\zeta=0.2$ .....	183
3.29	Time-dependent variations of dynamic contact angle for Type-B nonuniform tube .....	185
3.30	Velocity-dependent variations of dynamic contact angle .....	186
4.1	Image of RCP paper machine .....	192
4.2	Schematic diagram of paper machine .....	193
4.3	Close-up view of RCP press section .....	197
4.4	Schematic fragmentary sectional view of RCP papermaking machine .....	198
4.5	Fragmentary sectional views taken along sectional lines a-a through f-f .....	201
4.6	A fragmentary top plan view of the RCP porous medium [Ensign et al. 2000] .....	203
4.7	Microscope view of each layer of the RCP porous medium .....	204
4.8	Dutch twilled woven structure .....	207
4.9	Plain square woven structure .....	207
4.10	Schematic of RCP flow test cell .....	211

## List of Figures-continued

4.11 view of RCP flow test cell .....	212
4.12 Removed water volume with respect to time under different vacuum pressure .....	213
4.13 The correlation between the total flow rate and the vacuum pressure for the RCP medium with 0.1m-diameter circular open area .....	214
4.14 The experimental and theoretical corre- lations between the net flow rate and the vacuum pressure for the RCP medium with 0.1m-diameter circular open area .....	217
4.15 Removal water results under different vacuum pressure at machine velocity of 30fpm .....	221
4.16 Removal water results under different vacuum pressure at machine velocity of 40fpm .....	221
4.17 Removal water results under different vacuum pressure at machine velocity of 50fpm .....	222
4.18 Removal water results under different vacuum pressure at machine velocity of 60fpm .....	222
4.19 Removal water results under different vacuum pressure at machine velocity of 70fpm .....	223
4.20 Schematic of multi-layer porous media .....	228
4.21 The comparison of the penetration length results for $P_v=6$ inHg, $v_m=70$ fpm and $R_f=10$ $\mu\text{m}$ .	233
4.22 Simulated penetration length results under different vacuum pressure for $v_m=70$ fpm and $R_f=10$ $\mu\text{m}$ .....	235
4.23 Simulated penetration length results for different pulp pore size with $v_m=70$ fpm and $P_v=10$ inHg .....	237

List of Figures-continued

4.24 Comparison of the Weibull and Gaussian  
distribution of the pore size in paper web ...240

4.25 Comparison of the theoretical and experiment  
results of the removal water under different  
vacuum pressure .....242

4.26 The effect of the machine speed on the water  
remove rate .....244

## NOMENCLATURE

$A$	Sinusoidal amplitude
$B$	Numerical constant related to the surface tension
$c_1, c_2, c_3, c_4, c_5$	Geometrical parameters of the non-uniform capillary model
$Ca$	Capillary number
$C_v$	Numerical constant of hydrodynamic contact angle models
$F_c$	Additional frictional force
$g$	Gravity acceleration
$H_i$	Thickness of the $i$ -th layer
$h$	Capillary rise height
$h_e$	Equilibrium capillary rise height
$K$	Square of the ratio of the semi-major axis to the semi-minor axis
$K_{zs}$	Constant of slip model
$L$	Sinusoidal waveness
$L_H$	Characteristic length of the flow in the outer region
$L_s$	Slip length at the inner region
$N$	pore number area density
$N_i$	pore number area density of $i$ -th layer
$\hat{n}$	unit vector normal to the interface

## Nomenclature—continued

$P$	Pressure
$Q$	Flow rate
$R$	Radius of the capillary Tube
$R_f$	Radius of pulp fiber
$R_{p1}, R_{p2}$	two principal radii of curvature at the interface
$R_s$	Radius of spherical meniscus
$R_0$	Base radius
$U$	Contact line velocity
$v$	Velocity
$v_x, v_y, v_z$	Velocity components
$V_c$	Factor of the nonuniformity effect on the axial viscous term
$x, y, z$	Cartesian coordinates
$\beta$	Viscosity ratio of the two contacting fluids
$\Delta p$	differential pressure across the capillary interface
$\kappa$	Net frequency
$\kappa^+$	Frequency in the forward direction
$\kappa^-$	Frequency in the backward direction
$\kappa^0$	Equilibrium frequency
$\lambda$	Nondimensionalized sinusoidal wave-ness

## Nomenclature—continued

$\rho$	Density
$\theta$	Contact angle
$\theta_d$	Dynamic contact angle
$\theta_m$	Microscopic contact angle
$\theta_s$	Static contact angle
$\theta_Y$	Young angle
$\gamma$	Surface tension
$\mu$	Viscosity
$\zeta$	Contact line friction coefficient

# **CHAPTER 1**

## **INTRODUCTION**

Capillary phenomena, widespread in our encompassing world, have become an important subject of research since about two centuries ago and still are today because of their extensive applications in modern industries, such as flip-chip packaging [Huang 2002; Wan 2004; Wan and Zhang 2005, Wan et al. 2007, 2008; Hashimoto et al. 2008], microfluidics and nanofluidics [Ralston 2008; Franke and Wixforth 2008; Fang 2009], flows in soil[Watanabe and Flury 2008] and other porous media[Yang 1985; Lockington 2004; Lavi 2008]. An introduction of and literature reviews on the various aspects of the research of the capillary phenomena are provided in this chapter. The motivation of this dissertation is also presented.

### **1.1 Capillary Interface and Capillary Pressure**

An identical feature of all the capillary phenomena is that a capillary interface forms when the two immiscible fluids are situated adjacent to each other.

The differential pressure across the curved interface appears due to the presence of surface tension on the fluid-fluid interface. Thomas Young (1805) developed the qualitative theory of surface tension and introduced the mathematical concept of mean curvature to describe the pressure difference across the capillary interface. The mathematical description of the mean curvature was completed by Laplace in 1806. The so-called Young-Laplace equation is expressed as [Rowlinson and Widom 2002]:

$$\Delta p = 2\gamma J = \gamma \nabla \cdot \hat{n} = \gamma \left( \frac{1}{R_{p1}} + \frac{1}{R_{p2}} \right) \quad (1.1)$$

where,  $\Delta p$  is the differential pressure across the capillary interface,  $\gamma$  is the surface tension,  $J$  is the mean curvature of the interface,  $\hat{n}$  is the unit vector normal to the curvature interface, and  $R_{p1}$  and  $R_{p2}$  are the two principal radii of curvature at the interface.

For a circular tube with a radius of  $r$  as shown in Figure 1.1, the capillary interface between two fluids forms a spherical meniscus with a radius  $R_s$ , which is equal to the two principal radii and related to the contact angle  $\theta$  by :

$$R_s = R_{p1} = R_{p2} = \frac{r}{\cos \theta} \quad (1.2)$$

Thus, the pressure difference can be written as:

$$\Delta p = \frac{2\gamma \cos \theta}{r} \quad (1.3)$$

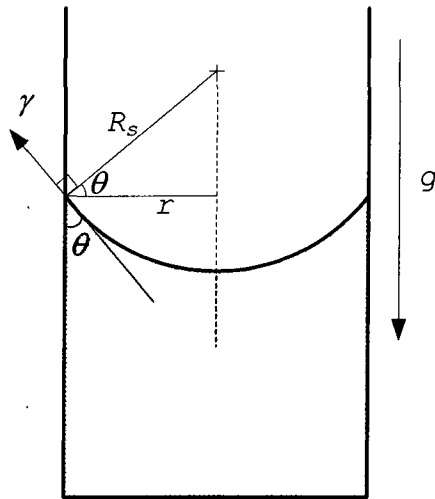


Figure 1.1 Capillary interface in circular tube.

This pressure difference is also often called "capillary pressure" to describe the driving force in capillary flow in the tube. Considering the pressure in the gas phase constant and the contact angle less than  $90^\circ$ , a pressure gradient will be established in the liquid phase due to the capillary pressure to drive the flow into the tube. This flow will continue until the capillary driven force is balanced by the induced gravitational force and a stable curvature condition of

the interface is obtained, where the corresponding contact angle,  $\theta_s$ , is called the equilibrium contact angle or static contact angle. For a vertical tube with a radius of  $r$ , the equilibrium height of the interface,  $h_e$ , can be written as:

$$h_e = \frac{2\gamma \cos \theta_s}{\rho g r} \quad (1.4)$$

Prior to the equilibrium state, the contact angle,  $\theta$ , of the moving liquid-gas interface is determined by the balance of surface tension force and viscous retarding force. The contact angle is usually termed as the dynamic contact angle,  $\theta_d$ , to describe the dynamic wetting process.  $\theta_d$  depends on two groups of factors: (i) the material properties of the fluids and solid surface; (ii) the parameters of the flow field [Blake et al. 1999].

## **1.2 Experimental Studies on Dynamic Contact Angle**

Earlier experiments indicate that the dynamic wetting process depends on the viscosity, the surface tension of the interface, the kinetic adsorption of surfactants, the state of the solid surface and possible

other parameters related to the composition of the contacting media [Blake 1999]. For example, Kwok and Neumann (2000) summarized recent experimental results of the low-rate dynamic contact angle for fourteen solid surfaces and provided an interpretation of the contact angle in terms of the solid-liquid and solid-vapor surface tension. Blake and Shikhmurzaev (2002) studied the dynamic contact angle for a series of water-glycerol solutions with viscosities ranging from 1.5 to 672 mPa · s. They considered the contact line is moving by the liquid rolling over the solid surface, and proposed a model to describe the dynamic wetting process of the disappearing of the liquid-gas interface and the forming of the liquid-solid interface. The viscosity dependence of the phenomenological parameters of their model brings them a conclusion that the microscopic physical mechanism of the interface formation is diffusive in nature. However, as noted in [Blake et al. 1999; Blake 2006], the precise mechanism of the wetting behavior still remains debatable, despite plenty of research over many years. This incomplete understanding is caused by two main difficulties. First, the scale of dynamic wetting ranges

from the macroscopic to the molecular level, but the experimental observations were usually restricted to the macroscopic properties at a resolution of micron level. Secondly, the separation of these factors is not straightforward because any change of a single parameter will inevitably alter other related physical-chemical properties.

Some studies focused on the influence of the capillary interface speed, also called contact-line speed, on the dynamic contact angle. It is widely accepted that there is a unique relationship between the contact-line speed and the dynamic contact angle. Rose and Heins (1962) reported that the advancing dynamic contact angle increased with the velocity of interface motion in a capillary tube for oleic acid and Nujol. Elliot and Riddiford (1967) found that advancing contact angles appear to be independent of the slow interfacial velocity in the range of 0-1mm/min and increase linearly with a velocity above 1 mm/min, but the rate of change diminishes at higher speeds, until a limiting value is reached. Cain et al. (1983), using the capillary rise method between smooth and roughened siliconized plates,

reported the similar studies of dependence of dynamic contact angles on the rate of advance of the three-phase contact. The dynamic contact angle depends on not only the velocity magnitude but also the direction. This is shown schematically in Figure 1.2.

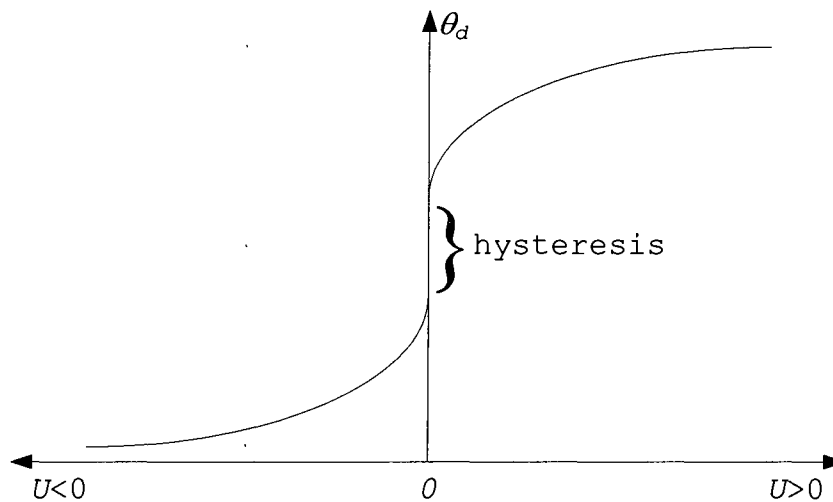


Figure 1.2 Velocity-dependence of the contact angle for a partially wetting liquid [after Dussan 1979; Blake 2006].

Nevertheless, such a conclusion of the velocity dependence of contact angle may be limited to viscous fluids. Recently, Tavana and Neumann (2006) reported that both the advancing angle and the receding angle are not influenced significantly by the contact-line speed up to 12 mm/min according to their experimental results of liquids with low viscosity. Figure 1.2 also exhibits the

hysteresis phenomenon between the advancing angle and the receding angle. The hysteresis of the contact angle is a characteristic to describe the surface wettability, but its origin has been in debate for over thirty years [Vedantam and Panchagnula, 2008]. Some important factors that have been shown to affect the contact angle hysteresis behavior consist of surface roughness [Eick et al. 1975; Oliver et al. 1980; Hennig et al. 2002], surface heterogeneity [Dettre and Johnson 1965; Schwartz and Garoff 1985; Brandon and Marmur 1996], molecular scale topography and rigidity of molecules [Fadeev and McCarthy 1999], molecular chains and surface configurations [Yasuda et al. 1994; Tavana et al. 2007], change in the electronic state of molecules at the uppermost layer of the solid film [Wang et al. 1994], penetration of liquid and swelling of the solid [Sedev et al. 1996], liquid sorption/retention on the surface [Lam et al. 2002], size and shape of liquid molecules [Lam et al. 2001] and strong interactions between molecules of solid and liquid at the three-phase line region [Extrand 2004; Chen et al. 2009]. Theoretically, contact angle hysteresis and surface tension arise from the kinetic

coefficients and the gradient term in the free energy respectively. Vedantam and Panchagnula (2008) introduced a constitutive phase field model to characterize the contact angle hysteresis of sessile drops and showed that the behavior of the drop on the surface with chemically heterogeneous islands is determined by material properties near the three-phase contact line in accordance with the experimental results in [Extrand 2003].

### **1.3 Theoretical Studies on Dynamic Contact Angle**

The attempts to explain the experimental results have inspired an abundance of theoretical studies on the underlying mechanisms of dynamical wetting. These analytical studies essentially can be divided into four approaches in terms of their conceptual framework: hydrodynamic theory, molecular kinetic theory, combined molecular hydrodynamic theory and Shikhmurzaev theory.

#### Hydrodynamic Models

In hydrodynamic theory, the viscous flow within the wedge of liquid in the vicinity of the moving contact

line is the main source of the dissipation [Blake, 2006]. There are three relevant length scales within the hydrodynamic model as shown in Figure 1.3.

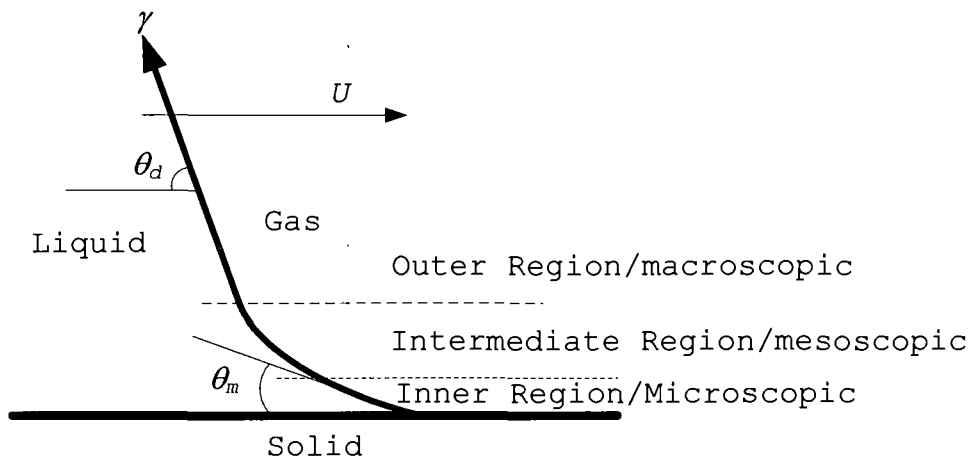


Figure 1.3 Viscous bending on the mesoscale for an advancing interface [after Blake 2006].

In the outer region, the capillary force is balanced by the gravitational force, and the fluid interface obeys the Laplace equation [Ralston et al. 2008]. In the inner region where is in the vicinity of the contact line, the interactions between the contacting phases play a determining role. However, The variations of the macroscopic dynamic contact angle,  $\theta_d$ , as observed in experiments, are attributed to viscous bending of the moving liquid-gas interface within the mesoscopic region where the capillary and viscous forces determine the

hydrodynamics [Blake 2006]. Moreover, the geometry of the system plays a role on the fluid interface profile in the outer region but not in the inner and intermediate regions [Ralston et al. 2008]. Governed by short-range intermolecular forces, the microscopic angle,  $\theta_m$ , is assumed to retain its static value,  $\theta_s$ . A well known drawback of the hydrodynamic model is the conflict between the moving contact line and the traditional no-slip boundary condition, which leads to unbounded stress at the wetting line and, therefore, an unphysical solution [Huh and Scriven 1971]. One treatment with this singularity is to artificially truncate the solution at the molecular scale, where the continuum description breaks down [Voinov 1976; Blake 2006]. Another usual treatment is to modify the flow equations and boundary condition by a relaxation of the no-slip condition in the vicinity of the contact line [Dussan 1976, 1979; Ngan and Dussan 1989; Huh and Scriven 1971; Huh and Mason 1977; Blake 2006]. Although the stresses on the three-phase contact line still remains unbounded in this case, the exerted force on the solid becomes finite. For both approaches, in a general function of capillary number,

$Ca$ , microscopic contact angle,  $\theta_m$ , and a number of parameters,  $\chi_i, i = 1, 2, 3, \dots$ , which represent material properties of the contact media, the macroscopic dynamic contact angle can be expressed as:

$$\theta_d = F(Ca, \theta_m, \chi_1, \chi_2, \chi_3 \dots) \quad (1.5)$$

The capillary number,  $Ca$ , is defined as:

$$Ca = \frac{\mu}{\gamma} \cdot U \quad (1.6)$$

where,  $\gamma$  is the surface tension,  $\mu$  is the liquid viscosity and  $U$  is the contact line velocity.

With the assumption of a small capillary number, the viscous bending is important only in the intermediate region. The liquid-gas interface far from the wetting line on the solid surface is considered to be in its static shape and can be determined by extrapolating the static interface of the inner region. By using the method of matched asymptotic expansions, the flow equations are solved and a simplest form of equation (1.6), correct to zero order in  $Ca$  for  $Ca \rightarrow 0$ , is obtained [Dussan et al. 1991; Blake 2006; Ralston et al. 2008]:

$$G(\theta_d) = G(\theta_m) + Ca \ln \left( \frac{L_H}{L_s} \right) \quad (1.7)$$

where the slip length  $L_s$  denotes the scale of the inner region,  $L_H$  the characteristic length of the flow in the outer region, and,

$$G(\theta) = \frac{1}{2} \int_b^\theta \left( \frac{\theta^*}{\sin \theta^*} - \cos \theta^* \right) d\theta^* \quad (1.8)$$

Voinov (1976) found an approximation of the above equation for  $\theta < 150^\circ$ :

$$G(\theta) \approx \frac{\theta^3}{9} \quad (1.9)$$

Cox (1986) considered up to the first order of  $Ca$  and the possibility of other sources of dissipation. A more complete solution is obtained by matching the asymptotic solutions for the inner, intermediate and outer regions for the contact line of two immiscible fluids moving on a smooth solid surface [Ralston et al. 2008]. It is written as:

$$G(\theta_d) = G(\theta_m) + Ca \left[ \ln \left( \frac{L_H}{L_s} \right) + \frac{Q_{in}}{f(\theta_m)} - \frac{Q_{out}}{f(\theta_d)} \right] \quad (1.10)$$

Equation (1.9) is valid for  $Ca \rightarrow 0$ ,  $L_s / L_H \rightarrow 0$  and

$Ca \cdot \ln(L_H / L_s) \rightarrow 1$ .  $Q_{in}$  is an integration constant for the capillary interface profile in the inner region that depends on  $\mu$ ,  $\theta_m$  and the particular slip law, while  $Q_{out}$

is the integration constant for the profile of the outer region that depends on  $\mu$ ,  $\theta_m$  and the geometry of the system. The functions  $G$  and  $f$  are defined in [Cox 1986]:

$$G(\theta) = \int_0^\theta \frac{1}{f(\theta^*)} d\theta^* \quad (1.11)$$

$$f(\theta) = \frac{2 \sin \theta \left\{ \beta^2 (\theta^2 - \sin^2 \theta) + 2\beta [\theta (\pi - \theta) + \sin^2 \theta] \right\}}{\left\{ \beta (\theta^2 - \sin^2 \theta) (\pi - \theta + \sin \theta \cos \theta) \right\} + \left\{ [(\pi - \theta)^2 - \sin^2 \theta] (\theta - \sin \theta \cos \theta) \right\}} \quad (1.12)$$

where  $\beta$  is the viscosity ratio of the two contacting fluids. For liquid-gas system,  $\beta \rightarrow 0$  and equation (1.10) reduces to equation (1.8).

Zhou (1990) and Sheng (1992) reported that the same relationship between macroscopic dynamic contact angle  $\theta_d$  and capillary number  $Ca$  can be obtained for different slip models if the slip length is normalized by a constant  $K_{zs}$  related to the chosen slip model:

$$G(\theta_d) = G(\theta_m) + Ca \cdot \ln \left( K_{zs} \cdot \frac{L_H}{L_s} \right) \quad (1.13)$$

For the liquid-gas system, the dynamic contact angle, by using Voinov's approximation as in equation (1.9), can be expressed explicitly as:

$$\theta_d = \left\{ \theta_m^3 + 9Ca \cdot \left[ \ln \left( \frac{L_H}{L_s} \right) - C_v \right] \right\}^{\frac{1}{3}} \quad (1.14)$$

where  $C_v$  is a numerical constant. A linear relationship between  $\theta_d^3$  and  $Ca$  is predicted in equation (1.14).

In the above theories, it is assumed that  $\theta_m$  is a constant and can be denoted by the Young angle  $\theta_Y$  for ideal surfaces. For real surfaces, the recommendations of Cox (1986) include the effective equilibrium angle defined by Wenzel (1936; 1949), the minimum static receding contact angle, or the maximum static advancing contact angle [Ralston et al. 2008]. Alternatively, Zhou and Sheng (1990) and Stokes et al. (1990) reported that  $\theta_m$  is also dependent on the contact line velocity because of an additional frictional force  $F_c$ , which can be approximated by:

$$F_c = B \cdot Ca^n, \quad 0 < n < 0.5 \quad (1.15)$$

which yields

$$\cos \theta_m = \cos \theta_s - B \cdot Ca^n \quad (1.16)$$

Substituting it into equation (1.14) in turn gives:

$$\theta_d = \left\{ \left[ \arccos(\theta_s - B \cdot Ca^n) \right]^3 + 9Ca \cdot \left[ \ln \left( \frac{L_H}{L_s} \right) - C_v \right] \right\}^{\frac{1}{3}} \quad (1.17)$$

The numerical constant  $B$  is related to surface tension, liquid density, viscosity, and solid surface properties [Zhou and Sheng, 1990].

### Molecular Kinetic Models

The molecular kinetic approach originates with the hypothesis that the liquid transport is a stress-modified molecular rate process [Blake 2006]. This approach focuses on the dissipation occurring in the immediate vicinity of the moving contact line. The dissipation arises from the dynamic friction associated with the moving contact line when the fluid molecules attach or detach to or from the solid surface, as schematically shown in Figure 1.4. There are only two length scales in this model: the molecular scale and the macroscopic scale [Blake 2006]. The dissipation occurs at the molecular scale and its effects are observed at the macroscopic scale. In contrast to the hydrodynamic theory, the contact angle at the microscopic scale is assumed to be

identical to the macroscopic observed angle, i.e.  $\theta_d = \theta_m$ , hence becomes also velocity-dependent.

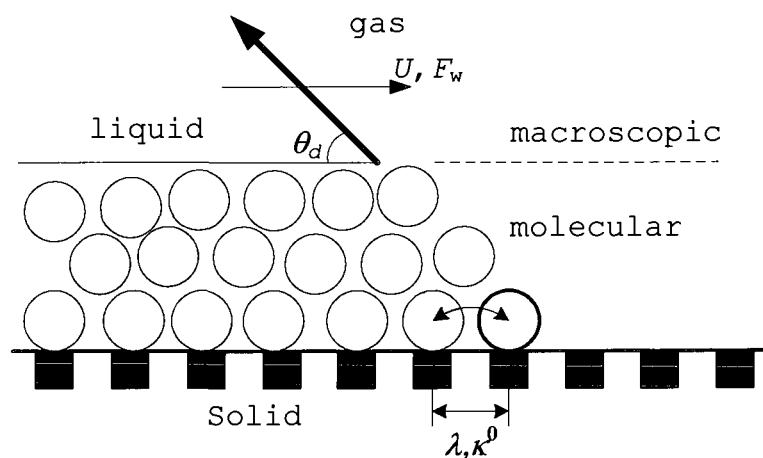


Figure 1.4 Dynamic wetting according to the molecular kinetic theory [after Blake, 2006].

According to the molecular kinetic theory, the molecules of one fluid phase must displace those of the other as shown in Figure 1.4. Even at equilibrium, the molecules will be subject to constant thermal activity, instead of stationary, and the wetting line will fluctuate locally around its mean position. The wetting line tends to move if the system is deviated from the equilibrium due to the external force or potential gradient.

The wetting process is related to the statistical dynamics of the molecules within a three-phase zone, and the velocity of the contact-line can be defined as:

$$U = \kappa\lambda = (\kappa^+ - \kappa^-) \lambda \quad (1.18)$$

where  $\lambda$  is the mean length of the individual molecular displacements that occur to and from the adsorption sites on the solid surface as in Figure 1.4. Therefore,  $\lambda$  is influenced by the liquid molecular size and the distance of the putative adsorption sites. Table 1.1 shows that  $\lambda$  generally decreases with increasing viscosity.  $\kappa$  is the net frequency resulting from  $\kappa^+$  in the forward direction and  $\kappa^-$  in the backward direction. At equilibrium, the velocity is zero, so is the net frequency  $\kappa$ , thus both  $\kappa^+$  and  $\kappa^-$  are identical the equilibrium frequency  $\kappa^0$ .

In the simplest form of the model [Blake 1969; 2006], the basic idea is that the disturbance of the adsorption equilibrium, due to the surface tension of the interface as the wetting line moves across the solid surface, is attributed to the velocity-dependence of the dynamic contact angle [Yarnold and Mason 1949].

Therefore, the out-of-balance surface tension force is

the force which drives the liquid-gas interface to overcome the energy barriers and move in a given direction, when the equilibrium is disturbed. It is written as:

$$F_w = \gamma (\cos \theta_s - \cos \theta_d) \quad (1.19)$$

Combining these ideas and applying the Frenkel-Eyring activated-rate theory [Glastone et al. 1941; Frenkel 1946; Blake and Coninck 2002;], the resultant equation for the contact line speed is:

$$U = 2\kappa^0 \lambda \sinh \left[ \frac{\lambda^2 \gamma (\cos \theta_s - \cos \theta_d)}{2k_B T} \right] \quad (1.20)$$

where  $T$  is the absolute temperature and  $k_B$  the Boltzmann constant. The net frequency  $\kappa^0$  may be written in terms of the wetting activation free energy  $\Delta G_w^*$ :

$$\kappa^0 = \left( \frac{k_B T}{h_p} \right) \exp \left( \frac{-\Delta G_w^*}{N_A k_B T} \right) \quad (1.21)$$

where  $h_p$  and  $N_A$  are the Planck constant and Avogadro number, respectively. The wetting activation free energy  $\Delta G_w^*$  has both surface and viscous contributions,  $\Delta G_s^*$  and  $\Delta G_v^*$ , such that

$$\Delta G_w^* = \Delta G_v^* + \Delta G_s^* \quad (1.22)$$

The viscosity of the liquid is related to  $\Delta G_v^*$  as

[Glastone et al. 1941]:

$$\mu = \frac{h_p}{V_m} \exp\left(\frac{-\Delta G_v^*}{N_A k_B T}\right) \quad (1.23)$$

where  $V_m$  is the molecular volume.

Table 1.1 Values of parameters obtained by applying the molecular-kinetic theory to experimental data for various system [after Blake 2006; deRuijter et al. 1997; Hoffman 1975].

Liquid-solid system	$\mu$ (Pa s)	$\gamma$ (mN/m)	$\theta_s$ ( $^\circ$ )	$\lambda$ (nm)	$\kappa^0$ ( $s^{-1}$ )	$\zeta$ (Pa s)
Water on PET <sup>a</sup>	0.001	72.4	82	0.36	$8.6 \times 10^9$	0.01
16% Glycerol/ water on PET	0.0015	69.7	72.5	0.46	$3.6 \times 10^9$	0.012
86% Glycerol/ water on PET	0.104	65.8	65	0.46	$3.5 \times 10^7$	1.2
Di-n-butyl phthalate on PET	0.196	34.3	<5	1.8	$1.1 \times 10^5$	6.4
Silicone oil on glass	0.958	21.3	0	0.8	$2.3 \times 10^5$	35.9
Silicone oil on glass	98.8	21.7	0	0.8	$2.3 \times 10^3$	3580

<sup>a</sup> Polyethelene terephthalate tape.

Defining the frequency of molecular displacements retarded only by solid-liquid interactions,  $\kappa_s^0$ , as

$$\kappa_s^0 = \frac{k_B T}{h_p} \exp\left(\frac{-\Delta G_s^*}{N_A k_B T}\right) \quad (1.24)$$

and combining equations (1.21), (1.22) and (1.23), a simple relationship between  $\kappa^0$  and viscosity was obtained:

$$\kappa^0 = \frac{\kappa_s^0 h_p}{\mu V_m} \quad (1.25)$$

and it shows that  $\kappa^0$  is inversely proportional to viscosity and consistent with the experimental observations as in Table 1.1.

To further investigate the effect of solid-liquid interaction on dynamic wetting, the specific activation free energy of wetting per unit area  $\Delta g_w^*$  and its surface interaction component  $\Delta g_s^*$  are introduced as:

$$\Delta g_w^* = \frac{\Delta G_w^*}{\lambda^2 N_A}, \quad \Delta g_s^* = \frac{\Delta G_s^*}{\lambda^2 N_A} \quad (1.26)$$

Here,  $\Delta g_s^*$  describes the size of the energy barriers of the adsorption/desorption events when the contact line moves across unit area of the solid surface, and it can, in a first approximation, be equal to the reversible adhesion work between the solid and the liquid:

$$\Delta g_s^* = \gamma (1 + \cos \theta_s) \quad (1.27)$$

Combining equations (1.24), (1.25), (1.26) and (1.27), the equilibrium frequency of the liquid molecular motion can be written as:

$$\kappa^0 = \frac{k_B T}{\mu V_m} \exp \left[ \frac{-\lambda^2 \gamma (1 + \cos \theta_s)}{k_B T} \right] \quad (1.28)$$

Hence, substituting equation (1.28) into equation (1.20), an explicit relationship between the dynamic contact angle and the contact line speed can be obtained as:

$$U = 2 \frac{\lambda k_B T}{\mu V_m} \exp \left[ \frac{-\lambda^2 \gamma (1 + \cos \theta_s)}{k_B T} \right] \sinh \left[ \frac{\lambda^2 \gamma (\cos \theta_s - \cos \theta_d)}{2k_B T} \right] \quad (1.29)$$

If the sinh function is small, the contact-line velocity can be approximated by a linear form:

$$U = \frac{\gamma (\cos \theta_s - \cos \theta_d)}{\zeta} \quad (1.30)$$

where  $\zeta$  is the friction coefficient of contact line and can be defined as:

$$\zeta = \frac{k_B T}{\lambda^3 \kappa_0} \quad (1.31)$$

Substitution of equations (1.22) and (1.25) into equation (1.28) gives:

$$\zeta = \frac{\mu V_m}{\lambda^3} \exp \left[ \frac{\lambda^2 \gamma (1 + \cos \theta_s)}{k_B T} \right] \quad (1.32)$$

Equation (1.32) indicates that the friction of the contact line increases both with the liquid viscosity and the adhesion work. Experimentally,  $\zeta$ , with the same units as dynamic viscosity, is usually larger than the viscosity as observed and increases both with viscosity and the strength of liquid-solid interactions as shown in Table 1.1.

With a strong connection between  $\kappa^0$  and the work of adhesion, the molecular kinetic model predicts a good range of experimental data very well [Blake 1993, 2006; Schneemilch et al. 1998; Petrov et al. 2003]. Because there is no definitive way to predict the values of  $\lambda$ ,  $\kappa^0$  and  $\zeta$  for a given solid-liquid system, they must be considered as adjustable parameters, but the values obtained by curve-fitting to the experimental data are always unreasonable [Petrov et al. 1992; Gribanova 1992; Cazabat 1992; Hayes and Ralston 1993; Sharpe et al. 2002]. The lack of a link to the wider hydrodynamics region of the liquid-solid system is another weakness of the molecular kinetic model. An ad hoc way of making such

a link is to combine the molecular kinetic model with the hydrodynamic model although they are from two very different theoretical frameworks.

### Combined Molecular Hydrodynamic Models

Although the hydrodynamic theory and molecular kinetic theory are fundamentally different, both the hydrodynamic and molecular-kinetic models have been shown to be effective in describing the observation of the dynamic wetting in a range of capillary systems [Blake 2006]. Therefore, it is possible to combine the two models. deGennes (1985) proposed that the total dissipation of the dynamic wetting include both the bulk viscous dissipation and the nonviscous dissipation at the moving contact line. Brochard-Wyart and deGennes (1992) considered that the process of dynamic wetting is irreversible, and proposed that the rate of energy dissipation per unit length of the contact line is the product of the out-of-balance surface tension force and the flux  $U$ . It is written as:

$$\gamma (\cos \theta_s - \cos \theta_d) U = \frac{6\mu U}{\theta_d} \ln \left( \frac{L_H}{L_s} \right) + \zeta U^2 \quad (1.33)$$

The first term on the right hand side denotes the viscous losses in the wedge of liquid in the vicinity of the moving contact line, and the second one represents the contact line friction using the lubrication approximation where the friction coefficient  $\zeta$  is evaluated by equation (1.32). Therefore, a combined model of hydrodynamic and molecular kinetic theories describing the relation between dynamic contact angle  $\theta_d$  and capillary number  $Ca$  is obtained:

$$Ca = \frac{\cos \theta_s - \cos \theta_d}{\frac{\zeta}{\mu} + \frac{6}{\theta_d} \ln \left( \frac{L_H}{L_s} \right)} \quad (1.34)$$

Equation (1.33) indicates that the viscous friction term predominates for small contact angles, and nonhydrodynamic friction for large contact angles.

According to the energy conservation of the wetting process, the free-energy change,  $\Delta G_s$ , caused by the moving contact line and the work  $W_p$  done by the surface tension force should be equal to the sum of the energy dissipation at the contact line  $E_c$  and the bulk viscous energy dissipation  $E_v$  [Voinov, 1976]. Using the creeping-flow model for the intermediate region, the bulk

quantities  $W_p$  and  $E_v$  can be evaluated for large contact angles. Voinov (1976) ignored the capillary pressure work  $W_p$  with the planar assumption and derived the relationship between the contact angle and the contact line frictional force  $F_c$ :

$$\cos \theta_s - \cos \theta_m = \frac{F_c}{\gamma} \quad (1.35)$$

For the symmetric cases, the frictional force  $F_c$  can be substituted by the nonlinearized Blake-Haynes expression [Blake and Haynes 1969; Petrov and Petrov 1992]:

$$F_c = \frac{2k_B T}{\lambda^2} \sinh^{-1} \left( \frac{U}{2\kappa^0 \lambda} \right) \quad (1.36)$$

Combining equation (1.35) from molecular kinetic theory with equation (1.14) based on the hydrodynamics approach, the dynamic contact angle can be modeled as:

$$\theta_d = \left\{ \left[ \cos^{-1} \left( \cos \theta_s - \frac{2k_B T}{\gamma \lambda^2} \sinh^{-1} \left( \frac{\gamma}{2\kappa^0 \lambda \mu} Ca \right) \right) \right]^3 + 9Ca \cdot \left[ \ln \left( \frac{L_H}{L_s} \right) - C_v \right] \right\}^{\frac{1}{3}} \quad (1.37)$$

The unknown parameters  $\lambda$ ,  $\kappa^0$  and  $\ln(L_H / L_s) - C_v$  can be obtained by the curve fit of experimental  $\theta_d - Ca$  data.

The combination of the traditional hydrodynamic model and the molecular kinetic models provides better agreement with experimental data than either one alone, and the value of parameters appeared more reasonable [Petro and Petro 1992; Blake 2006]. However, the combined model is essentially phenomenological and lacks robustness in the fitted values. Moreover, the model still remains restricted to small capillary numbers.

#### Shikhmurzaev Model

Shikhmurzaev (1993; 1994; 1997) has proposed a potentially far-reaching model to mathematically describe the advancing contact-line motion on a smooth solid surface. The standard hydrodynamic channels are adopted for the dissipation in his continuum treatment, and the non-equilibrium thermodynamics is used for the dissipation that is sourced from the formation and destruction processes of the moving contact interface. Hence, the microscopic dynamic contact angle is coupled directly to the flow [Blake 2006]. An emphasized fact of this model is the liquid at the liquid-gas interface transfers to the solid-liquid interface when the liquid

interface advances on the solid surface. The experimental observation of the material flux from the liquid-gas interface to the solid-liquid interface through the contact line has been reported in [Dussan and Davis 1974], but this flux is ignored in the traditional model. The difference of the properties, such as surface tension, density and structure, of the liquid-gas interface and the solid-liquid interface leads to a reorganization process of the molecules of the interfacial regions. Such a process is naturally diffusive and requires some time to complete. Accordingly, the tension of the solid-liquid interface will be disturbed from its equilibrium value and the balance of the interfacial tensions at the contact line will be broken down [Blake 2006], which will affect the microscopic contact angle  $\theta_m$ .  $\theta_m$  is largely responsible for the macroscopic dynamic contact angle  $\theta_d$ .

The starting point of this model is that the well-known Young equation [Young 1805] is still validated for the moving capillary interface. For the stationary liquid, the static contact angle  $\theta_s$  is defined by the Young equation [Blake et al. 1999]:

$$\gamma_{1e} \cos \theta_s = \gamma_{3e} - \gamma_{2e} \quad (1.38)$$

where  $\gamma_{1e}$ ,  $\gamma_{2e}$  and  $\gamma_{3e}$  are the equilibrium surface tensions of the liquid-gas, solid-liquid, and gas-solid interfaces, respectively.

For the moving contact line, the order-of-magnitude analysis [Shikhmurzaev 1993] indicates that the convective momentum fluxes along the interfaces are negligible compared to the surface tensions. Therefore, the Young equation, describing the force balance on the direction tangent to the solid surface, is still valid,

$$\gamma_1 \cos \theta_d = \gamma_3 - \gamma_2 \quad (1.39)$$

Within the framework of fluid mechanics, the deviation of at least one of  $\gamma_i$  ( $i=1,2,3$ ) from its equilibrium value  $\gamma_{ie}$  is the only possible reason leading to the fact that  $\theta_d$  deviates from  $\theta_s$  for moving contact line. Experiments in [Blake et al. 1999] show that the length scale of the variation of the surface tension is comparable with that of the flow field variations in the vicinity of the contact line.

The experiments of the liquid spreading on the solid surface indicate that the free surface undergoes a

rolling motion to pass through the contact line to become the liquid-solid interface [Dussan and Davis 1974; Dussan 1979]. Thus, there will be a fluid element, initially belong to the free surface, reaches the three-phase interaction region, traverses in a finite time to become an element of the solid-liquid interface and finally moves away from the contact line [Blake et al. 1999]. Thus, the surface properties including the surface tension, which are related to this fluid element, will be altered because of its location change from liquid-gas interface to liquid-solid interface. Besides the temperature, Shikhmurzaev (1993) characterized the current interface state by the surface density  $\rho^s$ , and introduced a linear equation of state:

$$\gamma_i = \zeta (\rho_0^s - \rho_i^s), \quad (i=1,2) \quad (1.40)$$

where  $\rho_0^s$  is a phenomenological constant.  $\zeta$  is the equilibrium property independent of viscosity and inversely proportional to the liquid compressibility [Blake 2006]. For the free surface,  $\rho^s$  is always less than  $\rho_0^s$  and then  $\gamma_1 > 0$ , while for the liquid-solid

interface,  $\gamma_2$  can be positive or negative [Blake et al. 1999].

Because the special fluid elements belong to the entire flow field, the surface tension relaxation process and the surface tension distribution along the interfaces are related to the flow geometry and the characteristics of the bulk hydrodynamics. For a moving contact line with speed of  $U$ , the length scale  $L$  of the surface tension relaxation can be defined as:

$$L = U\tau \quad (1.41)$$

where  $\tau$  is introduced as the surface tension relaxation time.

To remove the shear-stress singularity at the contact line, the boundary conditions for the Navier-Stokes equations, with the assumption that the displaced gas is inviscid, have been outlined in the following.

On the gas-liquid interface,

$$\mathbf{n} \cdot \mathbf{P} \cdot \mathbf{n} + p_0 = \gamma_1 \kappa \quad (1.42)$$

$$(\mathbf{I} - \mathbf{nn}) \cdot \mathbf{P} \cdot \mathbf{n} + \nabla \gamma_1 = 0 \quad (1.43)$$

$$\gamma_1 = \zeta (\rho_0^s - \rho_1^s) \quad (1.44)$$

$$\frac{\partial \rho_1^s}{\partial t} + \nabla \cdot (\rho_1^s \mathbf{v}_1^s) = -\frac{\rho_1^s - \rho_{1e}^s}{\tau} \quad (1.45)$$

$$(1 + 4\alpha\beta) \nabla \gamma_1 = 4\beta (\mathbf{v}_1^s - \mathbf{u}) \quad (1.46)$$

and on the liquid-solid interface:

$$(\mathbf{I} - \mathbf{nn}) \cdot \mathbf{P} \cdot \mathbf{n} + \frac{1}{2} \nabla \gamma_2 = \beta (\mathbf{u} - \mathbf{U}) \quad (1.47)$$

$$\gamma_2 = \zeta (\rho_0^s - \rho_2^s) \quad (1.48)$$

$$\frac{\partial \rho_2^s}{\partial t} + \nabla \cdot (\rho_2^s \mathbf{v}_2^s) = -\frac{\rho_2^s - \rho_{2e}^s}{\tau} \quad (1.49)$$

$$\mathbf{v}_2^s = \frac{1}{2} (\mathbf{u} + \mathbf{U}) + \alpha \nabla \gamma_2 \quad (1.50)$$

where  $\mathbf{u}$  is the bulk velocity evaluated at the interface,  $\mathbf{I}$  is the metric tensor,  $\mathbf{n}$  is the inward normal to the gas-liquid interface,  $\kappa = \nabla \cdot \mathbf{n}$  is the curvature of the gas-liquid interface,  $\mathbf{U}$  is the velocity of the solid,  $\mathbf{v}_1^s$  and  $\mathbf{v}_2^s$  denotes the surface velocity of the gas-liquid and liquid-solid interfaces,  $\rho_{1e}^s$  and  $\rho_{2e}^s$  are phenomenological coefficients as  $\rho_0^s$ ,  $\mathbf{P}$  is the stress tensor in the liquid defined as:

$$\mathbf{P} = -p\mathbf{I} + \mu [\nabla \mathbf{u} + (\nabla \mathbf{u})^T] \quad (1.51)$$

Here,  $p$  is the pressure and  $\mu$  is the viscosity.

Therefore,  $(\mathbf{I} - \mathbf{nn}) \cdot \mathbf{P} \cdot \mathbf{n}$ , which appears in equations (1.43) and (1.47) represents the shear stress acting on the liquid-solid. Equations (1.45) and (1.49) are the surface continuity equation of the gas-liquid and solid-liquid interfaces, respectively. Equation (1.46) is proposed to relate the gradient of the surface tension to the liquid-gas surface velocity  $\mathbf{v}_1^s$  and the bulk velocity  $\mathbf{u}$ . Parameters  $\alpha$  and  $\beta$  are introduced to characterize the viscous properties of the interfaces with respect to the external torque and the surface tension gradient [Shikhmurzaev 1993; 1994; Blake et al. 1999].

The equilibrium surface tensions on the two interfaces are denoted as:

$$\gamma_{1e} = \gamma_1 \rho_{1e}^s \quad (1.52)$$

$$\gamma_{2e} = \gamma_2 \rho_{2e}^s \quad (1.53)$$

The distributions of the surface tensions at the contact line are related through equation (1.39), where  $\gamma_3$  is assumed to be a constant ( $\gamma_3 = \gamma_{3e}$ ), and the rolling motion of the liquid at the contact line gives:

$$\rho_1^s \mathbf{v}_1^s \cdot \mathbf{e}_f = \rho_2^s \mathbf{v}_2^s \cdot \mathbf{e}_g \quad (1.54)$$

where  $\mathbf{e}_f$  and  $\mathbf{e}_g$  are unit vectors normal to the contact line and tangential to the liquid-gas and solid-liquid interfaces, respectively.

Hitherto, a closed set of the boundary conditions is provided. The singularity of the shear stress is removed in equation (1.47), while the true kinematics of the flow is preserved in equation (1.54) and the dynamic contact angle is given in equation (1.39). For the region far from the contact line, boundary conditions (1.42)-(1.50) reduce to the classical ones. Within the framework of surface hydrodynamics and irreversible thermodynamics, Shikhmurzaev's model is self-consistent.

Based the hydrodynamic equations under the above conditions, an analytical expression is obtained with simplifications for some cases [Shikhmurzaev, 1993; 1994; 1997]. For  $Ca \rightarrow 0$ , the free surface near the contact line is assumed to be locally planar, and the surface tension relaxation region can be separated into two asymptotic subdomains: one is dominated by viscous effect, the other by surface effects. The flow parameters are determined in the framework of the classical formulations. By matching the solutions for the different

regions, the following analytical expression for the velocity dependence of the contact angle for the cases of small capillary numbers is derived as:

$$\cos \theta_s - \cos \theta_d = \frac{2 Sc \cdot Ca (\rho_{2e}^{s*} + \rho_{1e}^{s*} u_0)}{(1 - \rho_{1e}^{s*}) \left\{ \left[ \rho_{2e}^{s*} + (Sc \cdot Ca)^2 \right]^{\frac{1}{2}} + Sc \cdot Ca \right\}} \quad (1.55)$$

where  $\rho_{ie}^{s*} = \rho_{ie}^s / \rho_0^s$ ,  $Ca = \mu U / \gamma_{1e}$  and the scaling factor  $Sc$  is written as:

$$Sc = \left[ \frac{\gamma_{1e}^2 \tau \beta}{\mu^2 \rho_0^s \zeta (1 + 4\alpha\beta)} \right]^{1/2} \quad (1.56)$$

The function  $u_0$ , dependent on  $\theta_d$  and scaled by contact line velocity  $U$ , is the tangential component of the free surface velocity in the reference frame moving with the contact line and takes the form:

$$u_0(\theta_d) = \frac{\sin \theta_d - \theta_d \cos \theta_d}{\sin \theta_d \cos \theta_d - \theta_d} \quad (1.57)$$

If the viscosity of the gas is considered, the above equation is replaced by:

$$u_0(\theta_d, k_\mu) = \frac{(\sin \theta_d - \theta_d \cos \theta_d) K(\theta_2) - k_\mu (\sin \theta_2 - \theta_2 \cos \theta_2) K(\theta_d)}{(\sin \theta_d \cos \theta_d - \theta_d) K(\theta_2) + k_\mu (\sin \theta_2 \cos \theta_2 - \theta_2) K(\theta_d)} \quad (1.58)$$

where  $\theta_2 = \pi - \theta_d$ ,  $K(\theta) = \theta^2 - \sin^2 \theta$ , and  $k_\mu$  denotes the gas-to-liquid viscosity ratio.

Equation (1.55) describes the velocity dependence of the dynamic contact angle for certain simplifying conditions. The model can fit the experimental data for different capillary systems reported in [Blake and Shikhmurzaev 2002]. Intrinsically, the model can be applied to solve many complex dynamic wetting problems, such as wetting on residual films and wetting with surfactant solutions, with parameters determined by independent experiments [Ralston et al. 2008]. It is shown that the macroscopic dynamic behavior of wetting can be influenced by the microscopic characteristics of the system, such as the flow field near the contact line [Blake et al. 1999], but the mechanism of how the surface characteristics are related to the action of intermolecular forces remains to be explored.

#### **1.4 Dynamics of Capillary Flow**

To understand and describe the physical processes associated with the capillary penetration in porous media is of considerable importance for a variety of fields and

applications, such as soil science [Watanabe K and Flury M 2008], powder technology [Lazghab M et al. 2005], suspensions and emulsions stability [Cui et al. 2005], and paper-making technology [Stelljes MG et al. 2004]. For applications dependent on the rate of capillary penetration into the porous media with extremely complex structures, the detailed modeling of capillary penetration into them is yet unrealistic. For the practical characterization or design purpose, a simplified and widely-used model is the capillary penetration method. The model is based on the assumption that an equivalent cylindrical capillary can be defined by equating the penetration rate into this capillary to that in the studied porous medium. There are two parameters, the equivalent radius and the equivalent contact angle, that need to be determined from experimental data by comparing with the Lucas-Washburn equation [Washburn 1921], which describes the capillary flow in a circular uniform tube.

Although what the Lucas-Washburn equation describes is the process of the liquid penetration into cylindrical capillaries, Washburn (1921) suggested that this equation

can be applied to the penetration of liquids into any porous media by assuming the porous body consists of assemblies of cylindrical capillary tubes which is the basic idea of the capillary penetration method of the porous media characterization. Elley and Pepper (1946) used such a cylindrical tube model to determine the adhesion tension of Nujol, benzene, and water in a vertical plug of Pyrex glass powders. Studebaker and Snow (1955) developed a method for determining contact angles of capillary flow in porous media. In this method, the times required for two liquids: the reference liquid with zero contact angle and the purpose liquid with a finite contact angle, to travel a given distance through a particular powder bed. The mean apparent radius,  $r_a$ , of the powder bed is obtained by comparing the data of the reference liquid with the calculated results of Lucas-Washburn equation. With the assumption that the geometrical contributions to flow behavior are the same for both liquids, the contact angle of the second liquid can be calculated from the following equation:

$$\cos \alpha = \frac{\gamma_1 \mu_2 t_1}{\gamma_2 \mu_1 t_2} \quad (1.59)$$

This method is also called the two-liquid method. Similar studies estimating adhesion tension and contact angles of liquids with powders using this approach have been carried out by Crowl and Wooldridge (1967), and Bruil and Van Aartsen (1974). Good (1973) discussed the validity of the Washburn equation when applied to a porous medium and found an additional driving force due to the reduction in free energy of the solid covered by an adsorbed vapor film which may lead to a faster rate of penetration than that predicted by the Washburn equation. Recently, Lavi et al. (2008) assessed the validity of using the Washburn equation for porous media characterization by the two-liquid capillary penetration method numerically and experimentally. It was found that using the Washburn equation and ignoring inertia and dynamic contact angle effects may lead to very erroneous assessment of the capillary radius and the equilibrium contact angle, for a relatively wide range of capillary radii and equilibrium contact angles.

The core problem of the dynamic capillary rise in porous media and the porous media characterization is establishing a simplified model describing the physical

process of the dynamic capillary flow in a single tube, which approximately represents the characteristic geometry in the real porous media. The reported models include the circular uniform tube model, also called cylindrical tube model or Lucas-Washburn model, noncircular uniform tube model and nonuniform tube model which are reviewed hereafter in this section.

#### Capillary Flow in Circular Uniform Tubes

Washburn (1921) developed the equation to describe the rate of penetration of liquids into small cylindrical capillaries based on the laws of hydraulics. He assumed that the distance traveling in the initial turbulence period is negligible, and the Poiseuille region covers practically the entire flow. According to Poiseuille's law, neglecting the air resistance, the rate of flow through a cylindrical takes the following form:

$$Q = \frac{\pi \Delta p}{8 \mu h} (r^4 + L_s r^3) \quad (1.60)$$

where,  $r$  is the radius of the tube,  $h$  is the capillary penetration distance,  $L_s$  is the slip length.  $Q$  is the rate of flow and for a cylindrical tube it is written by:

$$Q = \pi r^2 \frac{dh}{dt} \quad (1.61)$$

The total effective driving pressure,  $\Delta p$ , consists of the external pressure,  $P_e$ , the hydrostatic pressure,  $P_h$  and the capillary pressure given by Young-Laplace equation (1.1). Combining Equations (1.1), (1.59) and (1.60) and neglecting the slip length gives the so-called Lucas-Washburn equation:

$$\frac{dh}{dt} = \frac{r^2}{8\mu h} \left( P_e + P_h + \frac{2\gamma \cos \theta}{r} \right) \quad (1.62)$$

If there is no external pressure, a commonly used form of Lucas-Washburn equation is written as:

$$8\mu h \frac{dh}{dt} = 2r\gamma \cos \theta - \rho g h r^2 \sin \varphi \quad (1.63)$$

where  $\varphi$  is the incline angle of the tube with respect to the horizontal surface. Equation (1.62) indicates that the surface tension driven force is balanced by the viscous force and the gravitational force. For capillary flow in a horizontal cylindrical tube or where the gravitational force is negligible, an analytical solution

of equation (1.62) excluding the last term can be obtained with the initial condition  $h(0) = 0$ :

$$h = \sqrt{\frac{r\gamma \cos \theta}{2\mu}} \cdot \sqrt{t} \quad (1.64)$$

Equation (1.63) implies that the wetting length of the liquid driven by surface tension force is dependent on the square root of time. Rideal (1922) also obtained this equation through a rather simple derivation. Brittin (1946) derived a more rigorous formulation of Lucas-Washburn equation by including the momentum of the liquid in the tube and the end-effect drag on the fluid entering the tube:

$$h \frac{d^2h}{dt^2} + \frac{5}{4} \left( \frac{dh}{dt} \right)^2 + \frac{8\mu}{\rho r^2} h \frac{dh}{dt} + gh \sin \varphi - \frac{2\gamma \cos \theta}{\rho r} = 0 \quad (1.65)$$

Analogous to the above derivation for the rate of penetration of a liquid into a cylindrical tube, Levine and Neale (1975) derived the equation for the rate of wetting in a porous medium based on Darcy's law and evaluated the value of permeability by a Happel's cell-type model, which regards the porous medium as one consisting of identical spherical particles. Levine et al. (1977) later investigated various factors governing

the rate of wetting/dewetting of porous media and derived a macroscopic equation for the capillary phenomenon by including the energy dissipation due to irreversible movement of the meniscus.

Xiao et al. (2006) considered the entrance pressure loss effects by using recent Dreyer's (1993) model and dynamic contact angle effect by Newman's (1968) model to further modified Lucas-Washburn equation:

$$\begin{aligned} (h + 1.028r) \frac{d^2h}{dt^2} + 0.958 \left( \frac{dh}{dt} \right)^2 + \frac{8\mu}{\rho r^2} (h + 0.25r) \frac{dh}{dt} \\ + gh \sin \varphi - \frac{2\gamma \cos \theta_d}{\rho r} = 0 \end{aligned} \quad (1.66)$$

The modified Washburn equation is a second-order non-linear differential equation, the solution of which can be obtained in the form of a double Dirichlet series [Brittin 1946; Xiao et al. 2006]. Other modifications of Lucas-Washburn equation by using a different dynamic contact angle model as discussed in the previous section can be found in [Joos et al. 1990; Hamraoui and Nylander 2002; Popescu et al. 2008]. Fisher and Lark (1979) validated the Lucas-Washburn equation for the flow of water and cyclohexane in very fine glass capillaries. The application of the Washburn equation in simple geometric

systems has also been shown in Blake et al. (1967) in examining two-phase capillary flow at various applied pressures. Dimitrov et al. (2007) investigated the capillary rise in nanopores and provided a molecular dynamics evidence for the Lucas-Washburn equation by taking the slip length into account.

#### Capillary Flow in Noncircular Uniform Tubes

In addition to the commonly used circular uniform tube model, describing the capillary flow in porous media, similar approaches have also been extended to consider irregular geometries. For example, the modeling of fluid flow in porous petroleum reservoir rocks can be improved upon by considering the pores to be triangular tubes [Dong and Chatzis 1995; Dong et al. 1995; Lago and Araujo 2001; Helland and Skjaeveland 2006; Jia et al. 2008]. Moreover, the capillary effect may become prevalent in the fluid system in a microgravity environment of space where capillary imbibitions flow in interior corners, also called grooves or wedges, which are of particular importance in space applications including all kinds of fluid management and control such

as fuel propellants and biological wastes, design of heat exchangers and heat pipes [Su and Lai 2004].

The static capillary behavior of liquids in irregular cross-sectional geometries has been well addressed by literature. Concus and Finn reported the effect of the contact angle and corner half-angle [Concus and Finn 1974a; 1974b] and container aspect ratio and corner rounding [Concus and Finn 1990] on the static capillary free surface in a wedge. Mason and Morrow (1991) investigated the meniscus curvature in cylindrical capillaries with a triangular cross section. Wong et al. (1992) proposed a novel solution approach to describe three dimensional menisci in polygonal capillaries based on the inclusion of molecular forces. Mason and Morrow (1994) examined the effects of the pore shape in porous media and the contact angle on the capillary displacement curvatures in pore throats formed by the surfaces of equal spheres. Mittelman and Zhu (1996) described a numerical method to determine the shape of capillary surfaces with differing contact angles on adjacent faces of the corner. Strictly based on the Gauss-Laplace equation, deLazzer et al. (1996) derived the mathematical

relations for the mean curvature,  $H$ , of wedge-wetting interfaces in cylindrical containers of  $N$ -polygonal cross section, which are written as:

$$H = \cos \theta \cdot \sqrt{\frac{N}{S} \tan \left( \frac{\pi}{N} \right)}, \quad \theta \geq \frac{\pi}{N} \quad (1.67)$$

$$H = \frac{1}{2} \sqrt{\frac{N}{S}} \left[ \cos \theta \sqrt{\tan \left( \frac{\pi}{N} \right)} + \sqrt{\cos \theta \cos \theta + \frac{\pi}{N} - \theta} \right], \quad \theta < \frac{\pi}{N} \quad (1.68)$$

where  $S$  is the area of the cross section and  $\theta$  is the contact angle.

A significant amount of attention has also been devoted to the dynamics of capillary flow in irregular geometries. Ayyaswamy et al. (1974) proposed that the evolution of the liquid obeys a nonlinear convection-diffusion equation by assuming the advancing liquid flow is quasi-unidirectional and the inertial effect is negligible. The coefficients of the equation are found to be dependent on a friction factor or the hydraulic resistance of the walls to the flow. A similar two dimensional hydrodynamic solution of the capillary flow in a wedge is also obtained by Ransohoff and Radke (1988), although, a different nondimensional velocity distribution at any cross section along the flow

direction was used. They both discussed the effects of the variation of the contact angle and wedge angle on the flow behavior. Dong and Chatzis (1995) adopt this formulation to analyze the liquid imbibition in the corners of the square cross sectional capillary tube and found a similarity solution applicable to their problem.

Ma et al. (1994) obtained an analytical expression of velocity distribution of any cross section by assuming a constant velocity of the free surface and numerically studied the liquid-gas frictional interaction of the flow in triangular microgrooves. The analysis of the heat transfer in microheat pipes were reported in their later work [Peterson and Ma 1996a; 1996b; Ma and Peterson 1997a; 1997b].

Catton and Stroes (2002) proposed a semi-analytical, one-dimensional model for predicting the wetted length of inclined triangular capillary grooves subject to below heating. The model utilizes a macroscopic approach with the concept of an apparent contact angle and the assumption of constant liquid properties. Beyond the studies on the dynamics of the steady-state flow behavior, Romero and Yost (1996) considered the capillary

flow in a V-shaped surface groove. The similarity solution of the diffusion equation, derived from the law of mass conservation and the Poiseuille flow conditions, show that the location of the contact line is proportional to  $(Dt)^{1/2}$  where  $D$  is a diffusion coefficient written as:

$$D = \frac{\gamma h_0}{\mu} K(\theta, \alpha) \quad (1.69)$$

where  $\gamma$  is the gas-liquid surface tension,  $\mu$  is the liquid viscosity,  $h_0$  is the depth of the groove depth,  $\theta$  is the contact angle,  $\alpha$  is the groove angle, and

$$K(\theta, \alpha) = \frac{\Gamma(\theta, \alpha) \sin(\alpha - \theta) \tan \alpha}{\hat{A}(\theta, \alpha)} \quad (1.70)$$

$$\hat{A}(\theta, \alpha) = \frac{\sin^2(\alpha - \theta) \tan \alpha - (\alpha - \theta) + \sin(\alpha - \theta) \cos(\alpha - \theta)}{\tan^2 \alpha \cdot \sin^2(\alpha - \theta)} \quad (1.71)$$

$$\Gamma(\theta, \alpha) \approx \frac{1}{6} \cdot \left( 1 + \cot \alpha \cdot \frac{\cos(\alpha - \theta) - 1}{\sin(\alpha - \theta)} \right)^3 \left( \frac{\hat{A}(\theta, \alpha)}{\cot \alpha} \right)^{1/2} \quad (1.72)$$

$$\frac{\cot^3 \alpha + 3.4 \cot^4 \alpha + \cot^5 \alpha}{1 + 3.4 \cot \alpha + 4 \cot^2 \alpha + 3.4 \cot^3 \alpha + \cot^4 \alpha}$$

Verbist et al. (1996) and Kovscek and Radke (1996) modified the governing equation to include the effect of the gravity force on the spreading process.

Weislogel and Lichter (1998) reported their measurements of the capillary flow in an interior corner from a 2.2s drop tower and found three stages in a transient capillary wedge flow: the start-up stage governed by inertia; the intermediate regime modeled by a constant-flow-like similarity solution; and the final stage with constant interface height. Theoretically, they considered the spontaneous redistribution of capillary flow along an interior corner and obtained an asymptotic formulation on the limit of a slender liquid column with small inertia and low gravity. For the constant flow region and the constant height region, their similarity solutions indicate that the tip location of the liquid column increases as  $t^{3/5}$  and  $t^{1/2}$ , respectively. The same relations are obtained by Su and Lai (2004) in both the analytic solutions and the numerical simulations for a capillary flow in a wedge with constant contact angle interfacial shear stress, contact angle and wedge angle. They also found that the functional relationship becomes invalid when the interface shear-stress varies in the flow direction.

Higuera et al. (2008) studied the time evolution of capillary rise of a wetting liquid in the gap between two vertical plates with a small wedge angle numerically and experimentally. They found that the height of the liquid increases proportionally to time in the first stage of evolution, and the effect of the gravity is negligible in a region around the edge of the gap. However, the maximum height, attained outside of this region, is proportional to the cubic root of time.

The motion of long bubbles in angular capillary tubes is investigated by Kolb and Cerro (1993) and Bico and Quéré (2002). For low gravity applications, a collection of solutions for capillary driven flows in interior corners of interest is provided by Weislogel (2003).

Turian and Kessler (2000) analyzed the 1-D axial capillary-driven flow in uniform capillaries with general noncircular cross section subject to quadrant symmetry constraints. Ichikawa et. al. (2004) extended the analyses for circular cylindrical tubes to rectangular micro channels. Experimentally, Jong, et. al.(2007)

reported results of capillary flow in rectangular microchannels under gravity.

### Capillary Flow in Nonuniform Tubes

The drawback with the uniform tube model discussed above is that an effective capillary radius cannot be ascribed to describe the nature of the real porous media with constrictions and expansions along the flow paths. Typically, kinetics of capillary rise by taking an average pore radius based on the pore size distribution was found to be faster than that observed experimentally [Patro et al. 2007; Patro and Jayaram 2008]. More realistic models of nonuniform capillaries have been proposed to incorporate the essential convergent-divergent nature of flow path in a porous medium. Dullien (1977) attempted to approximate the nature of flow in a porous medium by a simple stepped tube model which ascribed the slow capillary rise in porous media to the small driving forces on the meniscus in the divergent sections. Einset (1996) used the two-sized single pore model to analyze the rate of capillary rise of a liquid into a porous medium made up of consolidated

particulates, and the predicted infiltration rate is consistent with the experimental results. Sinusoidal capillary models (Sharma, 1991; Staples and Shaffer, 2002) with convergent-divergent sections have been developed as a more realistic representation of flow paths in porous bodies. Erickson et al (2002) studied the dynamic capillary driven flow in straight convergent-divergent and divergent-convergent capillary tubes by using finite element numerical simulation. Young (2004) extended the sinusoidal capillary model to analysis the capillary driven flow in Erickson et al. (2002)'s specific non-uniform geometries. Patro et al. (2007) adopted the same non-uniform capillary model to explain the capillary rise kinetics inside porous  $\text{Al}_2\text{O}_3$  compacts by using a sinusoidal capillary wall with convergent-divergent sections to approximate the real flow path in the porous medium.

### **1.5 Objectives of the Research**

The current models for capillaries of axially varying cross sectional shapes [Sharma and Ross 1991; Staples and Shaffer 2002; Young 2004; Patro et al. 2007; Patro and Jayaram 2008] considered the nonuniform

geometry effect on the viscous terms in the cross sectional plane. But the likely variation of the axial velocity component in the main stream direction has not been accounted for in the viscous terms. The inertial effects were also ignored in the models. There are industrial applications of capillary flow in complex porous media where the axial flow variation and the inertial effects can be important. For instance, the rigid-capillary-pressing (RCP) technology is used to improve the dewatering efficiency in the paper-making process [Stelljes et al. 2004]. The paper industry is one of the major industrial energy users, and a large proportion of this energy is used to dry the wet paper web. Large mechanical presses are used for many paper grades to reduce the water content from approximately 3 kg water / kg fiber to about 1.5 kg water/ kg fiber, with thermal energy being used to further reduce the water content to about 0.05 kg water / kg fiber. In addition, there are many grades of paper, such as bath and facial tissue, which cannot be mechanically pressed to dewater the sheet in order to maintain end-use properties. For these grades, virtually 100% of the water

(approximately 3 kg water / kg fiber) is currently removed via evaporation. Removal of some of this water via capillary action has the potential to substantially decrease the thermal energy use needed to dry these grades. Experiments have shown that capillary dewatering, using the layered, porous structures can remove approximately 0.5 to 0.7 kg water/kg fiber, which results in 16 - 20% thermal energy savings. During this dewatering process, the capillary flow passes through a thin porous medium with large change in pore sizes. The porous medium is composed of layers of lamina of pore sizes ranging possibly from  $10\mu\text{m}$  to  $1000\mu\text{m}$ .

A more physically realistic modeling of the capillary rise will help advance the understanding of the various fluid dynamic mechanisms at work in such porous media. A general non-uniform capillary model is proposed to describe the capillary flow kinetics in any varying cross-sectional tubes. The analysis started from the Navier-stokes equation and was based on the parabolic velocity profile assumption in the primary axis direction. The governing equation is derived by the

integration of the axial momentum equation over the liquid volume.

The present model is first validated by comparing the solutions of circular cylindrical tubes, rectangular cylindrical tube and the convergent-divergent and divergent-convergent tubes with the previous solutions. The proposed model is then applied to four different tube geometries, including a linearly divergent/convergent wall, parabolic varying wall, sinusoidal wall, and sinusoidal divergent wall. The nonuniformity effects are investigated in detail. The simulation results, especially for the capillary flow under the influence of gravity, show that the present model predicts significant effects of nonuniformity in comparison with the previous model.

Using perturbation method, a closed-form expression of velocity distribution is obtained by an asymptotic series solution of stream function in a circular tube of varying radius, which offers an improvement over the parabolic form. Based on the new velocity distribution, a new governing equation is derived using the proposed theoretical approach. The modified capillary model also

considers the dynamic contact angle (DCA) effect. A new DCA model, combining the current velocity-dependent model based on molecular-kinetic theory and empirical time-dependent model based on experiments, is proposed to describe the dynamic transition process of the gas-liquid interface. The applicable scope of the new DCA model is extended to the entire process from the initial state to the equilibrium state. The proposed model is validated by examining a series of experiments of the capillary rise in nonuniform tubes.

The similar analytical approach has also been extended to investigate the capillary flow kinetics in a specific multi-layer porous medium, called Rigid-Capillary-Pressing (RCP) medium, which is invented by the Procter & Gamble company and is used for a high-efficiency dewatering in the paper making process. An analytical model has been developed to model the RCP dewatering process. In comparison with the experimental data, the proposed theoretical model predicts well the dewatering performance of the device, and hence, can potentially be used as an industrial design optimization tool.

This analytical work also can be applied to the capillary flow in other complex geometries and various porous media.

## **CHAPTER 2**

### **MODELING OF CAPILLARY FLOW OF CONSTANT CONTACT ANGLE IN TUBES OF NONUNIFORM ELLIPTICAL CROSS SECTION**

In this chapter, the capillary flows in nonuniform capillaries with elliptical cross section are investigated analytically. The analysis starts from the Navier-Stokes equations, and a governing equation is derived by the integration of the axial momentum equation over the liquid volume. The analysis has been developed by assuming a parabolic distribution for the velocity component in the primary flow direction and has considered the secondary flow components based on mass conservation. Compared to the classic Lucas-Washburn equation [Washburn 1921; Brittin 1946; Hamraoui and Nylander 2002; Xiao et al. 2006] and the existing nonuniform capillary model equations [Sharma and Ross 1991; Staples and Shaffer 2002; Young 2004; Patro et al. 2007; Patro and Jayaram 2008], the model presented in this chapter incorporates the inertial terms and the viscous terms for nonuniform geometries with the constant contact angle assumption. The derived nonlinear, second-

order differential equation is complex, and a MatLab code has been developed to solve the equation numerically by using the adaptive Runge-Kutta-Fehlberg method [Curtis and Patrick 1994]. The present model is first validated by comparing its solution with that of the existing model equations for the circular cylindrical tubes, rectangular cylindrical microchannels [Ichikawa et al. 2004; Jong et al. 2007], and convergent-divergent (C-D) and divergent-convergent (D-C) capillaries [Erickson 2002]. The proposed model is then applied to capillaries with parabolic varying wall, simple sinusoidal wall, and divergent sinusoidal wall. The nonuniform geometry effects are investigated in detail. The simulation results, especially those for capillaries with large variations of cross section, show that there are significant effects of nonuniform geometry in the cases studied.

## **2.1 Model Equation**

The proposed model equation is first derived, and its characters are discussed in the section.

### Derivation of the Governing Equation

For Newtonian, incompressible fluid flows of constant density and viscosity, the Navier-Stokes equations can be written in the Cartesian coordinates ( $x$ ,  $y$ ,  $z$ ) as,

$$\frac{\partial v_x}{\partial x} + \frac{\partial v_y}{\partial y} + \frac{\partial v_z}{\partial z} = 0 \quad (2.1)$$

$$\begin{aligned} \rho \left( \frac{\partial v_x}{\partial t} + v_x \frac{\partial v_x}{\partial x} + v_y \frac{\partial v_x}{\partial y} + v_z \frac{\partial v_x}{\partial z} \right) \\ = \mu \left( \frac{\partial^2 v_x}{\partial x^2} + \frac{\partial^2 v_x}{\partial y^2} + \frac{\partial^2 v_x}{\partial z^2} \right) - \frac{\partial p}{\partial x} \end{aligned} \quad (2.2)$$

$$\begin{aligned} \rho \left( \frac{\partial v_y}{\partial t} + v_x \frac{\partial v_y}{\partial x} + v_y \frac{\partial v_y}{\partial y} + v_z \frac{\partial v_y}{\partial z} \right) \\ = \mu \left( \frac{\partial^2 v_y}{\partial x^2} + \frac{\partial^2 v_y}{\partial y^2} + \frac{\partial^2 v_y}{\partial z^2} \right) - \frac{\partial p}{\partial y} \end{aligned} \quad (2.3)$$

$$\begin{aligned} \rho \left( \frac{\partial v_z}{\partial t} + v_x \frac{\partial v_z}{\partial x} + v_y \frac{\partial v_z}{\partial y} + v_z \frac{\partial v_z}{\partial z} \right) \\ = \mu \left( \frac{\partial^2 v_z}{\partial x^2} + \frac{\partial^2 v_z}{\partial y^2} + \frac{\partial^2 v_z}{\partial z^2} \right) - \frac{\partial p}{\partial z} \end{aligned} \quad (2.4)$$

where,  $v_x$ ,  $v_y$ , and  $v_z$  are velocity components in  $x$ ,  $y$ , and  $z$  directions, respectively.  $t$ ,  $\rho$ ,  $p$ , and  $\mu$  denote time, density, pressure, and viscosity, respectively.

The surface tension driven liquid flows in tubes with nonuniform cross section distribution along the axis of the tube are considered. Figure 2.1 shows a sketch of

such a capillary tube. Elliptic cross section is assumed, and the perimeter of the cross section is governed by:

$$x^2 + Ky^2 = R^2(z) \quad (2.5)$$

where  $R$  denotes the semi-major axis that varies along the  $z$  direction.  $K$  denotes the square of the ratio of the semi-major axis to the semi-minor axis.

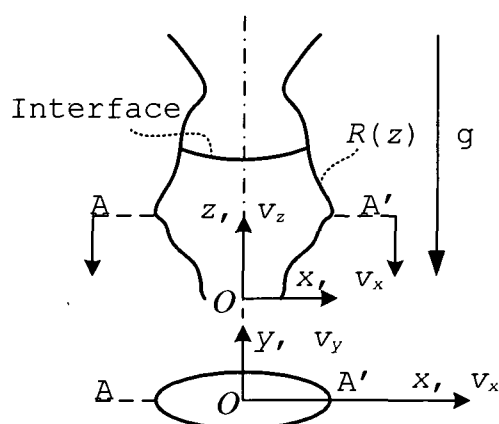


Figure 2.1 Schematic of a nonuniform tube with elliptical cross-section.

The elliptical cross section allows for the modeling of tubes with a cross section ranging from circular to near rectangular. In this analysis, the length scale of the local axial variation of the cross sectional dimension is assumed small compared with the length of the capillary considered, which is valid for most engineering applications.

Due to the small Reynolds number, the capillary flows are laminar in nature, and a parabolic profile is assumed for the axial velocity component  $v_z$ . That is,

$$v_z(x, y, z, t) = 2 \frac{dh}{dt} \frac{R^2(h)}{R^2(z)} \left( 1 - \frac{x^2}{R^2(z)} - K \frac{y^2}{R^2(z)} \right), \quad z < h \quad (2.6)$$

where  $h$  represents the height of the capillary rise and  $dh / dt$  the average velocity of the flow front. Similar parabolic axial velocity distributions are widely used for the axial velocity component. Such a velocity distribution is not expected in regions near the entrance of the capillary and near the meniscus. However, for uniform circular capillaries, the entrance length was reported to be about two hydraulic diameters [Duarte et al. 1996], which is small compared with the length of the tubes studied here. The meniscus depth is also assumed small compared with tube length considered. Therefore, the error introduced by the approximation of  $v_z$  is limited to a very short-time period after the meniscus is allowed to rise in the capillary tube. For  $v_x$  and  $v_y$ , we consider a radial flow model and assume that:

$$\frac{v_y}{v_x} = \frac{y}{x} \quad (2.7)$$

From Equations (2.1), (2.6), and (2.7), the expressions for  $v_x$  and  $v_y$  are obtained as:

$$v_x(x, y, z, t) = 2 \frac{R^2(h)}{R^2(z)} \frac{dh}{dt} \frac{dR(z)}{dz} \left( -\frac{x^3 + Ky^2x}{R^3(z)} + \frac{x}{R(z)} \right) \quad (2.8)$$

$$v_y(x, y, z, t) = 2 \frac{R^2(h)}{R^2(z)} \frac{dh}{dt} \frac{dR(z)}{dz} \left( -\frac{yx^2 + Ky^3}{R^3(z)} + \frac{y}{R(z)} \right) \quad (2.9)$$

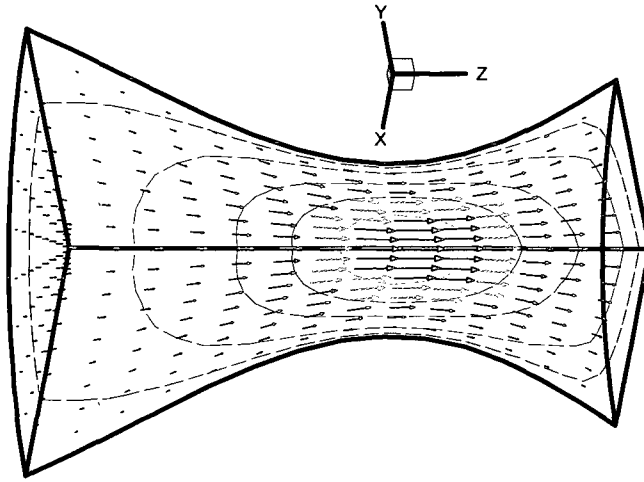


Figure 2.2 Velocity contour and velocity vector for sinusoidal tube.

Equations (2.6), (2.8), and (2.9) describe the three-dimensional velocity field model used in the current formulation for nonuniform cross sections. The velocity vectors and the velocity magnitude contours, normalized by  $2 \frac{R^2(h)}{R^2(z)} \frac{dh}{dt}$ , on the quarter planes for a sinusoidally varying tube are shown in Figure 2.2. The

velocity field model satisfies the no-slip boundary condition on the tube wall. At the limit of an interface height reaching equilibrium where  $dh / dt \rightarrow 0$ , the three modeled velocity components diminish, and the flow represented by the model becomes stationary. The velocity model suggests that the magnitudes of secondary velocity components vary with the axial variation of the cross sections  $dR / dz$ . For cases with uniform cross sections, or  $dR / dz = 0$ , the secondary flow, represented by  $v_x$  and  $v_y$ , becomes zero, which agrees with the widely used unidirectional flow approximation. For axially divergent tubes, where  $dR / dz > 0$ , the modeled secondary flow moves radially outward. Similarly, the modeled secondary flow moves inward for convergent tubes. According to the velocity model, the ratio of the velocity magnitude of the secondary flow to that of the primary flow is:

$$\frac{\sqrt{v_x^2 + v_y^2}}{v_z} = \frac{\sqrt{x^2 + y^2}}{R(z)} \cdot \frac{dR(z)}{dz} \quad (2.10)$$

For tubes with small divergence/convergence, the secondary flow is small, and the velocity model is valid. For tubes with large divergence/convergence, the secondary flow components are always small near the tube

centerline, but can become significant toward the perimeter of the tube. In this region, the approximation that the axial velocity component distributes in a parabolic manner can be less satisfactory.

To examine a transient capillary rise problem where the interface, starting from  $z = 0$  at  $t = 0$ , has reached a height of  $z = h$  at time  $t$ , a control volume enclosing the liquid in the capillary between the inlet and the interface is selected. The  $z$ -momentum Equation (2.4) is integrated in the control volume, which gives:

$$\begin{aligned} & \iiint \rho \left( \frac{\partial v_z}{\partial t} + v_x \frac{\partial v_z}{\partial x} + v_y \frac{\partial v_z}{\partial y} + v_z \frac{\partial v_z}{\partial z} \right) dV & (2.11) \\ & = \iiint \mu \left( \frac{\partial^2 v_z}{\partial x^2} + \frac{\partial^2 v_z}{\partial y^2} + \frac{\partial^2 v_z}{\partial z^2} \right) dV + \iiint \left( -\frac{\partial p}{\partial z} \right) dV \end{aligned}$$

Using the expressions of the velocity components  $v_x$ ,  $v_y$ ,  $v_z$  as shown in Equations (2.6), (2.8) and (2.9), the terms appeared in Equation (2.11) can be expressed as follows after the calculation of the area integration on the cross section.

$$\iiint \rho \frac{\partial v_z}{\partial t} dV = \frac{\pi}{\sqrt{K}} \rho \frac{d}{dt} \left[ \frac{dh}{dt} R(h)^2 h \right] \quad (2.12)$$

$$\begin{aligned} & \iiint \rho v_x \frac{\partial v_z}{\partial x} dV & (2.13) \\ &= \frac{4\pi}{3} \frac{(K^2 - 14K - 3)}{\sqrt{K}(1+K)(3K+1)(3+K)} \rho \left(\frac{dh}{dt}\right)^2 R(h)^4 \int_0^h \frac{1}{R(z)^3} \frac{dR(z)}{dz} dz \end{aligned}$$

$$\begin{aligned} & \iiint \rho v_y \frac{\partial v_z}{\partial y} dV & (2.14) \\ &= -\frac{4\pi}{3} \frac{\sqrt{K}(3K^2 + 14K - 1)}{(3K+1)(K+1)(K+3)} \rho \left(\frac{dh}{dt}\right)^2 R(h)^4 \int_0^h \frac{1}{R(z)^3} \frac{dR(z)}{dz} dz \end{aligned}$$

$$\iiint \rho v_z \frac{\partial v_z}{\partial z} dV = -\frac{4\pi}{3\sqrt{K}} \rho \left(\frac{dh}{dt}\right)^2 R(h)^4 \int_0^h \frac{1}{R(z)^3} \frac{dR(z)}{dz} dz \quad (2.15)$$

$$\iiint \mu \frac{\partial^2 v_z}{\partial x^2} dV = -\frac{4\pi}{\sqrt{K}} \mu \frac{dh}{dt} R(h)^2 \int_0^h \frac{1}{R(z)^2} dz \quad (2.16)$$

$$\iiint \mu \frac{\partial^2 v_z}{\partial y^2} dV = -4\pi\sqrt{K}\mu \frac{dh}{dt} R(h)^2 \int_0^h \frac{1}{R(z)^2} dz \quad (2.17)$$

$$\iiint \mu \frac{\partial^2 v_z}{\partial z^2} dV = -\frac{8\pi}{\sqrt{K}} \mu R(h)^2 \frac{dh}{dt} \int_0^h \left(\frac{dR(z)}{dz}\right)^2 \frac{1}{R(z)^2} dz \quad (2.18)$$

For the pressure term, it is known [Sharma and Ross 1991] that  $\partial p / \partial z$  is proportional to  $1 / R(z)^4$ . A general expression is adopted here,

$$\frac{\partial p}{\partial z} = \frac{E}{R(z)^4} \quad (2.19)$$

where the function  $E$  is independent of  $z$ . Since we are considering capillary-driven flow,

$$\int_0^h \frac{E}{R(z)^4} dz = \frac{2\gamma \cos \theta}{r_E} - \rho gh \quad (2.20)$$

where,  $\gamma$  is the surface tension coefficient,  $\theta$  is the contact angle.  $r_E$  is the effective radius of the cross section at the interface position. For the ellipse at  $z = h$ , the effective radius can be calculated by

$$r_E = \frac{\pi R(h)}{\pi + 2(\sqrt{K} - 1)} \quad (2.21)$$

Therefore,

$$E = \left( \frac{2\gamma \cos \alpha}{r_E} - \rho gh \right) \cdot \left[ \int_0^h \frac{1}{R(z)^4} dz \right]^{-1} \quad (2.22)$$

Then, the pressure term can be obtained as:

$$\begin{aligned} & \iiint \left( -\frac{\partial p}{\partial z} \right) dV \quad (2.23) \\ &= \frac{\pi}{\sqrt{K}} \cdot \left[ \frac{2\gamma \cos \alpha (\pi + 2(\sqrt{K} - 1))}{\pi R(h)} - \rho gh \right] \cdot \frac{\int_0^h \frac{1}{R(z)^2} dz}{\int_0^h \frac{1}{R(z)^4} dz} \end{aligned}$$

By rearranging the terms, we may write the above equation as:

$$\begin{aligned} & \rho \frac{d}{dt} \left\{ \frac{dh}{dt} R(h)^2 h \right\} - \frac{8}{3} \rho \left( \frac{dh}{dt} \right)^2 R(h)^4 c_1 \quad (2.24) \\ &= -8\mu R(h)^2 \frac{dh}{dt} \left[ c_2 + \frac{(1+K)c_3}{2} \right] \\ &+ \frac{2 \left[ \pi + 2(\sqrt{K} - 1) \right] \gamma \cos \theta}{\pi R(h)} \cdot \frac{c_3}{c_4} - \rho gh \cdot \frac{c_3}{c_4} \end{aligned}$$

$\theta$  is the contact angle that, when incorporating the effect of the wall curvature [Patro et al. 2007], can be written as:

$$\theta = \theta_s + \theta_g \quad (2.25)$$

Here,  $\tan \theta_g = \frac{dR(z)}{dz}$  is the slope of the wall profile and  $\theta_g$ , the equilibrium contact angle.

The coefficients  $c_1$ ,  $c_2$ ,  $c_3$  and  $c_4$  that appear in Equation (2.12) are written as:

$$c_1 = \int_0^h \frac{1}{R(z)^3} \frac{dR(z)}{dz} dz \quad (2.26)$$

$$c_2 = \int_0^h \left( \frac{dR(z)}{dz} \right)^2 \frac{1}{R(z)^2} dz \quad (2.27)$$

$$c_3 = \int_0^h \frac{1}{R(z)^2} dz \quad (2.28)$$

$$c_4 = \int_0^h \frac{1}{R(z)^4} dz \quad (2.29)$$

The governing equation (2.24) incorporates the nonuniformity geometry effect through the above parameters and the contact angle which is discussed thereafter.

### Characteristics Analysis

The second-order nonlinear differential equation (2.24) governs the transient rise of the liquid interface in the nonuniform cross sectional capillary. Equation (2.24) contains terms commonly found in various forms of capillary equations. They are the viscous terms, the surface tension terms, and the gravity term, which, respectively, are the first, second, and the third terms on the right hand side of equation. In addition, the present model also includes the effects of fluid inertia on the left hand side of the equation.

For a circular ( $\kappa = 1$ ) cylindrical capillary of radius  $R_0$ , Equation (2.24) can be written as:

$$\pi\rho R_0^2 h \frac{d^2 h}{dt^2} + \pi\rho R_0^2 \left( \frac{dh}{dt} \right)^2 = -8\pi\mu h \frac{dh}{dt} + 2\pi\gamma R_0 \cos \theta_s - \pi\rho g R_0^2 h \quad (2.30)$$

That is, the current model equation reduces to the modified Lucas-Washburn equation [Hamraoui and Nylander 2002]. For a nonuniform tube with circular cross section, Equation (2.24) can be written as:

$$I_c + 8\mu N_c \cdot (1 + V_c) \cdot \frac{dh}{dt} = 2\gamma \cos \theta_s - \rho g h \cdot R(h) \quad (2.31)$$

where,

$$I_c = \frac{c_4}{c_3} \cdot \rho R(h) \frac{d}{dt} \left[ \frac{dh}{dt} R^2(h)h \right] - \frac{8c_1c_4}{3c_3} \cdot \rho \left( \frac{dh}{dt} \right)^2 R^5(h) \quad (2.32)$$

$$V_c = c_2 / c_3 \quad (2.33)$$

$$N_c = c_4 R^3(h) \quad (2.34)$$

When the fluid inertia effect is negligible, equation (2.31) reduces to:

$$8\mu N_c \cdot (1 + V_c) \cdot \frac{dh}{dt} = 2\gamma \cos \theta - \rho gh \cdot R(h) \quad (2.35)$$

A comparison of Equation (2.35) and the equation reported by Staples and Shaffer (2002) and Young (2004) for nonuniform, circular capillary flows,

$$8\mu N_c \cdot \frac{dh}{dt} = 2\gamma \cos \theta - \rho gh \cdot R(h) \quad (2.36)$$

shows that both equations contain terms accounting for viscous, surface tension, and gravity effects and neglect inertia term  $I_c$ .  $N_c$  appears in both models, and it

represents the nonuniform geometry effect associated with

the two viscous terms on the cross sectional plane:  $\mu \frac{\partial^2 v_z}{\partial x^2}$

and  $\mu \frac{\partial^2 v_z}{\partial y^2}$ .  $V_c$  represents the nonuniform geometry effects

in the viscous terms in the current model equation that

has not been considered in Equation (2.36) [Staples and

Shaffer 2002; Young 2004].  $V_c$  includes the nonuniformity

effect associated with the axial viscous normal stress

$\mu \frac{\partial^2 v_z}{\partial z^2}$ . This term was neglected in the derivation of

Equation (2.36). Equation (2.35) reduces to Equation (2.36) if  $V_c$  is set equal to zero. As will be shown, the effect of the axial variation of the viscous stress and the inertial terms can be significant in the cases studied.

The capillary interface will reach equilibrium state with the presence of gravity. At equilibrium,  $dh / dt = 0$  and Equation (2.31) becomes:

$$2\gamma \cos \theta - \rho gh \cdot R(h) = 0 \quad (2.37)$$

At the initial time,  $t \rightarrow 0$  and  $h \rightarrow 0$ , Equation (31) can be simplified as:

$$\rho R_{h \rightarrow 0} \left( \frac{dh}{dt} \right)_{t \rightarrow 0}^2 = 2\gamma \cos \theta_{t \rightarrow 0} \quad (2.38)$$

An estimation of the speed of the initial capillary rise under inertial effects can be made accordingly,

$$v_0 = \left. \frac{dh}{dt} \right|_{t \rightarrow 0} = \sqrt{\frac{2\gamma \cos \theta_{t \rightarrow 0}}{\rho R_{h \rightarrow 0}}} \quad (2.39)$$

Without inertial effect, as indicated in Equation (2.35), the initial capillary rise velocity approaches infinity in the limit of  $h \rightarrow 0$ . The inertial effect, therefore,

renders the initial capillary rising speed finite, which can be observed from the results shown in the following section.

## 2.2 Model Validation

To validate the proposed nonuniform capillary model, the capillary flows in several commonly found geometries, including the circular cylindrical capillary, rectangular cylindrical microchannels, and Erickson's nonuniform geometries [21], are investigated using the proposed model. For all the following cases, the second-order differential equation (2.31) and the first-order differential equations (2.35) and (2.36) are solved by using the Runge-Kutta method. The calculations start from an initial height of  $10^{-13}$ m at  $t = 0$ . The time step is adaptively adjusted by using the Fehlberg scheme [Curtis and Patrick 1994] with critique error of  $10^{-10}$ , and the initial time step  $\Delta t_{init} = 10^{-15}$ s. Numerical integration of Equation (2.31) is not sensitive to the value used for the initial velocity. For instance, the numerical solutions of different cases, of which the initial velocity ranges from zero up to 100m/s, quickly ( $<10^{-10}$ s)

asymptote to the same solution curve as that obtained by using the value based on Equation (2.39).

### Circular Cylindrical Capillary

To verify the model equations derived above, the rise of the meniscus in a capillary of a uniform circular cross section of radius  $R_0 = 50\mu\text{m}$  will be used as the first test problem.

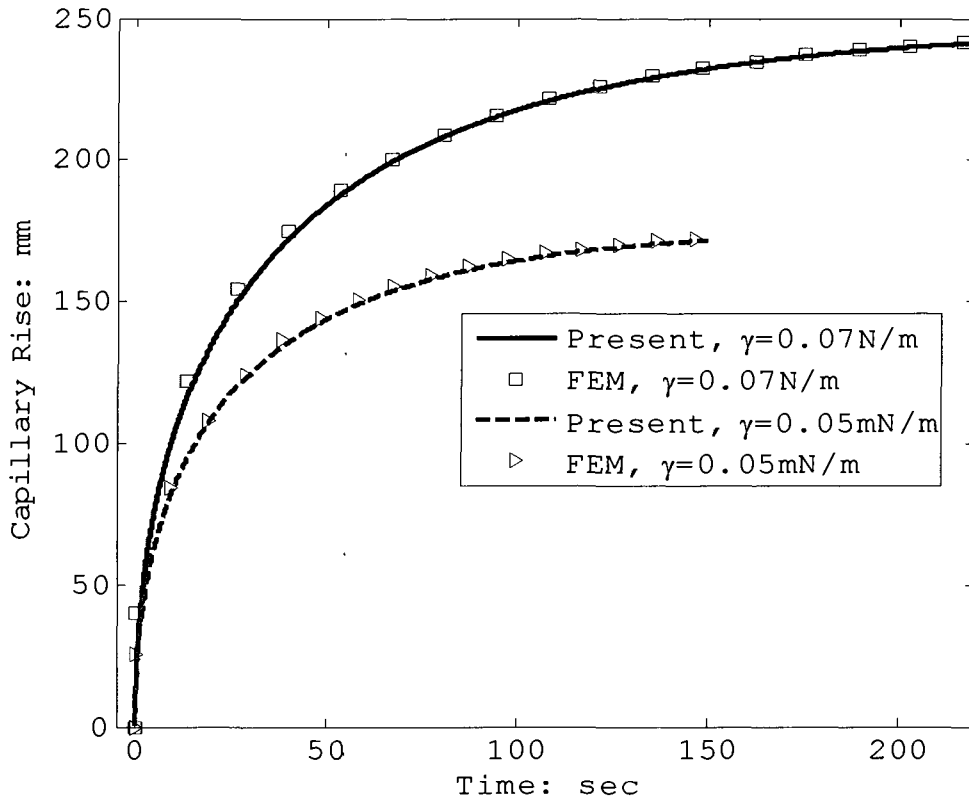


Figure 2.3 Comparison of the present model solution with the FEM solution [Erickson et al. 2002] for the capillary rise in a 100- $\mu\text{m}$ -diameter capillary tube.

The surface tensions used are 0.07 and 0.05 N/m, respectively. Also,  $\theta_s = 30^\circ$ ,  $\rho = 1000\text{kg/m}^3$ , and  $\mu = 0.001 \text{ kg} \cdot \text{m}^{-1}\text{s}^{-1}$ .

Figure 2.3 compares the results of the present model with the finite element method (FEM) results [Erickson et al. 2002]. As it can be seen, the advancement of the interfaces as calculated by the present model agrees with the numerical solution for both surface tensions.

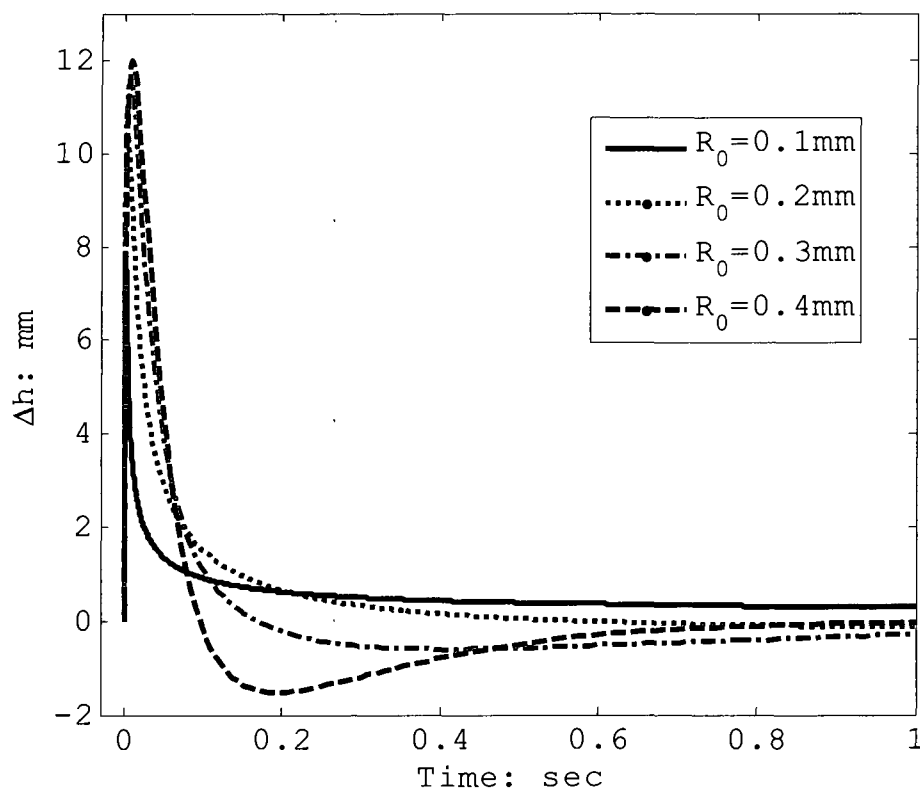


Figure 2.4 Effects of fluid inertia on the capillary rise in circular cylindrical tubes of different radius.

The inertia terms in the present model depend on the radius of the capillary,  $R_0$ , the rise velocity  $dh / dt$ , and  $d^2h / dt^2$ . To investigate the influence of the inertial terms on the capillary flow, we consider four tubes of different radii ( $R_0 = 0.1, 0.2, 0.3,$  and  $0.4\text{mm}$ ) with  $\gamma = 70\text{mN/m}$ . Figure 2.4 shows the time variation of the difference of the meniscus heights between that with the inertia terms included and that without. Without the fluid inertia, the flow fronts rise significantly faster initially for all four tubes. The meniscus for the two small tubes ( $R_0 = 0.1$  and  $0.2\text{ mm}$ ) remain ahead at later time ( $\Delta h > 0$ ), but the separation appear to decrease over the calculation time period.

For the tube with  $R_0 = 0.3\text{mm}$ ,  $\Delta h$  turns negative for  $t > 0.15\text{sec}$ . That is, the capillary rise is higher for the case with inertia than that without. For  $R_0 = 0.4\text{mm}$ , the change of sign occurs earlier around  $t = 0.1\text{sec}$ . At a later time, the effect of these overshoots disappears, and  $\Delta h$  approaches zero. Therefore, the fluid inertia can modify the initial capillary rise significantly and the effect diminishes with time.

### Rectangular Cylindrical Capillary

The capillary flows in uniform rectangular microchannels, that have been studied analytically [Ichikawa et al. 2004] and experimentally [Jong et al. 2007], are used as the second test problem for the present model.

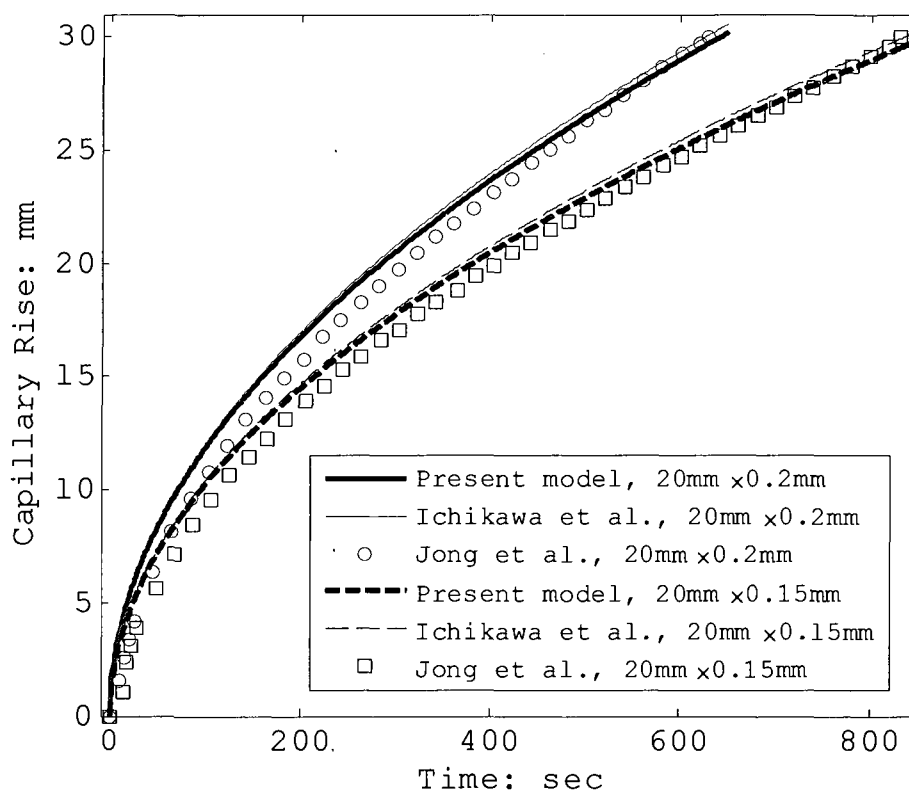


Figure 2.5 Comparison of capillary rises for rectangular cylindrical tubes.

The dimensions of the rectangular cross sections are 20mm x 0.15mm and 20mm x 0.2mm. The surface tension used

is 0.0212 N/m,  $\theta_s = 2^\circ$ ,  $\rho = 970\text{kg/m}^3$ , and  $\mu = 0.97\text{kg/ms}$ .

Since the aspect ratios of the rectangular cross sections are relatively large (133 and 100), it may be approximated by using the present elliptic cross section model in which the perimeters of the ellipses are the same as that of the rectangles, and the values of the corresponding  $K$  of the ellipses are 17,689 and 10,000, respectively.

As shown in Figure 2.5, the present solutions agree with both the measurement [Jong et al. 2007] and the analytical results obtained by Ichikawa's uniform rectangular capillary model [Ichikawa et al. 2004].

#### Circular Convergent-Divergent(C-D) and Divergent-Convergent(D-C) Capillary

The two test cases shown above validate the present model for uniform capillary flows with circular and rectangular cross sections. Since the present model is proposed for capillary flows in nonuniform tubes, the capillary flow in nonuniform geometries [Erickson et al. 2002] shown in Figure 2.6 is used as the third test problem.

The reported solutions [Erickson et al. 2002] were obtained by solving the Navier-Stokes equations using FEM without including the gravitational body force. The overall length of the two microchannels, and the corresponding length of the contraction and the expansion sections are the same between the two capillaries. They are  $H_1=20\text{mm}$ ,  $H_2 = H_4=2.8647\text{mm}$ ,  $H_3=40\text{mm}$ ,  $\theta_g=0.5^\circ$ . The cross section is circular and  $R_{\text{max}}=50\mu\text{m}$ ,  $R_{\text{min}}=25\mu\text{m}$ . The fluid properties are  $\rho = 1000 \text{ kg/m}^3$ ,  $\mu = 0.001 \text{ kg/ms}$ ,  $\gamma = 30 \text{ mN/m}$ ,  $\theta_s = 30^\circ$ .

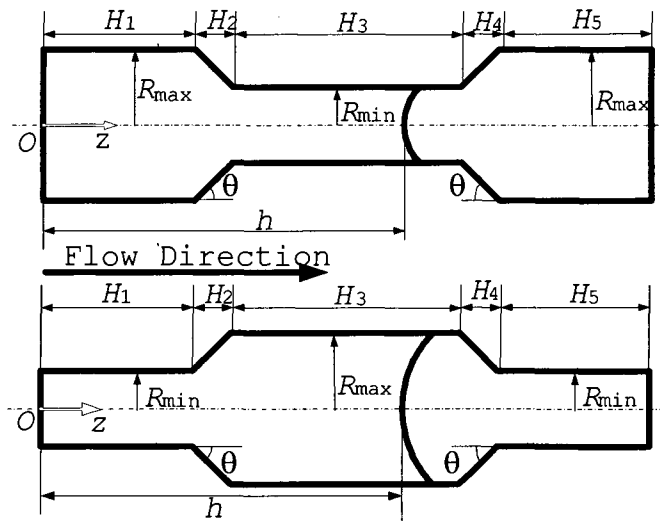


Figure 2.6 Convergent-divergent and divergent-convergent capillary geometries [Erickson et al. 2002].

Since the gravity effect is not considered [Erickson et al. 2002], the present model equation can be written as:

$$I_c + 8\mu N_c \cdot (1 + V_c) \cdot \frac{dh}{dt} = 2\gamma \cos \theta \quad (2.40)$$

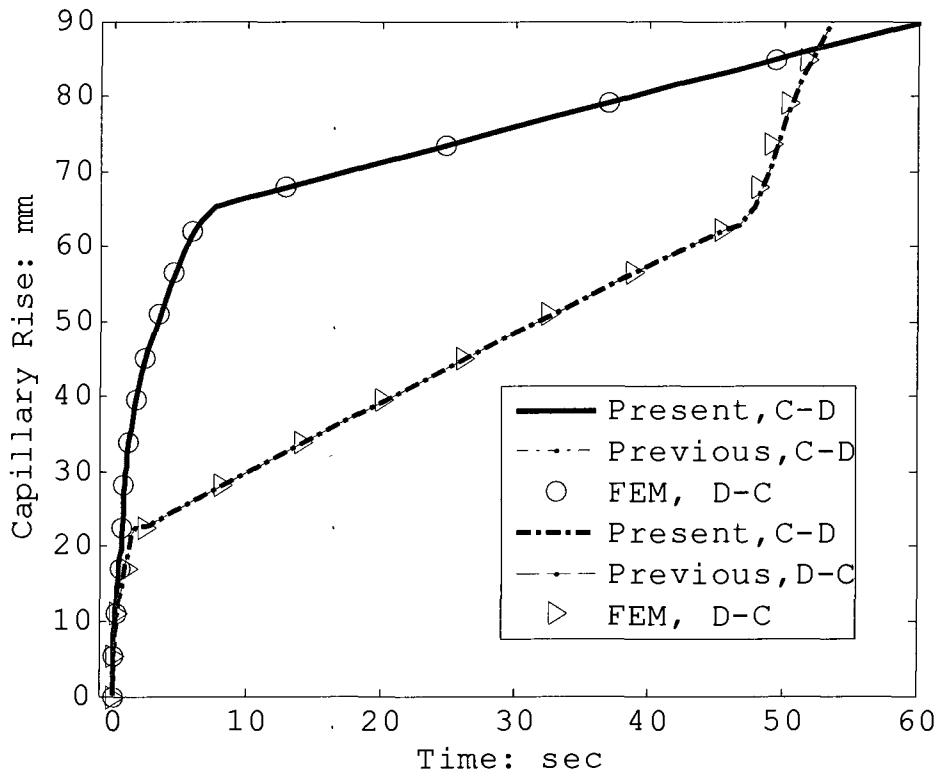


Figure 2.7 Convergent-divergent and divergent-convergent capillary geometries [Erickson et al. 2002].

The results for the capillary rises,  $h$  versus time  $t$ , are compared with the results obtained by using FEM [Erickson et al. 2002] as shown in Figure 2.7. For

comparison, the results obtained by using the previous model equation (2.36) [Staples and Shaffer 2002; Young 2004] less the gravity term are also included. That is,

$$8\mu N_c \cdot \frac{dh}{dt} = 2\gamma \cos \theta \quad (2.41)$$

Figure 2.7 shows that the present model results agree with both the FEM solution and that based on the model proposed by Staples and Shaffer (2002) and Young (2004). The results indicate that both the values of  $I_c$  and  $V_c$  are approximately zero. As was discussed earlier, the inertial effect diminishes with time, and the nonuniformity effect is related to the axial normal stress term  $\mu \frac{\partial^2 v_z}{\partial z^2}$ , which exists only when the flow interface passes through nonuniform cross sections. Since the converging/diverging sections (i.e.  $H_2$  and  $H_4$ ) are much shorter than the uniform sections (i.e.  $H_1$ ,  $H_3$  and  $H_5$ ) in the cases considered, the nonuniform effect in  $V_c$  is less apparent.

### 2.3 Results of Nonuniform Capillaries

The proposed model is applied to the capillary flow in tubes of nonuniform cross section. The capillary rises

in parabolic nonuniform tubes are assessed, and the nonuniformity effects appearing in the present model Equation (2.31) are investigated in detail. Moreover, the capillary flows in sinusoidal and divergent sinusoidal tubes, which model capillary flows in porous media, are also considered.

### Parabolic Nonuniform Capillary

To examine fully the nonuniform effect on the capillary rise, a microscale capillary with parabolic varying wall as shown in Figure 2.8 is considered.

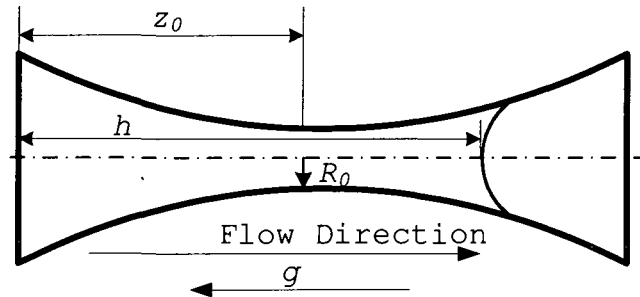


Figure 2.8 Sketch of capillary with parabolic wall.

The throat is located at  $z_0$ . Circular cross section is considered ( $K=1$ ), and the radius  $R(z) = R_0 + R_x (z - z_0)^2$ , where  $R_x$  is a constant. The base radius  $R_0 = 20\mu\text{m}$ . The fluid properties are  $\rho = 998.2\text{kg/m}^3$ ,  $\gamma = 72\text{mN/m}$ ,

$\mu = 0.001\text{kg/ms}$ , and  $\theta_s = 30^\circ$ . The coefficients  $c_1$ ,  $c_2$ ,  $c_3$ , and  $c_4$  in Equation (2.24) can be expressed explicitly by substituting the geometry relations into Equations (2.26)-(2.29) as follows:

$$c_1 = \frac{1}{2} \left[ \frac{1}{R(0)^2} - \frac{1}{R(h)^2} \right] \quad (2.42)$$

$$c_2 = 2 \left[ \frac{1}{\sqrt{R_0 / R_k}} \operatorname{atan} \left( \frac{h - z_0}{\sqrt{R_0 / R_k}} \right) + \frac{1}{\sqrt{R_0 / R_k}} \operatorname{atan} \left( \frac{z_0}{\sqrt{R_0 / R_k}} \right) - \frac{R_k (h - z_0)}{R_n} - \frac{R_k z_0}{R(0)} \right] \quad (2.43)$$

$$c_3 = \frac{1}{2R_0} \left[ \frac{h - z_0}{R(h)} + \frac{z_0}{R(0)} + \frac{\operatorname{atan} \frac{h - z_0}{\sqrt{R_0 / R_k}}}{\sqrt{R_k R_0}} + \frac{\operatorname{atan} \frac{z_0}{\sqrt{R_0 / R_k}}}{\sqrt{R_k R_0}} \right] \quad (2.44)$$

$$c_4 = \left[ \frac{1}{6} \frac{h - z_0}{R(h)^3 R_0} + \frac{5}{24} \frac{h - z_0}{R_0^2 R(h)^2} + \frac{5}{16} \frac{h - z_0}{R_0^3 R(h)} + \frac{1}{6} \frac{z_0}{R(0)^3 R_0} + \frac{5}{24} \frac{z_0}{R_0^2 R(0)^2} + \frac{5}{16} \frac{z_0}{R_0^3 R(0)} + \frac{5}{16} \frac{\operatorname{atan} \left( \frac{h - z_0}{\sqrt{R_0 / R_k}} \right)}{R_0^3 \sqrt{R_k R_0}} + \frac{5}{16} \frac{\operatorname{atan} \left( \frac{z_0}{\sqrt{R_0 / R_k}} \right)}{R_0^3 \sqrt{R_k R_0}} \right] \quad (2.45)$$

For  $R_k = 10$ , Figures 2.9 and 2.10 show the capillary rise and velocity of the present model obtained with and without inertia term  $I_c$ , respectively. They are compared

with that obtained by using the previous model equation (2.36) [Staples and Shaffer 2002; Young 2004]. Without the inertial terms, the solution of the present model agrees well with the solution obtained by using Equation (2.36) in the entire capillary rise. In the initial time period, these two solutions show faster interface rises compared to that obtained by the present model with the inertia terms included, as shown Figure 2.9b. The three solutions have the same equilibrium height of 13.89mm. Figure 2.10 gives the corresponding velocity variations. Without including the effect of the fluid inertia, the velocity curve of the present model equation (2.35) overlaps with that of Equation (2.36), and the capillary velocity monotonically decreases from large values initially to zero at equilibrium. With the inertial effect, the initial capillary rising velocity is 0.698m/s. The velocity increases from 0.698m/s to 4.33m/s at  $h=4.4\text{mm}$  before reaching the throat. From there, the velocity merges with that for the no-inertia cases.

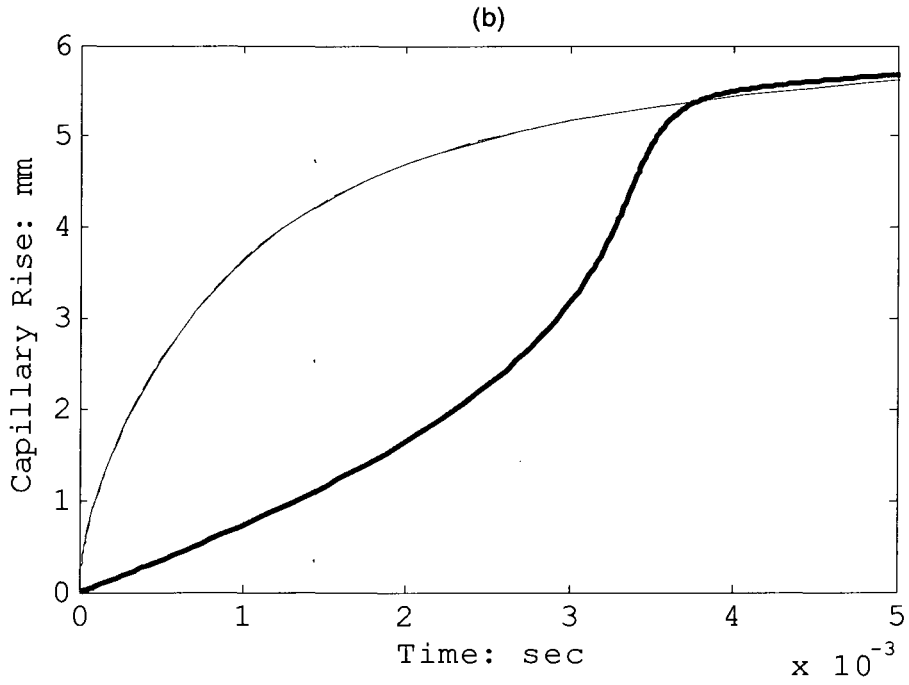
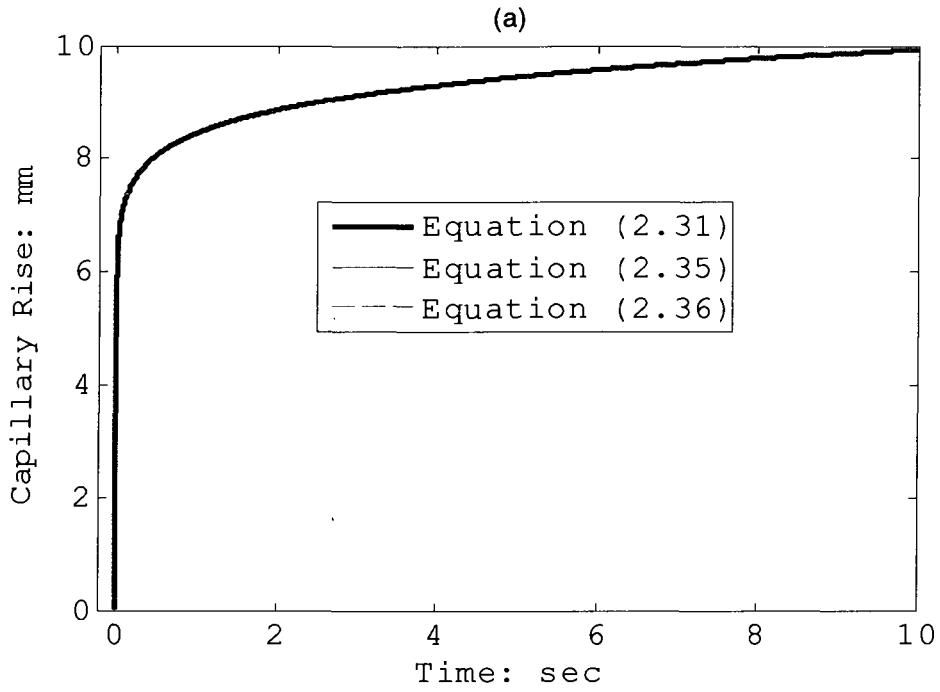


Figure 2.9 Capillary rise for parabolic circular tube with  $R_k = 10$ . (a),  $t = 0 \sim 10$  sec; (b),  $t = 0 \sim 5 \times 10^{-3}$  sec.

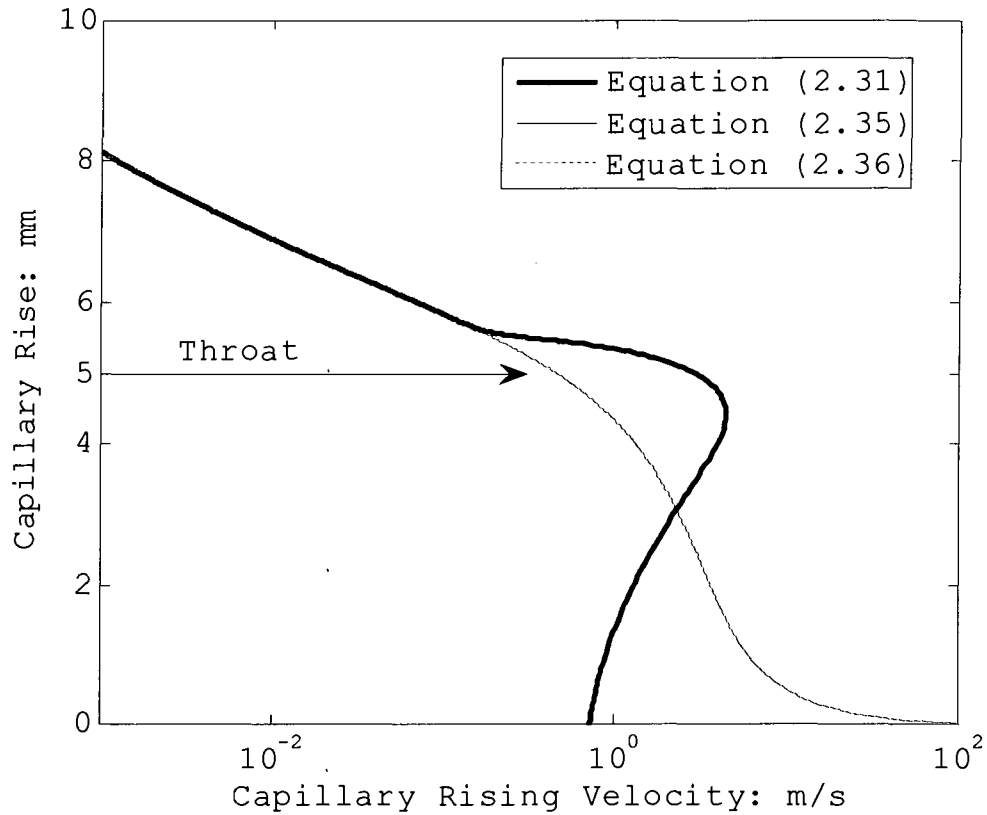


Figure 2.10 Comparison of capillary rise for parabolic circular tube with  $R_k = 10$ .

For wider geometry variation, a case with  $R_k = 100$  has been studied. Figures 2.11 and 2.12 show the capillary rise and velocity results. As shown in Figure 2.11c, the capillary rise curve of the present model without the inertial terms is lower than that of Equation (2.36) in the initial 0.4ms time period, and the two solutions merge at a later time.

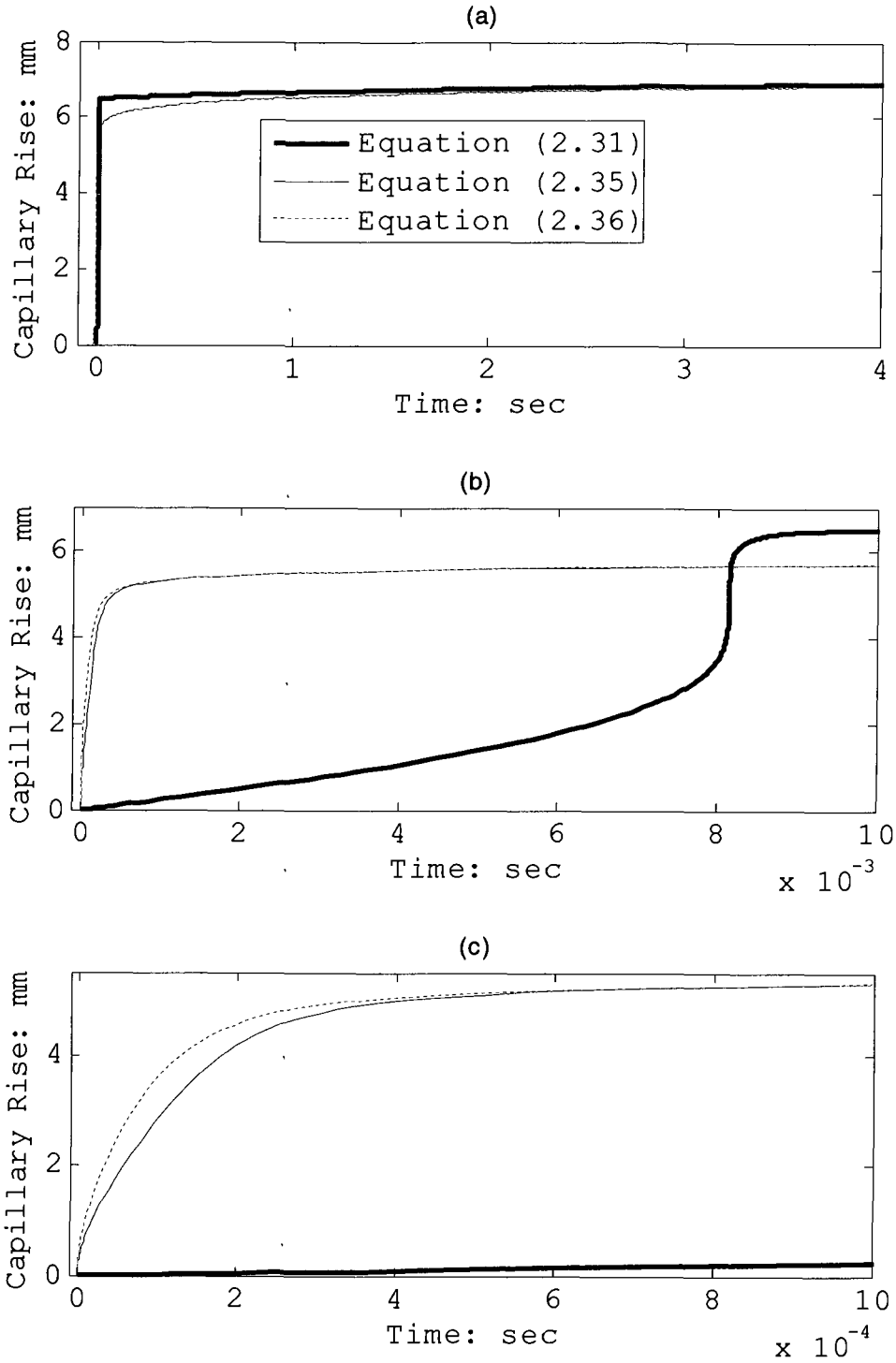


Figure 2.11 Capillary rise for parabolic circular tube with  $R_k = 100$ . (a),  $t=0\sim 4$  sec; (b),  $t=0\sim 1 \times 10^{-2}$  sec; (c),  $t=0\sim 1 \times 10^{-3}$  sec.

With the inertial terms, the capillary rise curve is lower than the other two curves without the inertial effect before  $t = 8\text{ms}$  as shown in Figure 2.11b. Figure 2.11a shows that the three solutions tend to converge in later time  $t > 1\text{sec}$ , and the calculations show that they have the same equilibrium height of  $7.972\text{mm}$ , which is lower than the equilibrium height  $13.892\text{mm}$  for  $R_k = 10$ .

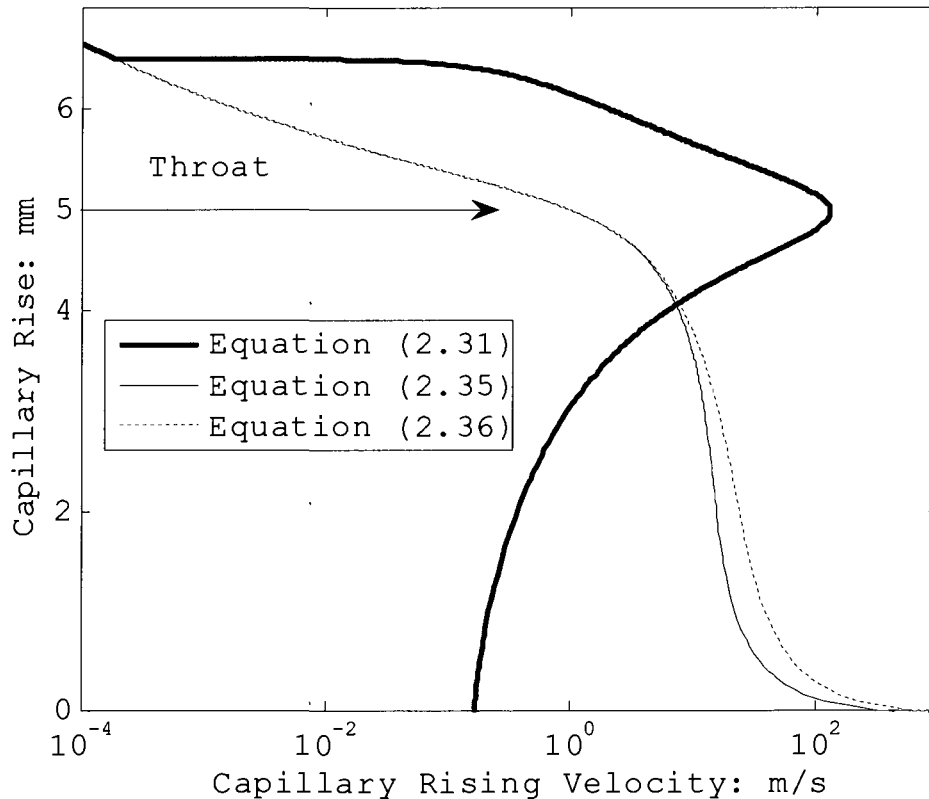


Figure 2.12 Comparison of capillary rise for parabolic circular tube with  $R_k = 100$ .

Figure 2.12 gives the velocity variation. Without the inertial effect, the velocity predicted by the present model is smaller than that of the previous model, due to the geometry effect on viscous terms represented by  $V_c$  until the capillary interface reaches the height of about 4mm. The capillary rise speed with inertia included gradually increases from an initial value of 0.235m/s to the maximum velocity of 183.6m/s at the throat ( $h=5\text{mm}$ ). The rise merges with the curves without the inertial effects later ( $h=6.4\text{mm}$ ) as the speeds decrease to zero.

The results shown above for the parabolic varying nonuniform capillary tubes suggest that the inertial effect is responsible for keeping the initial capillary rise speed finite. When the capillary interface rises toward the throat,  $R$  and  $dR / dz$  decrease and, consequently, so does the inertial effect. The decreasing inertia effect results in an increasing capillary velocity until the interface reaches the throat region. The difference between the present model without inertial effect Equation (2.35) and the previous model Equation (2.36) is the geometry effect on viscous terms, which is

represented by  $V_c$ . Substituting the expressions of  $c_2$  and  $c_3$  in Equations (2.42) and (2.43) into  $V_c$ , we obtain,

$$V_c = c_2 / c_3 \tag{2.46}$$

$$= 4R_k R_0 \cdot \frac{\frac{\operatorname{atan} \frac{h-z_0}{\sqrt{R_0 / R_k}}}{\sqrt{R_k R_0}} + \frac{\operatorname{atan} \frac{z_0}{\sqrt{R_0 / R_k}}}{\sqrt{R_k R_0}} - \frac{h-z_0}{R(h)} - \frac{z_0}{R(0)}}{\frac{\operatorname{atan} \frac{h-z_0}{\sqrt{R_0 / R_k}}}{\sqrt{R_k R_0}} + \frac{\operatorname{atan} \frac{z_0}{\sqrt{R_0 / R_k}}}{\sqrt{R_k R_0}} + \frac{h-z_0}{R(h)} + \frac{z_0}{R(0)}}$$

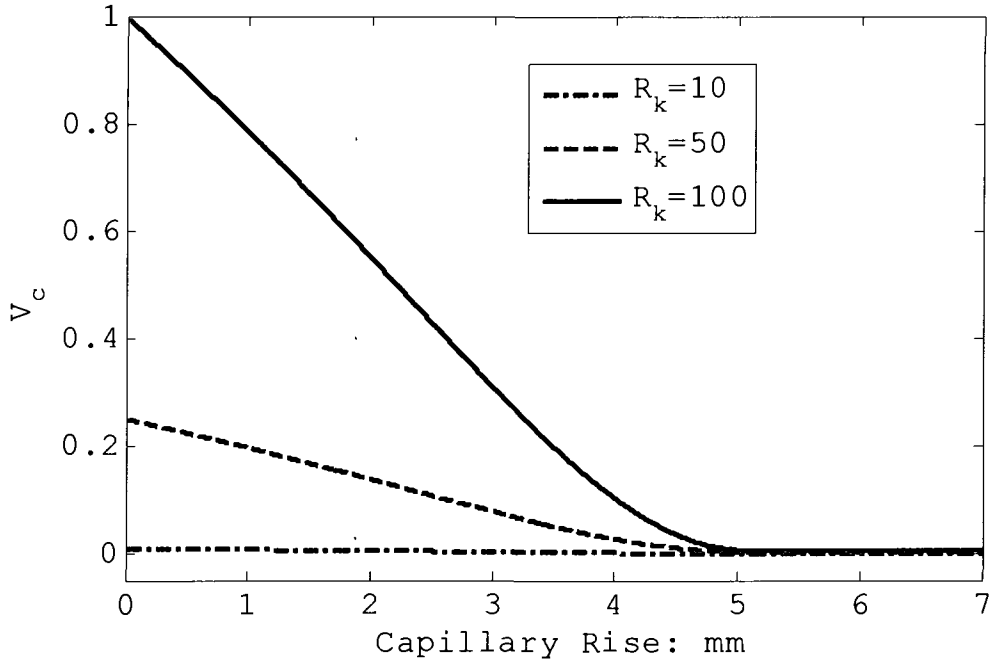


Figure 2.13 Viscous effect for parabolic circular tubes.

Figure 2.13 shows the relation between the viscous factor  $V_c$  and capillary rise,  $h$ , for different value of  $R_k$ . For  $R_k=10$ , the viscous factor is near zero, while

for  $R_x=100$ , the viscous factor is large at  $h=0$  and decreases with the rise of the interface height up to the throat area.

### Sinusoidal Varying Wall Capillary

The surface tension driven flow in nonuniform tubes with sinusoidal wall is now considered. The radius of the sinusoidal varying wall can be described as

$$R(z) = R_0 [1 + A \sin(2\pi z / LR_0)], \text{ where } R_0 \text{ is the base radius.}$$

$A$  and  $L$  are, respectively, the sinusoidal amplitude and the wavelength that are nondimensionalized by  $R_0$ . The flow was previously investigated [Patro et al. 2007; Patro and Javaram 2008; Sharma and Ross 1991; Staples and Shaffer 2002] because of its potential applications in porous media flow cases.

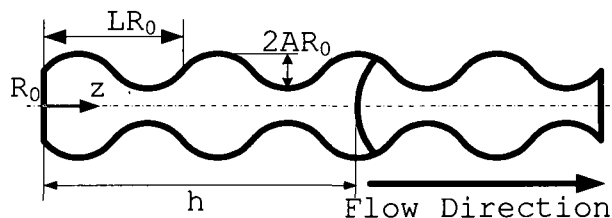


Figure 2.14 Sinusoidal geometry.

The sketch of the sinusoidal varying tube is given in Figure 2.14. The fluid properties are  $\rho = 998.2\text{kg/m}^3$ ,

$\gamma = 72\text{mN/m}$ ,  $\mu = 0.001\text{kg/ms}$ , and  $\theta_s = 20^\circ$ .

Four sinusoidal geometries with  $R_0 = 200 \mu\text{m}$  are considered in this section. They are for two amplitudes ( $A=0.3$  and  $0.6$ ) and two wavelengths ( $L=2$  and  $4$ ). Figures 15-18 show the comparison of the capillary rise results predicted by the present model with the inertial terms, Equation (2.31), and the present model without the inertia term, Equation (2.35), and the previous model, Equation (2.36). The coefficients  $c_1$ ,  $c_2$ ,  $c_3$  and  $c_4$  in the present model are obtained via numerical integration. The comparison of the capillary rise solutions of Equations (2.35) and (2.36) in Figure 2.15a-2.18a indicates that the geometry nonuniformity effect in the viscous terms  $V_c$  has no influence on the equilibrium height. It slows down the capillary rise and increases the time to reach the equilibrium state. This effect increases with the rate of change of the cross section  $dR / dz$ . Dynamically, the existence of the fluid inertia gives a much slower capillary rise at the initial time for all the four cases as can be seen from Figures 2.15b-2.18b.

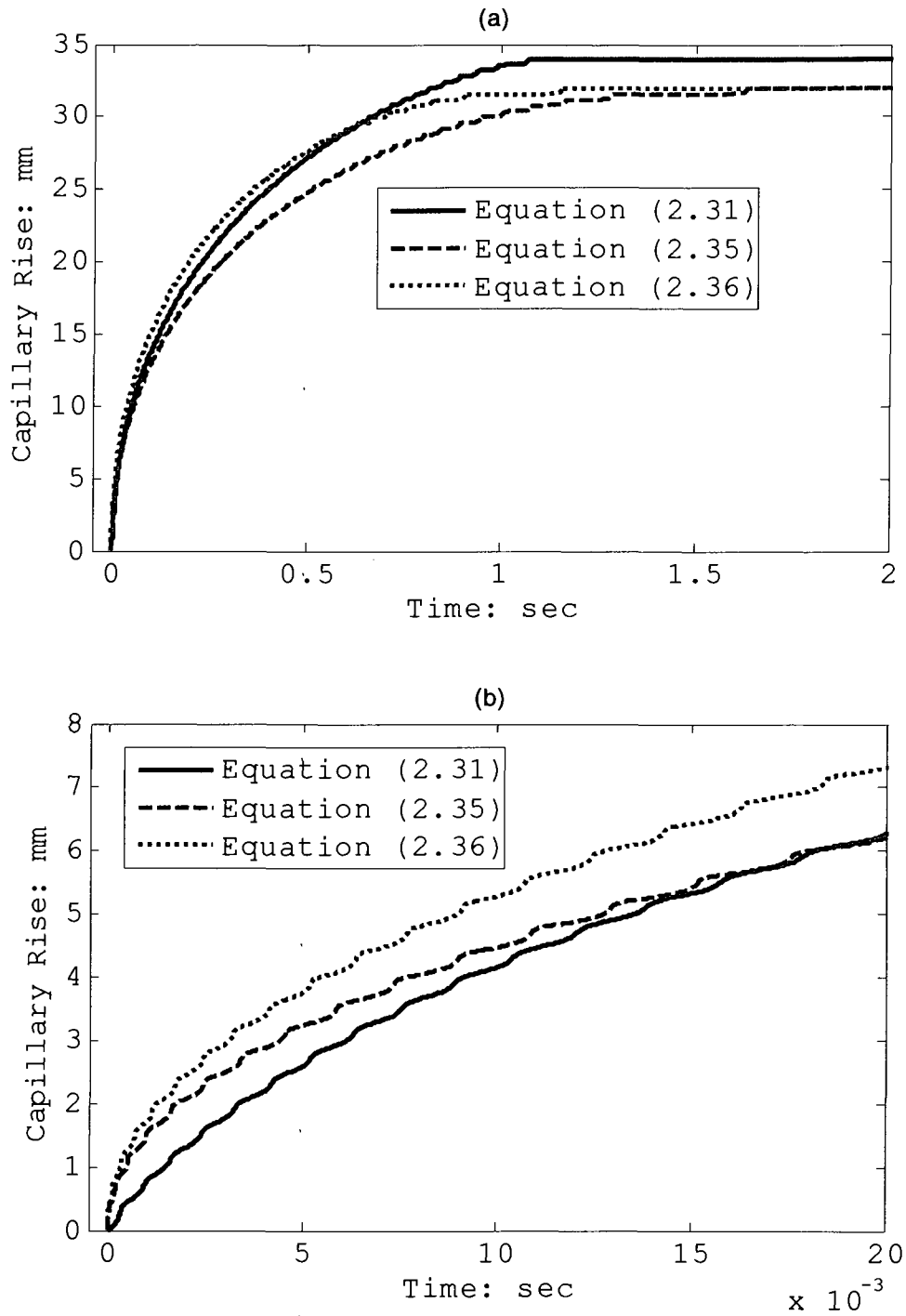


Figure 2.15 Comparison of capillary rise for sinusoidal circular tubes with  $L = 2$  and  $A = 0.3$ . (a),  $t=0\sim 2$  sec; (b),  $t=0\sim 20 \times 10^{-3}$  sec.

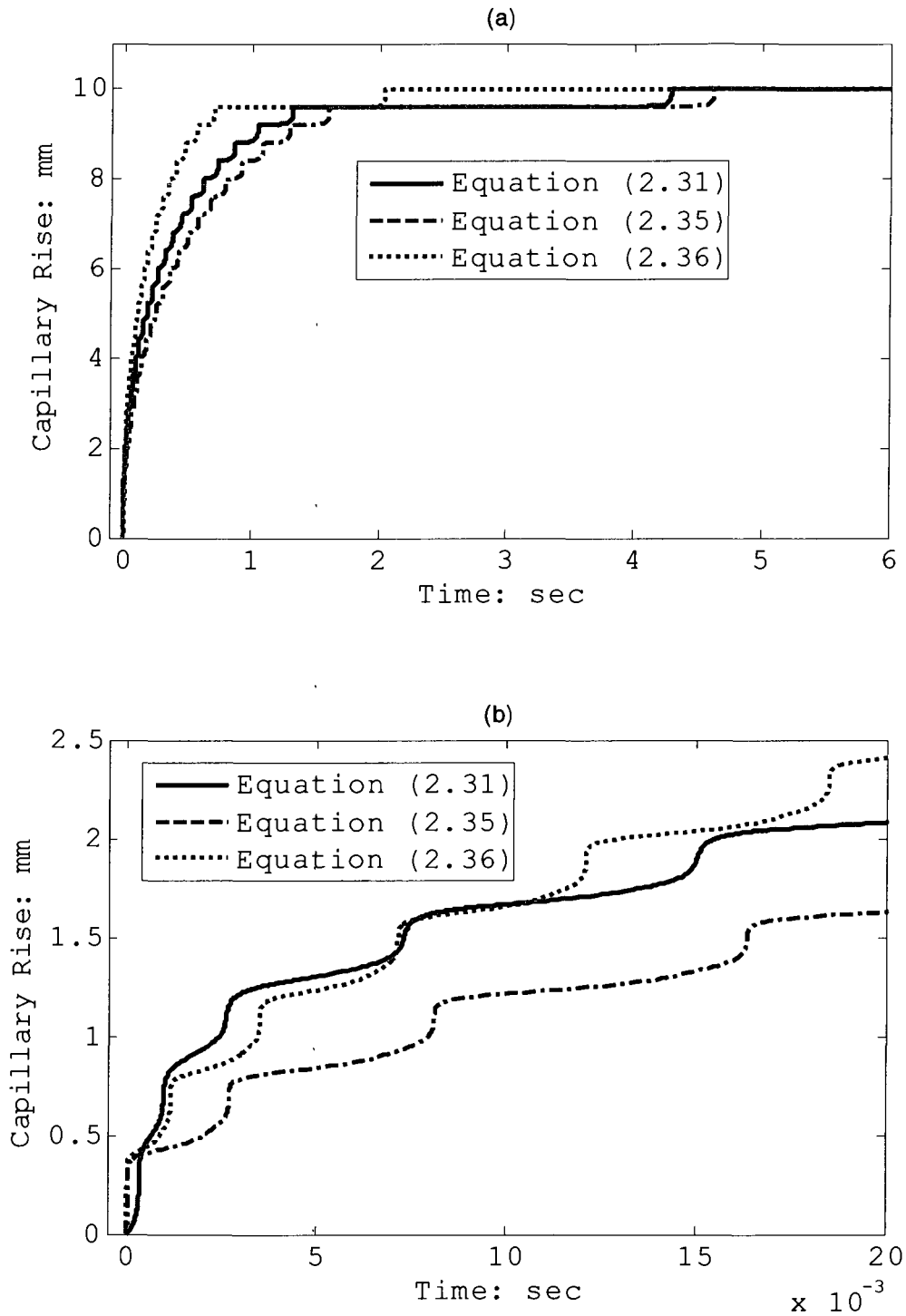


Figure 2.16 Comparison of capillary rise for sinusoidal circular tubes with  $L = 2$  and  $A = 0.6$ . (a),  $t=0\sim 6$  sec; (b),  $t=0\sim 20 \times 10^{-3}$  sec.

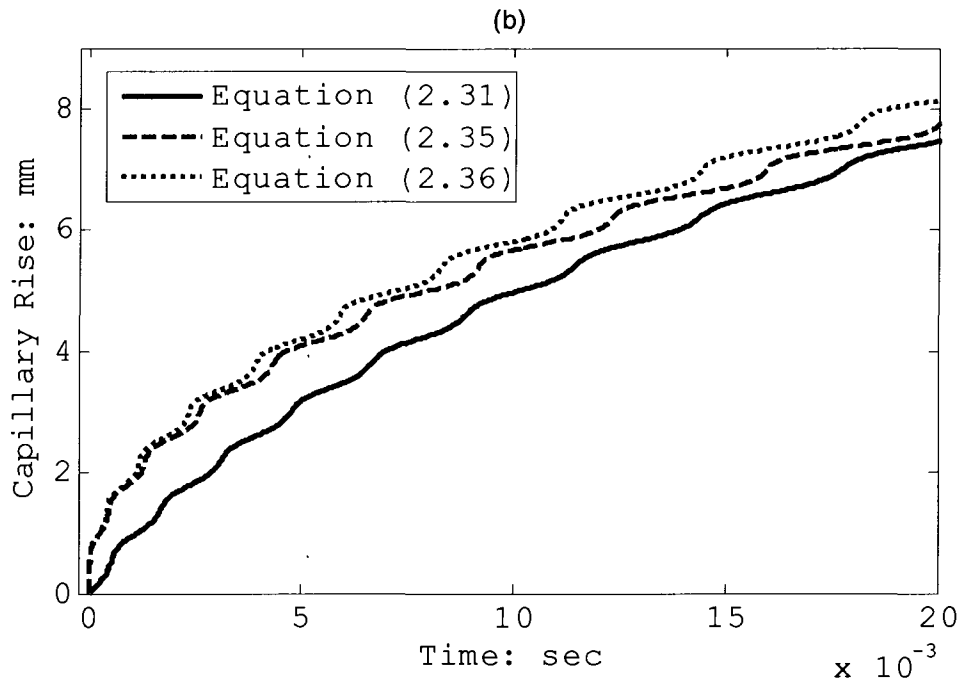
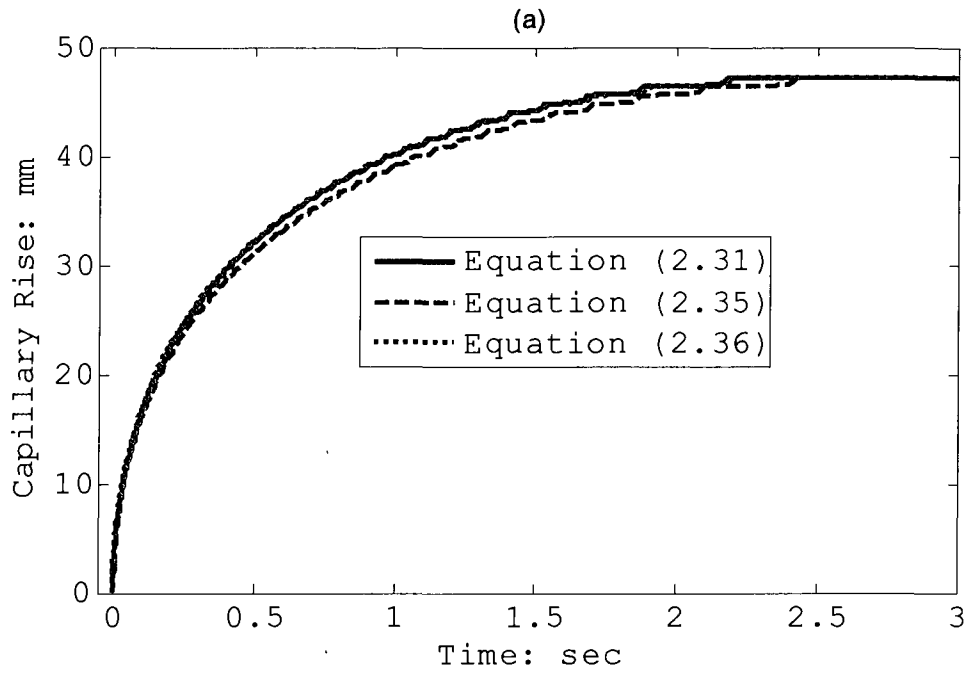


Figure 2.17 Comparison of capillary rise for sinusoidal circular tubes with  $L = 4$  and  $A = 0.3$ . (a),  $t=0\sim 3$  sec; (b),  $t=0\sim 20 \times 10^{-3}$  sec.

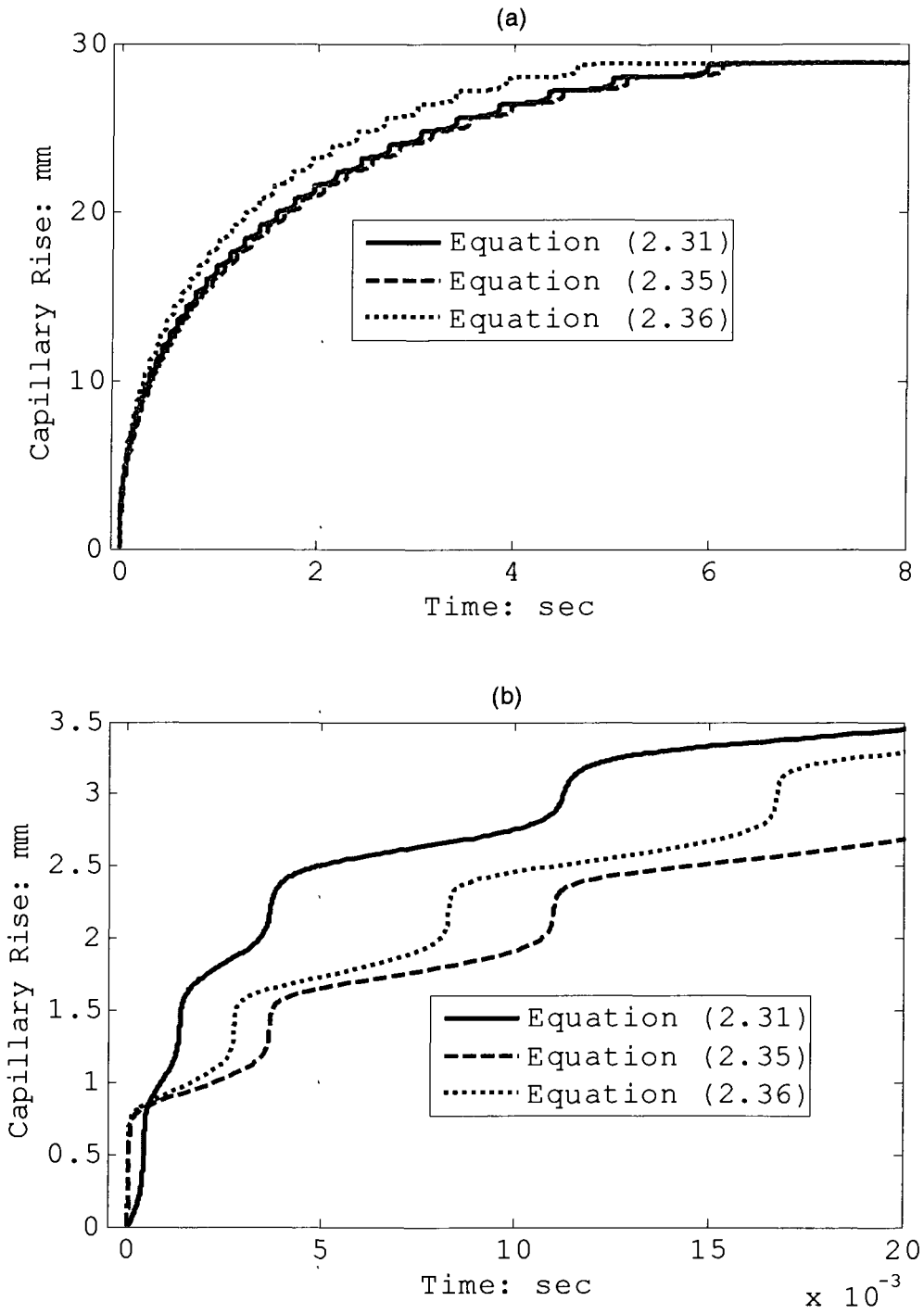


Figure 2.18 Comparison of capillary rise for sinusoidal circular tubes with  $L = 4$  and  $A = 0.6$ . (a),  $t=0\sim 8$  sec; (b),  $t=0\sim 20 \times 10^{-3}$  sec.

However, similar to the parabolic wall cases studied, the capillary rises for the cases with the inertia terms would catch up with those without at later locations. As was observed in [Duarte et al. 1996] for circular uniform tubes, the fluid inertia can also cause a slight overshoot of the equilibrium location. Figure 15a also shows that the equilibrium height for the cases with the inertia terms included is different from those without. The observed overshoot and the equilibrium height variation for the nonuniform tubes will be studied in more detail later.

Figures 2.19-2.22 give the variation of the capillary rise velocity  $dh / dt$  at initial stage and equilibrium close stage. For reference, the actual tube geometries are also provided at the bottom of all the figures. The velocity varies with sinusoidal waviness of the nonuniform capillary tube, increasing at the converging sections and decreasing at the diverging sections.

The interface velocity for the current model with inertia varies in a similar manner with the wall waviness as those of the non-inertia cases.

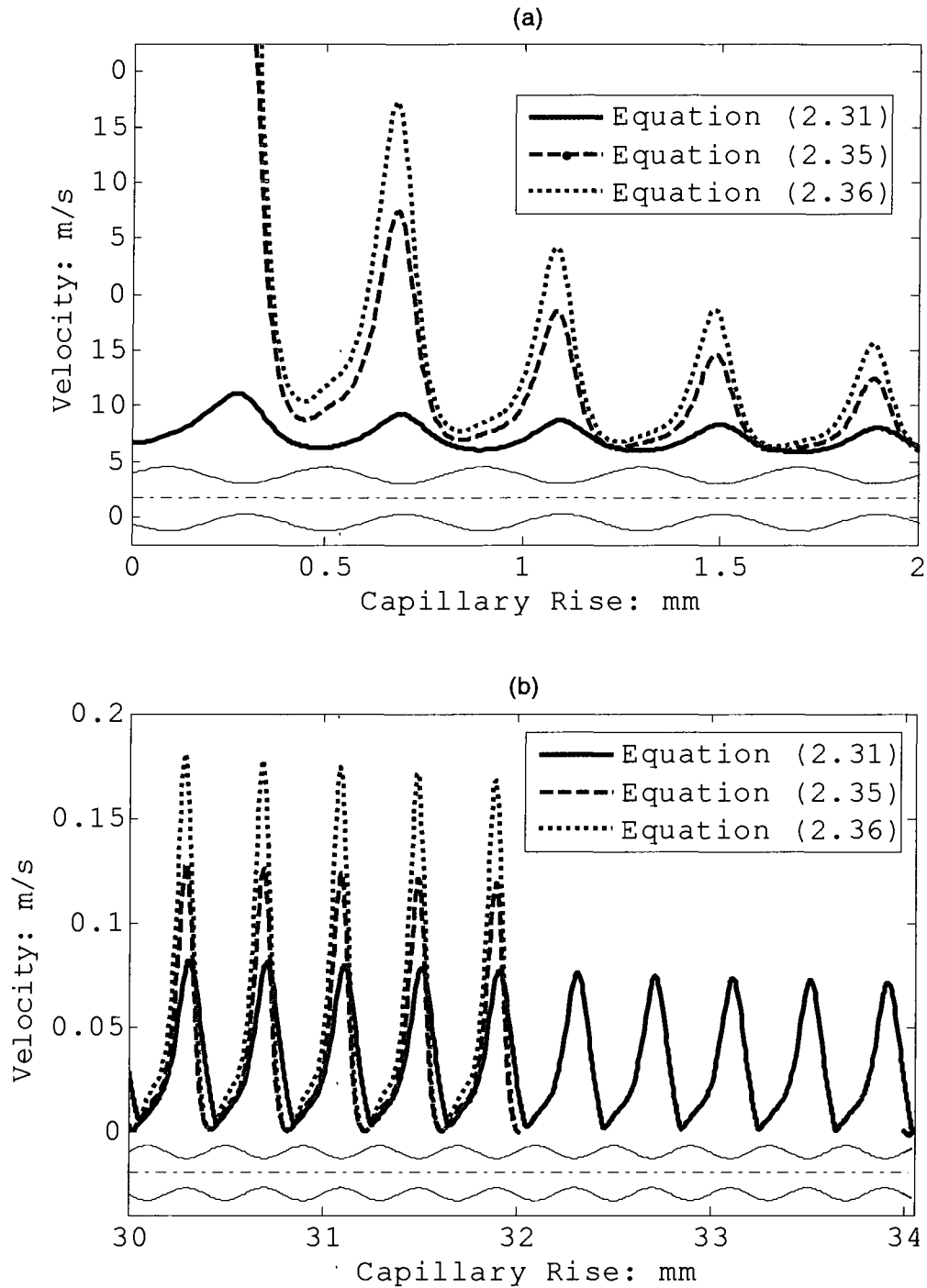


Figure 2.19 Comparison of capillary rise velocity for sinusoidal circular tubes with  $L = 2$  and  $A = 0.3$ .  
(a), Initial stage; (b), equilibrium stage.

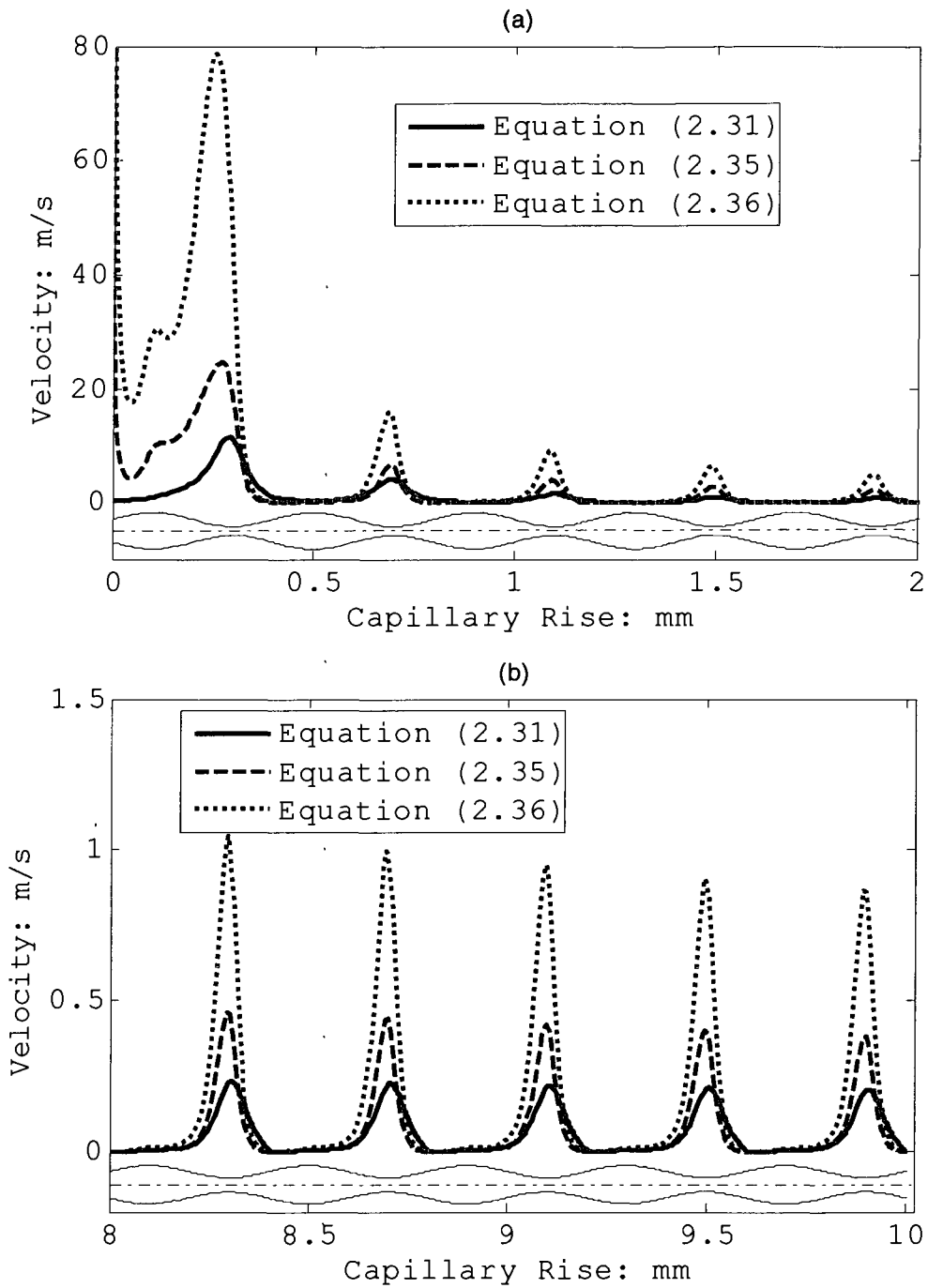


Figure 2.20 Comparison of capillary rise velocity for sinusoidal circular tubes with  $L = 2$  and  $A = 0.6$ . (a), Initial stage; (b), equilibrium stage.

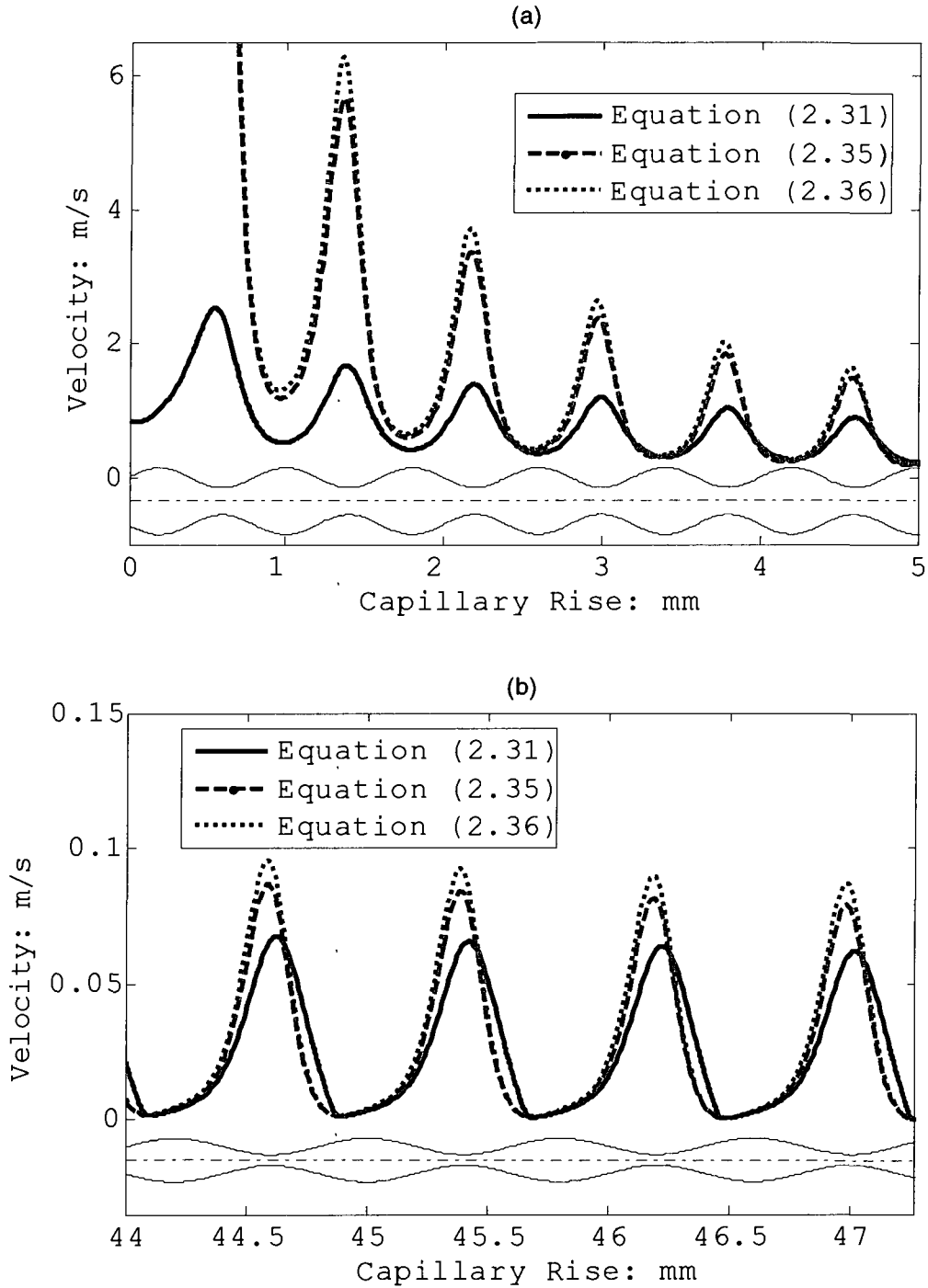


Figure 2.21 Comparison of capillary rise velocity for sinusoidal circular tubes with  $L = 4$  and  $A = 0.3$ . (a), Initial stage; (b), equilibrium stage.

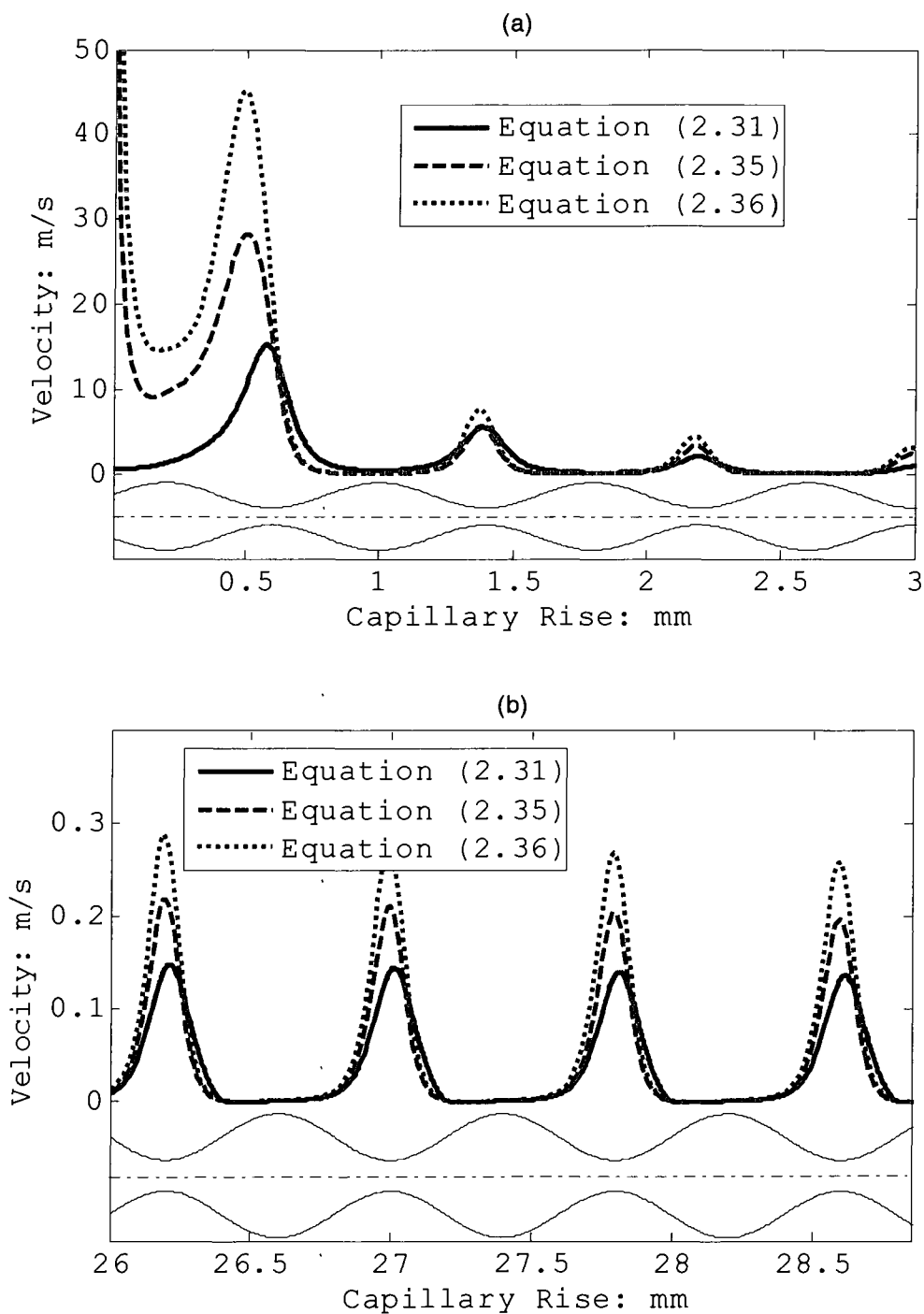


Figure 2.22 Comparison of capillary rise velocity for sinusoidal circular tubes with  $L = 4$  and  $A = 0.6$ .  
(a), Initial stage; (b), equilibrium stage.

The curves with inertia are slightly offset from those non-inertia curves with smaller amplitudes. At equilibrium, the interface ceases to move farther up, and its speed drops to zero.

The viscous terms in the previous model equation (2.36) and that in the present model are different by a factor of  $V_c$ . The geometry nonuniformity effect in the viscous term  $V_c$  renders lower interface speed for the present model than that from the previous model Equation (2.36).

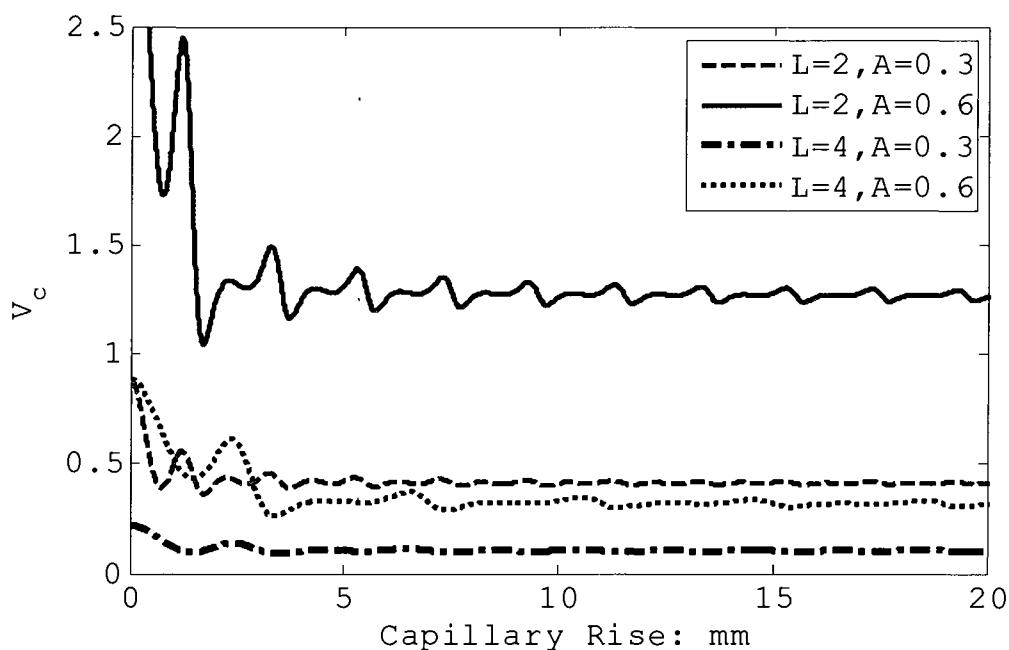


Figure 2.23 Viscous effect for sinusoidal tubes.

Figure 2.23 gives the relation between the viscous factor  $V_c$  and the capillary rise height.  $V_c$  oscillates with the waviness of the sinusoidal tube wall with large fluctuation at the initial time. The fluctuations decay at later time for all cases. The overall values of  $V_c$  increase with the increase of amplitude and with the decrease of wavelength. This dependence of the value of  $V_c$  on the wall amplitude and the wavelength in the present model has resulted in the difference of the interface velocity between the present model (without the inertial terms) and those obtained by Equation (2.36) shown in Figures 2.15-2.18.

In Figure 2.19b, for the flow with  $L=2$ ,  $A=0.3$ , the smaller velocity variation in its amplitude for the case with inertia helps maintain a finite velocity when the solutions for the two cases without inertial effects show zero velocity, i.e. reaching equilibrium. In fact, the interface speed for the inertia-included case did not drop below machine accuracy for another ten radii ( $R_0$ ) downstream. That is to say, for the case with the inertial effects included, the interface equilibrium height is about  $10R_0$  higher than those without taking

consideration of the inertial effect. This can also be observed in Figure 2.15a.

To further study of the inertial effects in the current non-uniform sinusoidal capillaries, we first examine the equilibrium height of the interface. According to Equation (2.37), we define a force function  $F(h)$ ,

$$F(h) = 2\gamma \cos \alpha / R(h) - \rho gh \quad (2.47)$$

such that the equilibrium height of the interface can be found by the zeros of  $F(h)$ . It can be shown that, due to the periodic nature of  $R(h)$ ,  $F(h) = 0$  has a series of solutions that, when arranged in increasing magnitude, can be denoted by  $h_{e1}$ ,  $h_{e2}$ ,  $h_{e3}$ ,  $h_{e4}$ ,  $\dots$ . When the inertial effects are not considered, such as that in the Washburn equation, and an initial value problem is solved starting from a zero interface height, the interface will asymptote to  $h_{e1}$ , and  $h_{e1}$  becomes the equilibrium height. Results shown in Figure 15a-18a indicate that, for all but one ( $L=2$  and  $A=0.3$ ) of the four cases calculated,  $h_{e1}$  is also the equilibrium height when the inertia terms are included. For  $L=2$  and  $A=0.3$ , the noninertial equilibrium height is lower than that with the inertial effects.

Figure 2.24 gives a composite plot of the function  $F(h)$  and the variation of interface height  $h$  with time for the case of  $L=2$  and  $A=0.3$ . For clarity, the time, in Figure 2.24, is offset by a factor  $t_f$  which is the time to reach a height of 31mm in Figure 2.24.

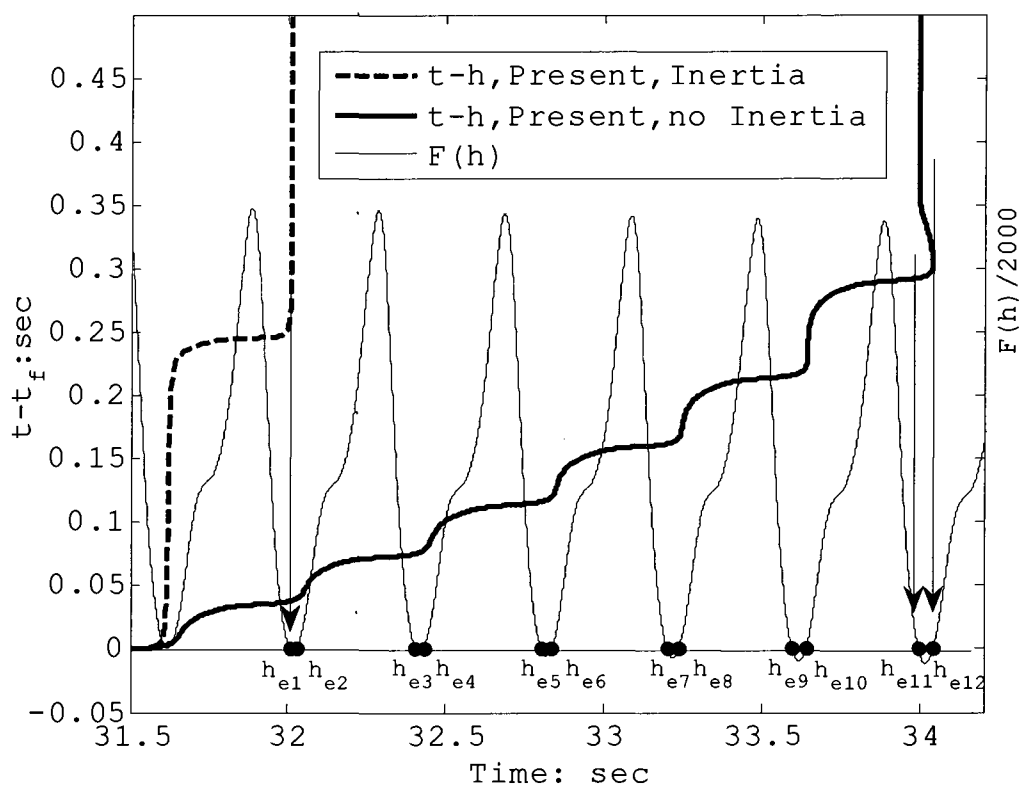


Figure 2.24 Force function  $F(h)$  and equilibrium heights for  $L = 2$ ,  $A = 0.3$ .

The phenomenon that the capillary interface overshoots the equilibrium height in uniform capillaries has been reported [Duarte et al. 1996] and contributed to

the effects of the fluid inertia. A similar phenomenon may also be observed in the capillary rise results predicted by the present model with inertia as shown in Figure 2.24. If the inertia is ignored, there would be no overshoot and the interface will reach the first equilibrium height  $h_{e1}$  and stop there. With the inertia included, the interface will overshoot  $h_{e1}$ . There is one pair of equilibrium height solutions in each sinusoidal section. When the overshoot exceeds  $h_{e2}$  also, the interface will be elevated to the next equilibrium height  $h_{e3}$ . Figure 2.24 shows that the interface continues to rise until the overshoot fails to overcome the difference between the pair of the equilibrium heights  $h_{e11}$  and  $h_{e12}$ , and  $h_{e11}$  becomes the final equilibrium height.

#### Divergent Sinusoidal Wall Capillary

In the paper industry, rigid-capillary-pressing technology is used to improve the dewatering efficiency in the paper making process [Stelljes et al. 2004]. During this process, the capillary flow passes through a thin porous medium laminated with a number of layers of pores of different sizes. The sizes can vary from 10  $\mu\text{m}$

to 1mm. This configuration can be approximated by a sinusoidal divergent wall in the current model framework. One such approximation is studied in this section. The cross section of the capillary is considered circular. The radius  $R$  that varies along the axial direction  $z$  can be described as:

$$R(z) = R_0(z) \left\{ 1 + A \sin \left[ \frac{2\pi z}{\lambda(z)} \right] \right\} \quad (2.48)$$

The base radius  $R_0$  and wavelength  $\lambda$  are also varying along the  $z$  direction to simulate the increasing pore size along the flow path. That is,

$$R_0(z) = R_{\min} + \frac{z}{H_t} (R_{\max} - R_{\min}), \quad \lambda(z) = \lambda_{\min} + \frac{z}{H_t} (\lambda_{\max} - \lambda_{\min}) \quad (2.49)$$

where  $H_t$  is the length of the tube.  $R_{\max}$ ,  $R_{\min}$ ,  $\lambda_{\max}$ , and  $\lambda_{\min}$  represent the maximum and minimum radius and wavelength of the tube, respectively. Figure 2.25 shows a sketch of such capillaries.

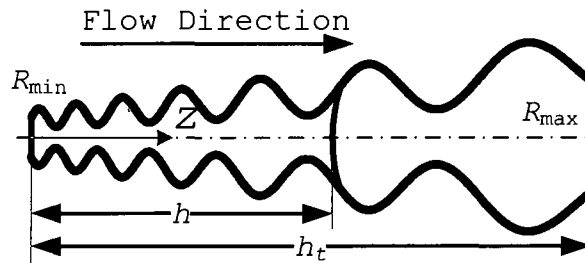


Figure 2.25 Sketch of sinusoidal divergent tube.

In the following simulation example,  $R_{\min} = 50\mu\text{m}$ ,  $R_{\max} = 500\mu\text{m}$ ,  $\lambda_{\min} = 100\mu\text{m}$ ,  $\lambda_{\max} = 1\text{mm}$ , and  $H_t = 50\text{mm}$ . The fluid properties are:  $\gamma = 72 \text{ mN/m}$ ,  $\theta_s = 20^\circ$ ,  $\rho = 998.2 \text{ kg/m}^3$ , and  $\mu = 0.001 \text{ kg/ms}$ . The coefficients  $c_1, c_2, c_3$ , and  $c_4$  that appear in Equation (2.31) are obtained via numerical integration. The calculation results for two cases of  $A = 0.3$ , and  $0.6$  are given in Figure 2.26. For comparison, the result for a linearly divergent wall with  $A=0$  is also shown.

Figure 2.26a shows the capillary rises immediately after the simulations begin from  $h = 0$  and the long-time behavior of the capillary rises is shown in Figure 2.26b. Comparing with the case of the linear wall ( $A=0$ ), we can see that the sinusoidal variation of the geometry introduces fluctuations into the capillary rise. By referencing to the local geometry shown on the right hand side of the capillary rise curves in Fig. 2.14, it can be seen that the velocity of the capillary rise increases in the convergent section and decreases in the divergent section for the cases of  $A=0.3$  and  $0.6$ . Compared with the linear wall case, the sinusoidal geometry slows down the

capillary rises. This effect increases with the amplitude

A.

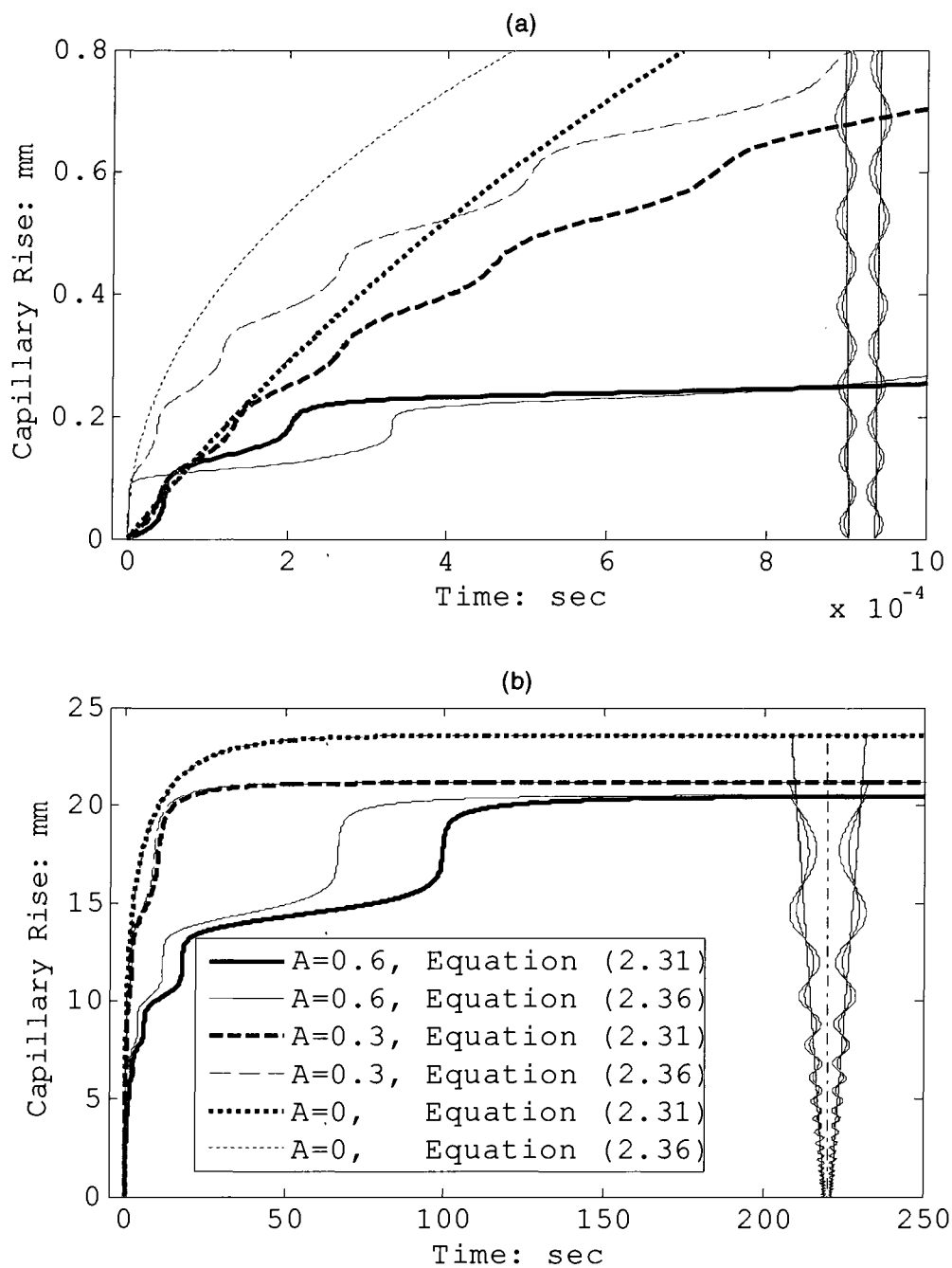


Figure 2.26 Capillary rise velocity for sinusoidal divergent tubes. (a), Initial stage; (b), entire stage.

Figure 2.26a shows that, at the initial time, the present model has a much slower initial velocity than those of the previous model Equation (2.36). As a result, the capillary rise in the initial time for the present model is slower than that obtained by Equation (2.36). For  $A=0.3$ , the capillary interface of the present model remains behind that of Equation (2.36) until they reach the same equilibrium height. For  $A=0.6$ , the interface height calculated by the present model becomes higher for a period of time, but lags again and remains behind the interface calculated by Equation (2.36) until they reach equilibrium. As was discussed above, the inertial effect is dominant in the initial time, but negligible when compared with the effect of  $V_c$  when the interface is close to the equilibrium height. The viscous effect prolongs the time it takes for the interface to pass through the divergent sections of the tube. This effect increases with the amplitude,  $A$ , as shown in Figure 2.26b. The equilibrium heights for the three cases are located in the divergent section.

Figure 2.27 shows that the variation of  $V_c$ , which is a factor that reflects the nonuniformity effect in the

viscous terms in the present model. For the case of  $A = 0$ ,  $V_c = \tan^2 \theta$ . With the slope angle of  $\theta = 0.516^\circ$ ,  $V_c = 8.1 \times 10^{-5}$ . From the initial stage to the equilibrium,  $V_c$  decreases from 0.9 to 0.296 for the case of  $A = 0.3$ , and from 3.53 to 0.895 for  $A = 0.6$ . Figure 2.27 show that  $V_c$ , overall, increases with the amplitude of the sine function  $A$ .

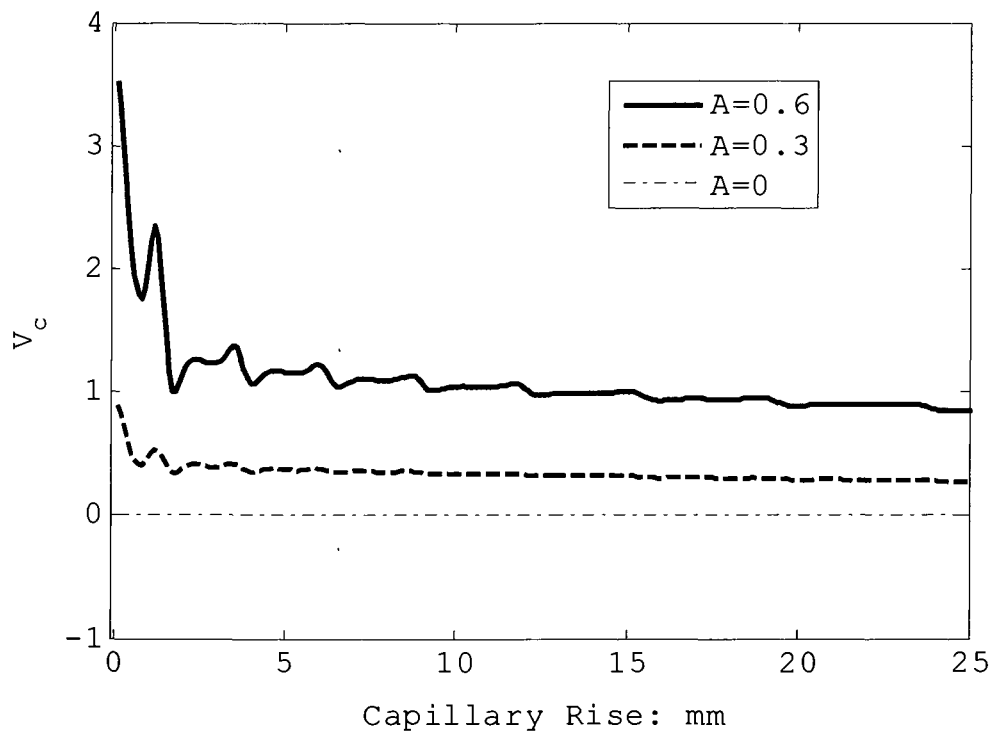


Figure 2.27 Nonuniformity effect in viscous terms.

## 2.4. Conclusions

A new model for the time-dependent rise of the capillary interface in a tube with cross sections that are not uniformly varying along its axis is proposed. Compared with the existing models, the proposed model includes the full viscous terms and the effects of the fluid inertia. The results for the cases studied, which include capillaries of five different wall variations, show the following.

(1) The nonuniformity effects on the viscous terms can be underestimated in the existing nonuniform cross section models. The impact of the viscous terms included in the proposed model is proportional to the slope of the wall. The viscous effects tend to slow down the rise of the capillary interface, but have no influence on the initial capillary rise velocity and on the equilibrium height.

(2) For nonuniform capillaries, the capillary rise velocity at the convergent section is faster than that at the divergent section. The interface reaches the equilibrium height at the divergent section for all the cases considered.

(3) It is shown that, with the inertial effects included, an estimation of the initial rise velocity of the interface can be obtained analytically. The initial velocity depends on the liquid density, surface tension, contact angle, the capillary geometry, and is of finite value. During the initial dynamic capillary rise process, inertia can counter balance the effect of viscosity.

(4) Due to the fact that the equilibrium height solutions are non-unique for the periodic, sinusoidal capillary case, the inertial effect considered in the proposed model can drive the interface to overshoot the lowest equilibrium location and reach a different equilibrium height, compared with the height reached without including the inertial effects.

The present model is applicable to industrial capillary flow problems under gravity with arbitrary wall profile. The developed approach can be extended to predict the dynamic capillary flow of arbitrary irregular capillaries with well-defined geometry.

## **CHAPTER 3**

### **MODELING OF CAPILLARY FLOW WITH DYNAMIC CONTACT ANGLE IN TUBES OF NONUNIFORM CIRCULAR CROSS SECTION**

In this chapter, the capillary flows in nonuniform capillaries with circular cross section are investigated analytically. Firstly, a closed-form expression of velocity distribution is obtained by an asymptotic series solution of the stream function in a tube of varying radius, which offers an improvement over the parabolic form. Based on the new velocity distribution, a new governing equation is derived by the integration of the axial momentum equation over the liquid volume with an average operating in each cross section to include the nonuniformity effect on the pressure gradient. The dynamic contact angle model is also discussed in detail in this chapter. The proposed model is validated by examining a series of capillary rise experiments.

#### **3.1 Asymptotic Series Solution of Flow Field**

In this section, the asymptotic solution of stream function for low Reynolds number flow of a Newtonian

incompressible fluid through an axisymmetric tube with varying radius is obtained by using a perturbation analysis established by Manton (1971) which was later corrected by Van Dyke (1987) and validated by Sisavath et al. (2001).

The analysis starts from the Navier-Stokes equations in cylindrical coordinates  $(r, \theta, z)$ :

$$\frac{1}{r} \frac{\partial}{\partial r} (rv_r) + \frac{\partial}{\partial z} (v_z) = 0 \quad (3.1)$$

$$\begin{aligned} & \frac{\partial v_r}{\partial t} + v_r \frac{\partial v_r}{\partial r} + v_z \frac{\partial v_r}{\partial z} \\ &= -\frac{1}{\rho} \frac{\partial p}{\partial r} + \frac{\mu}{\rho} \left[ \frac{1}{r} \frac{\partial}{\partial r} \left( r \frac{\partial v_r}{\partial r} \right) + \frac{\partial^2 v_r}{\partial z^2} - \frac{v_r}{r^2} \right] \end{aligned} \quad (3.2)$$

$$\begin{aligned} & \frac{\partial v_z}{\partial t} + v_r \frac{\partial v_z}{\partial r} + v_z \frac{\partial v_z}{\partial z} \\ &= -\frac{1}{\rho} \frac{\partial p}{\partial z} + \frac{\mu}{\rho} \left[ \frac{1}{r} \frac{\partial}{\partial r} \left( r \frac{\partial v_z}{\partial r} \right) + \frac{\partial^2 v_z}{\partial z^2} \right] \end{aligned} \quad (3.3)$$

where,  $v_r$  and  $v_z$  are velocity components in the radial and axial directions, respectively. With the axisymmetric assumption of the geometry,  $v_\theta$  and all derivatives  $\partial / \partial \theta$  are set to zero.

Differentiations of Equations (3.2) and (3.3) with respect to  $z$  gives:

$$\begin{aligned} & \frac{\partial^2 v_r}{\partial t \partial z} + \frac{\partial}{\partial z} \left( v_r \frac{\partial v_r}{\partial r} \right) + \frac{\partial}{\partial z} \left( v_z \frac{\partial v_r}{\partial z} \right) \\ &= -\frac{1}{\rho} \frac{\partial^2 p}{\partial r \partial z} + \frac{\mu}{\rho} \left[ \frac{1}{r} \frac{\partial^2}{\partial r \partial z} \left( r \frac{\partial v_r}{\partial r} \right) + \frac{\partial^3 v_r}{\partial z^3} - \frac{1}{r^2} \frac{\partial v_r}{\partial z} \right] \end{aligned} \quad (3.4)$$

$$\begin{aligned} & \frac{\partial^2 v_z}{\partial t \partial r} + \frac{\partial}{\partial r} \left( v_r \frac{\partial v_z}{\partial r} \right) + \frac{\partial}{\partial r} \left( v_z \frac{\partial v_z}{\partial z} \right) \\ &= -\frac{1}{\rho} \frac{\partial^2 p}{\partial r \partial z} + \frac{\mu}{\rho} \frac{\partial}{\partial r} \left[ \frac{1}{r} \frac{\partial}{\partial r} \left( r \frac{\partial v_z}{\partial r} \right) + \frac{\partial^2 v_z}{\partial z^2} \right] \end{aligned} \quad (3.5)$$

The pressure terms are eliminated by subtracting equation (3.5) from equation (3.4),

$$\begin{aligned} & \frac{\partial}{\partial t} \left( \frac{\partial v_r}{\partial z} - \frac{\partial v_z}{\partial r} \right) + v_r \frac{\partial^2 v_r}{\partial r \partial z} + \frac{\partial v_r}{\partial r} \cdot \frac{\partial v_r}{\partial z} + v_z \frac{\partial^2 v_r}{\partial z^2} \\ &+ \frac{\partial v_r}{\partial z} \frac{\partial v_z}{\partial z} - v_r \frac{\partial^2 v_z}{\partial r^2} - \frac{\partial v_r}{\partial r} \cdot \frac{\partial v_z}{\partial r} - v_z \frac{\partial^2 v_z}{\partial z \partial r} - \frac{\partial v_z}{\partial r} \cdot \frac{\partial v_z}{\partial z} \\ &= \frac{\mu}{\rho} \left( \frac{\partial^3 v_r}{\partial r^2 \partial z} + \frac{1}{r} \frac{\partial^2 v_r}{\partial r \partial z} + \frac{\partial^3 v_r}{\partial z^3} - \frac{1}{r^2} \frac{\partial v_r}{\partial z} - \frac{\partial^3 v_z}{\partial r^3} \right. \\ & \quad \left. - \frac{1}{r} \frac{\partial^2 v_z}{\partial r^2} + \frac{1}{r^2} \frac{\partial v_z}{\partial r} - \frac{\partial^3 v_z}{\partial r \partial z^2} \right) \end{aligned} \quad (3.6)$$

Let's introduce the stream function,  $\psi$ , that is defined as:

$$v_r = -\frac{\partial \psi}{\partial r} \quad (3.7)$$

$$v_z = \frac{\partial \psi}{\partial z} \quad (3.8)$$

The stream function must satisfy the boundary conditions [Manton 1971; Van Dyke 1987; Sisavath et al. 2001]:

$$\left. \frac{\partial \psi}{\partial r} \right|_{r=R(z)} = 0 \quad (3.9)$$

$$\psi|_{r=R(z)} = \psi_c = \frac{q}{2\pi} \quad (3.10)$$

$$\psi|_{r \rightarrow 0} = O(r^2) \quad (3.11)$$

$$\left. \frac{1}{r} \frac{\partial \psi}{\partial z} \right|_{r \rightarrow 0} \rightarrow 0 \quad (3.12)$$

$$\left. \frac{\partial}{\partial r} \left( \frac{1}{r} \frac{\partial \psi}{\partial r} \right) \right|_{r \rightarrow 0} \rightarrow 0 \quad (3.13)$$

The condition (3.9) corresponds to the no-slip boundary condition, whereas conditions (3.10) and (3.11) specify that the flow rate  $q$  is constant along  $z$  direction. Condition (3.11) implies the boundary conditions (3.12) and (3.13) which ensure that the solution is regular along the axis of the tube.

Substituting Equations (3.7) and (3.8) into Equation (3.6) and neglecting the time-dependent terms by the steady state assumption give:

$$\begin{aligned} & \frac{3\psi_r \cdot \psi_z}{r^4} - \frac{2\psi_{zz} \cdot \psi_z}{r^3} - \frac{3\psi_{rr} \cdot \psi_z}{r^3} + \frac{\psi_{r,z} \cdot \psi_r}{r^3} \\ & + \frac{\psi_{r,zz} \cdot \psi_z}{r^2} - \frac{\psi_r \cdot \psi_{zzz}}{r^2} + \frac{\psi_{rrr} \cdot \psi_z}{r^2} - \frac{\psi_r \cdot \psi_{rr,z}}{r^2} \\ & = \frac{\mu}{\rho} \left( \frac{3\psi_r}{r^4} - \frac{3\psi_{rr}}{r^3} + \frac{2\psi_{r,zz}}{r^2} + \frac{2\psi_{rrr}}{r^2} - \frac{2\psi_{rr,zz}}{r} - \frac{\psi_{zzzz}}{r} - \frac{\psi_{rrrr}}{r} \right) \end{aligned} \quad (3.14)$$

which may be written in dimensionless form:

$$\begin{aligned} & \frac{\text{Re}}{\tilde{r}} \left( \frac{3}{\tilde{r}^2} \frac{\partial \tilde{\psi}}{\partial \tilde{r}} \cdot \frac{\partial \tilde{\psi}}{\partial \tilde{z}} - \frac{2}{\tilde{r}} \frac{\partial^2 \tilde{\psi}}{\partial \tilde{z}^2} \frac{\partial \tilde{\psi}}{\partial \tilde{z}} - \frac{3}{\tilde{r}} \frac{\partial^2 \tilde{\psi}}{\partial \tilde{r}^2} \frac{\partial \tilde{\psi}}{\partial \tilde{z}} + \frac{1}{\tilde{r}} \frac{\partial^2 \tilde{\psi}}{\partial \tilde{z} \partial \tilde{r}} \frac{\partial \tilde{\psi}}{\partial \tilde{r}} \right. \\ & \left. + \frac{\partial^3 \tilde{\psi}}{\partial \tilde{z}^2 \partial \tilde{r}} \frac{\partial \tilde{\psi}}{\partial \tilde{z}} - \frac{\partial \tilde{\psi}}{\partial \tilde{r}} \frac{\partial^3 \tilde{\psi}}{\partial \tilde{z}^3} + \frac{\partial^3 \tilde{\psi}}{\partial \tilde{r}^3} \frac{\partial \tilde{\psi}}{\partial \tilde{z}} - \frac{\partial \tilde{\psi}}{\partial \tilde{r}} \frac{\partial^3 \tilde{\psi}}{\partial \tilde{z} \partial \tilde{r}^2} \right) \quad (3.15) \\ & = \frac{3}{\tilde{r}^3} \frac{\partial \tilde{\psi}}{\partial \tilde{r}} - \frac{3}{\tilde{r}^2} \frac{\partial^2 \tilde{\psi}}{\partial \tilde{r}^2} + \frac{2}{\tilde{r}} \frac{\partial^3 \tilde{\psi}}{\partial \tilde{z}^2 \partial \tilde{r}} + \frac{2}{\tilde{r}} \frac{\partial^3 \tilde{\psi}}{\partial \tilde{r}^3} - 2 \frac{\partial^4 \tilde{\psi}}{\partial \tilde{z}^2 \partial \tilde{r}^2} - \frac{\partial^4 \tilde{\psi}}{\partial \tilde{z}^4} - \frac{\partial^4 \tilde{\psi}}{\partial \tilde{r}^4} \end{aligned}$$

where, a characteristic length scale  $R_c$  is introduced,

and other variables can be nondimensionalized as:

$$\text{Re} = \frac{\rho \psi_c}{\mu R_c}, \quad \tilde{r} = \frac{r}{R_c}, \quad \tilde{z} = \frac{z}{R_c}, \quad \tilde{\psi} = \frac{\psi}{\psi_c}, \quad (3.16)$$

$$\tilde{v}_z = v_z \cdot \frac{R_c^2}{\psi_c}, \quad \tilde{v}_r = v_r \cdot \frac{R_c^2}{\psi_c}, \quad \tilde{p} = p \cdot \frac{\mu \psi_c}{R_c^3}$$

To proceed with Manton's method, a small dimensionless perturbation parameter  $\tilde{\varepsilon}$ , characterizing the varying geometry nature, is introduced as:

$$\tilde{z} = \tilde{\varepsilon} \tilde{z} \quad (3.17)$$

which represents the contraction of the axial coordinate

and can transform the differential equation (3.15) to

$$\begin{aligned} & \frac{\text{Re}}{\tilde{r}} \left( \frac{3\tilde{\varepsilon}}{\tilde{r}^2} \frac{\partial \tilde{\psi}}{\partial \tilde{r}} \frac{\partial \tilde{\psi}}{\partial \tilde{z}} - \frac{2\tilde{\varepsilon}^3}{\tilde{r}} \frac{\partial^2 \tilde{\psi}}{\partial \tilde{z}^2} \frac{\partial \tilde{\psi}}{\partial \tilde{z}} - \frac{3\tilde{\varepsilon}}{\tilde{r}} \frac{\partial^2 \tilde{\psi}}{\partial \tilde{r}^2} \frac{\partial \tilde{\psi}}{\partial \tilde{z}} + \frac{\tilde{\varepsilon}}{\tilde{r}} \frac{\partial^2 \tilde{\psi}}{\partial \tilde{z} \partial \tilde{r}} \frac{\partial \tilde{\psi}}{\partial \tilde{r}} \right. \\ & \left. + \tilde{\varepsilon}^3 \frac{\partial^3 \tilde{\psi}}{\partial \tilde{z}^2 \partial \tilde{r}} \frac{\partial \tilde{\psi}}{\partial \tilde{z}} - \tilde{\varepsilon}^3 \frac{\partial \tilde{\psi}}{\partial \tilde{r}} \frac{\partial^3 \tilde{\psi}}{\partial \tilde{z}^3} + \tilde{\varepsilon} \frac{\partial^3 \tilde{\psi}}{\partial \tilde{r}^3} \frac{\partial \tilde{\psi}}{\partial \tilde{z}} - \tilde{\varepsilon} \frac{\partial \tilde{\psi}}{\partial \tilde{r}} \frac{\partial^3 \tilde{\psi}}{\partial \tilde{z} \partial \tilde{r}^2} \right) \quad (3.18) \\ & = \left( \frac{3}{\tilde{r}^3} \frac{\partial \tilde{\psi}}{\partial \tilde{r}} - \frac{3}{\tilde{r}^2} \frac{\partial^2 \tilde{\psi}}{\partial \tilde{r}^2} + \frac{2}{\tilde{r}} \tilde{\varepsilon}^2 \frac{\partial^3 \tilde{\psi}}{\partial \tilde{z}^2 \partial \tilde{r}} + \frac{2}{\tilde{r}} \frac{\partial^3 \tilde{\psi}}{\partial \tilde{r}^3} - 2\tilde{\varepsilon}^2 \frac{\partial^4 \tilde{\psi}}{\partial \tilde{z}^2 \partial \tilde{r}^2} \right. \\ & \left. - \tilde{\varepsilon}^4 \frac{\partial^4 \tilde{\psi}}{\partial \tilde{z}^4} - \frac{\partial^4 \tilde{\psi}}{\partial \tilde{r}^4} \right) \end{aligned}$$

We expand  $\tilde{\psi}$  in asymptotic power series in  $\tilde{\varepsilon}$  as:

$$\tilde{\psi}(\tilde{r}, \tilde{Z}) = \sum_{i=0}^{\infty} \tilde{\varepsilon}^i \tilde{\psi}_i(\tilde{r}, \tilde{Z}) \quad (3.19)$$

and substitute it into Equation (3.18) with neglecting the third order and higher terms:

$$\begin{aligned} & \left[ \begin{aligned} & \frac{3\tilde{\varepsilon}}{\tilde{r}^2} \left( \frac{\partial \tilde{\psi}_0}{\partial \tilde{r}} + \tilde{\varepsilon} \frac{\partial \tilde{\psi}_1}{\partial \tilde{r}} + \tilde{\varepsilon}^2 \frac{\partial \tilde{\psi}_2}{\partial \tilde{r}} \right) \cdot \left( \frac{\partial}{\partial \tilde{Z}} \tilde{\psi}_0 + \tilde{\varepsilon} \frac{\partial \tilde{\psi}_1}{\partial \tilde{Z}} + \tilde{\varepsilon}^2 \frac{\partial \tilde{\psi}_2}{\partial \tilde{Z}} \right) \\ & - \frac{2\tilde{\varepsilon}^3}{\tilde{r}} \left( \frac{\partial^2 \tilde{\psi}_0}{\partial \tilde{Z}^2} + \tilde{\varepsilon} \frac{\partial^2 \tilde{\psi}_1}{\partial \tilde{Z}^2} + \tilde{\varepsilon}^2 \frac{\partial^2 \tilde{\psi}_2}{\partial \tilde{Z}^2} \right) \left( \frac{\partial \tilde{\psi}_0}{\partial \tilde{Z}} + \tilde{\varepsilon} \frac{\partial \tilde{\psi}_1}{\partial \tilde{Z}} + \tilde{\varepsilon}^2 \frac{\partial \tilde{\psi}_2}{\partial \tilde{Z}} \right) \\ & - \frac{3\tilde{\varepsilon}}{\tilde{r}} \left( \frac{\partial^2 \tilde{\psi}_0}{\partial \tilde{r}^2} + \tilde{\varepsilon} \frac{\partial^2 \tilde{\psi}_1}{\partial \tilde{r}^2} + \tilde{\varepsilon}^2 \frac{\partial^2 \tilde{\psi}_2}{\partial \tilde{r}^2} \right) \left( \frac{\partial \tilde{\psi}_0}{\partial \tilde{Z}} + \tilde{\varepsilon} \frac{\partial \tilde{\psi}_1}{\partial \tilde{Z}} + \tilde{\varepsilon}^2 \frac{\partial \tilde{\psi}_2}{\partial \tilde{Z}} \right) \\ & + \frac{\tilde{\varepsilon}}{\tilde{r}} \left( \frac{\partial^2 \tilde{\psi}_0}{\partial \tilde{Z} \partial \tilde{r}} + \tilde{\varepsilon} \frac{\partial^2 \tilde{\psi}_1}{\partial \tilde{Z} \partial \tilde{r}} + \tilde{\varepsilon}^2 \frac{\partial^2 \tilde{\psi}_2}{\partial \tilde{Z} \partial \tilde{r}} \right) \left( \frac{\partial \tilde{\psi}_0}{\partial \tilde{r}} + \tilde{\varepsilon} \frac{\partial \tilde{\psi}_1}{\partial \tilde{r}} + \tilde{\varepsilon}^2 \frac{\partial \tilde{\psi}_2}{\partial \tilde{r}} \right) \\ & + \tilde{\varepsilon}^3 \left( \frac{\partial^3 \tilde{\psi}_0}{\partial \tilde{Z}^2 \partial \tilde{r}} + \tilde{\varepsilon} \frac{\partial^3 \tilde{\psi}_1}{\partial \tilde{Z}^2 \partial \tilde{r}} + \tilde{\varepsilon}^2 \frac{\partial^3 \tilde{\psi}_2}{\partial \tilde{Z}^2 \partial \tilde{r}} \right) \left( \frac{\partial \tilde{\psi}_0}{\partial \tilde{Z}} + \tilde{\varepsilon} \frac{\partial \tilde{\psi}_1}{\partial \tilde{Z}} + \tilde{\varepsilon}^2 \frac{\partial \tilde{\psi}_2}{\partial \tilde{Z}} \right) \\ & - \tilde{\varepsilon}^3 \left( \frac{\partial \tilde{\psi}_0}{\partial \tilde{r}} + \tilde{\varepsilon} \frac{\partial \tilde{\psi}_1}{\partial \tilde{r}} + \tilde{\varepsilon}^2 \frac{\partial \tilde{\psi}_2}{\partial \tilde{r}} \right) \left( \frac{\partial^3 \tilde{\psi}_0}{\partial \tilde{Z}^3} + \tilde{\varepsilon} \frac{\partial^3 \tilde{\psi}_1}{\partial \tilde{Z}^3} + \tilde{\varepsilon}^2 \frac{\partial^3 \tilde{\psi}_2}{\partial \tilde{Z}^3} \right) \\ & + \tilde{\varepsilon} \left( \frac{\partial^3 \tilde{\psi}_0}{\partial \tilde{r}^3} + \tilde{\varepsilon} \frac{\partial^3 \tilde{\psi}_1}{\partial \tilde{r}^3} + \tilde{\varepsilon}^2 \frac{\partial^3 \tilde{\psi}_2}{\partial \tilde{r}^3} \right) \left( \frac{\partial \tilde{\psi}_0}{\partial \tilde{Z}} + \tilde{\varepsilon} \frac{\partial \tilde{\psi}_1}{\partial \tilde{Z}} + \tilde{\varepsilon}^2 \frac{\partial \tilde{\psi}_2}{\partial \tilde{Z}} \right) \\ & - \tilde{\varepsilon} \left( \frac{\partial \tilde{\psi}_0}{\partial \tilde{r}} + \tilde{\varepsilon} \frac{\partial \tilde{\psi}_1}{\partial \tilde{r}} + \tilde{\varepsilon}^2 \frac{\partial \tilde{\psi}_2}{\partial \tilde{r}} \right) \left( \frac{\partial^3 \tilde{\psi}_0}{\partial \tilde{Z} \partial \tilde{r}^2} + \tilde{\varepsilon} \frac{\partial^3 \tilde{\psi}_1}{\partial \tilde{Z} \partial \tilde{r}^2} + \tilde{\varepsilon}^2 \frac{\partial^3 \tilde{\psi}_2}{\partial \tilde{Z} \partial \tilde{r}^2} \right) \end{aligned} \right] \quad (3.20) \\ & = \left[ \begin{aligned} & \frac{3}{\tilde{r}^3} \left( \frac{\partial \tilde{\psi}_0}{\partial \tilde{r}} + \tilde{\varepsilon} \frac{\partial \tilde{\psi}_1}{\partial \tilde{r}} + \tilde{\varepsilon}^2 \frac{\partial \tilde{\psi}_2}{\partial \tilde{r}} \right) - \frac{3}{\tilde{r}^2} \left( \frac{\partial^2 \tilde{\psi}_0}{\partial \tilde{r}^2} + \tilde{\varepsilon} \frac{\partial^2 \tilde{\psi}_1}{\partial \tilde{r}^2} + \tilde{\varepsilon}^2 \frac{\partial^2 \tilde{\psi}_2}{\partial \tilde{r}^2} \right) \\ & + \frac{2}{\tilde{r}} \tilde{\varepsilon}^2 \left( \frac{\partial^3 \tilde{\psi}_0}{\partial \tilde{Z}^2 \partial \tilde{r}} + \tilde{\varepsilon} \frac{\partial^3 \tilde{\psi}_1}{\partial \tilde{Z}^2 \partial \tilde{r}} + \tilde{\varepsilon}^2 \frac{\partial^3 \tilde{\psi}_2}{\partial \tilde{Z}^2 \partial \tilde{r}} \right) + \frac{2}{\tilde{r}} \left( \frac{\partial^3 \tilde{\psi}_0}{\partial \tilde{r}^3} + \tilde{\varepsilon} \frac{\partial^3 \tilde{\psi}_1}{\partial \tilde{r}^3} + \tilde{\varepsilon}^2 \frac{\partial^3 \tilde{\psi}_2}{\partial \tilde{r}^3} \right) \\ & - 2\tilde{\varepsilon}^2 \left( \frac{\partial^4 \tilde{\psi}_0}{\partial \tilde{Z}^2 \partial \tilde{r}^2} + \tilde{\varepsilon} \frac{\partial^4 \tilde{\psi}_1}{\partial \tilde{Z}^2 \partial \tilde{r}^2} + \tilde{\varepsilon}^2 \frac{\partial^4 \tilde{\psi}_2}{\partial \tilde{Z}^2 \partial \tilde{r}^2} \right) \\ & - \tilde{\varepsilon}^4 \left( \frac{\partial^4 \tilde{\psi}_0}{\partial \tilde{Z}^4} + \tilde{\varepsilon} \frac{\partial^4 \tilde{\psi}_1}{\partial \tilde{Z}^4} + \tilde{\varepsilon}^2 \frac{\partial^4 \tilde{\psi}_2}{\partial \tilde{Z}^4} \right) - \left( \frac{\partial^4 \tilde{\psi}_0}{\partial \tilde{r}^4} + \tilde{\varepsilon} \frac{\partial^4 \tilde{\psi}_1}{\partial \tilde{r}^4} + \tilde{\varepsilon}^2 \frac{\partial^4 \tilde{\psi}_2}{\partial \tilde{r}^4} \right) \end{aligned} \right] \end{aligned}$$

A feasible asymptotic solution of the above equation can be obtained by decomposing the equation in terms of the order of  $\tilde{\varepsilon}$  and solving the decomposed equations separately.

### Zeroth-order Stream Function Solution

For terms of  $\tilde{\varepsilon}^0$ , Equations (3.20) reduces to:

$$\tilde{r}^3 \frac{\partial^4 \tilde{\psi}_0}{\partial \tilde{r}^4} - 2\tilde{r}^2 \frac{\partial^3 \tilde{\psi}_0}{\partial \tilde{r}^3} + 3\tilde{r} \frac{\partial^2 \tilde{\psi}_0}{\partial \tilde{r}^2} - 3 \frac{\partial \tilde{\psi}_0}{\partial \tilde{r}} = 0 \quad (3.21)$$

The general solution of Equation (3.21) can be written as:

$$\tilde{\psi}_0(\tilde{r}, \tilde{z}) = C_1(\tilde{z}) + C_2(\tilde{z}) \tilde{r}^2 + C_3(\tilde{z}) \tilde{r}^2 \log(\tilde{r}) + C_4(\tilde{z}) \tilde{r}^4 \quad (3.22)$$

To remove the singularity at  $\tilde{r} = 0$ ,  $C_3$  should be set to zero. From conditions (3.9)-(3.11), the boundary conditions of Equation (3.22) can be written as:

$$\left. \frac{\partial \tilde{\psi}_0(\tilde{r}, \tilde{z})}{\partial \tilde{r}} \right|_{\tilde{r}=\tilde{R}(\tilde{z})} = 0 \quad (3.23)$$

$$\tilde{\psi}_0(\tilde{R}_e(\tilde{z}), \tilde{z}) = 1 \quad (3.24)$$

$$\tilde{\psi}_0(0, \tilde{z}) = 0 \quad (3.25)$$

$C_1$ ,  $C_2$  and  $C_4$  can be determined by conditions (3.23)-(3.25) and, finally,  $\tilde{\psi}_0$  can be expressed as:

$$\tilde{\psi}_0 = 2\eta^2 - \eta^4 \quad (3.26)$$

where

$$\eta = \frac{\tilde{r}}{\tilde{R}_\varepsilon(\tilde{Z})} \quad (3.27)$$

$$\tilde{R}_\varepsilon(\tilde{Z}) = \tilde{R}(\tilde{z}) = \frac{R(z)}{R_c} \quad (3.28)$$

The zeroth-order solution leads to the parabolic velocity distribution, that is the Hagen-Poiseuille solution of the pressure-driven flow in the uniform circular tube and adopted in the analysis in chapter 2.

### First-order Stream Function Solution

For terms of  $\tilde{\varepsilon}^1$ , Equations (3.20) reduces to:

$$\begin{aligned} & \frac{\text{Re}}{\tilde{r}} \left[ \frac{3\tilde{\varepsilon}}{\tilde{r}^2} \left( \frac{\partial \tilde{\psi}_0}{\partial \tilde{r}} \right) \cdot \left( \frac{\partial \tilde{\psi}_0}{\partial \tilde{Z}} \right) - \frac{3\tilde{\varepsilon}}{\tilde{r}} \left( \frac{\partial^2 \tilde{\psi}_0}{\partial \tilde{r}^2} \right) \left( \frac{\partial \tilde{\psi}_0}{\partial \tilde{Z}} \right) + \frac{\tilde{\varepsilon}}{\tilde{r}} \left( \frac{\partial^2 \tilde{\psi}_0}{\partial \tilde{Z} \partial \tilde{r}} \right) \left( \frac{\partial \tilde{\psi}_0}{\partial \tilde{r}} \right) \right] \\ & \left[ + \tilde{\varepsilon} \left( \frac{\partial^3 \tilde{\psi}_0}{\partial \tilde{r}^3} \right) \left( \frac{\partial \tilde{\psi}_0}{\partial \tilde{Z}} \right) - \tilde{\varepsilon} \left( \frac{\partial \tilde{\psi}_0}{\partial \tilde{r}} \right) \left( \frac{\partial^3 \tilde{\psi}_0}{\partial \tilde{Z} \partial \tilde{r}^2} \right) \right] \quad (3.29) \\ & = \frac{3}{\tilde{r}^3} \left( \tilde{\varepsilon} \frac{\partial \tilde{\psi}_1}{\partial \tilde{r}} \right) - \frac{3}{\tilde{r}^2} \left( \tilde{\varepsilon} \frac{\partial^2 \tilde{\psi}_1}{\partial \tilde{r}^2} \right) + \frac{2}{\tilde{r}} \left( \tilde{\varepsilon} \frac{\partial^3 \tilde{\psi}_1}{\partial \tilde{r}^3} \right) - \left( \tilde{\varepsilon} \frac{\partial^4 \tilde{\psi}_1}{\partial \tilde{r}^4} \right) \end{aligned}$$

Substituting the solution of  $\tilde{\psi}_0$  into Equation (3.29)

gives:

$$\begin{aligned}
& 3 \left( \frac{\partial \tilde{\psi}_1}{\partial \tilde{r}} \right) - 3\tilde{r} \left( \frac{\partial^2 \tilde{\psi}_1}{\partial \tilde{r}^2} \right) + 2\tilde{r}^2 \left( \frac{\partial^3 \tilde{\psi}_1}{\partial \tilde{r}^3} \right) - \tilde{r}^3 \left( \frac{\partial^4 \tilde{\psi}_1}{\partial \tilde{r}^4} \right) \\
& = 128 \operatorname{Re} \frac{d\tilde{R}_\epsilon(\tilde{Z})}{d\tilde{Z}} \left[ \frac{\tilde{r}^7}{\tilde{R}^9(\tilde{Z})} - \frac{\tilde{r}^5}{\tilde{R}^7(\tilde{Z})} \right]
\end{aligned} \tag{3.30}$$

The general solution of Equation (3.30) can be written as:

$$\tilde{\psi}_1 = -\frac{1}{36} \frac{1}{\tilde{R}_\epsilon(\tilde{Z})} \left[ \begin{aligned} & -36C_1\tilde{R}_\epsilon(\tilde{Z}) - 18C_2\tilde{R}_\epsilon(\tilde{Z})\tilde{r}^2 + 9C_3\tilde{R}_\epsilon(\tilde{Z})\tilde{r}^2 \\ & -18C_3\tilde{R}_\epsilon(\tilde{Z})\tilde{r}^2 \ln \tilde{r} - 9C_4\tilde{R}_\epsilon(\tilde{Z})\tilde{r}^4 \\ & -24 \operatorname{Re} \frac{d\tilde{R}_\epsilon(\tilde{Z})}{d\tilde{Z}} \frac{\tilde{r}^6}{\tilde{R}_\epsilon^6(\tilde{Z})} + 4 \operatorname{Re} \frac{d\tilde{R}_\epsilon(\tilde{Z})}{d\tilde{Z}} \frac{\tilde{r}^8}{\tilde{R}_\epsilon^8(\tilde{Z})} \end{aligned} \right] \tag{3.31}$$

Similar to the zeroth-order,  $C_3$  should be set to zero to remove the singularity at  $\tilde{r} = 0$ . From conditions (3.9)-(3.11), the boundary conditions of Equation (3.31) can be written as:

$$\left. \frac{\partial \tilde{\psi}_1(\tilde{r}, \tilde{Z})}{\partial \tilde{r}} \right|_{\tilde{r}=\tilde{R}_\epsilon(\tilde{Z})} = 0 \tag{3.32}$$

$$\tilde{\psi}_1(\tilde{R}_\epsilon(\tilde{Z}), \tilde{Z}) = 0 \tag{3.33}$$

$$\tilde{\psi}_1(0, \tilde{Z}) = 0 \tag{3.34}$$

$C_1$ ,  $C_2$  and  $C_4$  can be determined by conditions (3.32)-(3.34) and, finally,  $\tilde{\psi}_1$  can be expressed as:

$$\tilde{\psi}_1 = \frac{1}{18} \operatorname{Re} \frac{d\tilde{R}_\epsilon(\tilde{Z})}{d\tilde{Z}} \frac{1}{\tilde{R}_\epsilon(\tilde{Z})} (8\eta^2 - 18\eta^4 + 12\eta^6 - 2\eta^8) \tag{3.35}$$

For a uniform tube,  $\frac{d\tilde{R}_\varepsilon(\tilde{Z})}{d\tilde{Z}} = 0$  leads to  $\tilde{\psi}_1 = 0$  which

indicates that  $\tilde{\psi}_1$ , superimposing on  $\tilde{\psi}_0$ , is caused by the nonuniformity effect of the tube geometry.

### Second-order Stream Function Solution

For terms of  $\tilde{\varepsilon}^2$ , Equations (3.20) reduces to:

$$\begin{aligned} & \left[ \begin{aligned} & \frac{3\tilde{\varepsilon}}{\tilde{r}^2} \left( \tilde{\varepsilon} \frac{\partial \tilde{\psi}_0}{\partial \tilde{r}} \frac{\partial \tilde{\psi}_1}{\partial \tilde{Z}} + \tilde{\varepsilon} \frac{\partial \tilde{\psi}_1}{\partial \tilde{r}} \frac{\partial \tilde{\psi}_0}{\partial \tilde{Z}} \right) \\ & - \frac{3\tilde{\varepsilon}}{\tilde{r}} \left( \tilde{\varepsilon} \frac{\partial^2 \tilde{\psi}_0}{\partial \tilde{r}^2} \frac{\partial \tilde{\psi}_1}{\partial \tilde{Z}} + \tilde{\varepsilon} \frac{\partial^2 \tilde{\psi}_1}{\partial \tilde{r}^2} \frac{\partial \tilde{\psi}_0}{\partial \tilde{Z}} \right) \\ & + \frac{\tilde{\varepsilon}}{\tilde{r}} \left( \tilde{\varepsilon} \frac{\partial \tilde{\psi}_1}{\partial \tilde{r}} \frac{\partial^2 \tilde{\psi}_0}{\partial \tilde{Z} \partial \tilde{r}} + \tilde{\varepsilon} \frac{\partial^2 \tilde{\psi}_1}{\partial \tilde{Z} \partial \tilde{r}} \frac{\partial \tilde{\psi}_0}{\partial \tilde{r}} \right) \\ & + \tilde{\varepsilon}^2 \left( \frac{\partial \tilde{\psi}_1}{\partial \tilde{Z}} \frac{\partial^3 \tilde{\psi}_0}{\partial \tilde{r}^3} + \frac{\partial^3 \tilde{\psi}_1}{\partial \tilde{r}^3} \frac{\partial \tilde{\psi}_0}{\partial \tilde{Z}} - \frac{\partial^3 \tilde{\psi}_1}{\partial \tilde{Z} \partial \tilde{r}^2} \frac{\partial \tilde{\psi}_0}{\partial \tilde{r}} - \frac{\partial \tilde{\psi}_1}{\partial \tilde{r}} \frac{\partial^3 \tilde{\psi}_0}{\partial \tilde{Z} \partial \tilde{r}^2} \right) \end{aligned} \right] \quad (3.36) \\ = & \left[ \begin{aligned} & \frac{3}{\tilde{r}^3} \left( \tilde{\varepsilon}^2 \frac{\partial \tilde{\psi}_2}{\partial \tilde{r}} \right) - \frac{3}{\tilde{r}^2} \left( \tilde{\varepsilon}^2 \frac{\partial^2 \tilde{\psi}_2}{\partial \tilde{r}^2} \right) + \frac{2}{\tilde{r}} \tilde{\varepsilon}^2 \left( \frac{\partial^3 \tilde{\psi}_0}{\partial \tilde{Z}^2 \partial \tilde{r}} \right) + \frac{2}{\tilde{r}} \left( \tilde{\varepsilon}^2 \frac{\partial^3 \tilde{\psi}_2}{\partial \tilde{r}^3} \right) \\ & - 2\tilde{\varepsilon}^2 \left( \frac{\partial^4 \tilde{\psi}_0}{\partial \tilde{Z}^2 \partial \tilde{r}^2} \right) - \left( \tilde{\varepsilon}^2 \frac{\partial^4 \tilde{\psi}_2}{\partial \tilde{r}^4} \right) \end{aligned} \right] \end{aligned}$$

Substituting the solutions of  $\tilde{\psi}_0$  and  $\tilde{\psi}_1$  into Equation

(3.36) gives:

$$\begin{aligned}
& \left[ 3 \left( \frac{\partial \tilde{\psi}_2}{\partial \tilde{r}} \right) - 3\tilde{r} \left( \frac{\partial^2 \tilde{\psi}_2}{\partial \tilde{r}^2} \right) + 2\tilde{r}^2 \left( \frac{\partial^3 \tilde{\psi}_2}{\partial \tilde{r}^3} \right) - \tilde{r}^3 \left( \frac{\partial^4 \tilde{\psi}_2}{\partial \tilde{r}^4} \right) \right. \\
& \left. + 320 \frac{\tilde{r}^5}{\tilde{R}_\epsilon^6(\tilde{Z})} \left( \frac{d\tilde{R}_\epsilon(\tilde{Z})}{d\tilde{Z}} \right)^2 - 64 \frac{\tilde{r}^5}{\tilde{R}_\epsilon^5(\tilde{Z})} \frac{d^2\tilde{R}_\epsilon(\tilde{Z})}{d\tilde{Z}^2} \right] \\
& = \frac{2}{9} \operatorname{Re}^2 \left[ \begin{aligned} & \frac{d^2\tilde{R}_\epsilon(\tilde{Z})}{d\tilde{Z}^2} \frac{\tilde{r}^2}{\tilde{R}_\epsilon^4(\tilde{Z})} \left( \begin{aligned} & 144 \frac{\tilde{r}^3}{\tilde{R}_\epsilon^3(\tilde{Z})} - 432 \frac{\tilde{r}^5}{\tilde{R}_\epsilon^5(\tilde{Z})} \\ & + 384 \frac{\tilde{r}^7}{\tilde{R}_\epsilon^7(\tilde{Z})} - 96 \frac{\tilde{r}^9}{\tilde{R}_\epsilon^9(\tilde{Z})} \end{aligned} \right) \\ & + \left( \frac{d\tilde{R}_\epsilon(\tilde{Z})}{d\tilde{Z}} \right)^2 \frac{\tilde{r}^2}{\tilde{R}_\epsilon^5(\tilde{Z})} \left( \begin{aligned} & -848 \frac{\tilde{r}^3}{\tilde{R}_\epsilon^3(\tilde{Z})} + 2736 \frac{\tilde{r}^5}{\tilde{R}_\epsilon^5(\tilde{Z})} \\ & - 2496 \frac{\tilde{r}^7}{\tilde{R}_\epsilon^7(\tilde{Z})} + 608 \frac{\tilde{r}^9}{\tilde{R}_\epsilon^9(\tilde{Z})} \end{aligned} \right) \end{aligned} \right] \tag{3.37}
\end{aligned}$$

For convenience, let

$$\tilde{\psi}_2 = \tilde{\psi}_{21} + \tilde{\psi}_{22} + \tilde{\psi}_{23} \tag{3.38}$$

and divide equation (3.37) into:

$$\begin{aligned}
& 3 \frac{\partial \tilde{\psi}_{21}}{\partial \eta} - 3\eta \frac{\partial^2 \tilde{\psi}_{21}}{\partial \eta^2} + 2\eta^2 \frac{\partial^3 \tilde{\psi}_{21}}{\partial \eta^3} - \eta^3 \frac{\partial^4 \tilde{\psi}_{21}}{\partial \eta^4} \\
& + 64\eta^5 \left[ 5 \left( \frac{d\tilde{R}_\epsilon(\tilde{Z})}{d\tilde{Z}} \right)^2 - \tilde{R}_\epsilon(\tilde{Z}) \frac{d^2\tilde{R}_\epsilon(\tilde{Z})}{d\tilde{Z}^2} \right] = 0 \tag{3.39}
\end{aligned}$$

$$\begin{aligned}
& 3 \frac{\partial \tilde{\psi}_{22}}{\partial \eta} - 3\eta \frac{\partial^2 \tilde{\psi}_{22}}{\partial \eta^2} + 2\eta^2 \frac{\partial^3 \tilde{\psi}_{22}}{\partial \eta^3} - \eta^3 \frac{\partial^4 \tilde{\psi}_{22}}{\partial \eta^4} \\
& = \frac{2}{9} \frac{\operatorname{Re}^2}{\tilde{R}_\epsilon^2(\tilde{Z})} \left( \frac{d\tilde{R}_\epsilon(\tilde{Z})}{d\tilde{Z}} \right)^2 (-848\eta^5 + 2736\eta^7 - 2496\eta^9 + 608\eta^{11}) \tag{3.40}
\end{aligned}$$

$$\begin{aligned}
& 3 \frac{\partial \tilde{\psi}_{23}}{\partial \eta} - 3\eta \frac{\partial^2 \tilde{\psi}_{23}}{\partial \eta^2} + 2\eta^2 \frac{\partial^3 \tilde{\psi}_{23}}{\partial \eta^3} - \eta^3 \frac{\partial^4 \tilde{\psi}_{23}}{\partial \eta^4} \\
& = \frac{2}{9} \frac{\operatorname{Re}^2}{\tilde{R}_\epsilon(\tilde{Z})} \frac{d^2\tilde{R}_\epsilon(\tilde{Z})}{d\tilde{Z}^2} (144\eta^5 - 432\eta^7 + 384\eta^9 - 96\eta^{11}) \tag{3.41}
\end{aligned}$$

With the boundary conditions:

$$\left. \frac{\partial \tilde{\psi}_{2i}(\tilde{r}, \tilde{Z})}{\partial \tilde{r}} \right|_{\tilde{r}=\tilde{R}_\epsilon(\tilde{Z})} = 0 \quad (3.42)$$

$$\tilde{\psi}_{2i}(\tilde{R}_\epsilon(\tilde{Z}), \tilde{Z}) = 0 \quad (3.43)$$

$$\tilde{\psi}_{2i}(0, \tilde{Z}) = 0 \quad (3.44)$$

The solutions of Equations (3.39)-(3.41) are obtained:

$$\begin{aligned} \tilde{\psi}_{21} = & C_{10}(\tilde{Z}) - \frac{1}{4} C_{11}(\tilde{Z})\eta^2 + \frac{1}{2} C_{11}(\tilde{Z})\eta^2 \ln(\eta) + \frac{1}{2} C_{12}(\tilde{Z})\eta^2 \\ & + \frac{1}{4} C_{13}(\tilde{Z})\eta^4 + \frac{1}{3} \left[ 5 \left( \frac{d\tilde{R}_\epsilon(\tilde{Z})}{d\tilde{Z}} \right)^2 - \tilde{R}_\epsilon(\tilde{Z}) \frac{d^2\tilde{R}_\epsilon(\tilde{Z})}{d\tilde{Z}^2} \right] \eta^6 \end{aligned} \quad (3.45)$$

$$\begin{aligned} \tilde{\psi}_{22} = & C_{20}(\tilde{Z}) - \frac{1}{4} C_{21}(\tilde{Z})\eta^2 + \frac{1}{2} C_{21}(\tilde{Z})\eta^2 \ln(\eta) + \frac{1}{2} C_{22}(\tilde{Z})\eta^2 \\ & + \frac{1}{4} C_{23}(\tilde{Z})\eta^4 \\ & + \frac{\text{Re}^2}{\tilde{R}_\epsilon(\tilde{Z})} \frac{d^2\tilde{R}_\epsilon(\tilde{Z})}{d\tilde{Z}^2} \left( \frac{53}{54} \eta^6 - \frac{19}{36} \eta^8 + \frac{13}{90} \eta^{10} - \frac{19}{1350} \eta^{12} \right) \end{aligned} \quad (3.46)$$

$$\begin{aligned} \tilde{\psi}_{23} = & C_{30}(\tilde{Z}) - \frac{1}{4} C_{31}(\tilde{Z})\eta^2 + \frac{1}{2} C_{31}(\tilde{Z})\eta^2 \ln(\eta) + \frac{1}{2} C_{32}(\tilde{Z})\eta^2 \\ & + \frac{1}{4} C_{33}(\tilde{Z})\eta^4 \\ & + \frac{\text{Re}^2}{\tilde{R}_\epsilon(\tilde{Z})} \frac{d^2\tilde{R}_\epsilon(\tilde{Z})}{d\tilde{Z}^2} \left( -\frac{1}{6} \eta^6 + \frac{1}{12} \eta^8 - \frac{1}{45} \eta^{10} + \frac{1}{450} \eta^{12} \right) \end{aligned} \quad (3.47)$$

Applying the boundary conditions:

$$\left. \frac{\partial \tilde{\psi}_{2i}(\tilde{r}, \tilde{Z})}{\partial \tilde{r}} \right|_{\tilde{r}=\tilde{R}_\epsilon(\tilde{Z})} = 0 \quad (3.48)$$

$$\tilde{\psi}_{2i}(\tilde{R}_\epsilon(\tilde{Z}), \tilde{Z}) = 0 \quad (3.49)$$

$$\tilde{\psi}_{2i}(0, \tilde{z}) = 0 \quad (3.50)$$

and the similar treatment that set the logarithm terms to zero to remove the singularity at the axis, equations

(3.45)-(3.47) can be finally written as:

$$\tilde{\psi}_{21} = \frac{1}{3} \left[ 5 \left( \frac{d\tilde{R}_\varepsilon(\tilde{z})}{d\tilde{z}} \right)^2 - \tilde{R}_\varepsilon(\tilde{z}) \frac{d^2\tilde{R}_\varepsilon(\tilde{z})}{d\tilde{z}^2} \right] (\eta^2 - 2\eta^4 + \eta^6) \quad (3.51)$$

$$\tilde{\psi}_{22} = \frac{\text{Re}^2}{\tilde{R}_\varepsilon^3(\tilde{z})} \left( \frac{d\tilde{R}_\varepsilon(\tilde{z})}{d\tilde{z}} \right)^2 \left( \begin{array}{l} \frac{409}{1350} \eta^2 - \frac{479}{540} \eta^4 + \frac{53}{54} \eta^6 - \frac{19}{36} \eta^8 \\ + \frac{13}{90} \eta^{10} - \frac{19}{1350} \eta^{12} \end{array} \right) \quad (3.52)$$

$$\tilde{\psi}_{23} = \frac{\text{Re}^2}{\tilde{R}_\varepsilon(\tilde{z})} \frac{d^2\tilde{R}_\varepsilon(\tilde{z})}{d\tilde{z}^2} \left( \begin{array}{l} -\frac{13}{225} \eta^2 + \frac{29}{180} \eta^4 - \frac{1}{6} \eta^6 + \frac{1}{12} \eta^8 \\ -\frac{1}{45} \eta^{10} + \frac{1}{450} \eta^{12} \end{array} \right) \quad (3.53)$$

Hence, the perturbation solution of stream function is obtained:

$$\begin{aligned} \tilde{\psi} &= 2\eta^2 - \eta^4 \quad (3.54) \\ &+ \tilde{\varepsilon} \left\{ \frac{1}{18} \text{Re} \frac{d\tilde{R}_\varepsilon(\tilde{z})}{d\tilde{z}} \frac{1}{\tilde{R}_\varepsilon(\tilde{z})} [8\eta^2 - 18\eta^4 + 12\eta^6 - 2\eta^8] \right\} \\ &+ \tilde{\varepsilon}^2 \left\{ \begin{array}{l} \frac{1}{3} \left[ 5 \left( \frac{d\tilde{R}_\varepsilon(\tilde{z})}{d\tilde{z}} \right)^2 - \tilde{R}_\varepsilon(\tilde{z}) \frac{d^2\tilde{R}_\varepsilon(\tilde{z})}{d\tilde{z}^2} \right] (\eta^6 - 2\eta^4 + \eta^2) \\ + \frac{1}{2700} \frac{\text{Re}^2}{\tilde{R}_\varepsilon^2(\tilde{z})} \left( \frac{d\tilde{R}_\varepsilon(\tilde{z})}{d\tilde{z}} \right)^2 \left[ \begin{array}{l} -38\eta^{12} + 390\eta^{10} - 1425\eta^8 \\ + 2650\eta^6 - 2395\eta^4 + 818\eta^2 \end{array} \right] \\ + \frac{1}{2700} \frac{\text{Re}^2}{\tilde{R}_\varepsilon(\tilde{z})} \frac{d^2\tilde{R}_\varepsilon(\tilde{z})}{d\tilde{z}^2} \left[ \begin{array}{l} 6\eta^{12} - 60\eta^{10} + 225\eta^8 \\ -450\eta^6 + 435\eta^4 - 156\eta^2 \end{array} \right] \end{array} \right\} \end{aligned}$$

The resulting solution of stream function obtained by Manton's perturbation method [Manton 1971] is identical to that reported by Van Dyke (1987) who corrected an error in Manton's coefficients. This correct version is also tacitly confirmed by Kasivisvanathan et al. (1991), Kotorynski (1995) and Sisavath et al. (2001). The dependence on the perturbation parameter  $\tilde{\epsilon}$  can be removed by the expansion of axial coordinate  $\tilde{Z}$  to  $\tilde{z}$ :

$$\begin{aligned} \tilde{\psi} &= 2\eta^2 - \eta^4 & (3.55) \\ &+ \frac{1}{18} \operatorname{Re} \frac{d\tilde{R}(\tilde{z})}{d\tilde{z}} \frac{1}{\tilde{R}(\tilde{z})} (8\eta^2 - 18\eta^4 + 12\eta^6 - 2\eta^8) \\ &+ \frac{1}{3} \left[ 5 \left( \frac{d\tilde{R}(\tilde{z})}{d\tilde{z}} \right)^2 - \tilde{R}(\tilde{z}) \frac{d^2\tilde{R}(\tilde{z})}{d\tilde{z}^2} \right] (\eta^6 - 2\eta^4 + \eta^2) \\ &+ \frac{1}{2700} \frac{\operatorname{Re}^2}{\tilde{R}^2(\tilde{z})} \left( \frac{d\tilde{R}(\tilde{z})}{d\tilde{z}} \right)^2 \left[ \begin{array}{l} -38\eta^{12} + 390\eta^{10} - 1425\eta^8 \\ +2650\eta^6 - 2395\eta^4 + 818\eta^2 \end{array} \right] \\ &+ \frac{1}{2700} \frac{\operatorname{Re}^2}{\tilde{R}(\tilde{z})} \frac{d^2\tilde{R}(\tilde{z})}{d\tilde{z}^2} \left[ \begin{array}{l} 6\eta^{12} - 60\eta^{10} + 225\eta^8 \\ -450\eta^6 + 435\eta^4 - 156\eta^2 \end{array} \right] \end{aligned}$$

For small Reynolds number flows, the terms including the Reynolds number can be excluded,

$$\tilde{\psi} = 2\eta^2 - \eta^4 + \frac{1}{3} \left[ 5 \left( \frac{d\tilde{R}(\tilde{z})}{d\tilde{z}} \right)^2 - \tilde{R}(\tilde{z}) \frac{d^2\tilde{R}(\tilde{z})}{d\tilde{z}^2} \right] (\eta^6 - 2\eta^4 + \eta^2) \quad (3.56)$$

Figures 3.1 and 3.2 show the stream lines obtained from Equations (3.55) and (3.56) for sinusoidal tubes as depicted in Chapter 2 with  $\operatorname{Re}=0.1$  and  $\operatorname{Re}=4$ , respectively.

The geometry is described by  $\tilde{R}(\tilde{z}) = 1 + A \sin(2\pi\tilde{z} / L)$ .  $\tilde{R}$ ,  $\tilde{z}$  and  $L$  are nondimensionalized by  $R_c = 200\mu\text{m}$ . For the calculation,  $L=4$  and  $A=0.3$ . The analytical results are compared to the stream lines numerically obtained from FLUENT simulation. The basic setting in FLUENT is shown in Figure 3.1, where the parabolic profile is designated to both the inlet and outlet straight wall regions. One period section of the intermediate sinusoidal tube is selected for the observation of the geometrical effect on the laminar flow with different Reynolds numbers in Figure 3.2.

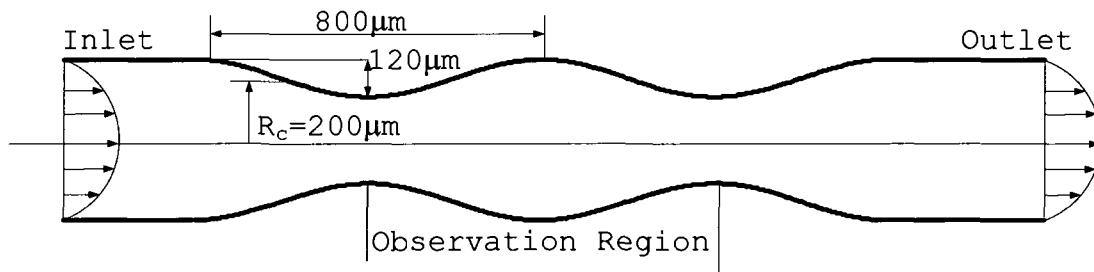


Figure 3.1 Schematic of geometry setting in FLUENT.

For the small Reynolds number, both the solutions of Equations (3.55) and (3.56) are consistent with that of FLUENT. However, as indicated in Figure 3.2b, the Reynolds number terms in Equation (3.55) become large for  $Re=4$  and produce unrealistic deviations from the FLUENT

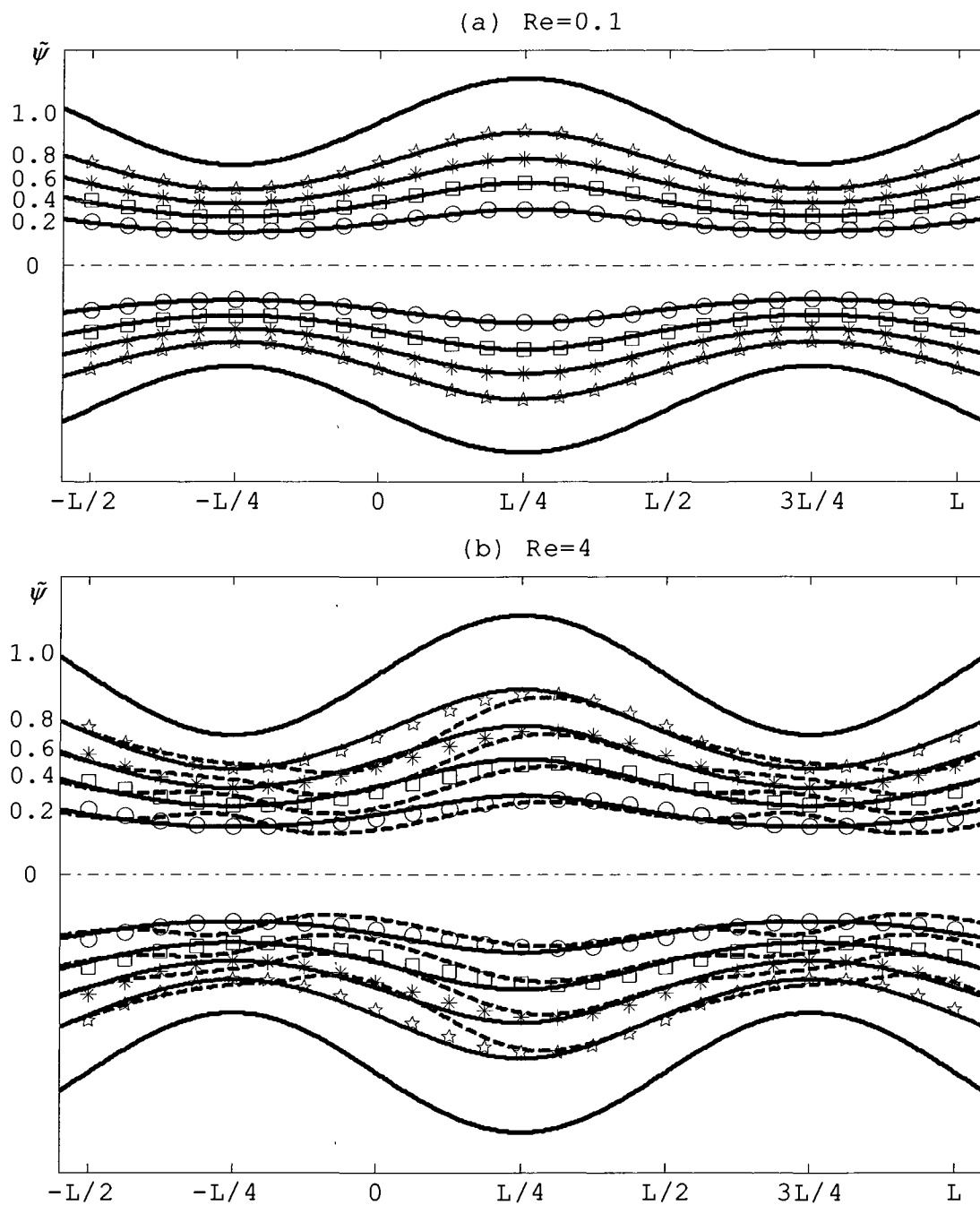


Figure 3.2 Stream line in sinusoidal tube.  
 Solid line: Equation (3.56); Dash line: Equation (3,55);  
 Discrete points: FLUENT Results.

stream lines, and Equation (3.56) still holds for  $Re=4$  giving results consistent with those of FLUENT. A further series of comparisons with FLUENT results for more Reynolds number implies that the asymptotic stream function solution excluding the Reynolds number terms as in Equation (3.56) may be applicable to laminar flow with a Reynolds number up to a critical value  $Re_{cr}=10$  where the flow separation happens for  $L=4$ ,  $A=0.3$ . Deiber and Schowalter (1979) reported  $Re_{cr}=75$  for the sinusoidal tube with  $L=10$ ,  $A=0.3$  through their experimental observations. It implies the critical value varies with different geometries.

From the definition of the stream function, the axial velocity component can be obtained using Equation (3.56):

$$\tilde{v}_z = \left\{ \begin{array}{l} \frac{4}{\tilde{R}^2(\tilde{z})} (1 - \eta^2) \\ + \frac{1}{3} \left[ 5 \frac{1}{\tilde{R}^2(\tilde{z})} \left( \frac{d\tilde{R}(\tilde{z})}{d\tilde{z}} \right)^2 - \frac{1}{\tilde{R}(\tilde{z})} \frac{d^2\tilde{R}(\tilde{z})}{d\tilde{z}^2} \right] (3\eta^4 - 4\eta^2 + 1) \end{array} \right\} \quad (3.57)$$

And the radial velocity component is written as:

$$\tilde{v}_r = \left\{ \begin{array}{l} \frac{4}{\tilde{R}^2(\tilde{z})} \frac{d\tilde{R}(\tilde{z})}{d\tilde{z}} (\eta - \eta^3) + \frac{10}{3} \frac{1}{\tilde{R}^2(\tilde{z})} \left( \frac{d\tilde{R}(\tilde{z})}{d\tilde{z}} \right)^3 (3\eta^5 - 4\eta^3 + \eta) \\ - \frac{1}{3} \frac{1}{\tilde{R}(\tilde{z})} \frac{d\tilde{R}(\tilde{z})}{d\tilde{z}} \frac{d^2\tilde{R}(\tilde{z})}{d\tilde{z}^2} (15\eta^5 - 26\eta^3 + 11\eta) \\ + \frac{1}{3} \frac{d^3\tilde{R}(\tilde{z})}{d\tilde{z}^3} (\eta^5 - 2\eta^3 + \eta) \end{array} \right\} \quad (3.58)$$

For a comparison, we write the simple velocity model, Equations (2.6), (2.8) and (2.9), used in Chapter 2 in the cylindrical coordinate system, and the same dimensionless form as:

$$\tilde{v}_z = \frac{4}{\tilde{R}^2(\tilde{z})} (1 - \eta^2) \quad (3.59)$$

$$\tilde{v}_r = \frac{4}{\tilde{R}^2(\tilde{z})} \frac{d\tilde{R}(\tilde{z})}{d\tilde{z}} (\eta - \eta^3) \quad (3.60)$$

It implies that the parabolic velocity model in Chapter 2 is essentially the zero-th order solution of the asymptotic analysis described in this section.

Figures 3.3 -3.8 present the comparison of the proposed velocity distribution with previous parabolic solution as well as FLUENT results and show that there are improvements with Equations (3.57) and (3.59) over the simple parabolic model to predict the velocity profiles in both axial and radial directions.

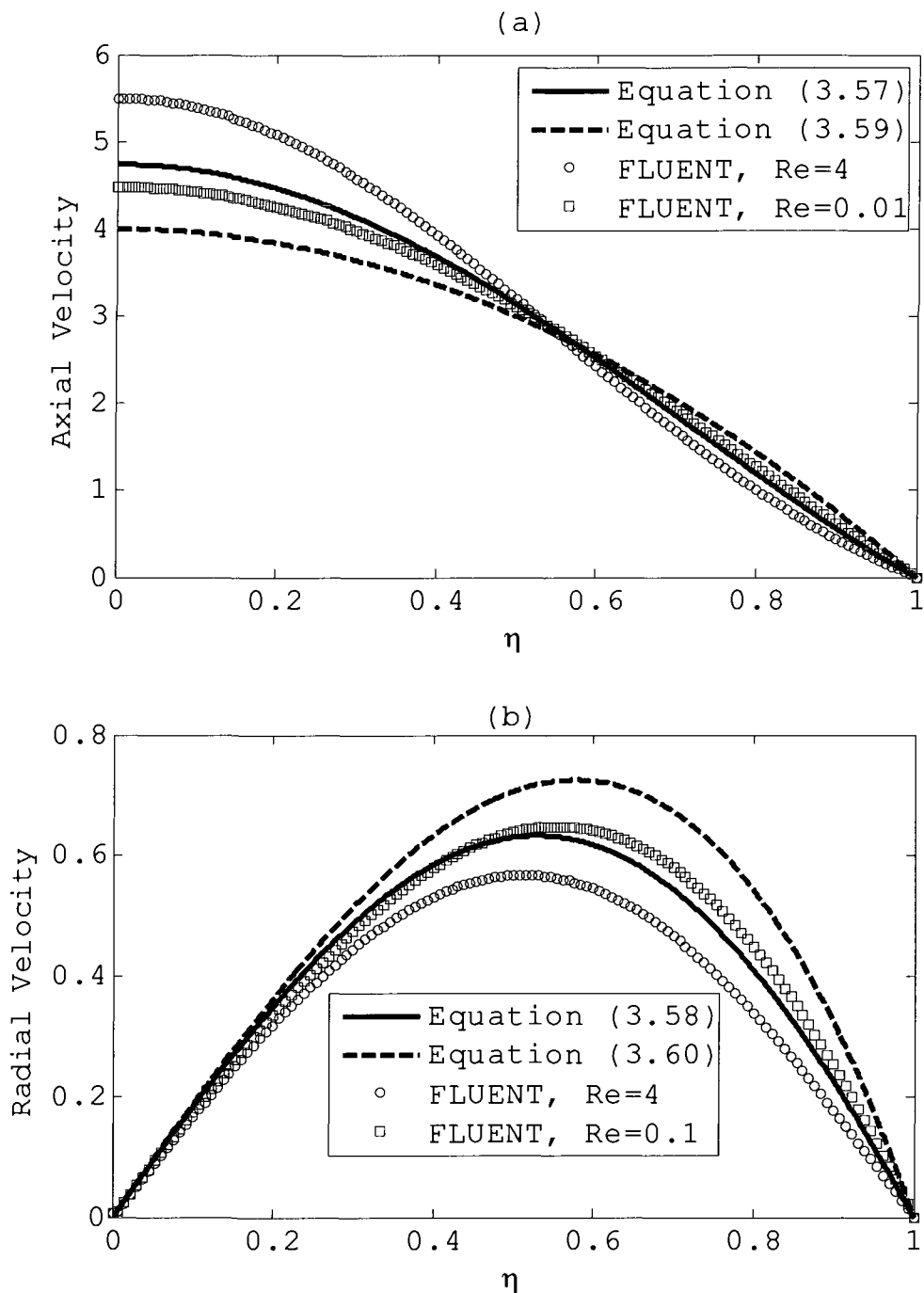


Figure 3.3 Velocity distribution in the cross section plane at  $z=0$  of a sinusoidal tube.

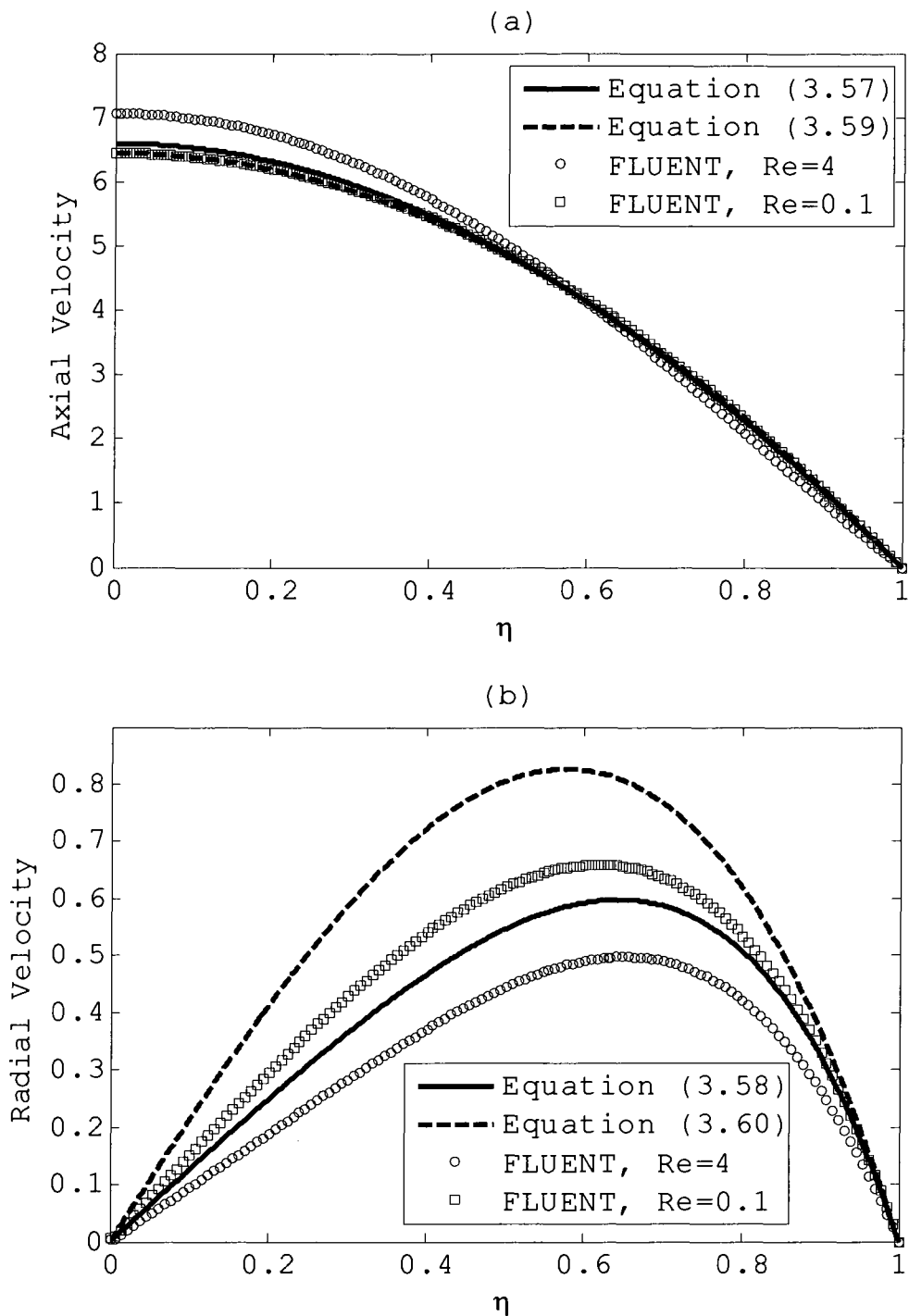


Figure 3.4 Velocity distribution in the cross section plane at  $z=-L/8$  of a sinusoidal tube.

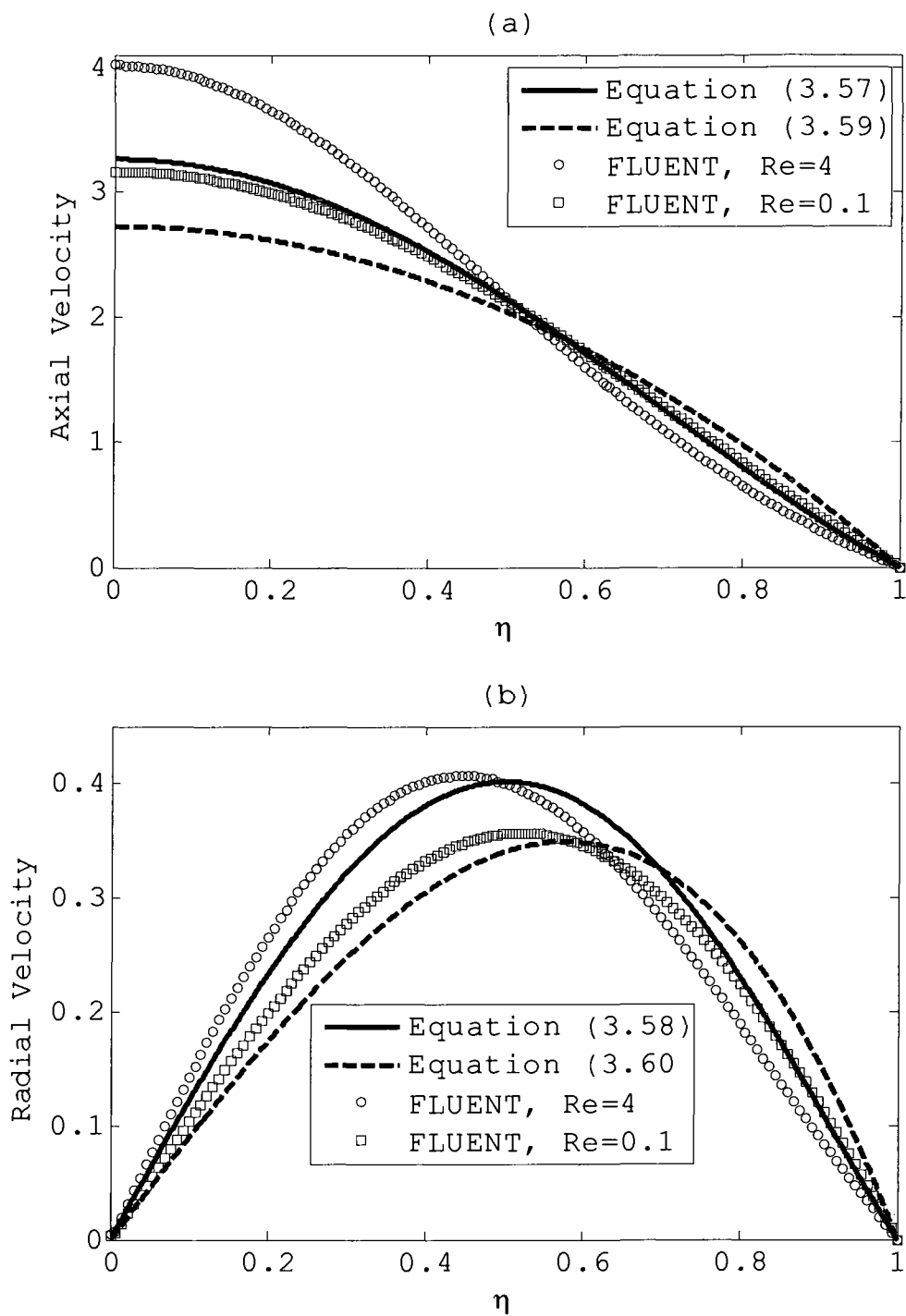


Figure 3.5 Velocity distribution in the cross section plane at  $z=L/8$  of a sinusoidal tube.

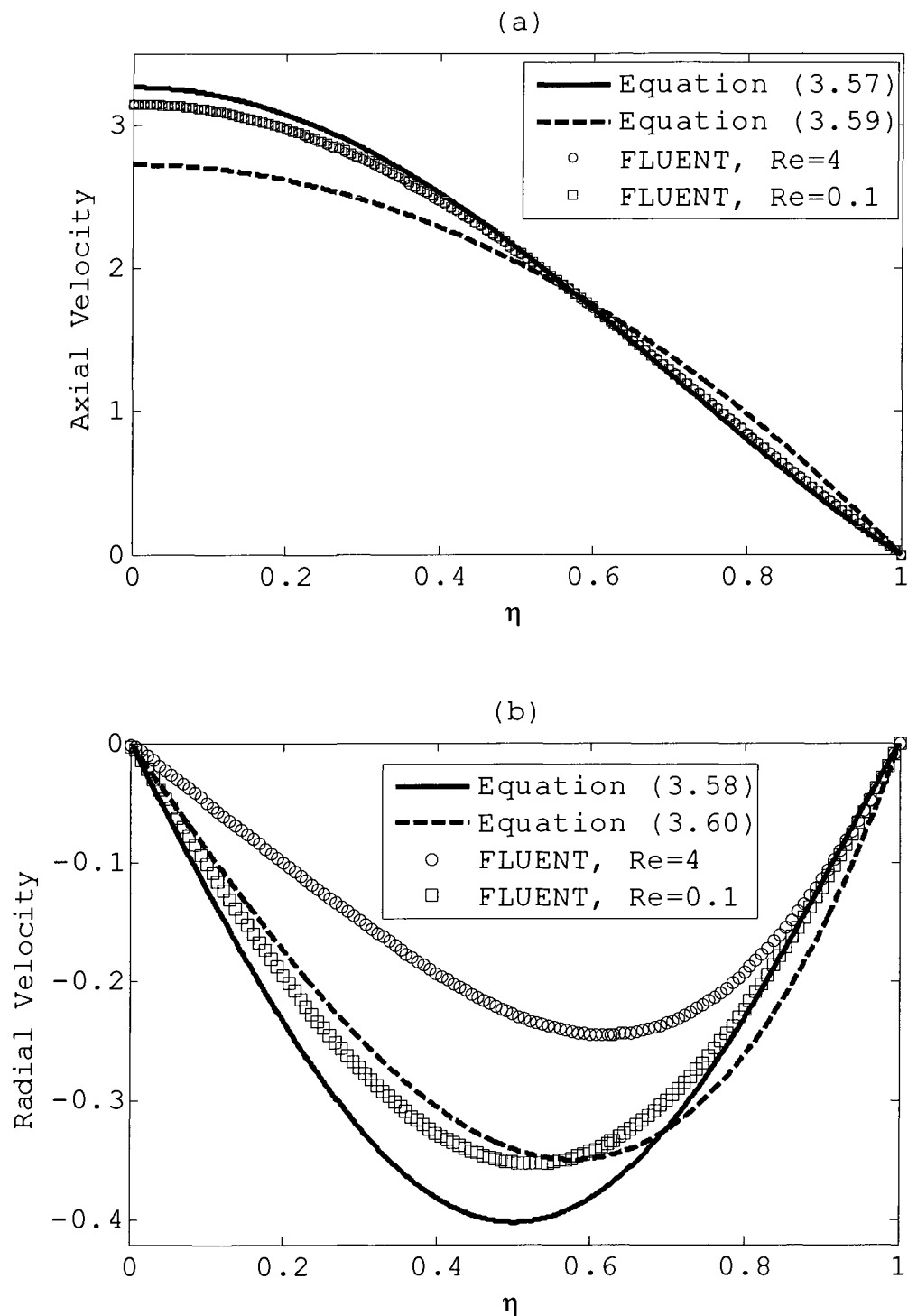


Figure 3.6 Velocity distribution in the cross section plane at  $z=3L/8$  of a sinusoidal tube.

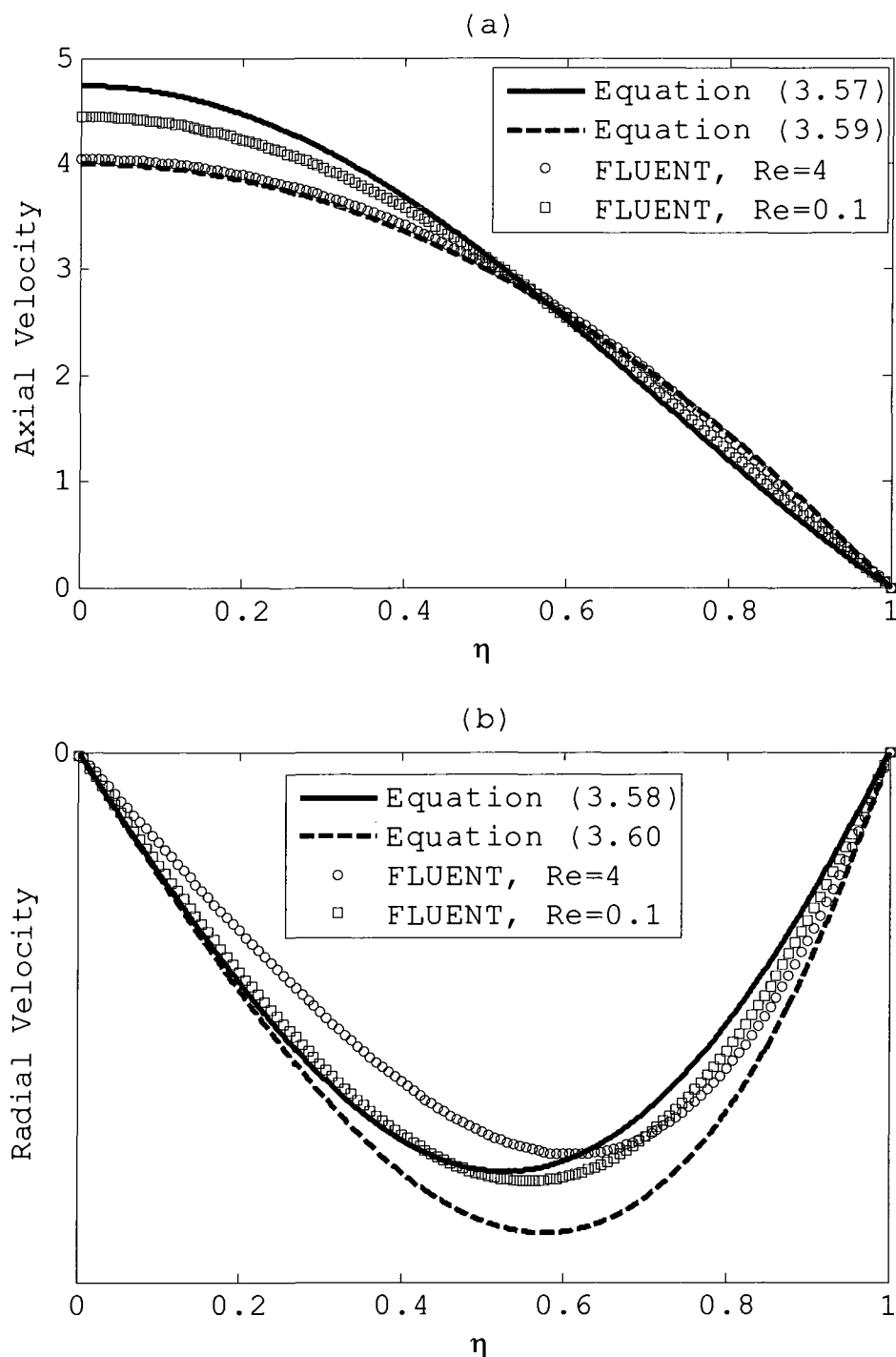


Figure 3.7 Velocity distribution in the cross section plane at  $z=4L/8$  of a sinusoidal tube.

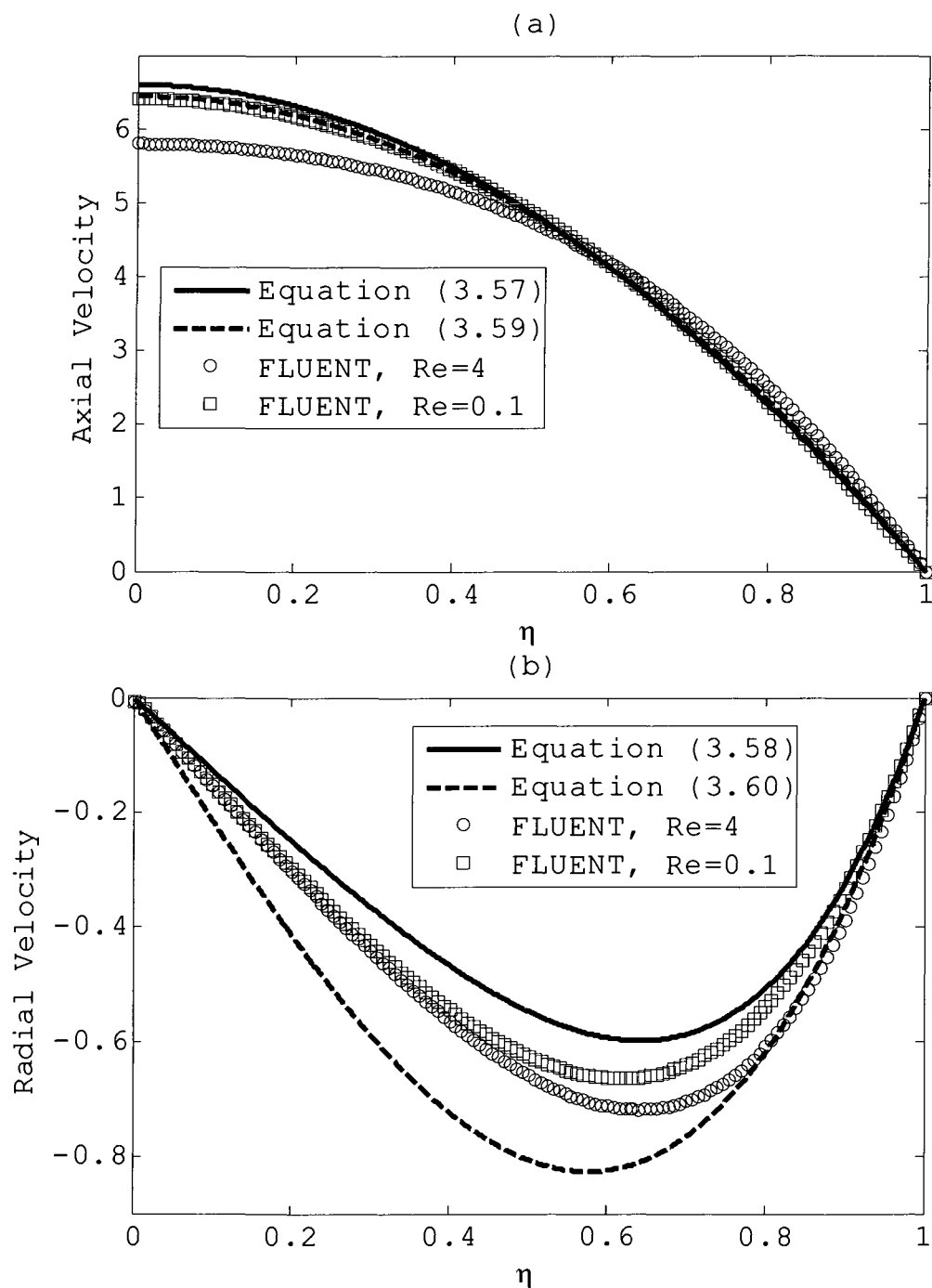


Figure 3.8 Velocity distribution in the cross section plane at  $z=5L/8$  of a sinusoidal tube.

According to Equations (3.2) and (3.3) and neglecting the time-dependent terms, the dimensionless pressure gradient in radial and axial directions can be expressed as:

$$\frac{\partial \tilde{p}}{\partial \tilde{r}} = \left[ \frac{1}{\tilde{r}} \frac{\partial}{\partial \tilde{r}} \left( \tilde{r} \frac{\partial \tilde{v}_r}{\partial \tilde{r}} \right) + \frac{\partial^2 \tilde{v}_r}{\partial \tilde{z}^2} - \frac{\tilde{v}_r}{\tilde{r}^2} \right] - \text{Re} \left( \tilde{v}_r \frac{\partial \tilde{v}_r}{\partial \tilde{r}} + \tilde{v}_z \frac{\partial \tilde{v}_r}{\partial \tilde{z}} \right) \quad (3.61)$$

$$\frac{\partial \tilde{p}}{\partial \tilde{z}} = \left[ \frac{1}{\tilde{r}} \frac{\partial}{\partial \tilde{r}} \left( \tilde{r} \frac{\partial \tilde{v}_z}{\partial \tilde{r}} \right) + \frac{\partial^2 \tilde{v}_z}{\partial \tilde{z}^2} \right] - \text{Re} \left( \tilde{v}_r \frac{\partial \tilde{v}_z}{\partial \tilde{r}} + \tilde{v}_z \frac{\partial \tilde{v}_z}{\partial \tilde{z}} \right) \quad (3.62)$$

Substituting the obtained expressions of the velocity components into Equations (3.57) and (3.58) and neglecting the  $\varepsilon^4$  and higher order terms give:

$$\frac{\partial \tilde{p}}{\partial \tilde{r}} = -\eta \left[ \begin{aligned} & 32 \frac{d\tilde{R}(\tilde{z})}{d\tilde{z}} \frac{1}{\tilde{R}(\tilde{z})^4} + 4 \frac{d^3\tilde{R}(\tilde{z})}{d\tilde{z}^3} \frac{1}{\tilde{R}(\tilde{z})^2} \left( \frac{1}{3} - \eta^2 \right) \\ & + 20 \frac{d^2\tilde{R}(\tilde{z})}{d\tilde{z}^2} \frac{d\tilde{R}(\tilde{z})}{d\tilde{z}} \frac{1}{\tilde{R}(\tilde{z})^3} \left( -\frac{5}{3} + 3\eta^2 \right) \\ & + 8 \left( \frac{d\tilde{R}(\tilde{z})}{d\tilde{z}} \right)^3 \frac{1}{\tilde{R}(\tilde{z})^4} \left( \frac{22}{3} - 15\eta^2 \right) \\ & + 8 \text{Re} \frac{d^2\tilde{R}(\tilde{z})}{d\tilde{z}^2} \frac{1}{\tilde{R}(\tilde{z})^4} (1 - 4\eta^2 + 2\eta^4) \\ & + 32 \text{Re} \left( \frac{d\tilde{R}(\tilde{z})}{d\tilde{z}} \right)^2 \frac{1}{\tilde{R}(\tilde{z})^5} (-1 + 2\eta^2 - \eta^4) \end{aligned} \right] \quad (3.63)$$

$$\frac{\partial \bar{p}}{\partial \tilde{z}} = \left[ \begin{aligned} & -16 \frac{1}{\tilde{R}(\tilde{z})^4} + \frac{d^2 \tilde{R}(\tilde{z})}{d\tilde{z}^2} \frac{1}{\tilde{R}(\tilde{z})^3} \left( \frac{8}{3} - 16\eta^2 \right) \\ & + \left( \frac{d\tilde{R}(\tilde{z})}{d\tilde{z}} \right)^2 \frac{1}{\tilde{R}(\tilde{z})^4} \left( -\frac{88}{3} + 80\eta^2 \right) \\ & + \operatorname{Re} \frac{d\tilde{R}(\tilde{z})}{d\tilde{z}} \frac{1}{\tilde{R}(\tilde{z})^5} (32 - 64\eta^2 + 32\eta^4) \\ & + \operatorname{Re} \frac{d^3 \tilde{R}(\tilde{z})}{d\tilde{z}^3} \frac{1}{\tilde{R}(\tilde{z})^3} \left( -\frac{16}{3} \eta^6 + \frac{20}{3} \eta^4 - \frac{32}{3} \eta^2 + \frac{8}{3} \right) \\ & + \operatorname{Re} \frac{d^2 \tilde{R}(\tilde{z})}{d\tilde{z}^2} \frac{d\tilde{R}(\tilde{z})}{d\tilde{z}} \frac{1}{\tilde{R}(\tilde{z})^4} \left( 80\eta^6 - \frac{584}{3} \eta^4 + \frac{648}{3} \eta^2 - \frac{104}{3} \right) \\ & + \operatorname{Re} \left( \frac{d\tilde{R}(\tilde{z})}{d\tilde{z}} \right)^3 \frac{1}{\tilde{R}(\tilde{z})^5} \left( -160\eta^6 + \frac{560}{3} \eta^4 - \frac{800}{3} \eta^2 + \frac{160}{3} \right) \end{aligned} \right] \quad (3.64)$$

Equation (3.63) shows that the geometry variation of the tube produces radial pressure gradient to cause the radial flow. For practical application, the axial pressure gradient averaging in the cross section is important. It can be written as:

$$\frac{\partial \bar{p}}{\partial \tilde{z}} = 2 \int_0^1 \eta \frac{\partial \bar{p}}{\partial \tilde{z}} d\eta \quad (3.65)$$

$$= \left[ \begin{aligned} & -16 \frac{1}{\tilde{R}(\tilde{z})^4} - \frac{16}{3} \frac{d^2 \tilde{R}(\tilde{z})}{d\tilde{z}^2} \frac{1}{\tilde{R}(\tilde{z})^3} + \frac{32}{3} \left( \frac{d\tilde{R}(\tilde{z})}{d\tilde{z}} \right)^2 \frac{1}{\tilde{R}(\tilde{z})^4} \\ & + \frac{32}{3} \operatorname{Re} \frac{d\tilde{R}(\tilde{z})}{d\tilde{z}} \frac{1}{\tilde{R}(\tilde{z})^5} - \frac{16}{9} \operatorname{Re} \frac{d^3 \tilde{R}(\tilde{z})}{d\tilde{z}^3} \frac{1}{\tilde{R}(\tilde{z})^3} \\ & + \frac{8}{3} \operatorname{Re} \frac{d^2 \tilde{R}(\tilde{z})}{d\tilde{z}^2} \frac{d\tilde{R}(\tilde{z})}{d\tilde{z}} \frac{1}{\tilde{R}(\tilde{z})^4} - \frac{520}{9} \operatorname{Re} \left( \frac{d\tilde{R}(\tilde{z})}{d\tilde{z}} \right)^3 \frac{1}{\tilde{R}(\tilde{z})^5} \end{aligned} \right]$$

Excluding the terms of Reynolds number, Equation (3.65) reduces to:

$$\frac{\overline{\partial \tilde{p}}}{\partial \tilde{z}} = -16 \frac{1}{\tilde{R}(\tilde{z})^4} - \frac{16}{3} \frac{d^2 \tilde{R}(\tilde{z})}{d\tilde{z}^2} \frac{1}{\tilde{R}(\tilde{z})^3} + \frac{32}{3} \left( \frac{d\tilde{R}(\tilde{z})}{d\tilde{z}} \right)^2 \frac{1}{\tilde{R}(\tilde{z})^4} \quad (3.66)$$

The pressure drop from  $z=z_1$  to  $z_2$  is:

$$\begin{aligned} \overline{\Delta \tilde{p}} = & -16 \int_{\tilde{z}_1}^{\tilde{z}_2} \frac{1}{\tilde{R}(\tilde{z})^4} d\tilde{z} - \frac{16}{3} \int_{\tilde{z}_1}^{\tilde{z}_2} \frac{d^2 \tilde{R}(\tilde{z})}{d\tilde{z}^2} \frac{1}{\tilde{R}(\tilde{z})^3} d\tilde{z} \\ & + \frac{32}{3} \int_{\tilde{z}_1}^{\tilde{z}_2} \left( \frac{d\tilde{R}(\tilde{z})}{d\tilde{z}} \right)^2 \frac{1}{\tilde{R}(\tilde{z})^4} d\tilde{z} \end{aligned} \quad (3.67)$$

Compared to the integral form of Hagen-Poiseuille equation which is used in the derivation of the capillary model in Chapter 2 and other nonuniform capillary model [Sharma and Ross 1991; Staples and Shaffer 2002; Young 2004; Patro et al. 2007; Patro and Jayaram 2008]:

$$\Delta \tilde{p} = -16 \int_{\tilde{z}_1}^{\tilde{z}_2} \frac{1}{\tilde{R}(\tilde{z})^4} d\tilde{z} \quad (3.68)$$

Equation (3.67) include two more terms related to the geometry variations. Figure 3.9 shows that the comparison of the analytical results of Equations (3.67) and (3.69) the numerical results obtained from FLUENT. In Figure 3.9, the abscissa represents the location in axial direction of the sinusoidal tube, while the ordinate denotes the dimensionless pressure drop refer to the location at  $x=-L/2$ . Figure 3.9 indicates that there is an improvement of the asymptotic solution beyond the classic Hagen-Poiseuille solution for the prediction of the

pressure gradient distribution in tubes of varying radius.

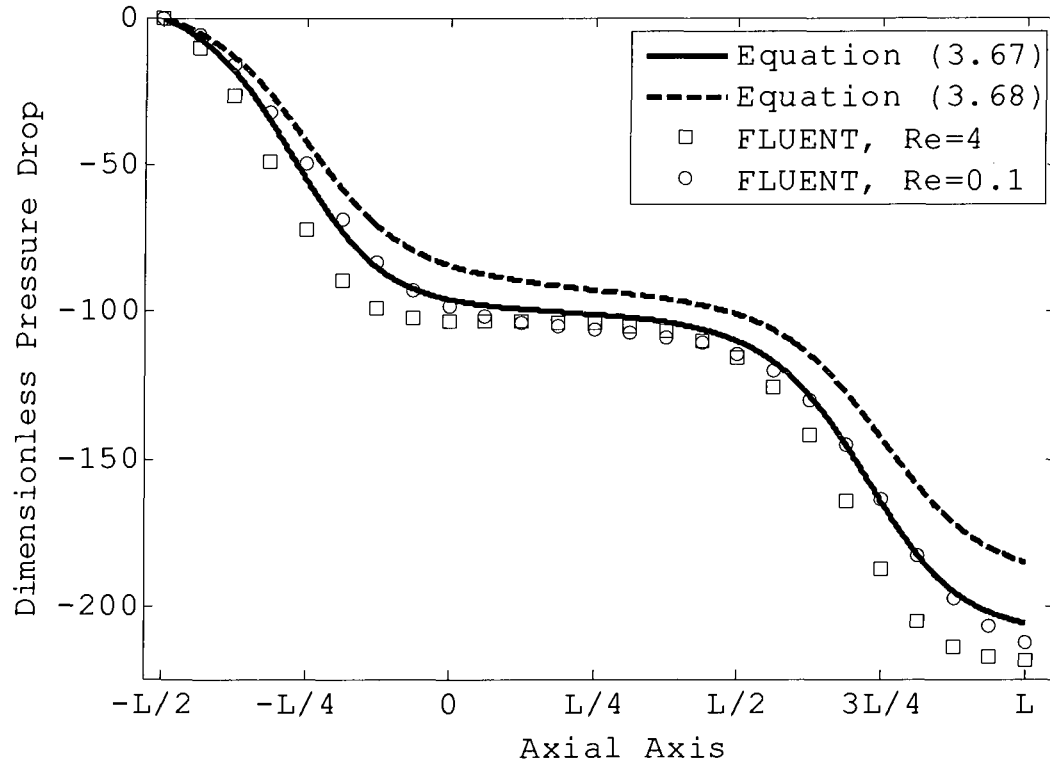


Figure 3.9 Pressure drop in axial direction of a sinusoidal tube.

### 3.2 New Derivation of Governing Equation of Capillary Flow

In this section, the governing equation of capillary flow in tubes of varying radius is derived based on the velocity distribution obtained in the previous section. The derivation is started from the integral form of the momentum equation in the axial direction:

$$\begin{aligned}
& \frac{d}{dt} \iiint v_z dV + \iiint v_r \frac{\partial v_z}{\partial r} dV + \iiint v_z \frac{\partial v_z}{\partial z} dV \\
& = - \iiint \frac{1}{\rho} \frac{\partial p}{\partial z} dV + \iiint \frac{\mu}{\rho} \left[ \frac{1}{r} \frac{\partial}{\partial r} \left( r \frac{\partial v_z}{\partial r} \right) + \frac{\partial^2 v_z}{\partial z^2} \right] dV
\end{aligned} \tag{3.69}$$

For the capillary rise problem, the average velocity of the capillary interface can be approximated by the time derivative of the rising height, i.e.  $\frac{dh}{dt}$ . Hence the

characteristic stream function  $\psi_c$  can be defined as:

$$\psi_c = \frac{1}{2} \frac{dh}{dt} R(h)^2 \tag{3.70}$$

and the dimensional velocity components, according to Equations (3.57) and (3.58), can be expressed as:

$$v_z = \frac{dh}{dt} \left\{ \begin{aligned} & \frac{2R(h)^2}{R^2(z)} (1 - \eta^2) \\ & + \frac{1}{6} \left[ 5 \frac{R(h)^2}{R^2(z)} \left( \frac{d\tilde{R}(\tilde{z})}{d\tilde{z}} \right)^2 - \frac{R(h)^2}{R(z)} \frac{d^2 R(z)}{dz^2} \right] (3\eta^4 - 4\eta^2 + 1) \end{aligned} \right\} \tag{3.71}$$

$$v_r = \frac{dh}{dt} \left\{ \begin{aligned} & \frac{2R(h)^2}{R^2(z)} \frac{dR(z)}{dz} (\eta - \eta^3) \\ & + \frac{5}{3} \frac{R(h)^2}{R^2(z)} \left( \frac{dR(z)}{dz} \right)^3 (3\eta^5 - 4\eta^3 + \eta) \\ & - \frac{1}{6} \frac{R(h)^2}{R(z)} \frac{dR(z)}{dz} \frac{d^2 R(z)}{dz^2} (15\eta^5 - 26\eta^3 + 11\eta) \\ & + \frac{1}{6} R(h)^2 \frac{d^3 R(z)}{dz^3} (\eta^5 - 2\eta^3 + \eta) \end{aligned} \right\} \tag{3.72}$$

Using the expression in Equation (3.65), the volume integration in the first term of Equation (3.69) can be calculated as:

$$\iiint v_z dV = \pi h R(h)^2 \frac{dh}{dt} \quad (3.73)$$

After decomposing the volume integration of other terms into cross section area integration and integration in the axial direction, Equation (3.69) can be written in the form:

$$\begin{aligned} & \int_0^h \frac{1}{h} \frac{d}{dt} \left( \pi h R(h)^2 \frac{dh}{dt} \right) dz + \int_0^h \iint v_r \frac{\partial v_z}{\partial r} dAdz \\ & + \int_0^h \iint v_z \frac{\partial v_z}{\partial z} dAdz \\ & = - \int_0^h \iint \frac{1}{\rho} \frac{\partial p}{\partial z} dAdz + \int_0^h \iint \frac{\mu}{\rho} \left[ \frac{1}{r} \frac{\partial}{\partial r} \left( r \frac{\partial v_z}{\partial r} \right) + \frac{\partial^2 v_z}{\partial z^2} \right] dAdz \end{aligned} \quad (3.74)$$

Since Equation (3.68) satisfies any positive  $h$ , it leads to:

$$\begin{aligned} & \frac{\rho}{h} \frac{d}{dt} \left( \pi h R(h)^2 \frac{dh}{dt} \right) + \rho \iint v_r \frac{\partial v_z}{\partial r} dA + \rho \iint v_z \frac{\partial v_z}{\partial z} dA \\ & = - \iint \frac{\partial p}{\partial z} dA + \iint \mu \left[ \frac{1}{r} \frac{\partial}{\partial r} \left( r \frac{\partial v_z}{\partial r} \right) + \frac{\partial^2 v_z}{\partial z^2} \right] dA \end{aligned} \quad (3.75)$$

which describes the momentum balance in the cross-sectional area integral form. We do an average operation on each term of Equation (3.69),

$$\begin{aligned}
& \frac{1}{\pi R(z)^2} \frac{\rho}{h} \frac{d}{dt} \left( \pi h R(h)^2 \frac{dh}{dt} \right) + \frac{1}{\pi R(z)^2} \rho \iint v_r \frac{\partial v_z}{\partial r} dA \\
& + \frac{1}{\pi R(z)^2} \rho \iint v_z \frac{\partial v_z}{\partial z} dA \\
& = - \frac{1}{\pi R(z)^2} \iint \frac{\partial p}{\partial z} dA + \frac{1}{\pi R(z)^2} \iint \mu \left[ \frac{1}{r} \frac{\partial}{\partial r} \left( r \frac{\partial v_z}{\partial r} \right) + \frac{\partial^2 v_z}{\partial z^2} \right] dA
\end{aligned} \tag{3.76}$$

Integrating each term in the axial direction from 0 to  $h$ , we derive:

$$\begin{aligned}
& \int_0^h \frac{1}{R(z)^2} \frac{\rho}{h} \frac{d}{dt} \left( h R(h)^2 \frac{dh}{dt} \right) dz \\
& + \int_0^h \frac{1}{\pi R(z)^2} \rho \iint \left( v_r \frac{\partial v_z}{\partial r} + v_z \frac{\partial v_z}{\partial z} \right) dA dz = - \int_0^h \frac{1}{\pi R(z)^2} \iint \frac{\partial p}{\partial z} dA dz \\
& + \int_0^h \frac{1}{\pi R(z)^2} \iint \mu \left[ \frac{1}{r} \frac{\partial}{\partial r} \left( r \frac{\partial v_z}{\partial r} \right) + \frac{\partial^2 v_z}{\partial z^2} \right] dA dz
\end{aligned} \tag{3.77}$$

Physically, the first term of the right hand side of the above equation is the integration of the average pressure gradient from the tube inlet to the capillary interface. It represents the average pressure drop from the inlet ( $z=0$ ) to the meniscus ( $z=h$ ) and consists of the combination of the capillary pressure, gravitational hydrostatic pressure, the pressure loss of the entry flow at the inlet and the excess pressure drop of the developing flow in the entrance region of the tube. Following the similar analysis of capillary flow in uniform tubes [Sparrow et al. 1964; Levine et al. 1976; Stange et al. 2003], it can be formulated as:

$$\begin{aligned}
-\int_0^h \frac{1}{\pi R(z)^2} \iint \frac{\partial p}{\partial z} dA dz &= \frac{2\gamma \cos \theta}{R(h)} - \rho g h - 2\mu \frac{R^2(h)}{R^3(0)} \frac{dh}{dt} \\
-\frac{73}{60} \rho \frac{1}{R(0)} \left[ R^2(h) \frac{d^2 h}{dt^2} + 2R(h) \frac{dR(h)}{dh} \left( \frac{dh}{dt} \right)^2 \right] &- K_s \rho \frac{R^2(h)}{R^2(0)} \left( \frac{dh}{dt} \right)^2
\end{aligned} \tag{3.78}$$

In the above expression,  $\theta$  is the apparent contact angle that will be discussed later.  $K_s$  is related to the excess pressure drop due to the velocity profile development within the entrance region of the tube and can be related to  $h$  as:

$$K_s(h) = \frac{1}{6} + \sum_{i=1}^{\infty} \frac{4}{\alpha_i^2} \left[ \exp\left(-\frac{4\alpha_i^2 \text{Re}_h}{\text{Re}_d^2}\right) - 3 \right] \cdot \exp\left(-\frac{4\alpha_i^2 \text{Re}_h}{\text{Re}_d^2}\right) \tag{3.79}$$

where,

$$\text{Re}_h = \frac{\rho}{\mu} h \frac{dh}{dt}, \quad \text{Re}_d = 2 \frac{\rho}{\mu} \frac{R^2(h)}{R(0)} \frac{dh}{dt} \tag{3.80}$$

and the first 25 values of  $\alpha_i$  for circular tubes are computed by Sparrow et al. (1964) as given in Table 3.1. For the laminar flow, the length scale of the entrance region  $L_e$  reads  $L_e / d \approx 0.06 \text{Re}_d$ . Equation (3.79) yields  $K_s = 1 / 6$  for  $h > L_e$ .

The second integration of Equation (3.77) is from the convection terms of Navier-Stokes equation. To reduce its nonlinearity, the simple parabolic velocity

distribution expressed in Equation (3.59) and (3.60) is used to calculate the convection terms as:

$$\int_0^h \frac{1}{\pi R^2(z)} \iint_A \rho \left( v_r \frac{\partial v_z}{\partial r} + v_z \frac{\partial v_z}{\partial z} \right) dA dz \quad (3.81)$$

$$= -\frac{8}{3} \rho R^4(h) \left( \frac{dh}{dt} \right)^2 \int_0^h \frac{dR(z)}{dz} \frac{1}{R^5(z)} dz$$

Table 3.1 Values of  $\alpha_i$  for circular tubes [after Sparrow et al. 1964].

$i$	$\alpha_i$	$i$	$\alpha_i$	$i$	$\alpha_i$
1	5.13562	10	33.7165	19	62.0162
2	8.41724	11	36.8629	20	65.1593
3	11.6198	12	40.0085	21	68.3022
4	14.7960	13	43.1535	22	71.4450
5	17.9598	14	46.2980	23	74.5877
6	21.1170	15	49.4422	24	77.7303
7	24.2701	16	52.5860	25	80.8728
8	27.4206	17	55.7296		
9	30.5692	18	58.8730		

Substituting the expressions of velocity components into the other terms of Equation (3.77), the final form of the governing equation can be written as:

$$\begin{aligned}
& \rho \left[ c_0 + \frac{73}{60} \frac{1}{R(0)} \right] R^2(h) \frac{d^2 h}{dt^2} \\
& + \rho \left[ c_0 \frac{R^2(h)}{h} + 2 \left( c_0 + \frac{73}{60} \frac{1}{R(0)} \right) R(h) \frac{dR(h)}{dh} \right] \left( \frac{dh}{dt} \right)^2 \\
& \left[ + K_s \frac{R^2(h)}{R^2(0)} - \frac{8}{3} \varpi c_3 R^4(h) \right] \\
& = \frac{2\gamma \cos \theta_d}{R(h)} - \rho g h - 8\mu \left( c_1 + c_2 - \frac{1}{3} c_4 + \frac{1}{4R^3(0)} \right) R^2(h) \frac{dh}{dt}
\end{aligned} \tag{3.82}$$

where  $c_0$ ,  $c_1$ ,  $c_2$ ,  $c_3$  and  $c_4$  are geometrical parameters

defined as:

$$c_0 = \int_0^h \frac{1}{R^2(z)} dz \tag{3.83}$$

$$c_1 = \int_0^h \frac{1}{R^4(z)} dz \tag{3.84}$$

$$c_2 = \int_0^h \frac{1}{R^4(z)} \left( \frac{dR(z)}{dz} \right)^2 dz \tag{3.85}$$

$$c_3 = \int_0^h \frac{1}{R^5(z)} \frac{dR(z)}{dz} dz \tag{3.86}$$

$$c_4 = \int_0^h \frac{1}{R^4(z)} \left[ \begin{aligned} & 5 \left( \frac{dR(z)}{dz} \right)^4 - R(z) \left( \frac{dR(z)}{dz} \right)^2 \frac{d^2 R(z)}{dz^2} \\ & - R(z) \frac{d^2 R(z)}{dz^2} + 5 \left( \frac{dR(z)}{dz} \right)^2 \end{aligned} \right] dz \tag{3.87}$$

In Equation (3.82), a relaxation parameter  $\varpi$  is

introduced as:

$$\varpi = \begin{cases} 0, & \frac{d^2R}{dh^2} < 0; \\ 1, & \frac{d^2R}{dh^2} > 0; \end{cases} \quad (3.88)$$

which is schematically shown in Figure 3.10. It is proposed to improve the stability of the model by ignoring the convection effect when the capillary interface, with a slow speed, passes the region of concave varying wall. Whereas, the convection effect is taken into account when the capillary interface, with a fast speed, passes the region of convex varying wall.

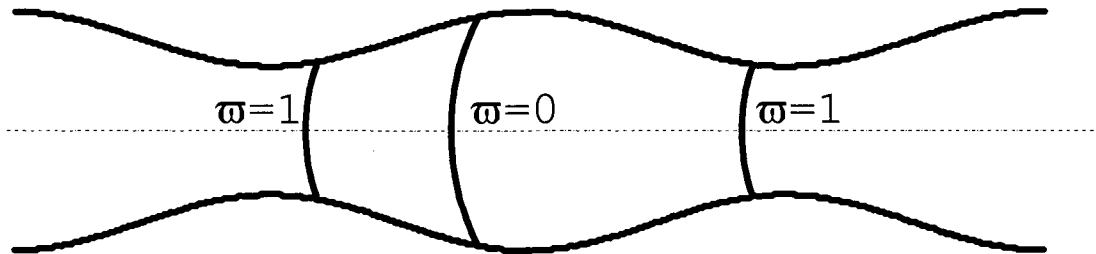


Figure 3.10 Convection parameter in a sinusoidal tube.

### 3.3 Dynamic Contact Angle Model of Capillary Flow in Nonuniform Tubes

The dynamic contact angle  $\theta_d$  is an important parameter of the dynamic wetting process. As summarized in Chapter 1, the dynamic variation of the contact angle of a moving contact line may depend on contact line

velocity, surface tension, viscosity and other possible contact surface properties.

Based on the hydrodynamics theory, the existing models of the dynamic contact angle can be written in a general form as:

$$\theta_d^3 = \theta_m^3 + 9Ca \cdot \left[ \ln \left( \frac{L_H}{L_s} \right) - C_v \right] \quad (3.89)$$

where  $L_H$  is the characteristic length of the flow. The slip length  $L_s$  and the numerical constant  $C_v$  are empirically determined by experiments.  $\theta_m$  is a constant contact angle on microscopic scale and is suggested by Cox (1986) to be the static contact angle  $\theta_s$ .

Alternatively, Zhou and Sheng (1990) and Stokes et al. (1990) reported that  $\theta_m$  is also dependent on the contact line velocity because of an additional frictional force and can be approximated by:

$$\cos \theta_m = \cos \theta_s - B \cdot Ca^n, 0 < n < 0.5 \quad (3.90)$$

where the numerical constant  $B$  is related to the surface tension, liquid density, viscosity and solid surface properties.

Nevertheless, a simpler expression of the velocity-dependent dynamic contact angle based on the Classic Molecular-kinetic theory is obtained as [Blake 2006]:

$$\cos \theta_d = \cos \theta_m - \frac{\zeta}{\gamma} \frac{dh}{dt} \quad (3.91)$$

where  $\zeta$  is the coefficient of wetting-line friction and physically defined in Equation (1.31). Practically,  $\zeta$  can be determined by experiments, and  $\theta_m$  is also suggested to be the value of static contact angle  $\theta_s$  by current researchers.

The author would like to point out that both the hydrodynamic and molecular kinetic models of dynamic contact angle are originated from the experimental studies of the dynamic wetting of a liquid drop on a solid surface. They describe the dynamic variation process of the contact angle from an initial angle to the sole equilibrium angle  $\theta_m$  when the capillary interface velocity reduces to zero. However,  $\theta_m$  may be velocity-dependent as indicated in Equation (3.90). It may also be time-dependent for some special cases such as capillary rise in tubes.

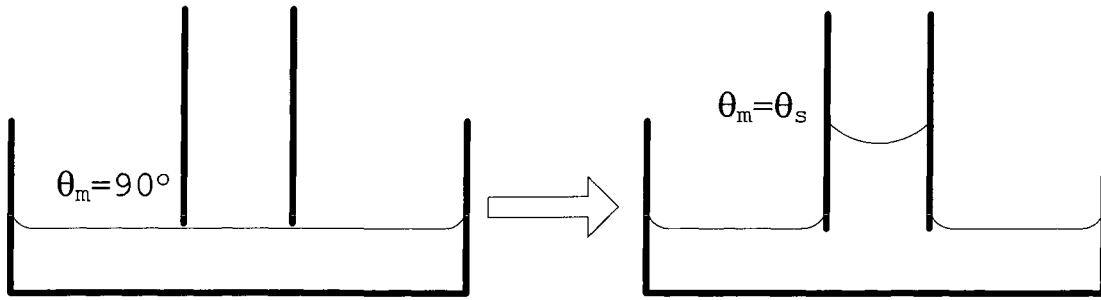


Figure 3.11 Transition of  $\theta_m$  in capillary rise problems.

In the capillary rise experiment as shown in Figure 3.11, the dimension of the outer liquid surface of the sink is much bigger than that of the capillary tube. Therefore, the initial contact angle  $\theta_0$  is in an equilibrium state and equal to  $90^\circ$  with respect to the vertical capillary tube before the tip of the solid tube contacts the liquid. Consequently,  $\theta_m$  is  $\theta_0$  at  $t=0$  when the liquid surface is brought in contact with the tube. As time progressing, there will be a stage transition of  $\theta_m$  from  $\theta_0$  to  $\theta_s$ . The time-dependent transition process can be described by an empirical relation based on a series of experiments:

$$\theta_m = \frac{\theta_0 + \theta_s}{2} + \left( \frac{\theta_0 - \theta_s}{2} \right) \cdot \frac{A_d \cdot e^{-B_d \cdot M_p(t-t_c)} - e^{M_p(t-t_c)}}{e^{-M_p(t-t_c)} + e^{M_p(t-t_c)}} \quad (3.92)$$

where,  $A_d$ ,  $B_d$ ,  $t_c$  and  $M_p$  are parameters to be determined experimentally and may relate to the practical setting

such as the depth of the tube dipped in the liquid. Compared to the existing models of dynamic contact angle, which are only applicable to the vicinity of the equilibrium state, the applicable scope of the present model has been extended to the initial stage. The combined dynamic contact angle model, Equation (3.92), and the nonuniform capillary model, Equation (3.82) is firstly validated by examining the reported experiments [Hamraoui et al. 2000; Stange et al. 2003] of capillary rise in uniform tubes in Section 2.4. The author also carried out a series of capillary rise experiments of nonuniform tubes as described, and reasonable agreements of theoretical and experimental data are presented in Section 3.5.

### **3.4 Validation of Capillary Flow in Circular Cylindrical Tubes**

The first validation is to compare theoretical results of the dynamic capillary rise in circular cylindrical tubes with Hamraoui et al. (2000)'s experiment results under gravity and Stange et al. (2003)'s results without gravity. The fluid properties of the liquids that they used are shown in Table 3.2.

Table 3.2 Fluid properties.

Liquid	$\rho$ (kg/m <sup>3</sup> )	$\mu$ (mPa.s)	$\gamma$ (mN.m <sup>-1</sup> )
Water <sup>a</sup>	998.2	1	72
Ethanol <sup>a</sup>	798.7	1.17	22
Water-Ethanol <sup>a</sup>	984.4	1	50.37
SF 0.65 <sup>b</sup>	761	0.5	15.6
SF 1.00 <sup>b</sup>	818	0.818	16.9
FC-77 <sup>b</sup>	1777	1.422	14.7

<sup>a</sup> from [Hamraoui et al. 2000];

<sup>b</sup> from [Stange et al. 2003].

For a circular cylindrical capillary of constant radius  $R_0$ , the governing equation (3.82) with the dynamic contact angle described in Equations (3.91) and (3.92) can be reduced to:

$$\rho \left( h + \frac{73}{60} R_0 \right) \frac{d^2 h}{dt^2} + \rho (1 + K_s) \left( \frac{dh}{dt} \right)^2 + 8\mu \left( \frac{h}{R_0^2} + \frac{1}{4R_0} \right) \frac{dh}{dt} \quad (3.93)$$

$$+ \rho g h = \frac{2\gamma}{R_0} \left\{ \cos \left[ \left( \frac{\pi}{4} + \frac{\theta_s}{2} \right) - \left( \frac{\pi}{4} - \frac{\theta_s}{2} \right) \tanh (M_p (t - t_c)) \right] \right. \\ \left. - \frac{\zeta}{\gamma} \frac{dh}{dt} \right\}$$

with  $A_d = 1$  and  $B_d = 1$ . For comparison, Hamraoui's model equation [Hamraoui et al. 2000; Hamraoui and Nylander 2002] is rewritten as follows:

$$\rho h \frac{d^2 h}{dt^2} + \rho \left( \frac{dh}{dt} \right)^2 + 8\mu \frac{h}{R_0^2} \frac{dh}{dt} + \rho g h = \frac{2\gamma}{R_0} \left( \cos \theta_s - \frac{\zeta}{\gamma} \frac{dh}{dt} \right) \quad (3.94)$$

and the traditional Lucas-Washburn equation with the constant static contact angle is [Brittin 1945]:

$$\rho h \frac{d^2h}{dt^2} + \frac{5}{4} \rho \left( \frac{dh}{dt} \right)^2 = \frac{2\gamma \cos \theta_s}{R_0} - \rho gh - 8\mu \frac{h}{R_0^2} \frac{dh}{dt} \quad (3.95)$$

The experimental data for capillary rise of water, ethanol and water-ethanol mixtures as a function of time, reported by Hamraoui et al. (2000), are shown in Figures 3.12-3.14, respectively, together with the theoretical results of Equation (3.93) proposed in this chapter, Equation (3.94) that is introduced in [Hamraoui and Nylander 2002], and the traditional Lucas-Washburn Equation (3.95) with static contact angle, where the radius  $R_0 = 0.295\text{mm}$ , the static contact angle  $\theta_s = 0$  and the gravitational acceleration  $g = 9.81\text{ms}^{-2}$ . In Figures 3.12-3.14, the time reference point where  $t = 0$  is set to be the moment when the meniscus reaches the height of the first experimentally measured point which can be denoted by  $h_0$ . For the three experiments of water, ethanol and water-ethanol mixture,  $h_0 = 2.20, 5.32, 1.56\text{mm}$ , respectively. All the calculations start from  $h=0\text{mm}$ , but the computed curves shift as a whole according to first experiment datum point.

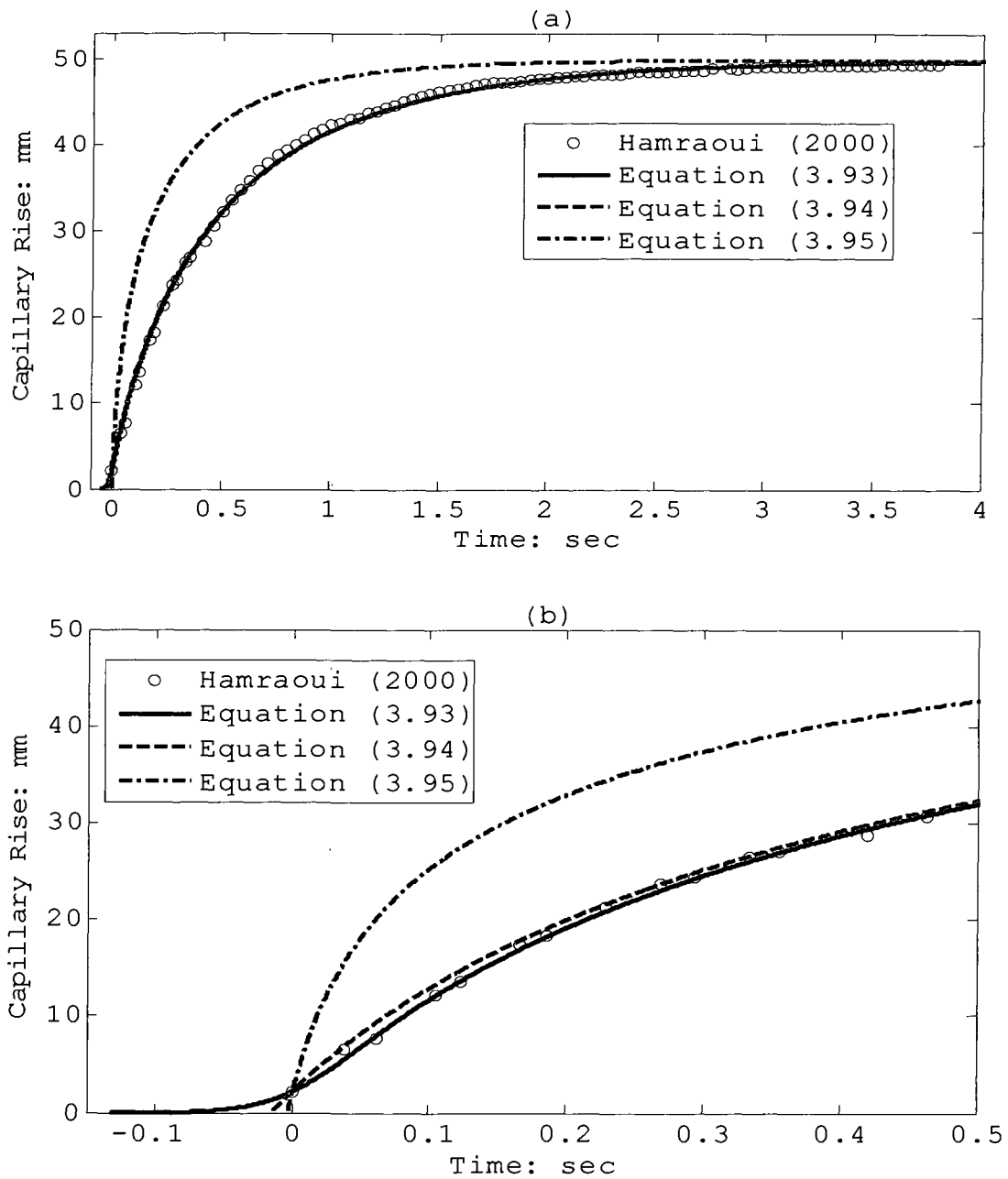


Figure 3.12 The capillary rise of water in a circular cylindrical tube with  $\zeta = 0.45$ ,  $t_c = 0.15$ ,  $M_p = 20$ .  
 (a),  $t = -0.15 - 4$  s; (b),  $t = -0.15 - 0.5$  s.

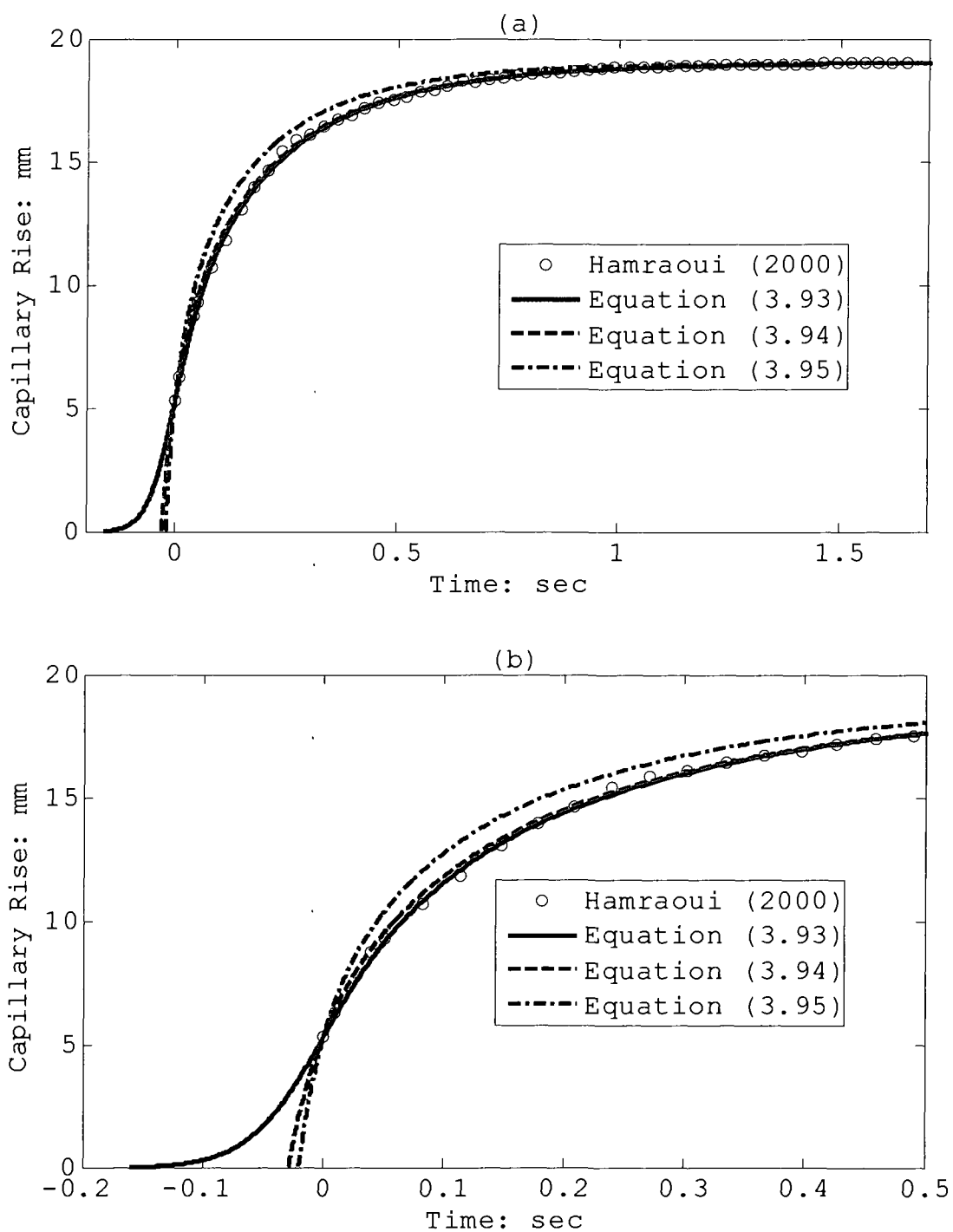


Figure 3.13 The capillary rise of ethanol in a circular cylindrical tube with  $\zeta = 0.04$ ,  $t_c = 0.15$ ,  $M_p = 20$ .  
 (a),  $t = -0.2 \sim 1.7$  sec; (b),  $t = -0.2 \sim 0.5$  sec.

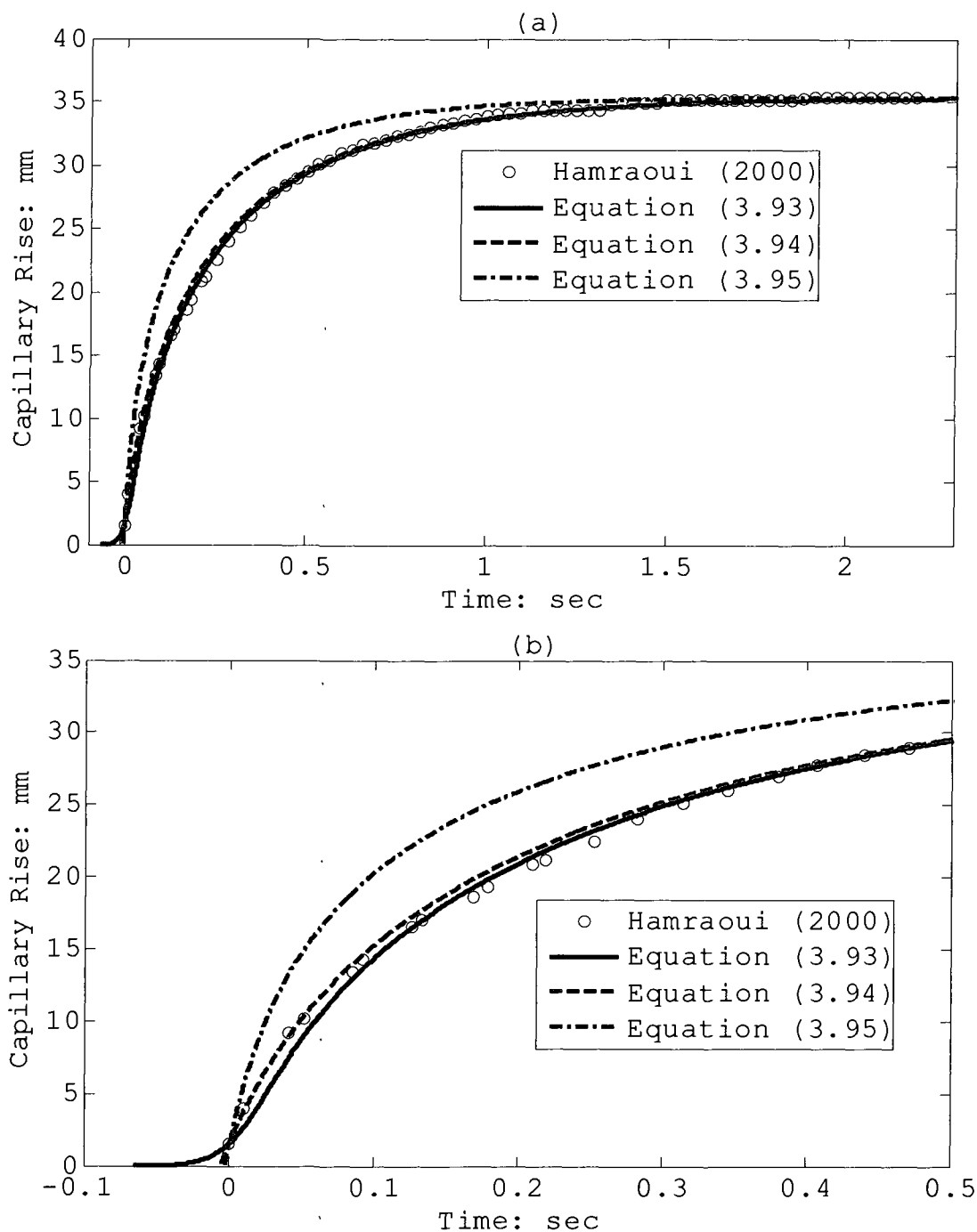


Figure 3.14 The capillary rise of water-ethanol mixture in a circular cylindrical tube with  $\zeta = 0.14$ ,  $t_c = 0.08$ ,  $M_p = 40$ . (a),  $t = -0.1 \sim 2.3$  s; (b),  $t = -0.1 \sim 0.5$  s.

It can be found in Figures 3.12a-3.14a that the equilibrium height of the three experiments can be well predicted by all the three equations. However, the experimental points during the stage when the rate of the capillary rise is not zero cannot be adequately described by the traditional Lucas-Washburn Equation (3.95) where the contact angle is assumed to be constant. When the dynamic contact angle effect is considered, good agreement between the experimental data and theoretical predictions of Equations (3.93) and (3.94) can be achieved, where the two equations take the same value of  $\zeta$  and  $\zeta = 0.45, 0.04, 0.14$  for the three liquids as suggested by Hamraoui et al. (2000). Nevertheless, their descriptions of the dynamic capillary rise before the the meniscus reaches the height of  $h_0$  are quite different as clearly shown in Figures 3.12b-3.14b. After correcting  $\theta_m$  by Equation (3.92) in the dynamic contact angle model, Equation (3.93) predicts much lower capillary rise rates than the previous model in the initial stage from  $h=0$  to  $h_0$  where the experimental observation are absent. After the meniscus passes  $h_0$ , Figures 3.12b-3.14b also present a

mild improvement of the prediction of Equation (3.93) over Equation (3.94) compared to the experiment data.

Stange et al. (2003) reported a series of experiments of the capillary-driven flow of three perfectly wetting liquids into circular cylindrical tubes in the microgravity environment, which is used as the second validation case of the proposed model in this chapter. For the capillary flow without gravity in a circular cylindrical capillary of constant radius  $R_0$ , the governing equation (3.82) can be reduced to:

$$\begin{aligned} & \rho \left( h + \frac{73}{60} R_0 \right) \frac{d^2 h}{dt^2} + \rho (1 + K_s) \left( \frac{dh}{dt} \right)^2 + 8\mu \left( \frac{h}{R_0^2} + \frac{1}{4R_0} \right) \frac{dh}{dt} \quad (3.96) \\ & = \frac{2\gamma}{R_0} \left\{ \cos \left[ \left( \frac{\pi}{4} + \frac{\theta_s}{2} \right) - \left( \frac{\pi}{4} - \frac{\theta_s}{2} \right) \tanh (M_p (t - t_c)) \right] - \frac{\zeta}{\gamma} \frac{dh}{dt} \right\} \end{aligned}$$

Similar to the above analysis, we rewrite the theoretical model equation introduced in [Stange et al. 2003] as follows for comparison:

$$\frac{d^2 h}{dt^2} = \frac{1}{h + \frac{73}{60} R_0} \left\{ \frac{\gamma}{\rho} \left[ \frac{2s (1 - 2 \tanh (4.96 \text{Ca}^{0.702}))}{R_0} - \frac{1}{R_c} \right] - \frac{\mu}{\rho} \left( \frac{8h}{R_0^2} + \frac{2}{R_0} \right) \frac{dh}{dt} - (1 + K_s) \left( \frac{dh}{dt} \right)^2 \right\} \quad (3.97)$$

In the above Stange's model, an empirical dynamic contact angle correlation that is proposed by Jiang et al. (1979)

based on Hoffman's (1976) experiment data is used, and the parameter  $s$  is introduced to describe the surface reorientation process after a step reduction in gravity:

$$s(t) = 1 - \exp \left( -11.14 \frac{t}{\sqrt{\frac{\rho R_0^3}{\gamma}}} \right) \quad (3.98)$$

Stange et al. (2003) performed the experiments in a drop tower, which has a free fall height of 110m with a microgravity time of 4.7s. The microgravity condition provides the convenience to use the wider diameter tubes from 4mm to 70mm for the observations. Only the data of 4mm-diameter tube are selected for the validation in this section. Three liquids were used: two Dow Corning 200 Silicone Fluids that are labeled by their kinematic viscosities (SF 0.65 and SF 1.00) and 3M Fluorinert Dielektrika FC-77. The fluid properties are shown in Table 3.2 (page:150). Figures 3.15-3.17 present the experimental observations of the dynamic progression of the meniscus height with time for three different liquids. Each figure gives two series of data with two different values of the depth of the tube in the liquid ( $h_1=10$  and 50mm). The meniscus height is referred to the

water surface. The comparisons in Figures 3.15-3.17 present a good agreement between the numerical solutions of Equations (3.96) and (3.97) and the experimental data.

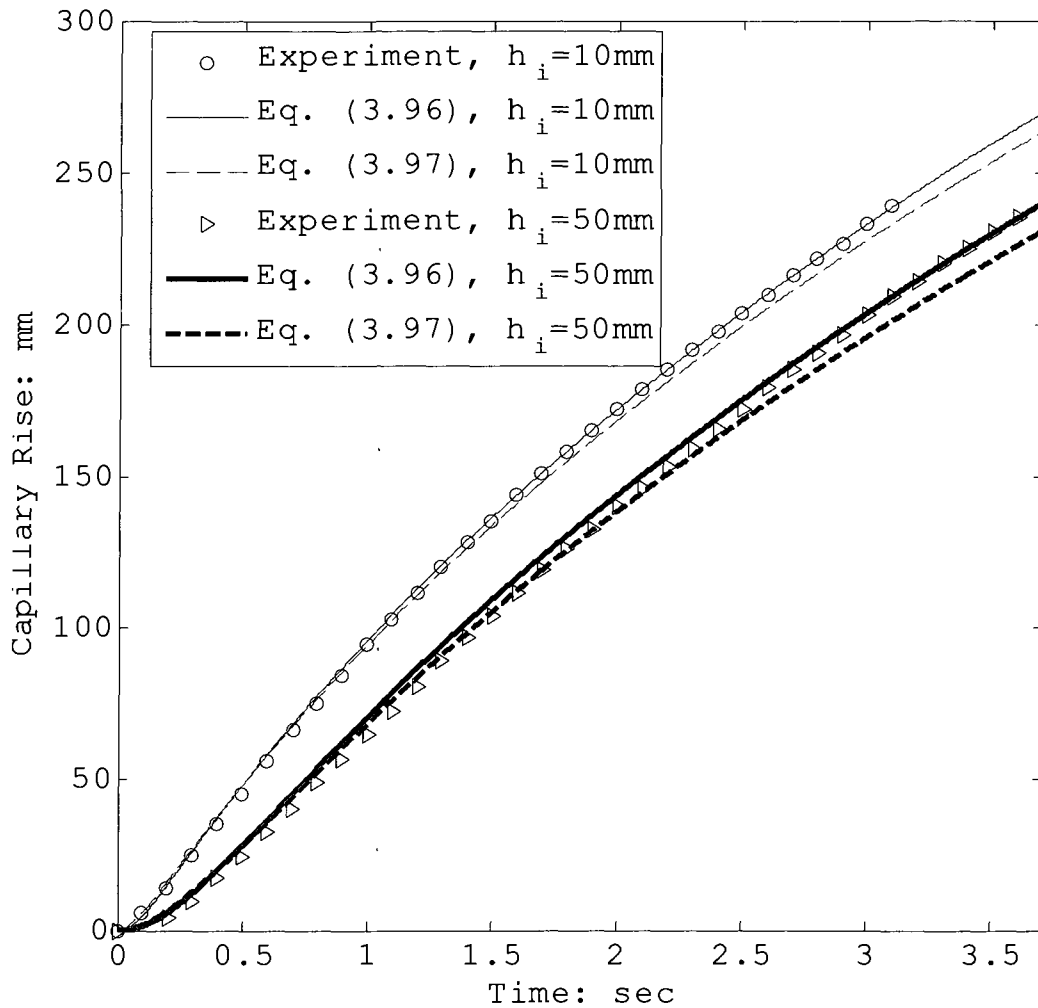


Figure 3.15 The capillary rise of SF 0.65 in a circular cylindrical tube with  $t_c = 0.08$ ,  $M_p = 40$ , and  $\zeta = 0.02$  for  $h_i = 10$ mm,  $\zeta = 0.015$  for  $h_i = 50$ mm.

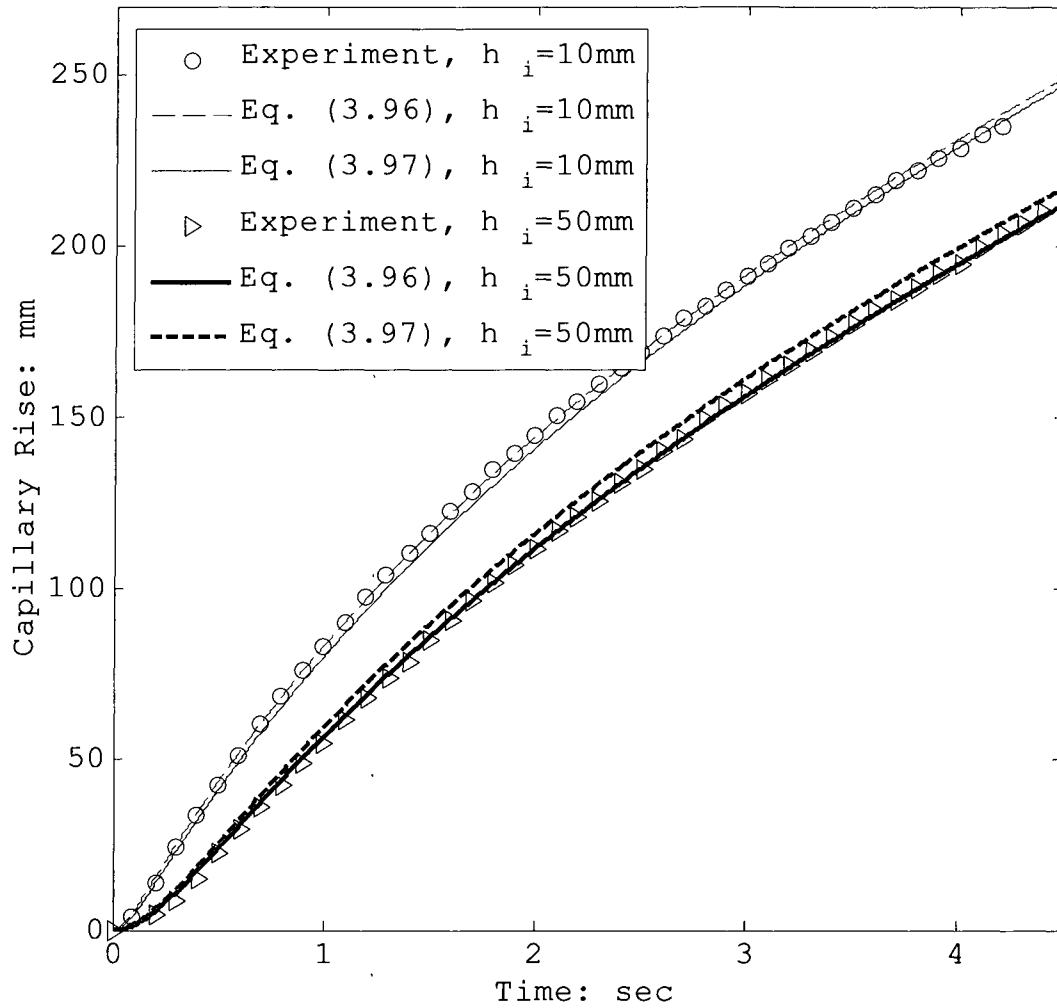


Figure 3.16 The capillary rise of SF 1.00 in a circular cylindrical tube with  $t_c = 0.02$ ,  $M_p = 80$ , and  $\zeta = 0.05$  for  $h_i = 10\text{mm}$ ,  $\zeta = 0.06$  for  $h_i = 50\text{mm}$ .

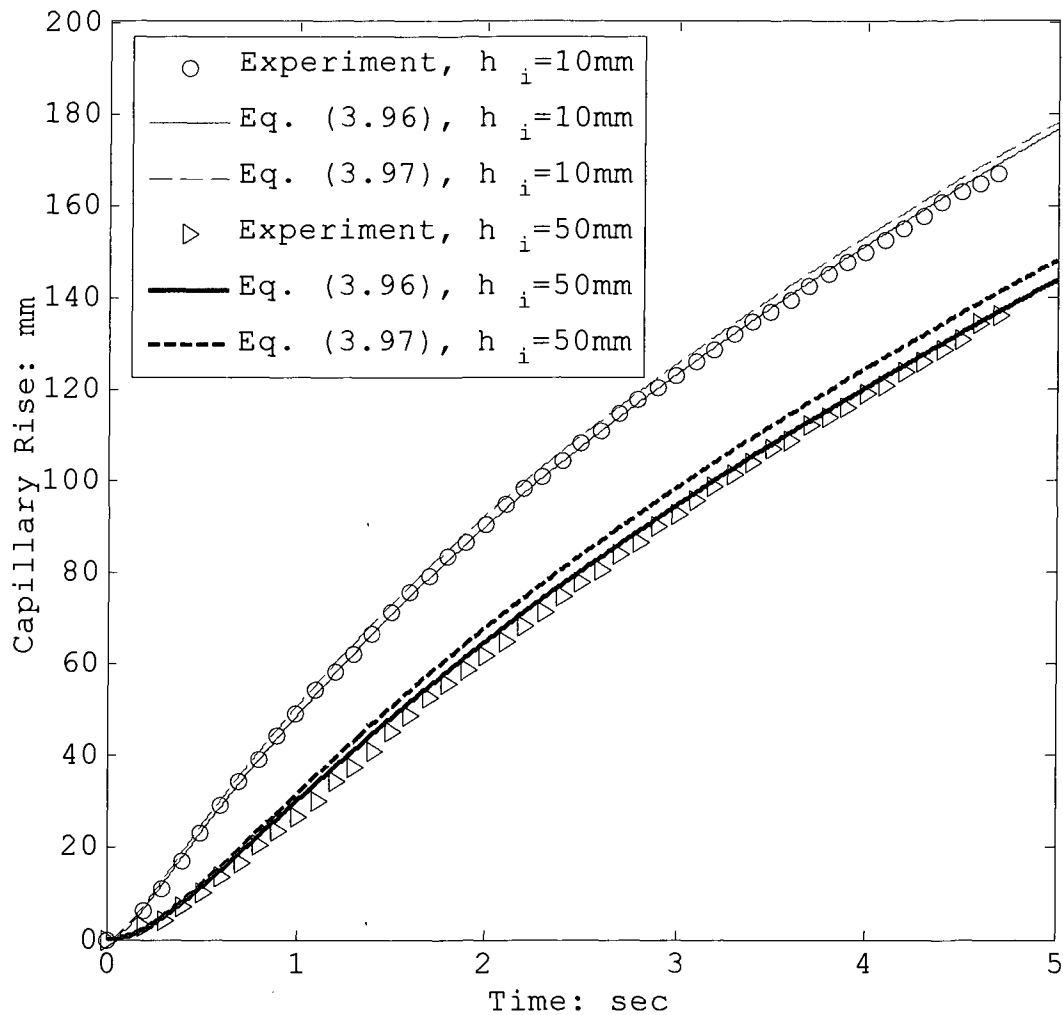


Figure 3.17 The capillary rise of FC-77 in a circular cylindrical tube with  $t_c = 0.02$ ,  $M_p = 80$  and  $\zeta = 0.08$  for  $h_i = 10\text{mm}$ ,  $\zeta = 0.1$  for  $h_i = 50\text{mm}$ .

### 3.5 Validation of Capillary Flow in Nonuniform Tubes

To further validate the proposed theoretical capillary model, a series of experiments on the surface tension-driven flow in vertical nonuniform tubes is

carried out. Three experimental cases of one uniform tube and two nonuniform tubes are reported in this section.

### Experimental Details

Figure 3.18 shows a schematic drawing of the experimental set-up. The capillary tube is fixed above a 30mm-diameter tank which is prefilled with distilled water up to about 98% full. The tip of the tube is located at the 2% void region. The remaining 2% space is filled by a medical I.V. set with a controlled slow flow rate of 1000ml/h through a small diameter tube on the side of the tank. The tube is connected with the tank at the bottom. When the I.V. set is switched on, the water surface rises up with a stable interface toward the tip of the capillary tube with a negligible speed of about 4  $\mu\text{m/s}$ .

This specific setting, distinct with the traditional experimental set-up where the tip of the capillary tube is brought in contact the liquid surface by moving the tube, allows us to eliminate the possible influence of the uncertain mechanical vibration of the tube and improve the repeatability of the experiment. The dynamic capillary rising process is observed and recorded by the

high speed video camera, Redlake HD-2000, with the frame rate of 125 f/s and the total record time of 16s. The monitor is useful to adjust the diffuser to obtain high quality images and position the tube at the same location for each case. The monitor also helps the observer decide when to start the recording right before the water surface contacts the tube tip. The recorded images marked with frame numbers in the camera were downloaded to the computer through the Ethernet and analyzed by Redlake MotionXtra software.

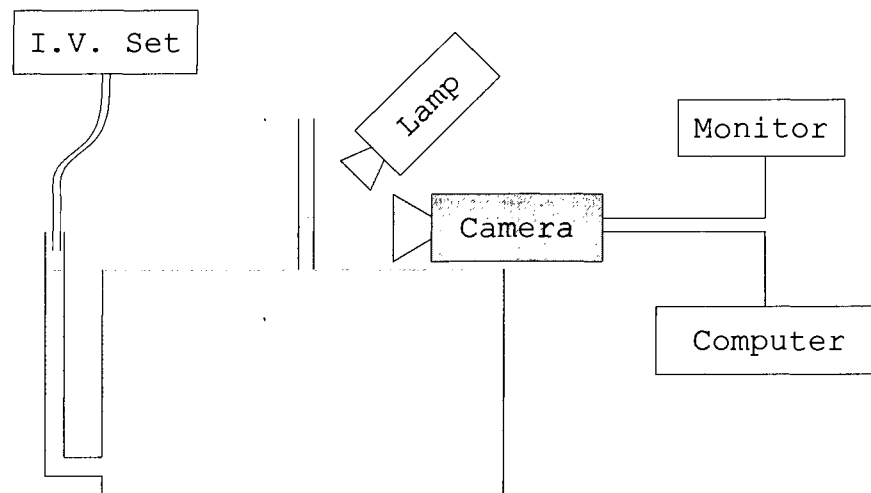


Figure 3.18 The experimental set-up.

The test liquid is 100% distilled water, and the material properties are:  $\rho = 998.2 \text{ kg/m}^3$ ,  $\mu = 0.001 \text{ Pa}\cdot\text{s}$ ,  $\gamma = 0.072 \text{ N/m}$  and  $\theta_s = 0$ . The customized glass capillary

tubes with curve walls are provided by Meints Glassblowing LLC and are washed with the distilled water before each trial. High-purity Acetone may be used to accelerate the drying process after experiments.

### Theoretical Governing Equation

The proposed governing fluid equation for the capillary flow in general irregular geometries is expressed by Equation (3.82) in which the actual contact angle  $\theta$ , with respect to the straight axis of the tube, is the summation of dynamic contact angle  $\theta_d$  referred to the tangential vector of the solid surface and the local geometrical slope angle  $\theta_g$ , i.e.

$$\theta = \theta_d + \theta_g \quad (3.99)$$

where,

$$\theta_g = \tan^{-1} [dR(h) / dh] \quad (3.100)$$

For different treatments of the dynamic contact angle,  $\theta_d$  can be expressed by various velocity-dependent relations. The four dynamic contact angle models discussed in this chapter can be outlined as:

1, Constant contact angle model

The dynamic contact angle is assumed to be constant and always equal to the static contact angle  $\theta_s$ , i.e.

$$\theta_d = \theta_s \quad (3.101)$$

## 2, Empirical Model

This empirical correlation was first introduced by Jiang et al. (1979) based on Hoffman's (1975) experimental data. The correlation is recently modified by Stange et al. (2003) who considered the surface tension reorientation process at the initial stage and successfully explained their experiments of capillary rise in a circular uniform tube under microgravity as mentioned in section 3.3. For the capillary flow, this correlation is written as:

$$\theta_d = \cos^{-1} \left\{ \left( 1 - e^{-11.14 \sqrt{\frac{\gamma}{\rho R_0^3}} t} \right) \left[ 1 - 2 \tanh(4.96 \text{Ca}^{0.702}) \right] \right\} \quad (3.102)$$

where  $\text{Ca} = \frac{\mu}{\gamma} \frac{dh}{dt}$  and  $R_0$  is the tube radius at the inlet.

## 3, Molecular-Kinetic model

Based on the Molecular-Kinetic theory, the velocity-dependent relation of the dynamic contact angle is:

$$\theta_d = \cos^{-1} \left( \cos \theta_s - \frac{\zeta}{\gamma} \frac{dh}{dt} \right) \quad (3.103)$$

The derivation of the above expression is provided in Chapter 1. Hamraoui's group [Hamraoui et al. 2000; 2002] studied this dynamic contact angle model through a series of experiments of capillary rise in circular uniform tubes under gravity as mentioned in the previous section and explained the molecular-kinetic parameter  $\zeta$  in terms of a friction coefficient.

#### 4, Modified Molecular-Kinetic Model

A new dynamic contact angle model is proposed in this chapter with a modification of the microscopic contact angle  $\theta_m$  in the Molecular-Kinetic model, where  $\theta_m$  is treated as a constant angle and is equal to the static contact angle  $\theta_s$ . Similar to the idea of the initial surface tension reorientation process at the initial capillary rise state, the transition of  $\theta_m$  from the initial contact angle to the static contact angle at equilibrium state is considered in the present model as described in Equation (3.93). Finally, the dynamic contact angle is expressed in the form of:

$$\theta_d = \cos^{-1} \left\{ \cos \left[ \frac{\theta_0 + \theta_s}{2} + \left( \frac{\theta_0 - \theta_s}{2} \right) \frac{A_d e^{-E_d M_p (t-t_c)} - e^{M_p (t-t_c)}}{e^{-M_p (t-t_c)} + e^{M_p (t-t_c)}} \right] - \frac{\zeta}{\gamma} \frac{dh}{dt} \right\} \quad (3.104)$$

Combined Equation (3.2) with the four dynamic contact angle model, four different governing equations are derived as follows respectively:

1, with constant contact angle model:

$$\begin{aligned}
 & \rho \left[ c_0 + \frac{73}{60} \frac{1}{R(0)} \right] R^2(h) \frac{d^2 h}{dt^2} \\
 & + \rho \left[ c_0 \frac{R^2(h)}{h} + 2 \left( c_0 + \frac{73}{60} \frac{1}{R(0)} \right) R(h) \frac{dR(h)}{dh} \right. \\
 & \left. + K_s \frac{R^2(h)}{R^2(0)} - \frac{8}{3} \varpi c_3 R^4(h) \right] \left( \frac{dh}{dt} \right)^2 \\
 & = \frac{2\gamma \cos \left[ \theta_s + \tan^{-1} \left( \frac{dR(h)}{dh} \right) \right]}{R(h)} - \rho g h \\
 & - 8\mu \left( c_1 + c_2 - \frac{1}{3} c_4 + \frac{1}{4R^3(0)} \right) R^2(h) \frac{dh}{dt}
 \end{aligned} \tag{3.105}$$

2, with empirical contact angle model:

$$\begin{aligned}
 & \rho \left[ c_0 + \frac{73}{60} \frac{1}{R(0)} \right] R^2(h) \frac{d^2 h}{dt^2} \\
 & + \rho \left[ c_0 \frac{R^2(h)}{h} + K_s \frac{R^2(h)}{R^2(0)} - \frac{8}{3} \varpi c_3 R^4(h) \right. \\
 & \left. + 2 \left( c_0 + \frac{73}{60} \frac{1}{R(0)} \right) R(h) \frac{dR(h)}{dh} \right] \left( \frac{dh}{dt} \right)^2 = \\
 & \frac{2\gamma}{R(h)} \cos \left\{ \tan^{-1} \left[ \frac{dR(h)}{dh} \right] + \cos^{-1} \left[ \begin{aligned} & \left( 1 - e^{-11.14 \sqrt{\frac{\gamma}{\rho R_0^3}} t} \right) \\ & \cdot \left[ 1 - 2 \tanh \left( 4.96 \text{Ca}^{0.702} \right) \right] \end{aligned} \right] \right\} \\
 & - \rho g h - 8\mu \left( c_1 + c_2 - \frac{1}{3} c_4 + \frac{1}{4R^3(0)} \right) R^2(h) \frac{dh}{dt}
 \end{aligned} \tag{3.106}$$

3, with Molecular-Kinetic contact angle model:

$$\begin{aligned}
 & \rho \left[ c_0 + \frac{73}{60} \frac{1}{R(0)} \right] R^2(h) \frac{d^2 h}{dt^2} & (3.107) \\
 & + \rho \left[ c_0 \frac{R^2(h)}{h} + 2 \left( c_0 + \frac{73}{60} \frac{1}{R(0)} \right) R(h) \frac{dR(h)}{dh} \right] \left( \frac{dh}{dt} \right)^2 \\
 & \quad + K_s \frac{R^2(h)}{R^2(0)} - \frac{8}{3} \varpi c_3 R^4(h) \\
 & = \frac{2\gamma}{R(h)} \cos \left\{ \tan^{-1} \left[ \frac{dR(h)}{dh} \right] + \cos^{-1} \left( \cos \theta_s - \frac{\zeta}{\gamma} \frac{dh}{dt} \right) \right\} \\
 & - \rho g h - 8\mu \left( c_1 + c_2 - \frac{1}{3} c_4 + \frac{1}{4R^3(0)} \right) R^2(h) \frac{dh}{dt}
 \end{aligned}$$

4, with modified Molecular-Kinetic contact angle model:

$$\begin{aligned}
 & \rho \left[ c_0 + \frac{73}{60} \frac{1}{R(0)} \right] R^2(h) \frac{d^2 h}{dt^2} & (3.108) \\
 & + \rho \left[ c_0 \frac{R^2(h)}{h} + K_s \frac{R^2(h)}{R^2(0)} - \frac{8}{3} \varpi c_3 R^4(h) \right] \left( \frac{dh}{dt} \right)^2 = \\
 & \quad + 2 \left( c_0 + \frac{73}{60} \frac{1}{R(0)} \right) R(h) \frac{dR(h)}{dh} \\
 & \frac{2\gamma}{R(h)} \cos \left\{ \tan^{-1} \left[ \frac{dR(h)}{dh} \right] + \cos^{-1} \left\{ \cos \left[ \frac{\theta_0 + \theta_s}{2} + \left( \frac{\theta_0 - \theta_s}{2} \right) \frac{A_d e^{-B_d M_p(t-t_c)} - e^{M_p(t-t_c)}}{e^{-M_p(t-t_c)} + e^{M_p(t-t_c)}} \right] - \frac{\zeta}{\gamma} \frac{dh}{dt} \right\} \right\} \\
 & - \rho g h - 8\mu \left( c_1 + c_2 - \frac{1}{3} c_4 + \frac{1}{4R^3(0)} \right) R^2(h) \frac{dh}{dt}
 \end{aligned}$$

where the parameters  $K_s$ ,  $c_0$ ,  $c_1$ ,  $c_2$ ,  $c_3$ ,  $c_4$  and  $\varpi$  are expressed in Equations (3.79), (3.83)-(3.88).

Results and Discussion

Three cases of one uniform tube and two nonuniform tubes are reported in this section. Figures 3.19-3.21 show three sequences of still frames taken from the three experimental videos, respectively. The first picture shows the fluid configuration before the tube tip contacts the water surface, and the second one is a sample frame selected from the capillary rising time.

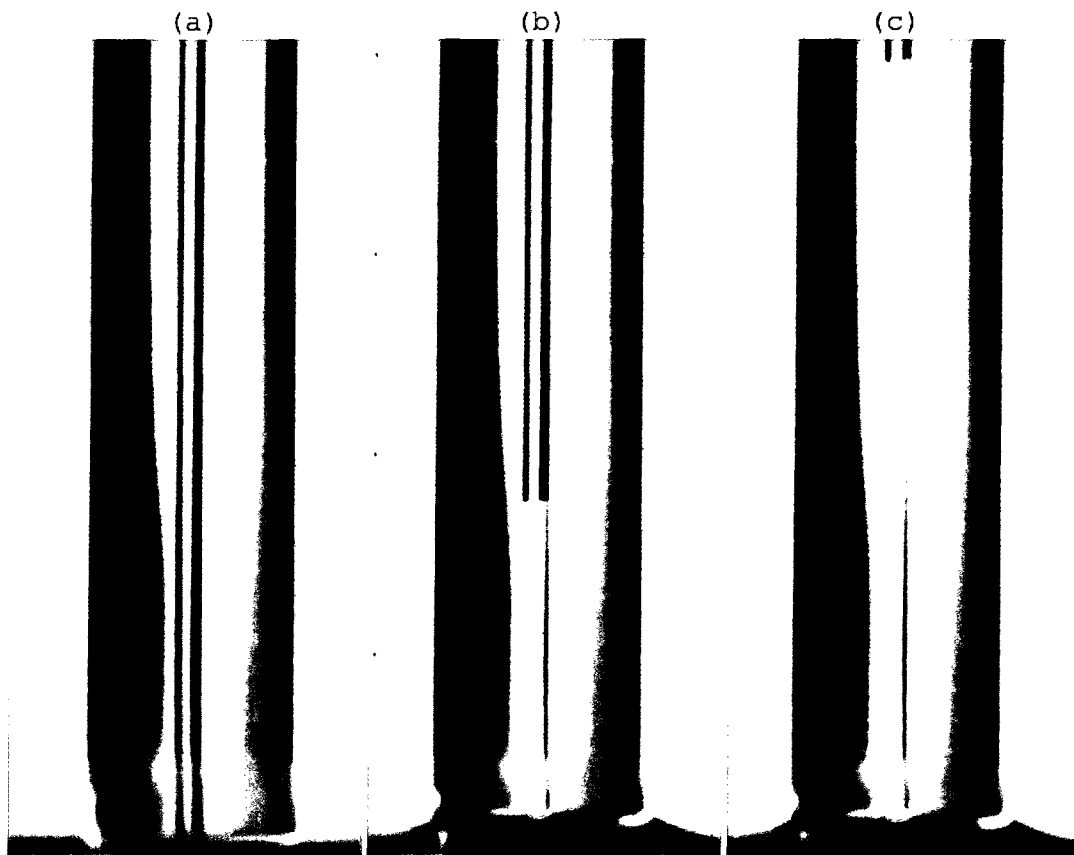


Figure 3.19 Surface tension-driven flow into a circular cylindrical tube. (a) the initial frame before contact; (b) the intermediate frame; (c) the final frame.

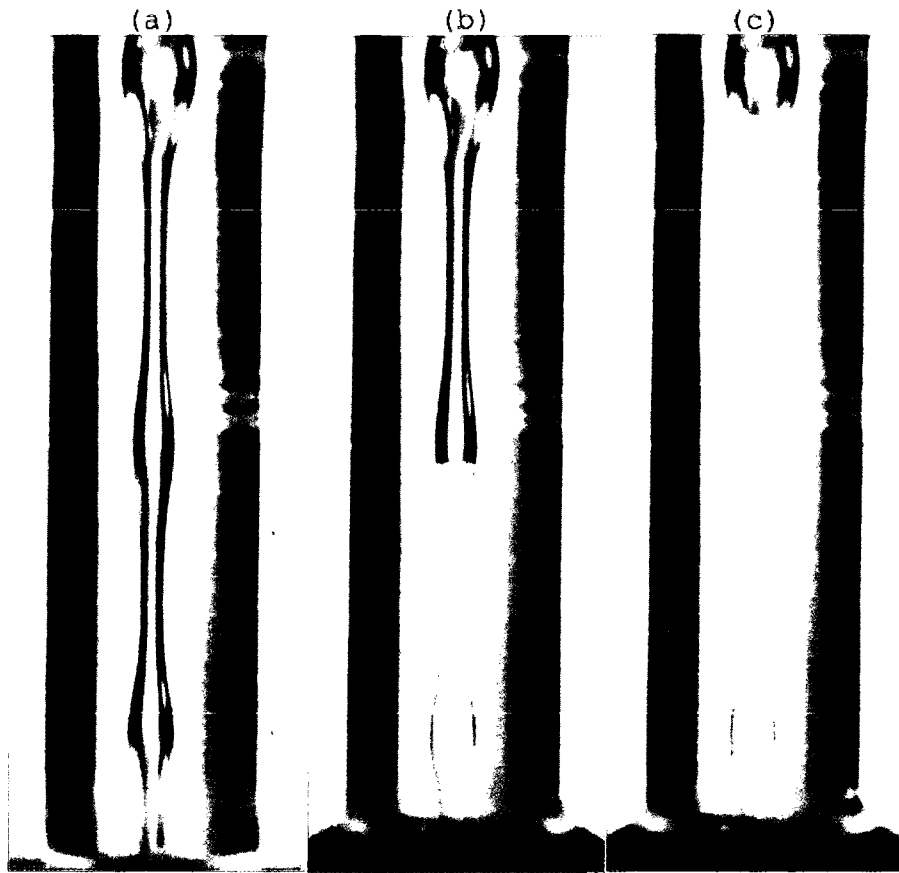


Figure 3.20 Surface-tension-driven flow into the A-type nonuniform tube. (a) the initial frame before contact; (b) the intermediate frame; (c) the equilibrium frame.

The third picture in Figure 3.19 is the last frame where the capillary interface is visible, and the third one in Figures 3.20 and 3.21 shows the frame when the capillary interface reaches the equilibrium state, and the equilibrium interfaces of the nonuniform tubes are located at the divergent region, which is consistent with the corresponding simulation conclusion in chapter 2.

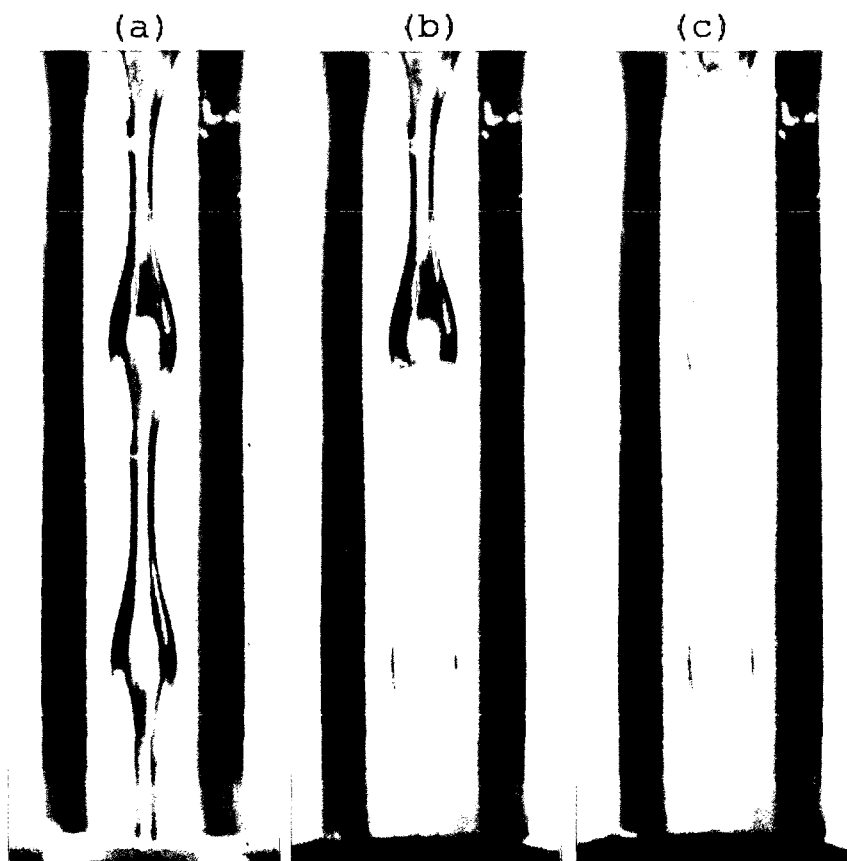


Figure 3.21 Surface tension-driven flow into the B-type nonuniform tube. (a) the initial frame before contact; (b) the intermediate frame; (c) the equilibrium frame.

Figure 3.22 presents three experimental observations of the progression of the meniscus height  $h$  with the time for the uniform circular tube shown in Figure 3.19. The meniscus height is the length measured from the three-phase contact line to the tube inlet. Although the capillary interface along the inner tube surface is unobservable from  $h=0\text{mm}$  to  $1.2\text{mm}$ , because it is hidden by

the slightly rising interface along the tube outer surface as shown in Figure 3.19, good consistence of the three series of data points are presented for  $h > 1.2\text{mm}$  and slow capillary rising velocity at the initial stage of  $h < 4\text{mm}$  is found which is similar to the findings of Stange et al.'s (2003) experiments under microgravity.

The theoretical predictions of Equations (3.105)-(3.108) of the uniform circular tube with measured constant radius  $R = 330\mu\text{m}$  are given together in Figure 3.22. Equation (3.105), where the dynamic contact effect is ignored, predicts a faster capillary velocity than that of the experiments during the entire observed time, and so is Equation (3.106) with a little bit of improvement. It indicates that the empirical correlation of the dynamic contact angle [Jiang et al. 1979] employed in Equation (3.106) that works well to Stange's experiments [Stange et al. 2003] may have a limitation of general applicability. With an appropriate shift of the experiment data along the time axis, the results of Equation (3.107), in which the molecular-kinetic dynamic contact angle model is employed with  $\zeta = 0.3$ , agrees well with the experiments for  $h > 4\text{mm}$ , whereas, the prediction

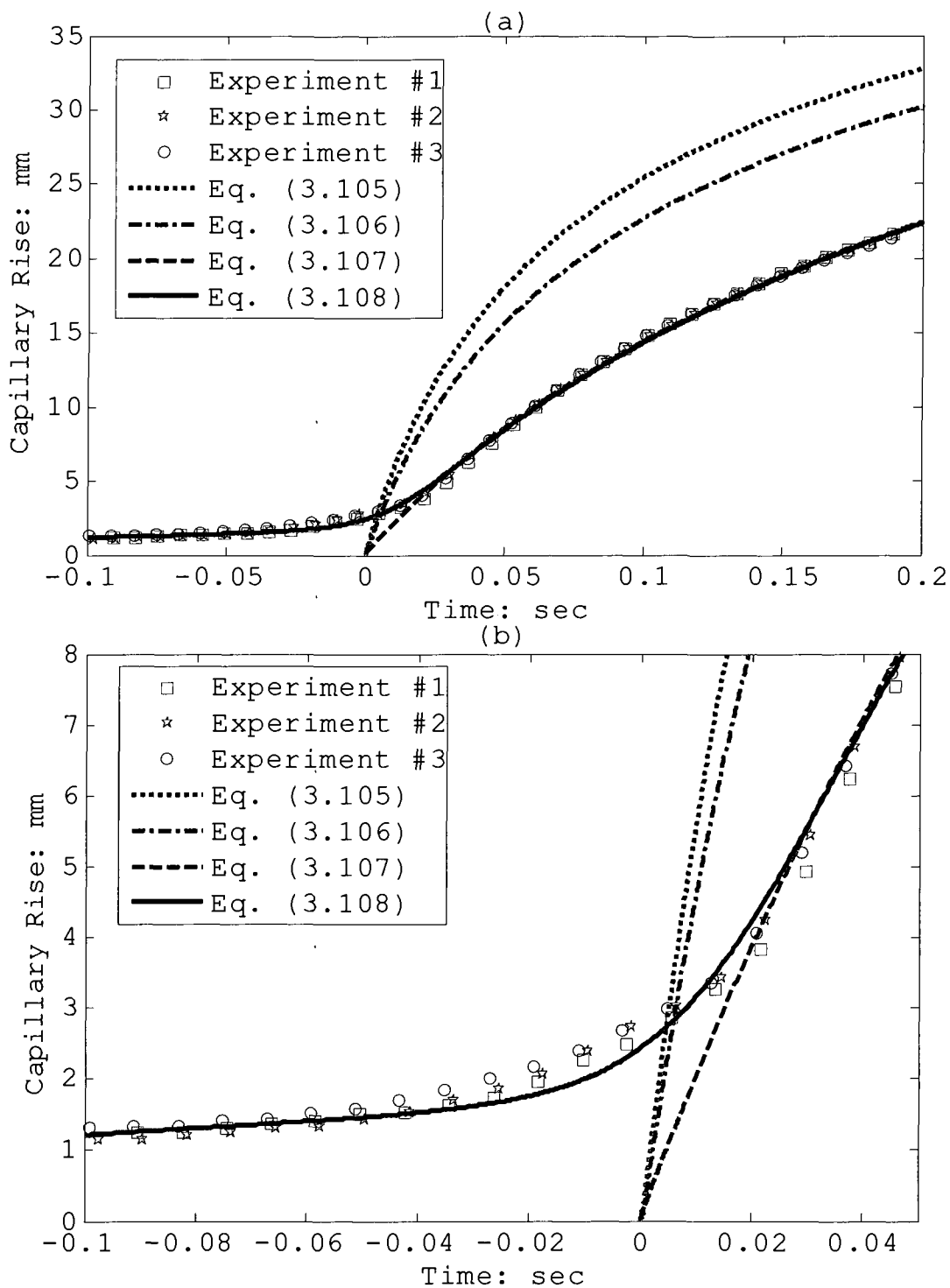
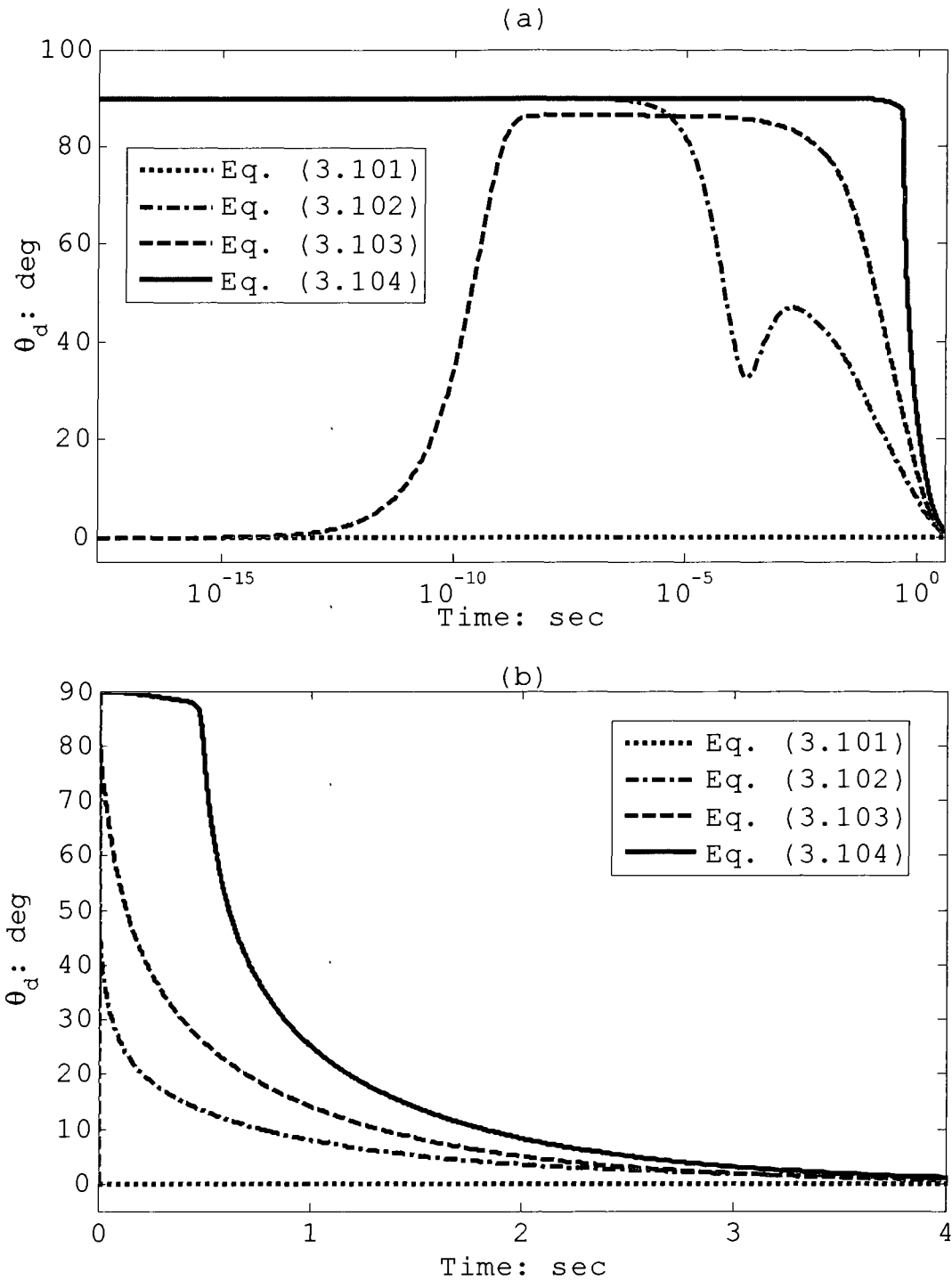


Figure 3.22 The capillary rise of distilled water in a circular cylindrical tube with  $t_c = 0.5$ ,  $M_p = 40$ ,  $A_d = 0.922$ ,  $B_d = 1.004$  and  $\zeta = 0.3$ .

of Equation (3.108) with  $t_c = 0.5$ ,  $M_p = 40$ ,  $A_d = 0.922$ ,  $B_d = 1.004$  and  $\zeta = 0.3$  fits the experimental data well in the entire observed region, where the time is shifted back 0.482s to be consistent with that of Equation (3.107).

The time-dependent variations of the dynamic contact angle of the four contact angle models can be obtained by substituting the relations of the capillary rise velocity versus the time in the solutions of Equations (3.105)-(3.108) back to Equations (3.101)-(3.104), respectively, and the results are shown in Figure 3.23. The variations at the micro time scale are shown in Figure 3.23a. Except the constant contact angle model gives  $\theta_d = \theta_s = 0$  for all the time, other three dynamic contact angle models predict that there is a period with the contact angle close to  $90^\circ$  as shown in Figure 3.23a, regardless the starting contact angle is  $90^\circ$  or  $0^\circ$ , and a stage transition for this angle to the static contact angle at the later time as shown in Figure 3.23b.



The underestimation of the period length when the contact angle maintains an angle close to  $90^\circ$  causes the two previous contact angle models, Equation (3.102) and (3.103), to miss the observed slow capillary rise at the initial stage.

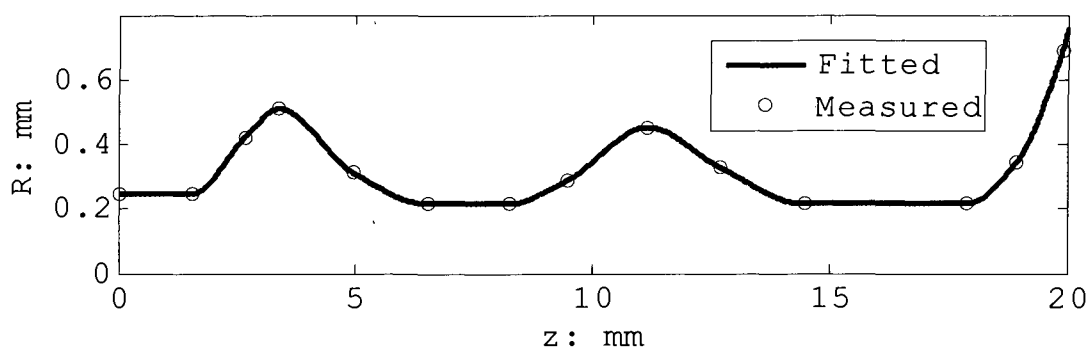


Figure 3.24 Geometry of Type-A nonuniform tube.

For the nonuniform circular tube comprising three bulbs as shown in Figure 3.20, three experimental observations of the progression of the meniscus height  $h$  with the time together with the theoretical results of Equations (3.105)-(3.108) are presented in Figure 3.25. The geometrical variation relation between the radius  $R$  and the axial location  $z$ , used in the theoretical calculations, is shown in Figure 3.24, which is obtained by numerical fitting the discrete point measured with

resolutions of  $50\mu\text{m}/\text{pixel}$  from the analysis on the video image as shown in Figure 3.20.

In Figure 3.25, the experimental results from the three independent runs show good repeatability from  $h=1.5\text{mm}$  to the equilibrium height  $19.85\text{mm}$ , which is located in the diverging region of the third bulb. It is found that there is a tardiness of the capillary interface at the initial stage of  $h<2\text{mm}$  as observed in the experiments of uniform tube. At a later time, the wavy changes of the capillary rise curve modulating to the corresponding varying tube geometry are apparent.

The comparison of the theoretical results and the experimental data leads to the conclusion similar to that of the uniform tube. Equations (3.105) and (3.106) predict faster capillary velocity than that of the experiments during the entire observed time. The results of Equation (3.107) with  $\zeta = 0.2$ , agree well with the experiments for  $h>4\text{mm}$  after an appropriate shift of the experiment data along the time axis. The present model achieves significantly better agreement with the data than those obtained by using the existing models.

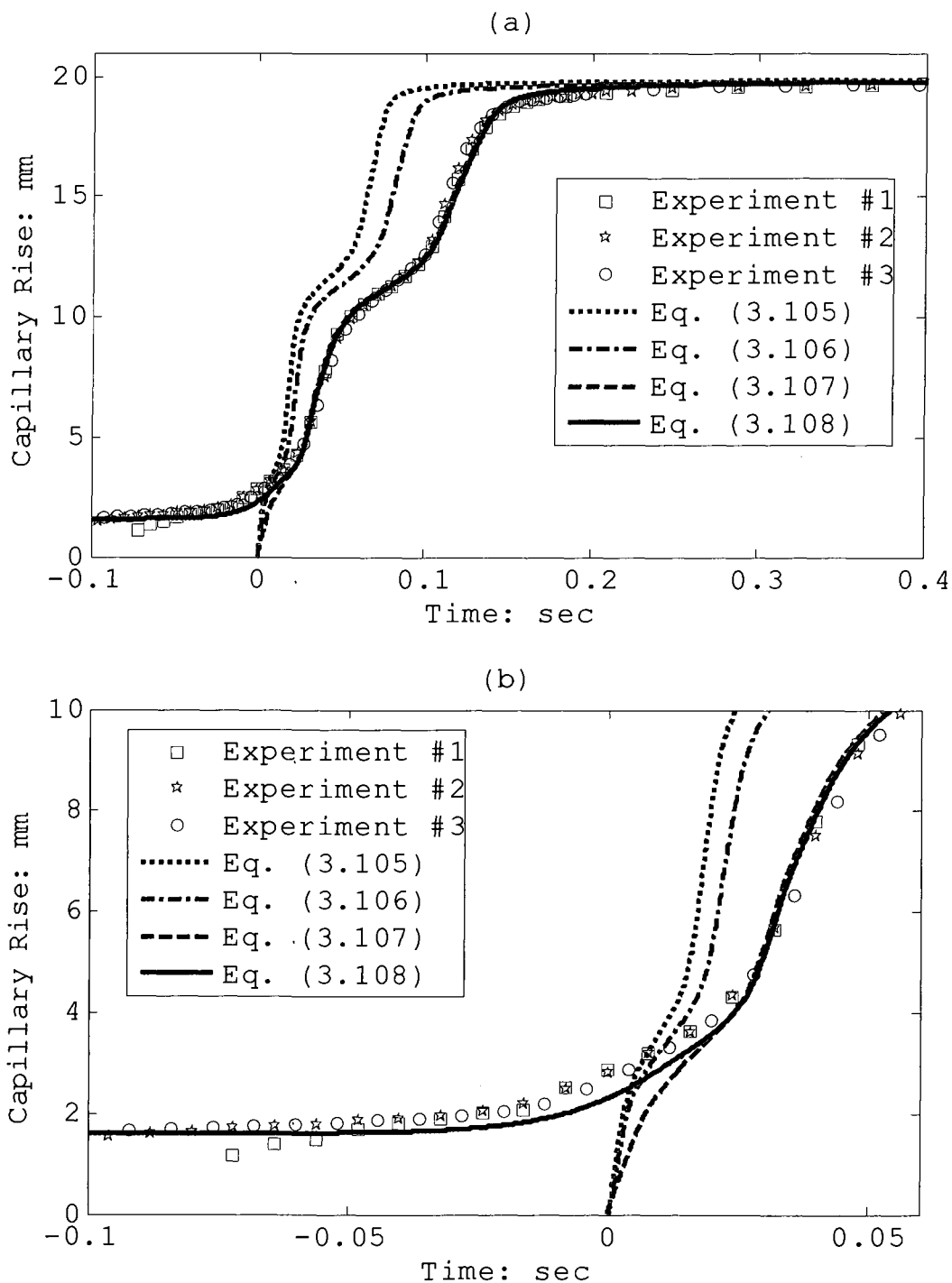


Figure 3.25 The capillary rise of distilled water in Type-A nonuniform tube with  $t_c = 0.5$ ,  $M_p = 40$ ,  $A_d = 0.922$ ,  $B_d = 1.004$  and  $\zeta = 0.2$ .

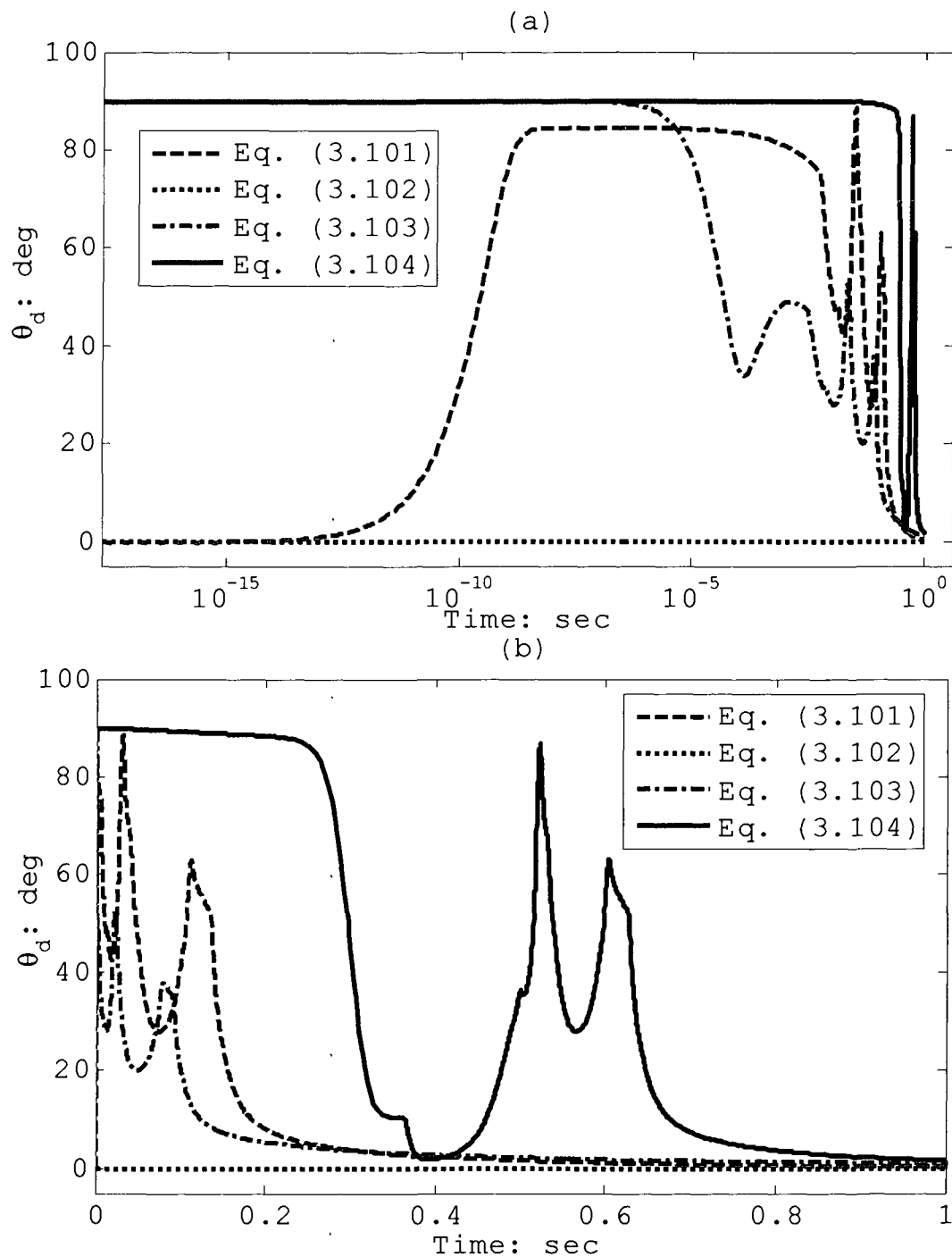


Figure 3.26 Time-dependent variations of dynamic contact angle for Type-A nonuniform tube.

(a) Logarithm time scale; (b) Linear time scale.

In Figure 3.25, Equation (3.108) fits the experimental data well in the entire observed region with  $t_c = 0.5$ ,  $M_p = 40$ ,  $A_d = 0.922$ ,  $B_d = 1.004$  and  $\zeta = 0.2$ . In the initial stage, the slow capillary rising is well predicted. After the time of solution of the Equation (3.108) shifts back 0.49s, it coincides with that of Equation (3.107) in the later time when  $h > 4\text{mm}$ .

The time-dependent variations of the dynamic contact angle of the four contact angle models obtained by substituting the solutions of Equations (3.105)-(3.108) back to Equations (3.101)-(3.104), are shown in Figure 3.26. The variations at the micro time scale are clearly shown in Figure 3.26a, which gives us an explanation of why the slow capillary rising phenomenon is absent in the results of the previous dynamic contact angle models. For the constant contact angle model,  $\theta_d = \theta_s = 0$  for all times, while the dynamic contact angles modeled by Equations (3.102) and (3.104) initially start from  $90^\circ$  and that of Equation (3.103) starts from  $0^\circ$  but increases up to a value close to  $90^\circ$  in short time, in the order of a nano second. When the contact angle is close to  $90^\circ$ , the surface tension driven force is very small, which is

the reason for the slow capillary rising at the initial time period. However, the angle of Equation (3.102) starts to drop down in time in the order of microsecond and that of Equation (3.103) in millisecond order time. Only Equation (3.104) can maintain the small surface-tension driven force and predict the slow capillary rising in the initial time scale close to the observations. Figure 3.26b presents the fluctuations of the curves of the dynamic contact angles in the later time when the capillary interface passes the irregular geometrical regions.

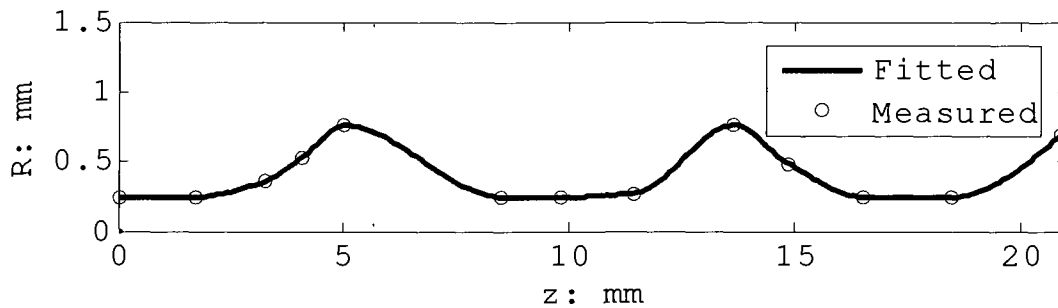


Figure 3.27 Geometry of Type-B nonuniform tube.

For the type-B nonuniform circular, which comprises three bulbs of bigger size than type-A, the geometrical variation relation between the radius  $R$  and the axial location  $z$  used in the theoretical calculations, is shown in Figure 3.27, which is obtained from the analysis on the video image as shown in Figure 3.21.

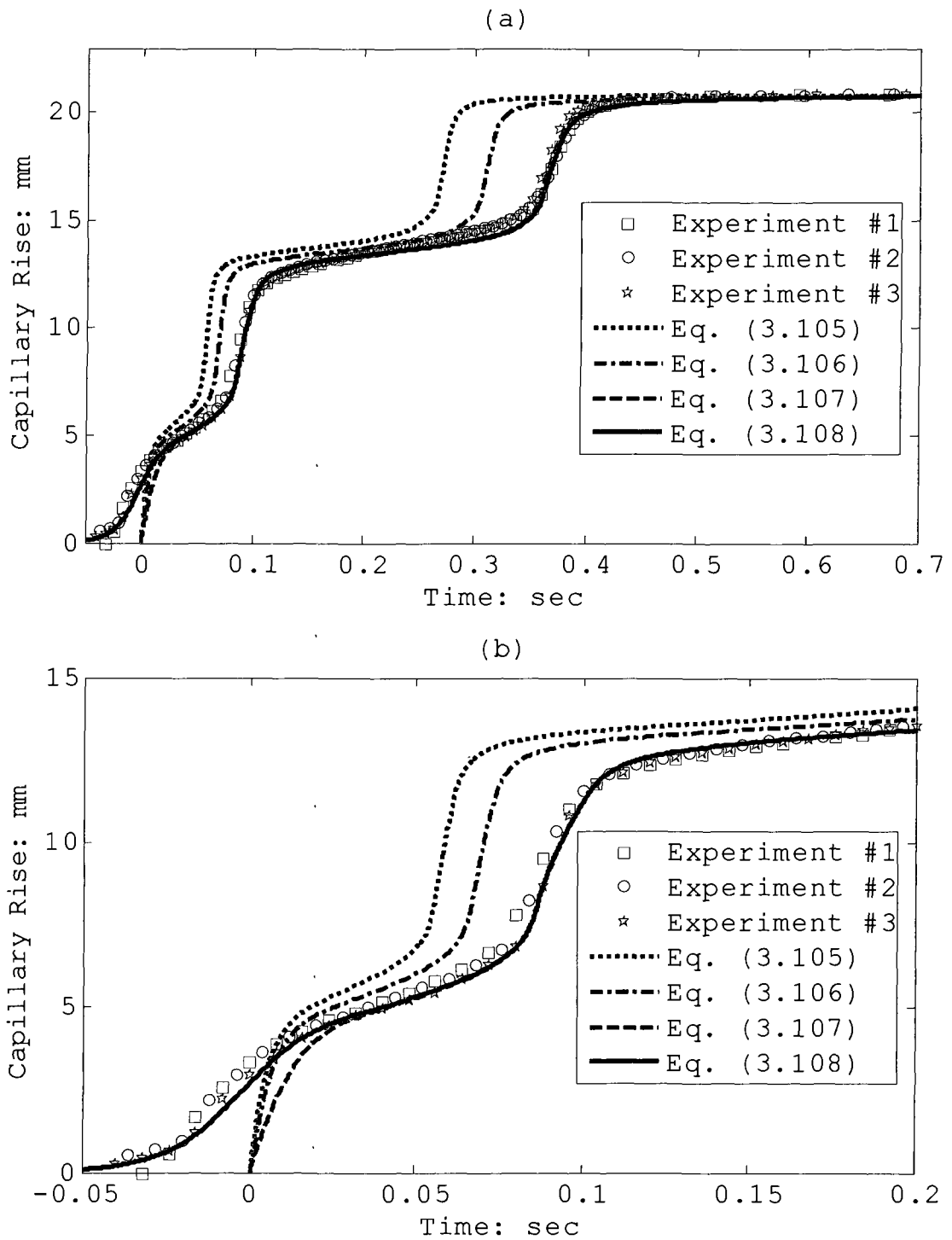


Figure 3.28 The capillary rise of distilled water in a sinusoidal tube with  $t_c = 0.1$ ,  $M_p = 40$ ,  $A_d = 0.99$ ,  $B_d = 1.0025$  and  $\zeta = 0.2$ .

The experimental observations of the progression of the meniscus height  $h$  with the time together with the theoretical results of Equations (3.105)-(3.108) are presented in Figure 3.28. The three series of experimental data with good repeatability show the slow capillary rising at the initial stage, the fluctuations with bigger amplitude than Type-A when the capillary interface passes the bulb region with bigger geometry variations, and the equilibrium height located at the diverging region of the third bulb. In the theoretical part, Equations (3.105) and (3.106) predict faster capillary velocity than that of the experiments during the entire observed time. The results of Equation (3.107) with  $\zeta = 0.2$ , agree well with the experiments for  $h > 5\text{mm}$  after an appropriate shift of the experiment data along the time axis. Equation (3.108) can fit the experimental data well in the entire observed region including the slow capillary rise region at the initial stage with  $t_c = 0.1$ ,  $M_p = 40$ ,  $A_d = 0.99$ ,  $B_d = 1.0025$  and  $\zeta = 0.2$ . After the time of solution of the Equation (3.108) shifts back 0.096s, it coincides with that of Equation (3.107) in the later time when  $h > 5\text{mm}$ .

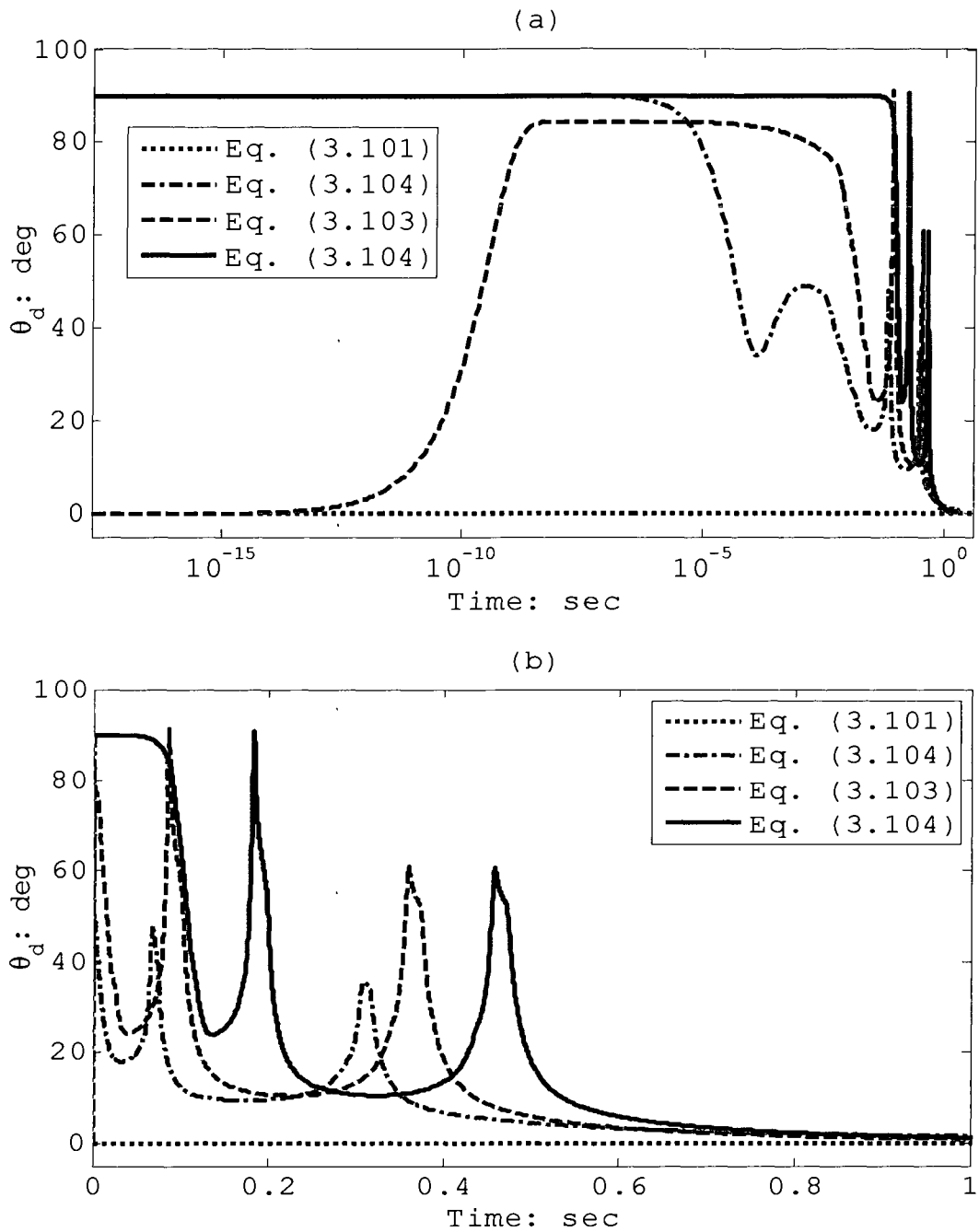


Figure 3.29 Time-dependent variations of dynamic contact angle for Type-B nonuniform tube.

(a) Logarithm time scale; (b) Linear time scale.

The time-dependent variations of the contact angle during the capillary rising process are shown in Figure 3.29. The transition in the micro time scale shown in Figure 3.29a and the geometrical effect on the dynamic contact angle shown in Figure 3.29b are similar to the observations of the type-A nonuniform tube in Figure 3.26.

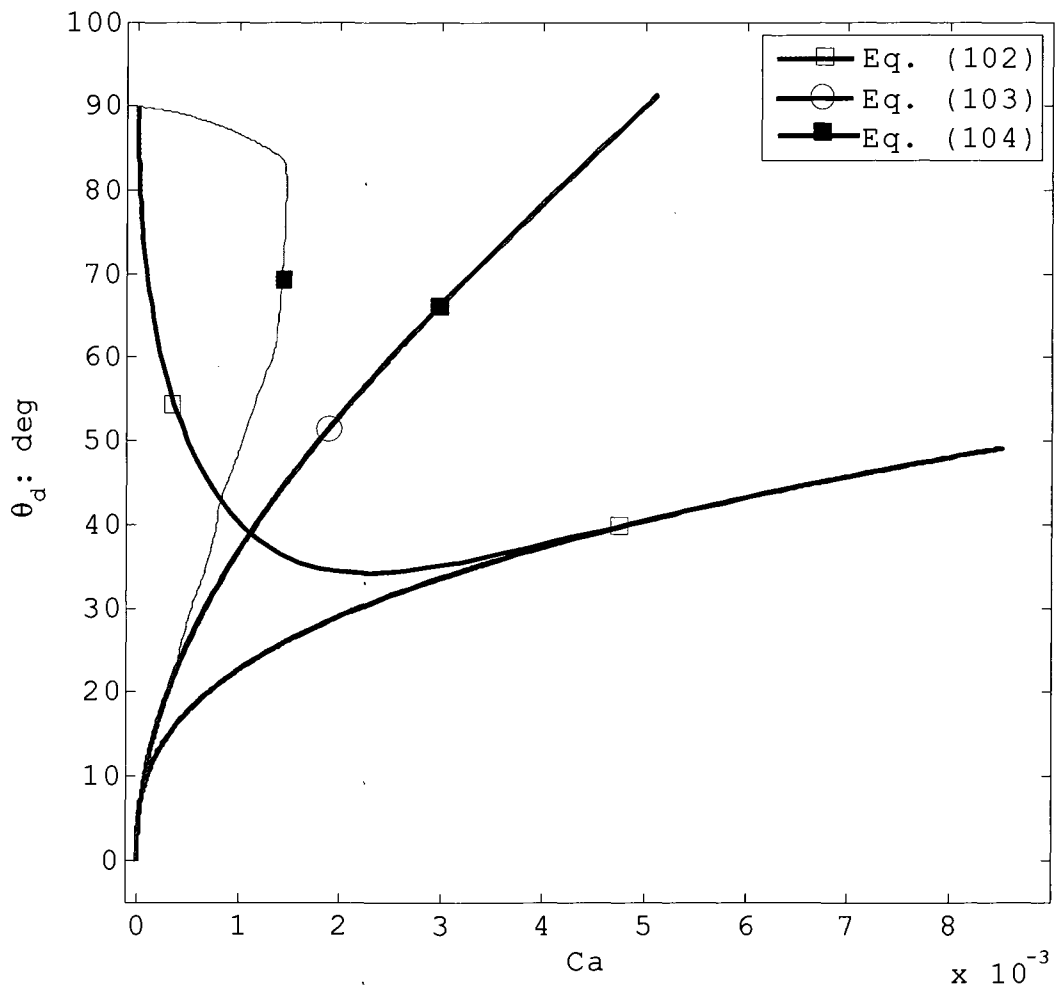


Figure 3.30 Velocity-dependent variations of dynamic contact angle.

The traditional dynamic contact angle model, whether the underlying theory is the hydrodynamic or molecular-kinetic theory, is velocity-dependent as indicated in Equation (3.103). On the other hand, the proposed dynamic contact model described in Equation (3.104) is dependent on time and velocity, as is the empirical model of [Jiang et al. 1979] described in Equation (3.102). The velocity-dependent relations determined by the three different dynamic contact angle models, Equations (102)-(104), are presented in Figure 3.30 where the velocity is represented by the nondimensional variable,  $Ca$ . All the data points are from the capillary rise solution of Equations (3.106)-(3.108) for the type-B nonuniform tube. As it is shown in Figure 3.30, the entire curve of Equation (3.103) is overlapped with part of the curve of Equation (3.104). For Equation (3.104), the contact angle varies monotonously on  $Ca$ , and the relation between  $\theta_d$  and  $Ca$  is a one-to-one mapping. However, it is two to one mapping between  $\theta_d$  and  $Ca$  for Equation (3.102) when  $Ca$  is in the interval of  $[0, 0.0035]$ , and three to one mapping for Equation (3.104) when  $Ca$  is in the interval of  $[0, 0.0015]$ . It implies that, for the capillary rise, the

velocity-dependent relation of the dynamic contact angle in the initial stage is different from that in the intermediate stage and equilibrium stage. Our experiments indicate that the time scale of initial stage is not ignorable, about 0.5s for type-A nonuniform tube and 0.1s for type-B nonuniform tube, but is neglected or underestimated in the traditional dynamic contact models.

### **3.6 Conclusions**

The model for the time-dependent rise of the capillary interface in a tube with cross sections that are not uniformly varying along its axis in chapter two is further developed in this chapter. Two improvements of the proposed model are:

- 1, the deviation of the velocity field to the Hagen-Poiseuille solution due to the nonuniform geometrical effect is considered by using asymptotic flow field solutions based on the perturbation method;

- 2, the dynamic contact angle effect is taking into account by incorporating a proposed new dynamic contact angle model which modified the traditional molecular-

kinetic model by bringing in the time-dependent relation in the initial stage.

The proposed model is first applied to the existing experiments of the capillary rise in uniform circular tubes and good agreements are achieved. A series of experiments of the capillary rise in nonuniform tubes are reported in this chapter. The experiment results validated the proposed model and presented the advantage of the model, explaining the observed tardiness phenomena in the initial stage.

The model will be further developed to model the capillary flow in multi-layer porous media in the next chapter.

## **CHAPTER 4**

### **MODELING OF CAPILLARY FLOW IN MULTI-LAYER POROUS MEDIUM**

In this chapter, the industrial application of my research work was explored by adopting the proposed model to describe the water flow passing through a multi-layer porous medium. This specific porous medium, composed of six layers with complex woven fabric structures and pore sizes that range from 5 $\mu$ m to 2mm, is used in Procter & Gamble's Rigid-Capillary-Press (RCP) dewatering device for paper making industries.

The capillary phenomenon is used here to improve the water removing efficiency and save energy. In the framework described in previous chapters, the flow in multi-layer porous media driven by surface tension and vacuum pressure is analytically investigated. The dewatering performance predicted by the analytical model is compared to the pilot plant experiments with good agreements. The potential of the model to be used as a parametric optimization tool for the industrial porous media design is discussed in this chapter.

## 4.1 Background

### Introduction of Paper Making Machine

Worldwide paper use has increased dramatically over the last few decades, from about 70 million tons in 1980 to 140 million tons in 1996, and is expected to exceed 396 million tons by 2010 [McCool 2008]. In 2006, there were approximately 450 paper mills in the United States, accounting for \$68 billion according to 2006 U.S.

Industry & Market Outlook. Although modern technology is developing with high-speed, the pulp and paper industry still remains extremely energy intensive, ranking fourth only behind chemicals, steel and petroleum in energy consumption [Asensio 2000].

Papermaking consists of spreading a suspension of pulp evenly across a paper machine, followed by its dewatering in a manner that yields a product with desirable properties. Figure 4.1 shows an actual image of a RCP paper machine and its diagram is shown in Figure 4.2. Generally, a paper machine consists of three main sections: forming, press, and dryer. In the forming section, the pulp is diluted and mixed to form the slurry of about 99.5% water and 0.5% pulp fiber and pumped to

the headbox. Through a narrow slot in the bottom of the headbox, the slurry is sprayed evenly onto the forming fabric which is circulating and supported by rolls or foils.

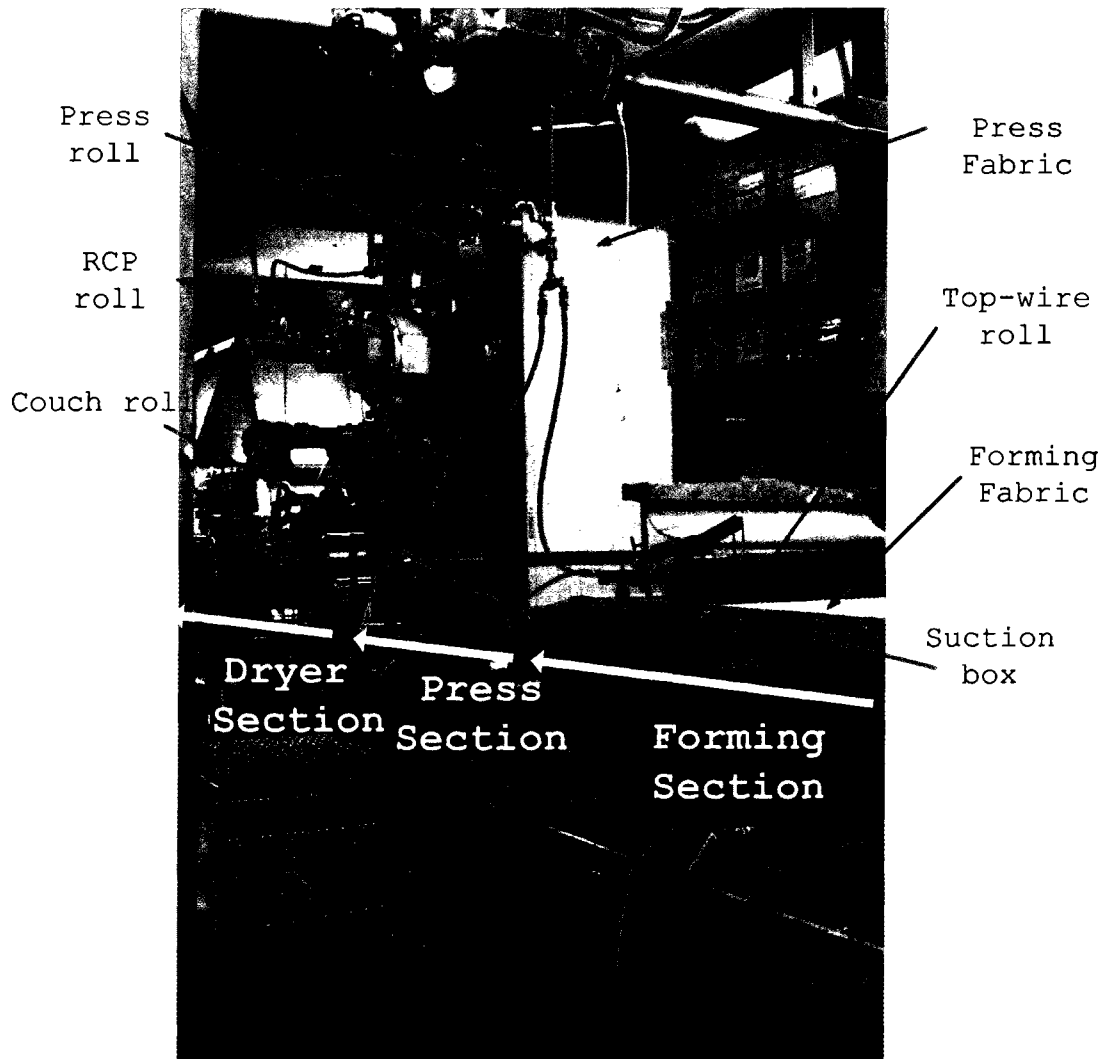


Figure 4.1 Image of RCP paper machine.

As the forming fabric moves along the forming section, the fabric filters part of water by gravity and

retains the pulp fibers to form the sheet. The fiber sheet then passes over the vacuum suction boxes to pull more water while a top-wire dewatering roll is mounted two-thirds of the way down the forming section to break up the lumps and improve the formation, and also remove the additional water from the top of the fiber sheet [Asensio 2000].

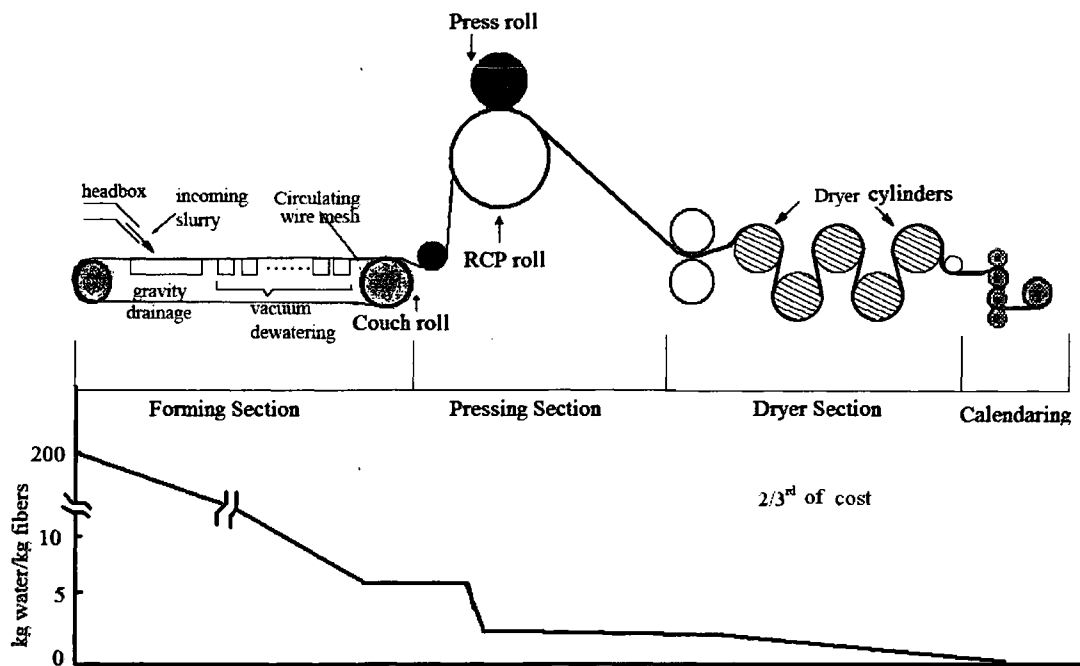


Figure 4.2 Schematic diagram of paper machine [Courtesy of Chokshi 2007].

After the couch roll, the press fabric carries the fiber sheet to enter the pressing section where the mechanical dewatering occurs. In this process, the fiber mat is mechanically compressed by press rolls to squeeze

out the water. As the sheet leaves the press section, it is typically 40% fiber and 60% water, depending on the sheet grade and the paper machine. Finally, the drying process is accomplished through the supply of heat to the sheet by large steam-heated cylinders in the dryer section where the paper web is dried to its finished condition of only 5% water. The final paper web has a relatively smooth surface and is relatively strong and stiff due to the interlocking of fibers and fiber-fiber hydrogen bonds.

For some grades, such as bath and facial tissue, a strong, compact, smooth sheet is not desired. Rather, a soft, open, high loft sheet is needed. For these grades, it is desirable to mechanically remove as much water as possible without significant pressing and then remove the remaining water by evaporation. The RCP dewatering process, to be described subsequently was developed to meet this need.

Figure 4.2 indicates the reduction of the water content when the paper web passes the dewatering sections. Approximately, the wood pulp contains 166-200 kg water/kg fiber in the headbox, 4-5 kg water/kg fiber after the forming section, 1.5 kg water/kg fiber after the press

section and 0.05 kg water/kg fiber after the dryer section [Chokshi 2007]. The amount of the removed water in the dryer section is moderate compared to those in other sections, but two thirds of the total energy consumption for the paper machine is consumed in this section. Normally, it costs more than 10 times as much to remove water by heat in the dryers than the mechanical dewatering in the press section. Consequently, research activity to improve press section efficiency has been, and still is, at a very high level.

Higher water removal rates without significant pressing can be achieved by using a new limiting orifice drying method, called Rigid-Capillary-Press (RCP) technology, invented by the Procter & Gamble company [Chuang and Thompson 1985; Ensign et al. 1994; 1996; 2000; Stelljes et al. 2000; 2004; Trokhan et al. 1999].

#### RCP Dewatering Process

Figure 4.3 shows a close-up view of the RCP press section, and Figure 4.4 presents a schematic side sectional view of the RCP papermaking machine. The mounting arrangement of the RCP press section, where the RCP roll and the press roll are mounted on the main frame

and the press roll is above the RCP roll as shown in Figure 4.3, is similar to that of the conventional paper machine, but the design of the RCP roll is quite different from the conventional press roll. The RCP roll has perforated shell which is covered with a specific designed multilayer porous medium, called the RCP medium. The woven structure of the RCP medium is discussed in detail later. According the description in the Proctor and Gamble's patent [Chuang et al. 1985], the internal space of the roll may be divided into six sectorial zones by the partitions with seals. The practical design, used in the pilot plant RCP paper making machine, is to only divide the space into two zones as shown in Figure 4.4: the vacuum zone and the pressure zone [Valmet-Karlstad 1999]. The vacuum zone is connected to the vacuum source through the vacuum pipe, while the pressure zone is connected the air source through the pressure pipe. Within the pressure zone, an array of internal showers is mounted for the purpose of lubrication and cleaning, which is connected to the water source through the water pipe. Below the RCP roll and within the trough, there is also an array of external showers to clean and prewet the outer surface of the RCP medium. A doctor blade

contacting the outside surface of the roll is mounted at the exit from the trough for the purpose of cleaning.

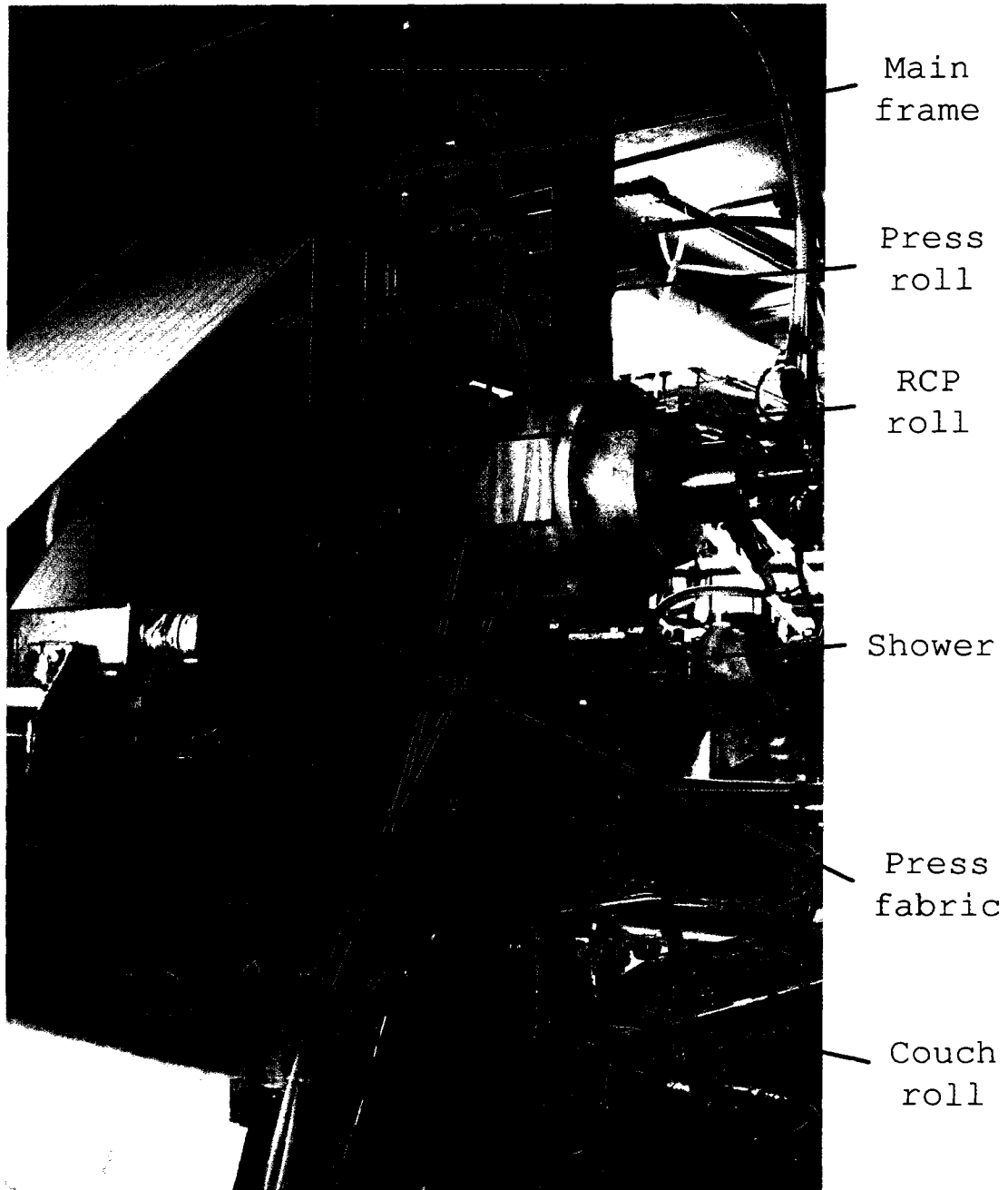


Figure 4.3 Close-up view of RCP press section.

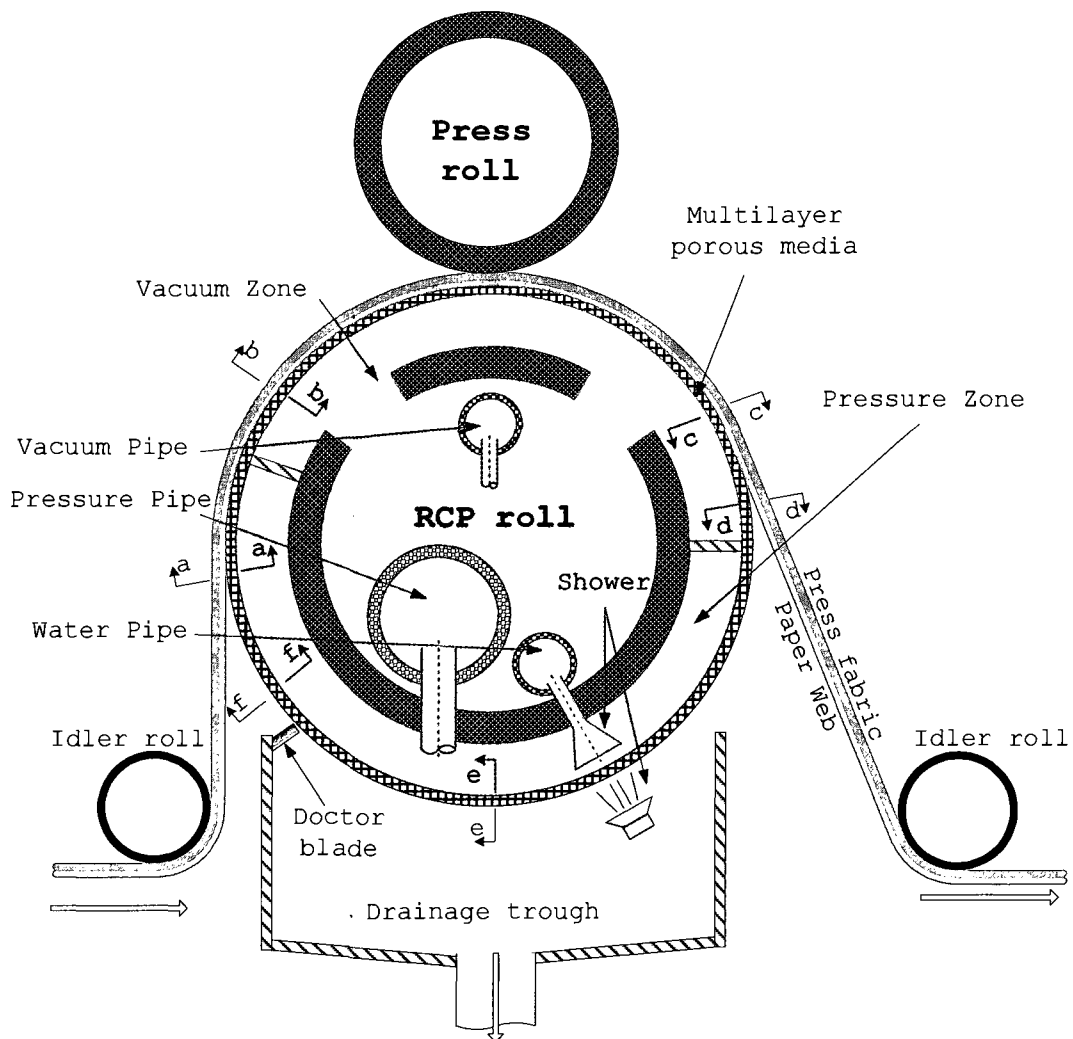


Figure 4.4 Schematic fragmentary sectional view of RCP papermaking machine.

The continuous wet paper web is carried by the press fabric to wrap part of the vacuum zone. The roll is covered by the RCP medium wherein the uniformly distributed pores of the top layer are effectively smaller than the pores formed by the pulp fibers of the paper web. Therefore, some of the liquid is driven by the

vacuum suction pressure and the capillary pressure to transfer from the pores of the paper web into the pores of the RCP medium. A description of an operational sequence of the water removing process of the RCP roll is presented in Figure 4.5, where the sectional views are taken along section lines a-a through f-f of Figure 4.4. In Figure 4.5(a-a), the paper web is being carried on the press fabric along a convergent path towards the RCP roll surface. The water disposed in the pore of the RCP medium has an outward meniscus with a slightly convex shape and an inward meniscus with a concave shape due to maintaining a slight positive pneumatic pressure in the pressure zone. After the paper web has come into contacting with the outer surface of the RCP medium as shown in Figure 4.5(b-b), the convex meniscus shown in Figure 4.5(a-a) helps the water disposed in the pore of the RCP medium achieve a continuous liquid-to-liquid continuity with the water in the paper web and the trapping of the air in the paper web is obviated. The vacuum suction pressure from the vacuum zone and the capillary pressure provided by the inward capillary interface in the RCP medium act together to pull the water from the pore of the paper web into the pores of

the RCP medium. This water-transferring process without airflow through the RCP porous medium results in great energy saving in the vacuum system and a higher level of fiber consistency in the paper web than that with conventional vacuum dewatering. The additional water removal, in turn, results in large thermal energy savings in the dryer section [Chuang and Thompson 1985]. Another advantage of the RCP technology is that the tension of the press fabric can be maintained at a low enough value to substantially minimize the compaction of the paper web as it passes over the RCP roll. This makes the RCP dewatering technology applicable to the paper making of the soft tissue paper.

After a long exposure time to the vacuum pressure as shown in Figure 4.5(c-c), the liquid-to-liquid continuity between the water remaining in the pores of the paper web and the water disposed in the RCP pores may be broken up and an outwardly facing meniscus with a concave shape is formed in the RCP pore. In this state, because the pore size is in the order of microns, the capillary pressure formed by the concave water surface may be enough to counteract the vacuum suction pressure.

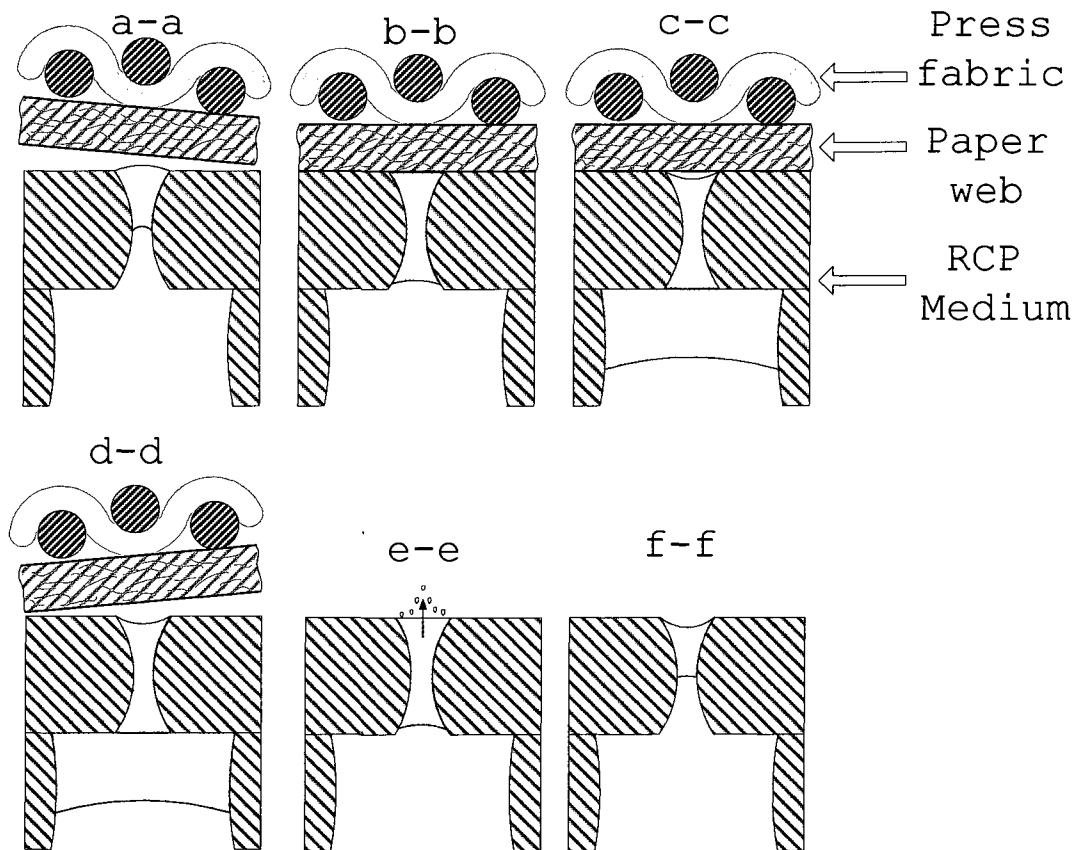


Figure 4.5 Fragmentary sectional views taken along sectional lines a-a through f-f.

In Figure 4.5(d-d), the paper web has commenced to diverge from the RCP medium. The concave capillary interface of the water in RCP pores eliminate the rewetting process that occurs when water is pulled back to the pores of the paper web during the departure time. Figure 4.5(e-e) depicts the outward pneumatic expulsion of water when the element arrives at the pressure zone, which is maintained at a positive pneumatic pressure. The

pressure is controlled at a sufficient level to precipitate expulsion but not large enough to cause total expulsion. Therefore, as shown in Figure 4.5(f-f), a relatively short residual column of water remains in the pore of the RCP medium and the RCP dewatering loop is completed. During the dewatering process, there is always a water column, long or short, remaining in the pore of the RCP which acts a liquid-seal to obviate both the vacuum and the positive pressure induced air flow through the pores of the RCP medium, and consequently, conserves the energy which would otherwise be expended to supply vacuum and compressed air.

#### RCP Porous Medium

As mentioned above, the RCP roll is covered by a multi-layer RCP medium which may comprise of six layers with a pore size gradient from the first layer to the sixth layer [Ensign et al. 2000]. Figure 4.6 shows a fragmentary top plan view of the RCP medium, and Figure 4.7 shows the microscope-observed images of the six plies, where the first layer image is from the top view and the other images is from the bottom view through the holes in the sixth layer.

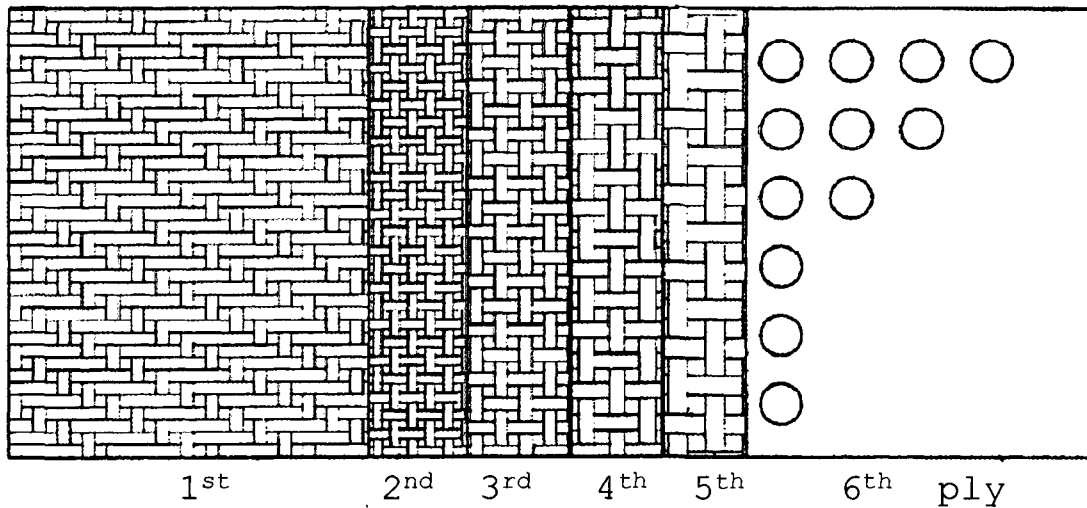


Figure 4.6 A fragmentary top plan view of the RCP porous medium [Ensign et al. 2000].

The six layers are arranged from the finest first layer to the coarsest sixth layer. The first layer provides the support to the paper web and builds a liquid-to-liquid connection to the water in the paper web to remove the water efficiently by taking advantage of the capillary phenomena in such small pores. The coarsest sixth layer provides the strength to the entire RCP medium. The other four layers in between the first and the sixth layers provide hydraulic connection and support for the first layer [Ensign et al. 2000].

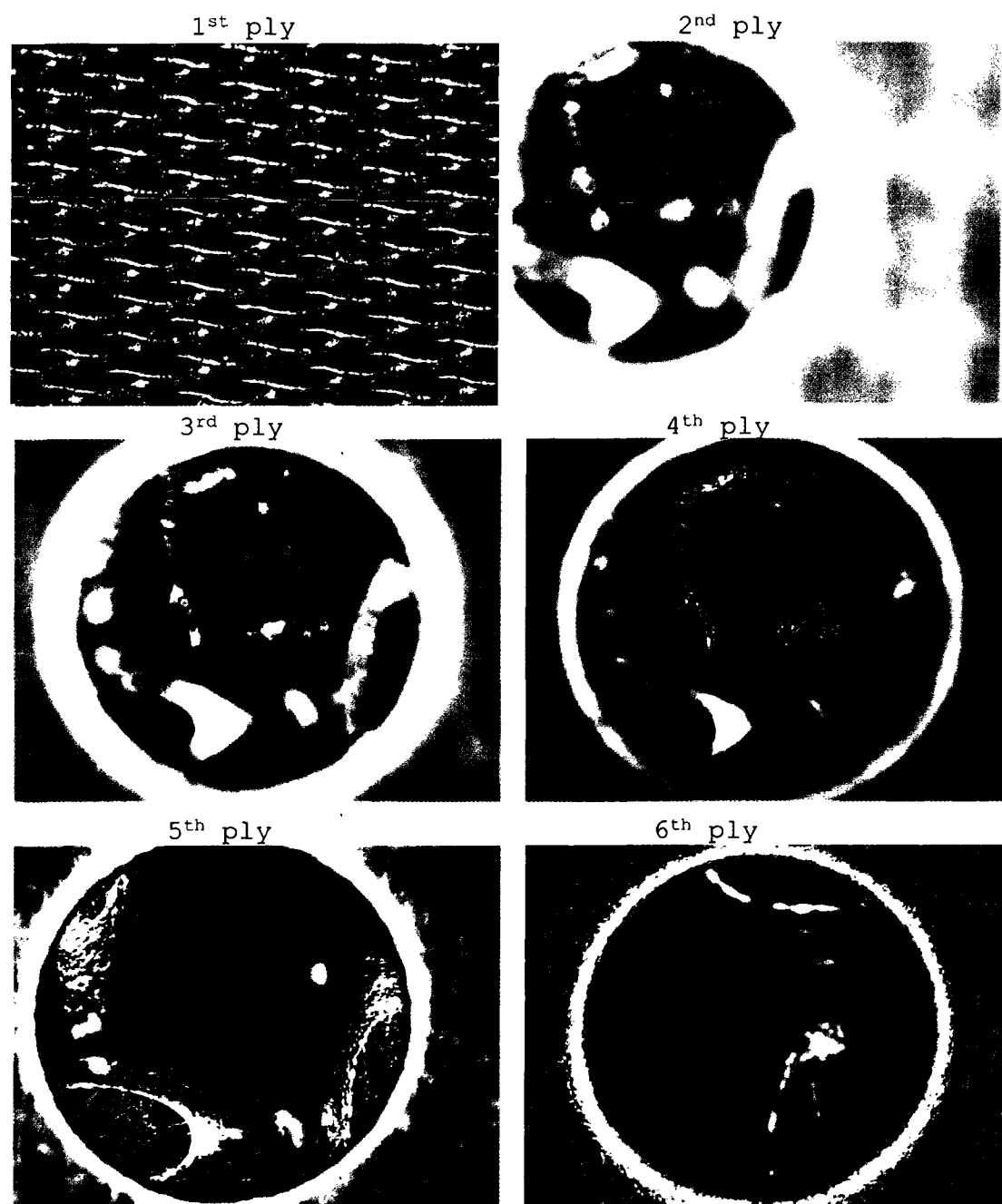


Figure 4.7 Microscope view of each layer of the RCP porous medium.

The connector layers are necessary to maintain the generally planar configuration of the first layer, because the first layer is so fine and deformable and would deform into the interstices of the sixth layer without the support of the intermediate layers. Such deformation would break the hydraulic connection between the first layer and the paper web. The RCP medium may be thought of as having a "Machine Direction" and a "Cross Direction". As used herein, the "Machine Direction" (MD) refers to the direction parallel to the transport of the paper web, and the "Cross Direction" (CD) refers to the direction parallel to the plane of transport of the paper web and orthogonal to the machine direction. For convenient description, the MD fiber diameter and the CD fiber diameter of the  $i$ -th layer are denoted by  $DM_i$  and  $DC_i$ , the fiber count per centimeter in MD and CD of the  $i$ -th layer are denoted by  $NM_i$  and  $NC_i$ , and the thickness of the  $i$ -th layer is denoted by  $H_i$ .

The Ensign patent [Ensign et al. 2000] describes the layers in detail. The following table summarizes the layer construction:

Table 4.1 Geometry summary of the RCP porous medium.

Layer	Weave	$DM_i$ ( $\mu\text{m}$ )	$NM_i$ (No./m)	$DC_i$ ( $\mu\text{m}$ )	$NC_i$ (No./m)	$H_i$ ( $\mu\text{m}$ )
1	Dutch Twill Fig. 4.8	71	6500	41	63000	111
2	Square plain Fig. 4.9	66	5900	66	5900	99
3	Square plain Fig. 4.9	191	2400	191	2400	285
4	Square plain Fig. 4.9	406	1200	406	1200	609
5	Square plain Fig. 4.9	710	630	710	630	800
5	Drilled Plate	N/A	N/A	N/A	N/A	600

The coarsest sixth layer is a perforated metal plate with a thickness of 0.6mm. The approximately 27% open area was provided by 1.5mm diameter holes bilaterally staggered at 60 degrees on a pitch of 2.7mm. Among the given geometry data of the RCP medium, the fiber diameter and fiber counts in each layer are from the Procter & Gamble's patent [Ensign et al. 2000] and are approximately validated by the image measurement in Figure 4.7. The thickness of each layer is estimated approximately based on the fiber diameter, the woven structure shown in the Figures 4.8 and 4.9, and the measured total thickness of the sample of the RCP medium.

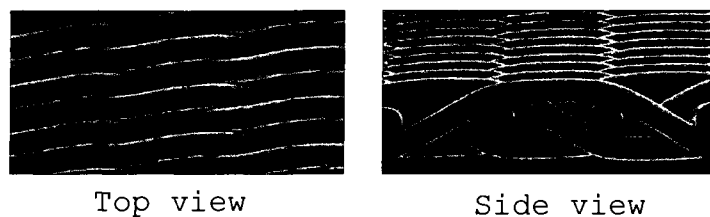


Figure 4.8 Dutch twilled woven structure.

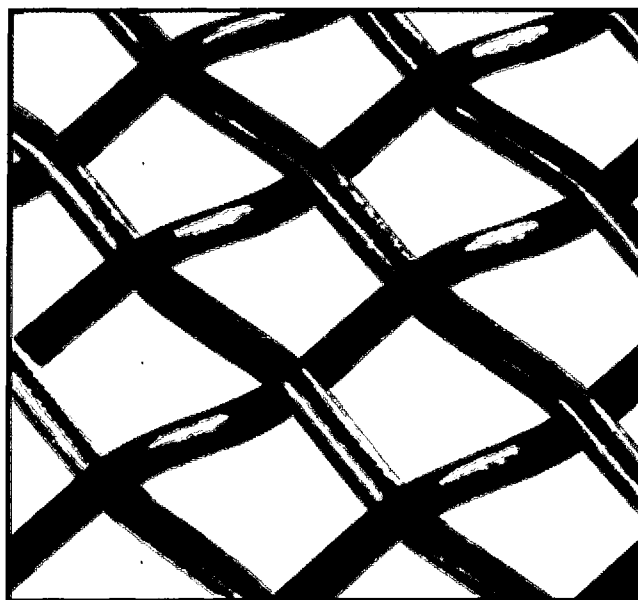


Figure 4.9 Plain square woven structure.

To apply the analytical model to the RCP porous media flow, a parameter,  $N_i$ , is introduced to describe the pore number density per unit area at the  $i$ -th layer, which is determined by the weave structure of the layer and assumed to be constant in the same layer. According the above geometry description of the RCP medium, the

pore number density per unit area for the six layers can be calculated as:

$$N_1 = \frac{65 \times 630}{(0.01)^2} = 4.095 \times 10^8 \text{ m}^{-2} \quad (4.1)$$

$$N_2 = \frac{59 \times 59}{(0.01)^2} = 3.481 \times 10^7 \text{ m}^{-2} \quad (4.2)$$

$$N_3 = \frac{24 \times 24}{(0.01)^2} = 5.76 \times 10^6 \text{ m}^{-2} \quad (4.3)$$

$$N_4 = \frac{12 \times 12}{(0.01)^2} = 1.44 \times 10^6 \text{ m}^{-2} \quad (4.4)$$

$$N_5 = \frac{6.3 \times 6.3}{(0.01)^2} = 3.969 \times 10^5 \text{ m}^{-2} \quad (4.5)$$

$$N_6 = \frac{\cos\left(\frac{\pi}{6}\right)}{3 \cdot \left(\frac{2.7 \times 10^3}{2}\right)^2} = 1.584 \times 10^5 \text{ m}^{-2} \quad (4.6)$$

For each layer, the void volume is obtained by subtracting the solid fiber volume from the total volume. If the void volume is assumed to be occupied by a bundle of circular cylinders which have the height of the thickness of the layer and uniformly distributed with number density  $N_i$ , the radius of this virtual cylinder is defined as the effective radius  $R_{0i}$  of the pore of the

layer. According to the geometry description, the effective pore radius for each layer can be calculated as:

$$R_{01} = 3.82 \mu\text{m} \quad (4.7)$$

$$R_{02} = 73.6 \mu\text{m} \quad (4.8)$$

$$R_{03} = 169 \mu\text{m} \quad (4.9)$$

$$R_{04} = 329 \mu\text{m} \quad (4.10)$$

$$R_{05} = 555 \mu\text{m} \quad (4.11)$$

$$R_{06} = 750 \mu\text{m} \quad (4.12)$$

The pore in the sixth layer is a cylindrical hole with radius of  $750\mu\text{m}$ , but the pores in other layers are formed by cylindrical fibers, and the actual geometry is complicated. By assuming the cross section of the pore is circular and the axis is straight, we use a cosine function

$$R_i(z) = R_{0i} \left\{ 1 + A \cdot \cos \left[ \frac{2\pi (z - h_{0i})}{L_i} \right] \right\} \quad (4.13)$$

to approximate the variations of the radius of the pores in the first five layers, where  $z$  is the axial direction pointing from the first layer to the sixth layer,  $h_{0i}$  is the location of the top surface of the  $i$ -th layer, and  $L_i$  is the wavelength which is taken as the thickness for each layer except for the first layer where it represents

a half of the thickness. The amplitude  $A$  will be determined later.

#### **4.2 Experimental Study of the Dewatering of RCP Medium**

Two fluid experiments of the RCP porous medium are described in this section. One is a flow rate test of the medium under different suction pressures which is carried out at the lab, the other is pilot plant test of the water removing rate of the RCP medium during the paper making process.

##### Flow Rate Test of RCP Medium

To obtain a basic understanding of the liquid flow passing through the RCP medium, a RCP flow test cell was built to investigate the correlation between the applied vacuum pressure and flow removal rate without the effect of the pulp fibers. Figure 4.10 and 4.11 show the schematic view and actual view of the flow test cell, respectively. A sample RCP medium provided by Procter & Gamble was fixed on the bottom of the top tank. The RCP sample is exposed to the water through an open circular area of 0.1m in diameter formed by a plastic flange which

also works as a barrier to block the water from entering the outer area of the RCP medium.

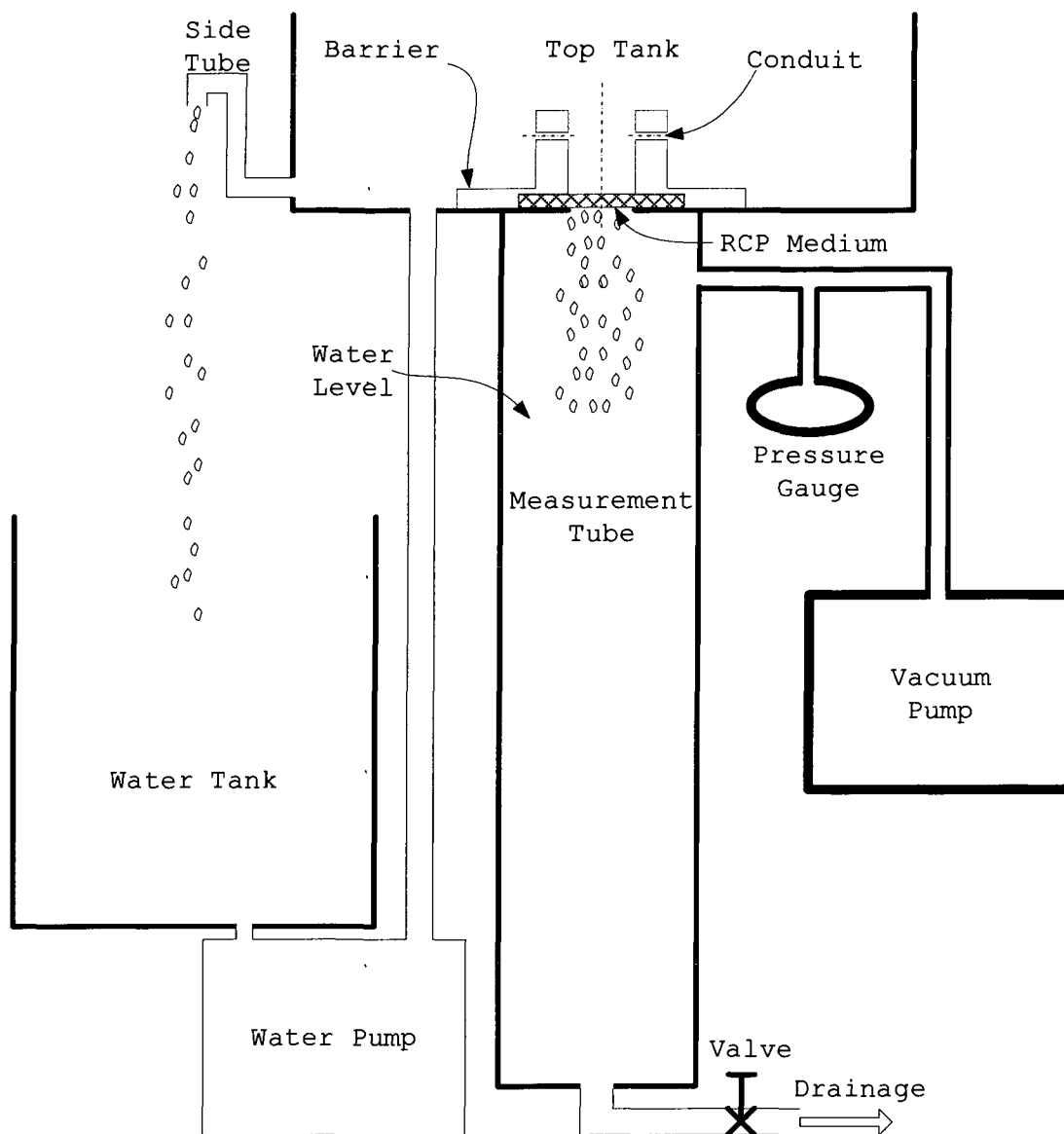


Figure 4.10 Schematic of RCP flow test cell.

The liquid used in the experiment is de-ionized water in which the suspended particles are filtered to

prevent the micropores of the RCP medium from blockage by the particles. The water in the top tank is supplied by the water pump which is connected to a prefilled water tank. A side tube can drain off the redundant water back to the water tank and maintain a constant water level about 0.15m in the top tank.

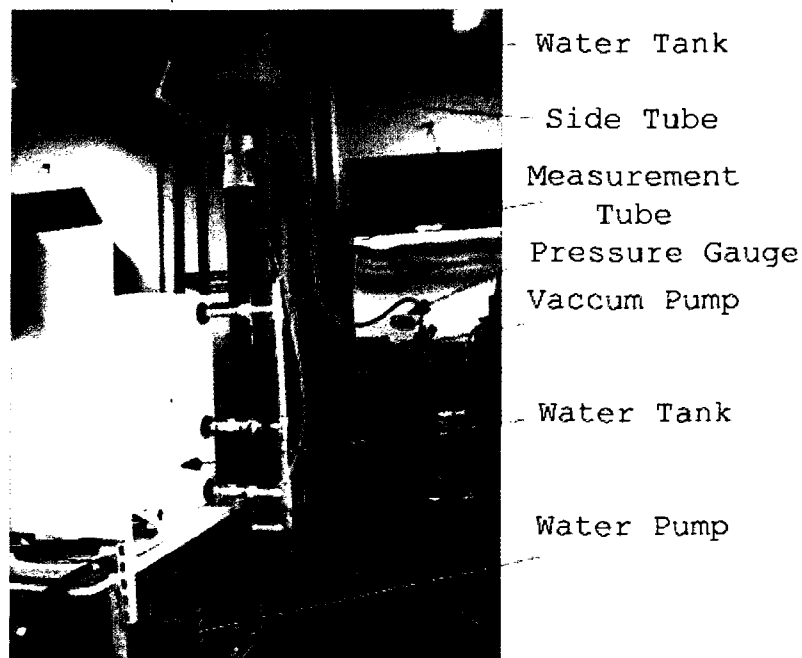


Figure 4.11 View of RCP flow test cell.

The water level in the top tank is preferably lower than the height of barrier but higher than the conduits which are small holes drilled in the plastic barrier. The conduits are the only passages of the water in the top tank to enter the cylinder space above the open area of the RCP medium, and therefore, the flow field in this

region is, to some extent, isolated from the disturbance from the water pump and can be maintained at a stable pattern. The water above the RCP medium is driven by the applied constant vacuum pressure on the measurement tube to pass through the medium.

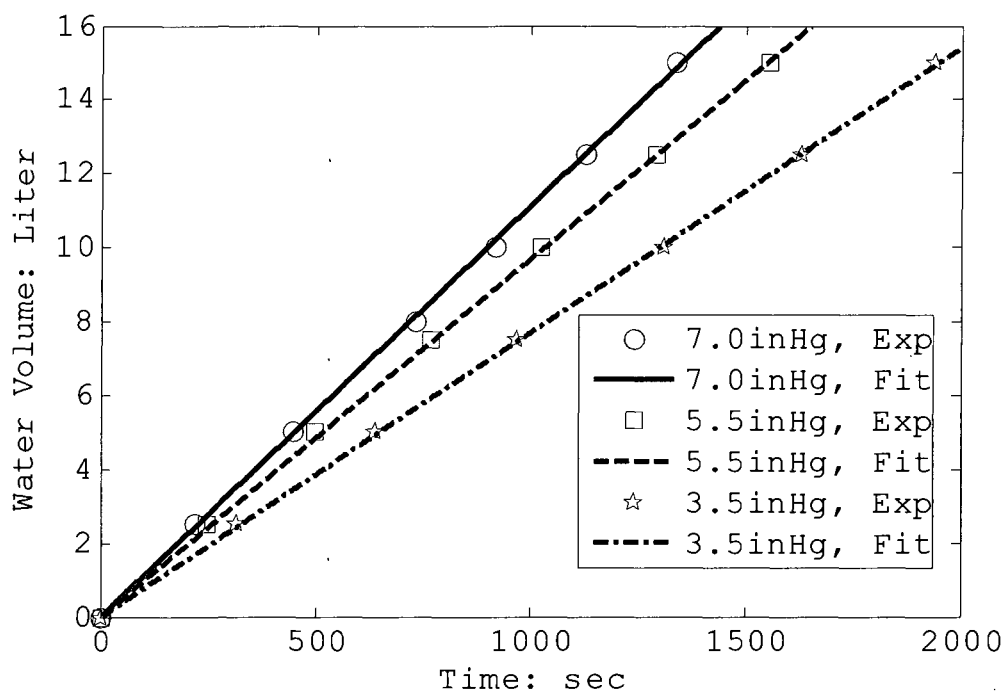


Figure 4.12 Removed water volume with respect to time under different vacuum pressure.

Figure 4.12 shows the time dependent variations of the water volume of the RCP medium removed from the top tank under three vacuum levels: 7.0inHg, 5.5inHg and 3.5inHg. The volume is calculated by multiplying the measured moving distance of water level in the

measurement tube with the cross section area of the tube with diameter of about 158.3mm. The linearity presented by the three data series continuously recorded in time implies that the sequences of the water level are measured with acceptable consistence.

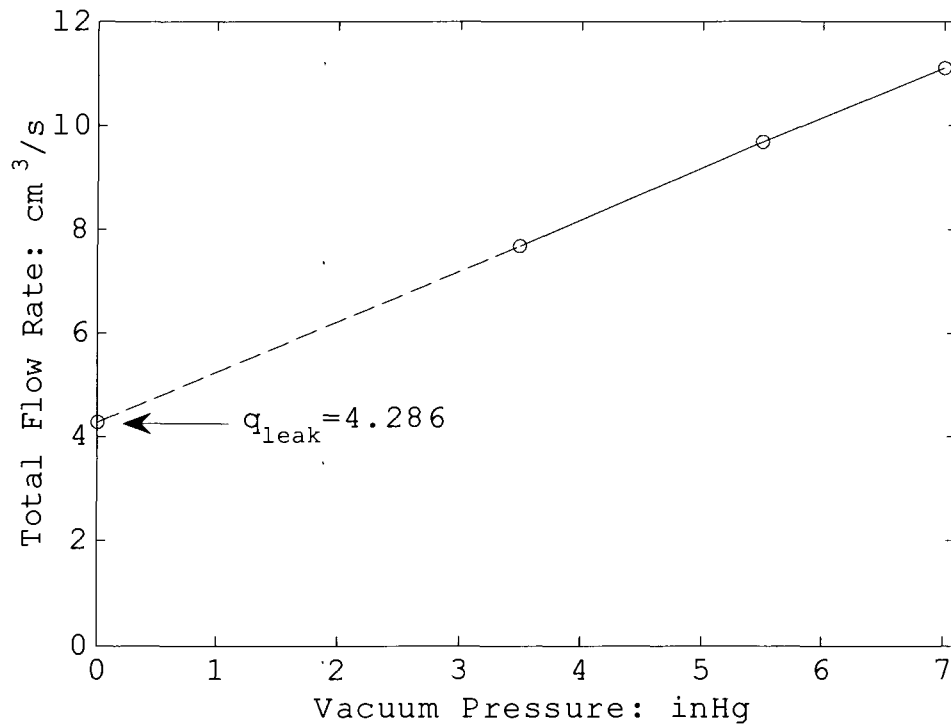


Figure 4.13 The correlation between the total flow rate and the vacuum pressure for the RCP medium with 0.1m-diameter circular open area.

The total flow rate  $q_t$  through the 0.1m-diameter circular open area can be obtained by linearly fitting the experimental data. As shown in Figure 4.13, they are

11.11, 9.67 and 7.69 cm<sup>3</sup>/s for the three vacuum pressures 7.0, 5.5 and 3.5 inHg, respectively.

A leak flow rate  $q_{leak}=4.286$  cm<sup>3</sup>/s, that may come from the lateral flow in the RCP medium or possible leakages through the gaps between the seals, is numerically obtained by linearly extrapolating the flow rate to 0inHg as shown in Figure 4.13. It should be pointed out that this moderate leak flow rate is not observed in the actual experiment when the vacuum pressure is set to zero. A possible explanation is that the capillary pressure, approximately 0.057inHg, formed by the surface tension force of the water droplet surface depending on the 1.5mm-diameter hole in the bottom layer of the RCP medium, is enough to hold the water droplet, or at least reduce the flow rate dramatically when there is no external applied suction pressure.

The net flow rate  $q$  passing the open area of the RCP medium induced by the vacuum pressure can be defined as:

$$q = q_t - q_{leak} \quad (4.14)$$

$$\overline{\Delta p} = \frac{\mu Q}{2\pi} \left[ -16 \int_{z_1}^{z_2} \frac{1}{R(z)^4} dz - \frac{16}{3} \int_{z_1}^{z_2} \frac{d^2 R(z)}{dz^2} \frac{1}{R(z)^3} dz + \frac{32}{3} \int_{z_1}^{z_2} \left( \frac{dR(z)}{dz} \right)^2 \frac{1}{R(z)^4} dz \right] \quad (4.15)$$

where  $Q$  is the flow rate of the pore. The pore flow rate  $Q_i$ , at the  $i$ -th layer, can be expressed as:

$$Q_i = \frac{400q}{\pi N_i} \quad (4.16)$$

Denoting  $H_i$  as the thickness of the  $i$ -th layer, the pressure drop in each layer can be written as:

$$\overline{\Delta p_i} = \frac{200\mu}{\pi^2 N_i} \left[ -16 \int_{h_{0i}}^{h_{0i}+H_i} \frac{1}{R(z)^4} dz - \frac{16}{3} \int_{h_{0i}}^{h_{0i}+H_i} \frac{d^2 R(z)}{dz^2} \frac{1}{R(z)^3} dz \right. \\ \left. + \frac{32}{3} \int_{h_{0i}}^{h_{0i}+H_i} \left( \frac{dR(z)}{dz} \right)^2 \frac{1}{R(z)^4} dz \right] \cdot q \quad (4.17)$$

Therefore, the linear relationship between the net flow rate passing the RCP medium and the applied vacuum pressure  $P_V$  is obtained as:

$$P_V = q \frac{200\mu}{\pi^2} \sum_{i=1}^6 \left\{ \frac{1}{N_i} \left[ 16 \int_{h_{0i}}^{h_{0i}+H_i} \frac{1}{R(z)^4} dz + \frac{16}{3} \int_{h_{0i}}^{h_{0i}+H_i} \frac{d^2 R(z)}{dz^2} \frac{1}{R(z)^3} dz \right] \right. \\ \left. - \frac{32}{3} \int_{h_{0i}}^{h_{0i}+H_i} \left( \frac{dR(z)}{dz} \right)^2 \frac{1}{R(z)^4} dz \right\} \quad (4.18)$$

Figure 4.14 shows the comparison of the experimental and theoretical correlations between the net flow rate and the vacuum pressure for the RCP medium with 0.1m-diameter circular open area. The theoretical results are obtained from the calculation of Equation (4.18) with geometry parameters described in Equations (4.1)-(4.13). Good agreement between the theoretical and experimental

results is obtained by taking the amplitude  $A=0.615$  in Equation (4.13). The validation of this cosine approximation to the real complex geometry in RCP medium will be discussed in the following sections.

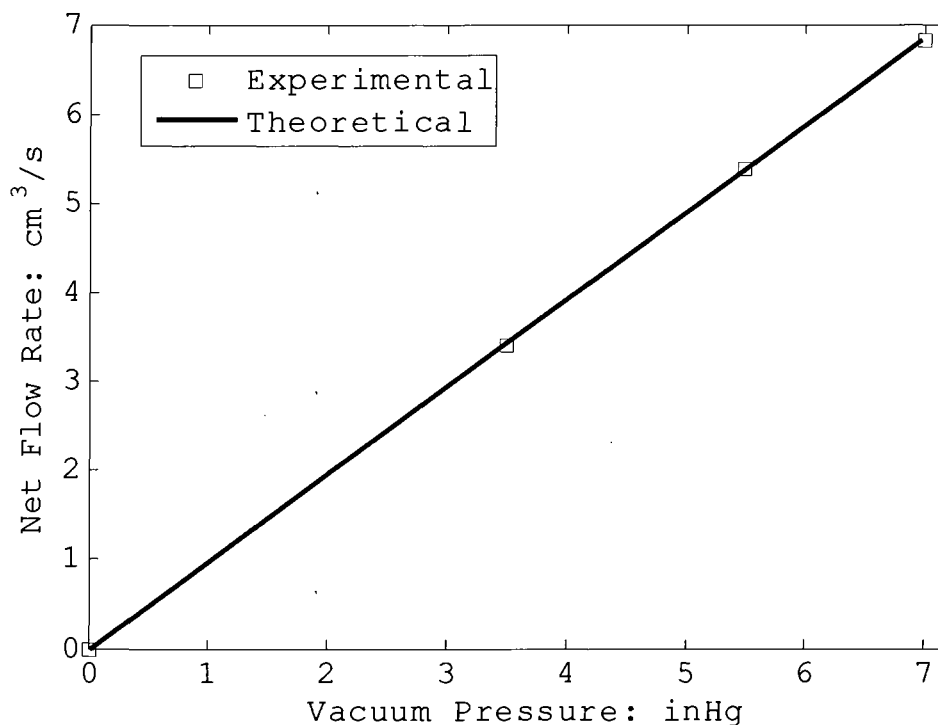


Figure 4.14 The experimental and theoretical correlations between the net flow rate and the vacuum pressure for the RCP medium with 0.1m-diameter circular open area.

#### Pilot Plant Dewatering Test of RCP Medium

The dewatering test was carried on the RCP paper machine as shown in Figure 4.3 in WMU's paper pilot plant. The purpose of this test is to investigate the correlations between the operation parameters of the RCP

roll (vacuum pressure and machine speed) and the dewatering performance. The machine speed ranges from 30 to 70 fpm and the vacuum pressure is from 0 to 11inHg. During the operation, the press roll is not loaded. Therefore, a low external press load, contributed by the tension of the press fabric belt, is maintained. Runs were done with the external cleaning shower on and off. To lower the cost, the width of the paper web, detached from the forming fabric to pass through RCP roll, is only one-thirds of the width of the RCP roll. The disadvantage of this setting is that the internal vacuum box leaks to the atmosphere through the pores of the unsealed RCP medium, and the variation of the vacuum level is up to  $\pm 0.5$ inHg.

The pulp is prepared with 80% IP soft wood and 20% Peace River hard wood with the freeness of CSF 430-480. The basis weight of the fiber ranges from 88-120 Lb/3000ft<sup>2</sup> with an average value of 110 Lb/3000ft<sup>2</sup>. High moisture content in the paper web before contacting RCP roll is maintained at 85-87%.

For each operational setting of vacuum pressure and machine speed, three samples of paper web after dewatered

by the RCP roll and one sample before contact the RCP roll were collected. The moisture/fiber ratio was obtained by measuring the total weight of the wet sample and the fiber weight after fully drying.

The measurement results of the dewatering process of the RCP medium under the different operation parameters are summarized in Table 4.2, where  $v_m$  is the machine speed, and  $P_v$  is the vacuum pressure. The moisture content in the paper web is expressed in the ratio of the weight of water with respect to the weight of the dry solid fiber. Figures 4.15-4.19 present the variations of the removal water with respect to vacuum pressure for  $v_m=30, 40, 50, 60$  and  $70$  respectively.

Table 4.2 Results of the RCP dewatering experiment.

$v_m$ (fpm)	$P_v$ (inHg)	Shower (ON/OFF)	Moisture Content (kg water/kg fiber)		
			Before RCP	After RCP	Change
30	0	OFF	5.69	3.74	1.95
30	5	OFF	5.69	3.29	2.39
30	6.5	OFF	5.82	3.38	2.44
30	8	OFF	5.66	3.18	2.48
30	10	OFF	5.95	2.88	3.07
30	0	ON	5.69	3.48	2.21
30	4	ON	5.51	3.14	2.36
30	6	ON	5.65	3.02	2.63
30	8.5	ON	5.65	2.93	2.73
30	10	ON	5.95	2.91	3.04

Table 4.2 -continued.

$V_m$ (fpm)	$P_v$ (inHg)	Shower (ON/OFF)	Moisture Content (kg water/kg fiber)		
			Before RCP	After RCP	Change
40	4	OFF	5.96	3.66	2.30
40	6	OFF	6.14	3.29	2.85
40	8	OFF	6.02	3.13	2.89
40	11	OFF	6.70	3.44	3.26
40	4	ON	6.06	3.51	2.55
40	6	ON	6.19	3.40	2.80
40	8	ON	6.09	3.35	2.74
40	11	ON	5.97	3.06	2.92
50	4	OFF	5.95	3.32	2.64
50	7.2	OFF	6.07	3.45	2.62
50	9.5	OFF	6.13	3.34	2.80
50	11	OFF	6.16	3.31	2.85
50	4	ON	5.95	3.5	2.45
50	7.2	ON	6.07	3.35	2.72
50	9.5	ON	6.13	3.21	2.92
50	11	ON	6.16	3.13	3.03
60	0	OFF	6.44	4.98	1.46
60	4	OFF	6.45	3.91	2.54
60	7	OFF	6.39	4.01	2.38
60	9.5	OFF	6.41	3.77	2.64
60	11	OFF	6.18	3.69	2.48
60	0	ON	6.44	4.60	1.84
60	4	ON	6.45	3.96	2.49
60	7	ON	6.39	3.84	2.54
60	9.5	ON	6.41	3.92	2.49
60	11	ON	6.18	3.18	3.00
70	0	OFF	6.19	4.65	1.54
70	7	OFF	6.18	4.17	2.01
70	9.5	OFF	6.57	4.33	2.24
70	0	ON	6.19	4.66	1.52
70	4	ON	6.04	4.03	2.01
70	7	ON	6.18	4.07	2.12
70	9.5	ON	6.57	4.11	2.46
70	11	ON	6.82	4.15	2.67

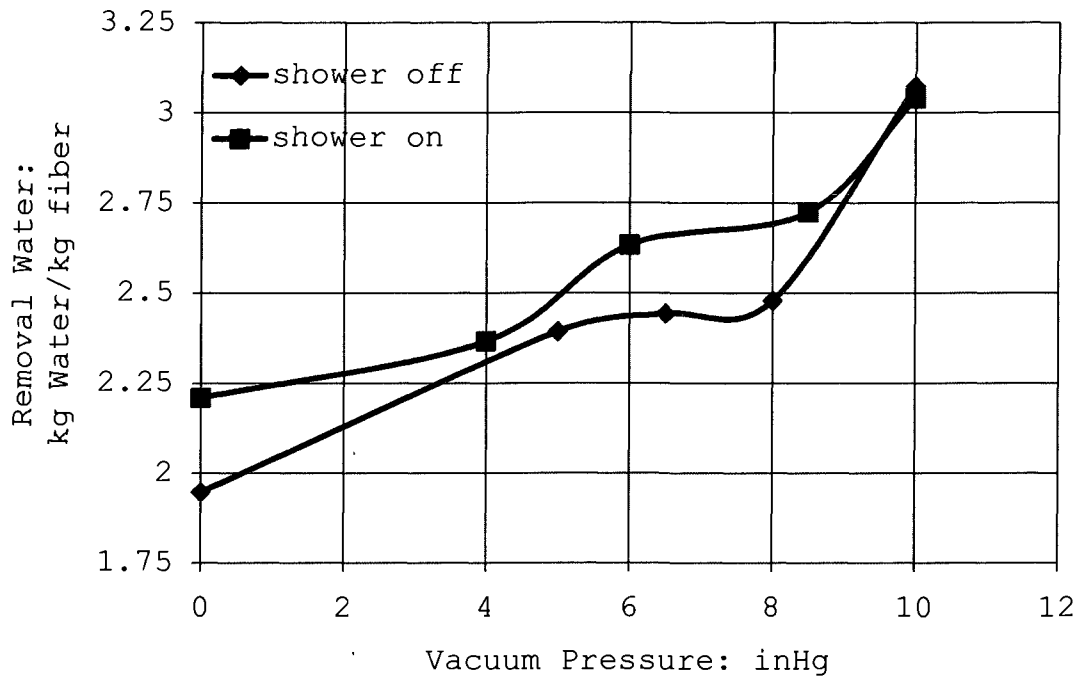


Figure 4.15 Removal water results under different vacuum pressure at machine velocity of 30fpm.

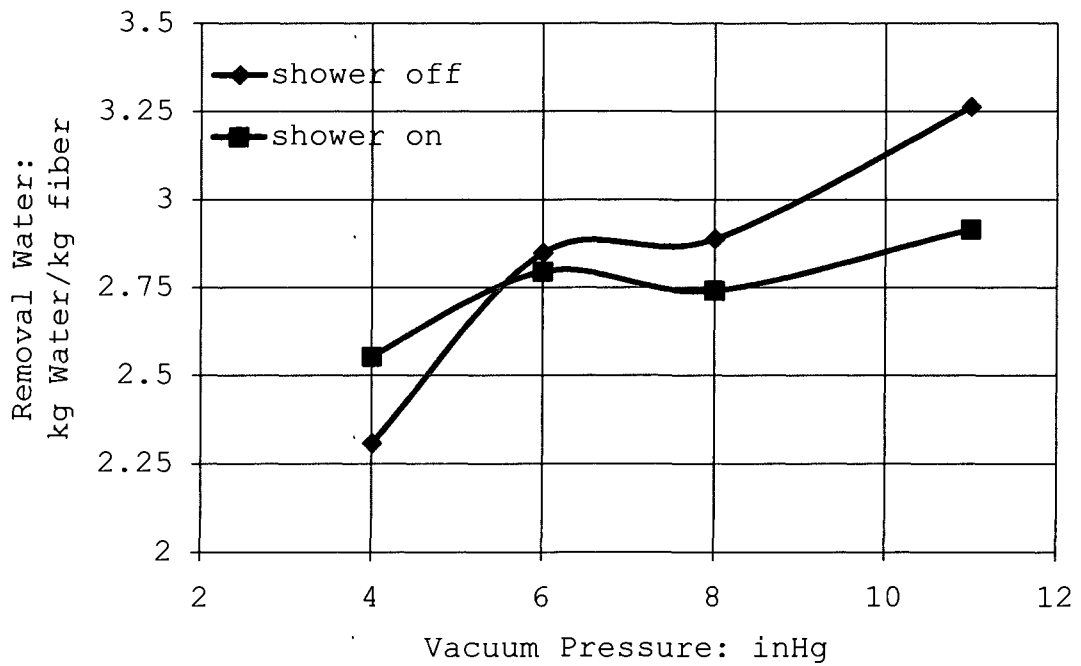


Figure 4.16 Removal water results under different vacuum pressure at machine velocity of 40fpm.

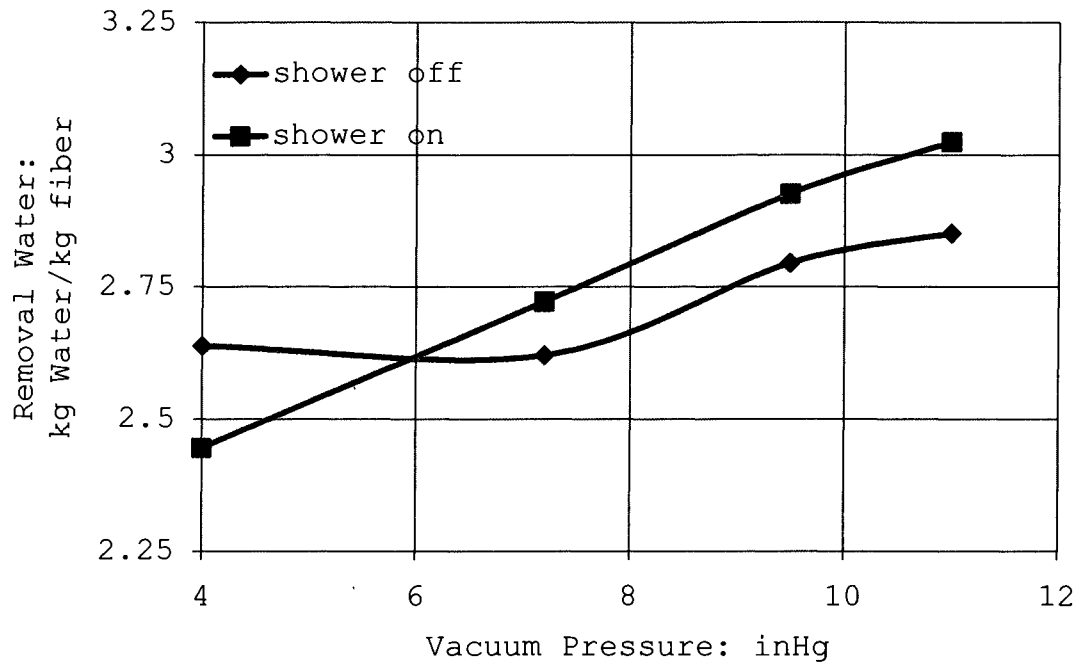


Figure 4.17 Removal water results under different vacuum pressure at machine velocity of 50fpm.

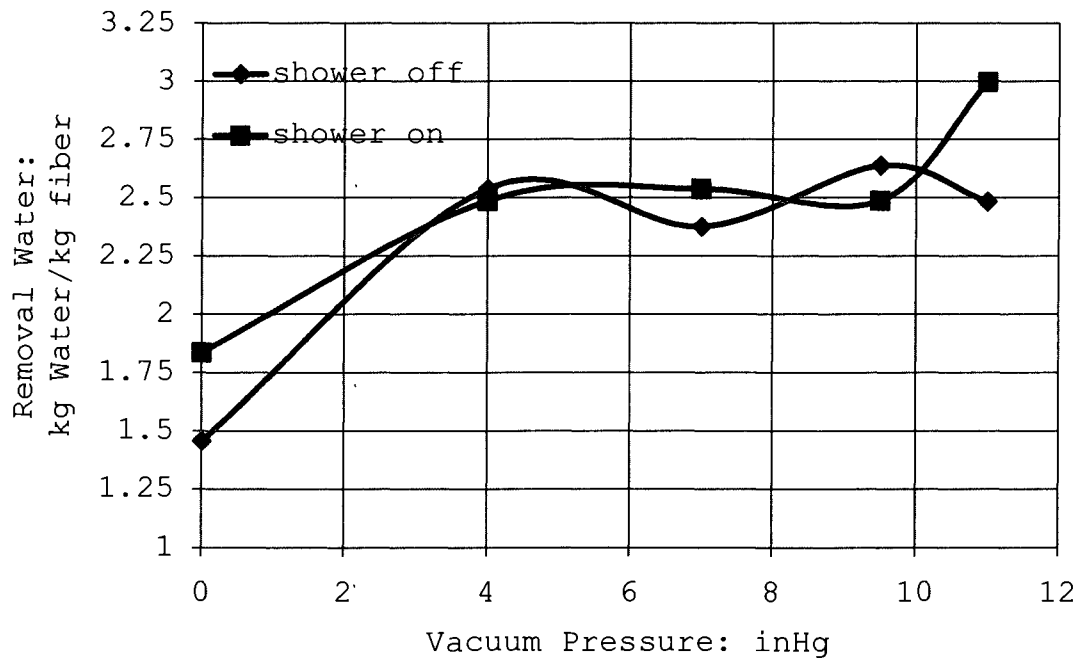


Figure 4.18 Removal water results under different vacuum pressure at machine velocity of 60fpm.

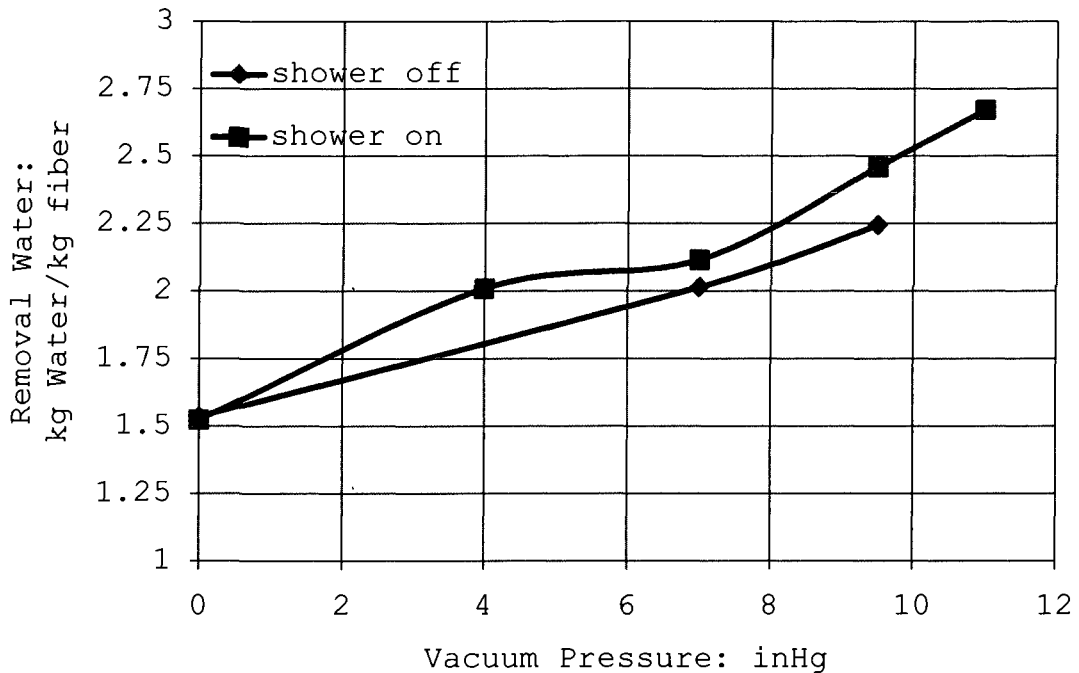


Figure 4.19 Removal water results under different vacuum pressure at machine velocity of 70fpm.

The results generally show that approximately 1.5-3 kg water per kg fiber can be removed through the RCP medium, and the removal water ratio is increased with the increase of the vacuum pressure. The status of the shower (ON or OFF), which is used to clean the RCP top surface and prewet the pores of the first layer, has a minor effect on the water removal rate, but there is no clear and consistent relation indicated from the observations. When the shower is on, the water removal rate is higher for  $v_m=30$ , 50 and 70 fpm, lower for  $v_m=40$  fpm and at the same level for  $v_m=60$ .

The available data of removal water at zero vacuum level for the machine speed of 30, 60 and 70 fpm as shown in Figures 4.15, 4.18 and 4.19 imply that the press load due to the tension of the press fabric belt can squeeze out about 1.5-2.0 kg water per kg solid fibers although the press roll is unloaded in our experiment. In the traditional press dewatering method, the water is squeezed by applying an external press force through the press roll. When the RCP roll with a multilayer porous medium on the roll surface and an internal vacuum suction box is used, the additional water about 1-1.5 kg water per kg solid fibers can be removed as shown in Figures 4.15-4.19. The detailed analysis of the RCP dewatering is provided in the next section.

### **4.3 Theoretical Studies of Capillary Flow in Multi-Layer Porous Media**

#### Derivation of the Governing Equation

The analysis approach proposed in chapter 3 can be extended to develop a model for describing the dewatering process in RCP porous medium in the paper making industry. The RCP porous media could include 5-6 layers with different porous properties, such as pore size, pore

shape and permeability. In the paper machine, the fiber matrix in the paper web, contacting the top surface of the RCP medium, can also be considered as a porous medium. After the free water is partly removed in the forming section of the paper machine, the remaining water in wet pulps can be classified as the intra-wall water and the inter-wall water [Ahrens and Xu 1999]. The intra-wall water is the water trapped in the nanoscale pores in the cell wall of the fibers, while the inter-wall water indicates the water between the fibers and in the lumen. The inter-wall water is held by the capillary force and can be removed partly in the press section.

Figure 4.20 shows a sketch of the multi-layer porous medium composed of the RCP medium and the medium formed by the pulp fibers, where  $H_0$  is the thickness of the fiber medium and  $H_i$  ( $i=1,2,3,4,5,6$ ) represents the thickness of the  $i$ -th layer of the RCP medium,  $P_v$  is the vacuum suction pressure,  $g$  is the gravitational acceleration and  $g_c$  is the centrifugal body force which is related to the machine speed  $v_m$ :

$$g_c = \frac{v_m^2}{R_d} \quad (4.19)$$

Here,  $R_d$  is the radius with respect to the rotating center and may vary with the moving the water bulk. Since the thickness of the total medium is as thin as 2-3mm,  $R_d$  can take the constant value, 0.203m, the radius of the RCP roll.  $\alpha$  is the angle between the flow direction and the horizontal direction in the lab reference of frame, which is related to the machine speed  $v_m$  and the time  $t$ :

$$\alpha = \frac{v_m}{R_d} \cdot t \quad (4.20)$$

The individual pore within each layer formed by the pulp fiber or the metal fiber in RCP medium can be considered as a circular capillary tube with varying radius which can be approximated by cosine function. The pores are distributed homogeneously on cross sectional plane within each layer.

As indicated in Figure 4.20, there are two types of capillary interfaces: the advancing interface facing inwardly in the RCP medium and the receding interface facing outwardly in the pulp fiber medium.  $h_a$  and  $h_r$  represent the distances of the advancing and receding interfaces with respect to the top surface of the paper web. According to the mass conservation law, the velocities of the two interfaces can be related as:

$$N_a R_a^2 \frac{dh_a}{dt} = N_r R_r^2 \frac{dh_r}{dt} \quad (4.21)$$

where  $N_a$  is the pore number per unit area within the layer where the advancing interface is located and  $N_r$  is for the receding interface.

The contact angles  $\theta_a$  and  $\theta_r$  of the two interfaces are written as:

$$\theta_a = \theta_s - \frac{\zeta}{\gamma} \frac{dh_a}{dt} + \tan^{-1} (dR_a / dz) \quad (4.22)$$

$$\theta_r = \theta_s - \tan^{-1} (dR_r / dz) \quad (4.23)$$

where  $z$  is along the flow direction and with respect to the top surface of the pulp fiber medium,  $\theta_s$  is the static contact angle and is close to zero for water.  $R_a$  and  $R_r$  are the pore radii at the advancing and receding interfaces.  $\gamma$  is the surface tension and  $\zeta$  is the parameter of the dynamic contact angle effect and is suggested to take the value of 0.2 for water in prewetted cases [Hamraoui et al. 2000]. For the receding interface driven by the vacuum pressure  $P_v$ , the dynamic contact angle effect is ignored.

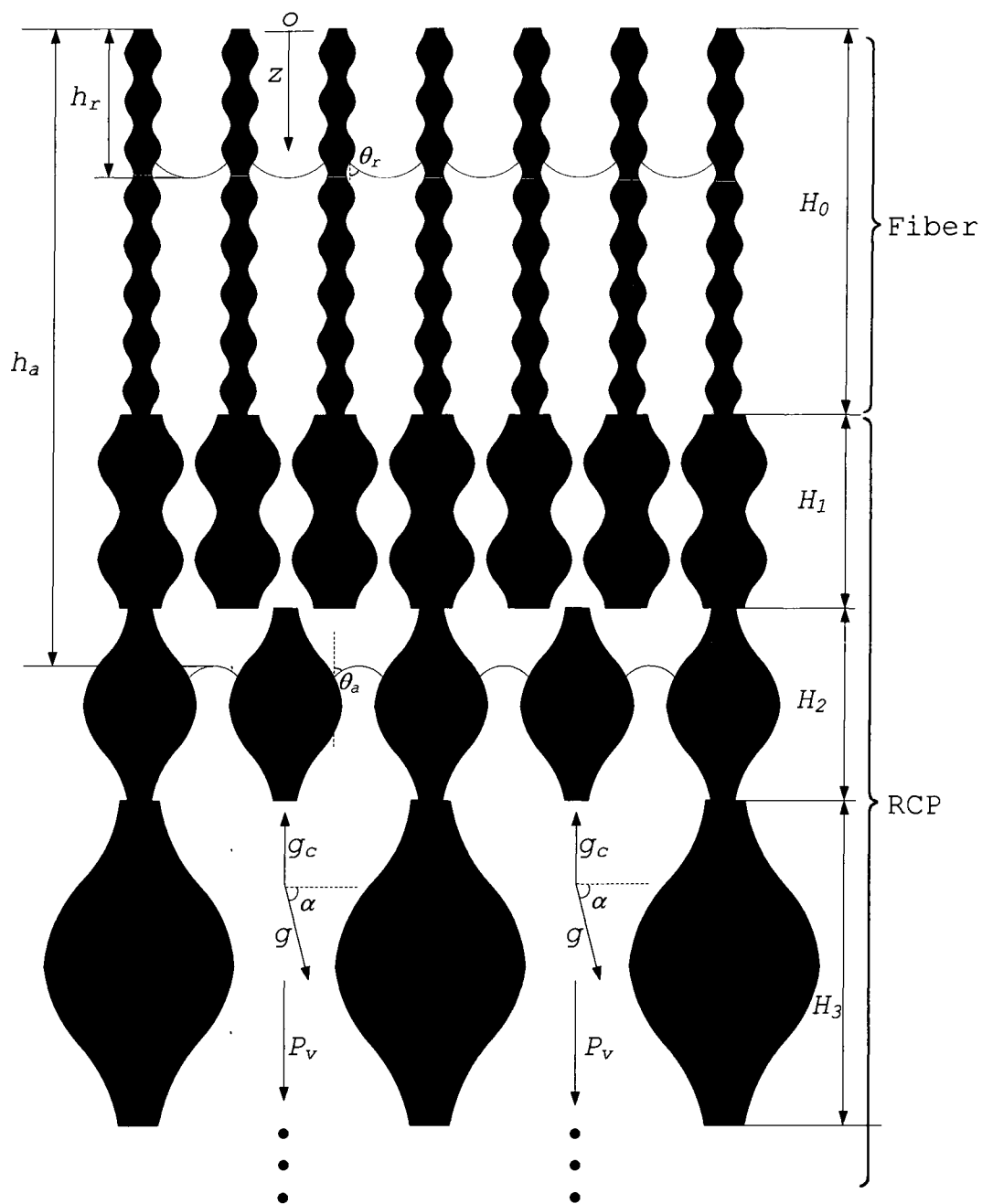


Figure 4.20 Schematic of multi-layer porous media.

Based on the law of mass conservation, the velocity distribution for the capillary flow in multi-layer porous media can be obtained by adding the area density of pore number into the velocity expressions, Equations (3.57) and (3.58) obtained by asymptotic series analysis in chapter 3, in the forms of:

$$v_z = 2 \frac{dh_a}{dt} \frac{N_a R^2(h)}{N_i R^2(z)} (1 - \eta^2) \quad (4.24)$$

$$+ \frac{1}{3} \frac{N_a}{N_i} \frac{dh_a}{dt} \left[ 5 \frac{R^2(h_a)}{R^2(z)} \left( \frac{dR(z)}{dz} \right)^2 - \frac{R^2(h_a)}{R(z)} \frac{d^2 R(z)}{dz^2} \right] (3\eta^4 - 4\eta^2 + 1)$$

$$v_r = 2 \frac{dh_a}{dt} \frac{N_a}{N_i} \frac{R^2(h_a)}{R^2(z)} \frac{dR(z)}{dz} (\eta - \eta^3) \quad (4.25)$$

$$+ \frac{N_a}{N_i} \left[ \begin{aligned} & \frac{5}{3} \frac{dh}{dt} \frac{R^2(h_a)}{R^2(z)} \left( \frac{dR(z)}{dz} \right)^3 (3\eta^5 - 4\eta^3 + \eta) \\ & - \frac{1}{6} \frac{dh}{dt} \frac{R^2(h_a)}{R(z)} \frac{dR(z)}{dz} \frac{d^2 R(z)}{dz^2} (15\eta^5 - 26\eta^3 + 11\eta) \\ & + \frac{dh}{dt} \frac{R^2(h_a)}{6} \frac{d^3 R(z)}{dz^3} (\eta^5 - 2\eta^3 + \eta) \end{aligned} \right]$$

Following the derivation in the section 3.2 of chapter 3, the governing equation for the capillary flow in the multi-layer porous media is obtained as:

$$\begin{aligned}
& \rho c_0 R^2(h_a) \frac{d^2 h_a}{dt^2} + \rho c_0 \frac{R^2(h_a)}{h_a - h_i} \left( \frac{dh_a}{dt} \right)^2 + 2\rho c_0 R(h_a) \frac{dR(h_a)}{dh_a} \left( \frac{dh_a}{dt} \right)^2 \quad (4.26) \\
& = P_v + \frac{2\gamma \cos \theta_a}{R(h_a)} - \frac{2\gamma \cos \theta_r}{R(h_r)} + \rho (h_a - h_r) \cdot \left( g \sin \alpha - \frac{v_m^2}{R_d^2} \right) \\
& - 8\mu c_1 \frac{dh_a}{dt} R^2(h_a) - 8\mu c_2 \frac{dh_a}{dt} R^2(h_a) \\
& + \frac{8\rho}{3} \omega c_3 \left( \frac{dh_a}{dt} \right)^2 R^4(h_a) + \frac{8}{3} \mu c_4 \frac{dh_a}{dt} R^2(h_a)
\end{aligned}$$

where,

$$c_0 = \int_{h_r}^{h_a} \frac{N_a}{N_i} \frac{1}{R^2(z)} dz \quad (4.27)$$

$$c_1 = \int_{h_r}^{h_a} \frac{N_a}{N_i} \frac{1}{R^4(z)} dz \quad (4.28)$$

$$c_2 = \int_{h_r}^{h_a} \frac{N_M}{N_i} \frac{1}{R^4(z)} \left( \frac{dR(z)}{dz} \right)^2 dz \quad (4.29)$$

$$c_3 = \int_{h_r}^{h_a} \left( \frac{N_M}{N_i} \right)^2 \frac{1}{R^5(z)} \frac{dR(z)}{dz} dz \quad (4.30)$$

$$c_4 = \int_{h_r}^{h_a} \frac{N_M}{N_i} \frac{1}{R^4(z)} \left[ \begin{aligned} & 5 \left( \frac{dR(z)}{dz} \right)^4 - R(z) \left( \frac{dR(z)}{dz} \right)^2 \frac{d^2 R(z)}{dz^2} \\ & - R(z) \frac{d^2 R(z)}{dz^2} + 5 \left( \frac{dR(z)}{dz} \right)^2 \end{aligned} \right] dz \quad (4.31)$$

If we use the zero-th order velocity expressions, i.e. ignoring the second part in Equations (4.24) and (4.25), and neglect the inertial terms, the first-order governing equation can be obtained as:

$$\begin{aligned}
& \left[ 8\mu c_1 R^2(h_a) + 8\mu c_2 R^2(h_r) \right] \frac{dh_a}{dt} \\
& = P_v + \frac{2\gamma \cos \theta_a}{R(h_a)} - \frac{2\gamma \cos \theta_r}{R(h_r)} + \rho (h_a - h_r) \cdot \left( g \sin \alpha - \frac{v_m^2}{R_d^2} \right)
\end{aligned} \tag{4.32}$$

Once the geometry of each layer is given, Equations (4.26) and (4.32) can be numerically solved by using the adaptive Runge-kutta method as described in chapter 2 to obtain the relations of  $h_a$  versus  $t$  and  $h_r$  versus  $t$ . The geometrical relations of the six layers of the RCP medium are summarized in Table 4.1 and Equations (4.1)-(4.13). For the pore geometry in the fiber medium, let's denote the  $D_f$  as the diameter of the fiber and  $R_f$  as the characteristic radius of the pore. The variation of the local pore radius can be approximated by the cosine function as in Equation (4.13):

$$R(z) = \left( R_f + \frac{D_f}{4} \right) \left[ 1 + \frac{D_f}{4R_f + D_f} \cos \left( \frac{2\pi z}{D_f} \right) \right] \tag{4.33}$$

Within the time when the pulp fibers pass the RCP roll, the volume of the removed water can be obtained through the volume integration along the penetration path of the receding interface.

## Results and Discussion

The simulation results of the liquid flow passing the multi-layer medium are given as follows. According to the reported observation by Fiber Quality Analyzer (FQA) [Park et al. 2006], the diameter of the softwood pulp fiber,  $D_f$ , has an average value of  $30.0\mu\text{m}$ . The measurement thickness of the wet pulp fiber sheet passing the RCP roll is ranging from  $0.6\text{--}1.0\text{mm}$ , hence,  $H_0$  is assumed to be the median value  $0.8\text{mm}$  in the simulation. We assume that the pores in the pulp fiber sheet are fully occupied by water to be removed and the first layer of the RCP medium is partly wetted in the length of one-fourth of the thickness of the first layer.  $h_0=H_0+0.25H_1$  is denoted as the initial wet length. Then, the penetration lengths of the receding interface and the advancing interface are set to be  $h_r=0$  and  $h_a= h_0$ .

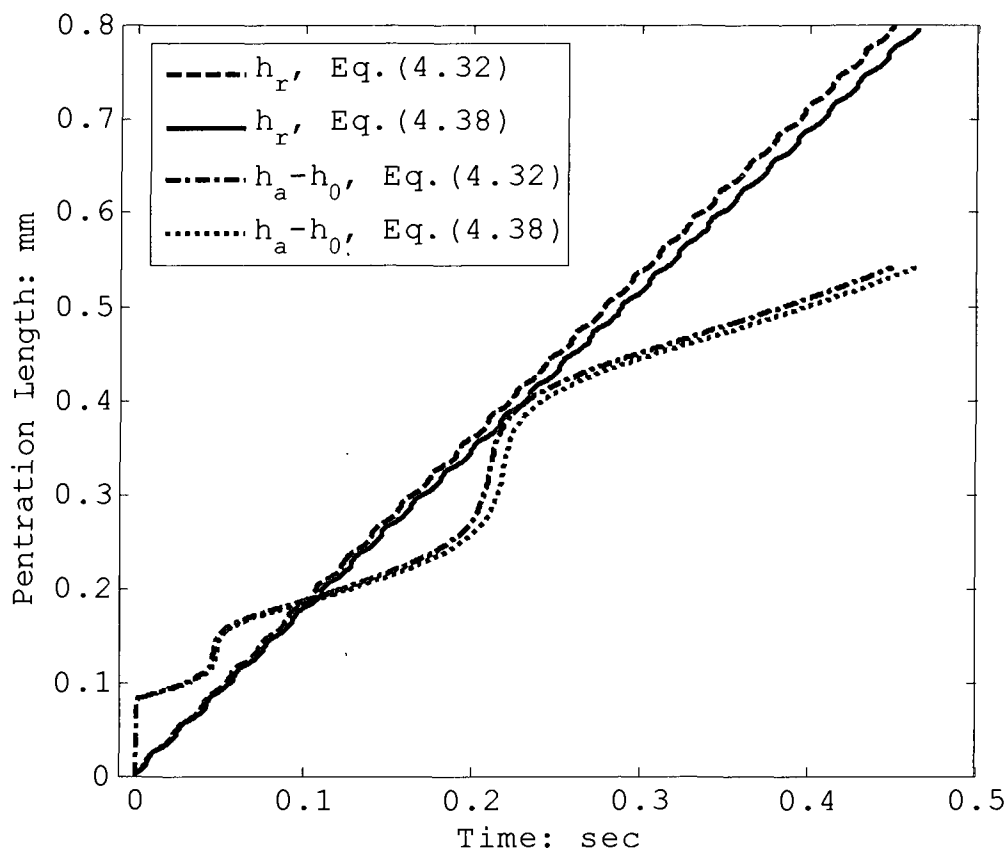


Figure 4.21 The comparison of the penetration length results for  $P_v=6$  inHg,  $v_m=70$  fpm and  $R_f=10$   $\mu\text{m}$ .

Figure 4.21 shows the comparison of the liquid penetration results obtained from Equation (4.26) and (4.32) for a typical case of  $P_v=6$  inHg,  $v_m=70$  fpm and  $R_f=10$   $\mu\text{m}$ . The penetration length of the advancing interface is expressed by  $h_a-h_0$ . The time for the receding interface to pass through the thickness of the fiber sheet is 0.45s predicted by Equation (4.26) and 0.464s by Equation (4.32). There is an error of about 3%

overestimation of the time to drainage 100% water in the fiber pores for the first order governing Equation (4.32). However, the computing time consumed by Equation (4.26) is about 70 times longer than that of Equation (4.32). For faster computing, Equation (4.32) is used in the following simulations.

Figure 4.22 presents the effect of the vacuum pressure on the liquid penetration length in the porous medium. The advancing interface for  $P_v=2$  inHg stops at the interface of the first and the second layers after it penetrates the first layer as fast as the other cases. The receding interface penetrates 8  $\mu\text{m}$  and only 1% of the water in the pore is removed. For  $P_v=6$  and 10 inHg, the receding interface penetrates the 0.8mm fiber medium and 100% of the water in the 10  $\mu\text{m}$  pores can be removed in 0.464 and 0.24 second, respectively, while the corresponding advancing interface enters the fourth layer of the RCP medium. To assure that 100% of the water in the pore can be removed, a critical value of the machine speed can be obtained by equating the time of the receding interface passing the paper web with the time of the paper web on the RCP roll passing the 165<sup>0</sup> sectional

vacuum chamber. For instance, the critical values of the machine speed for the 10  $\mu\text{m}$  pores are 248 fpm for  $P_v=6$  and 479 fpm for 10 inHg. If the machine speed is faster than the critical speed, less than 100% of the water can be removed.

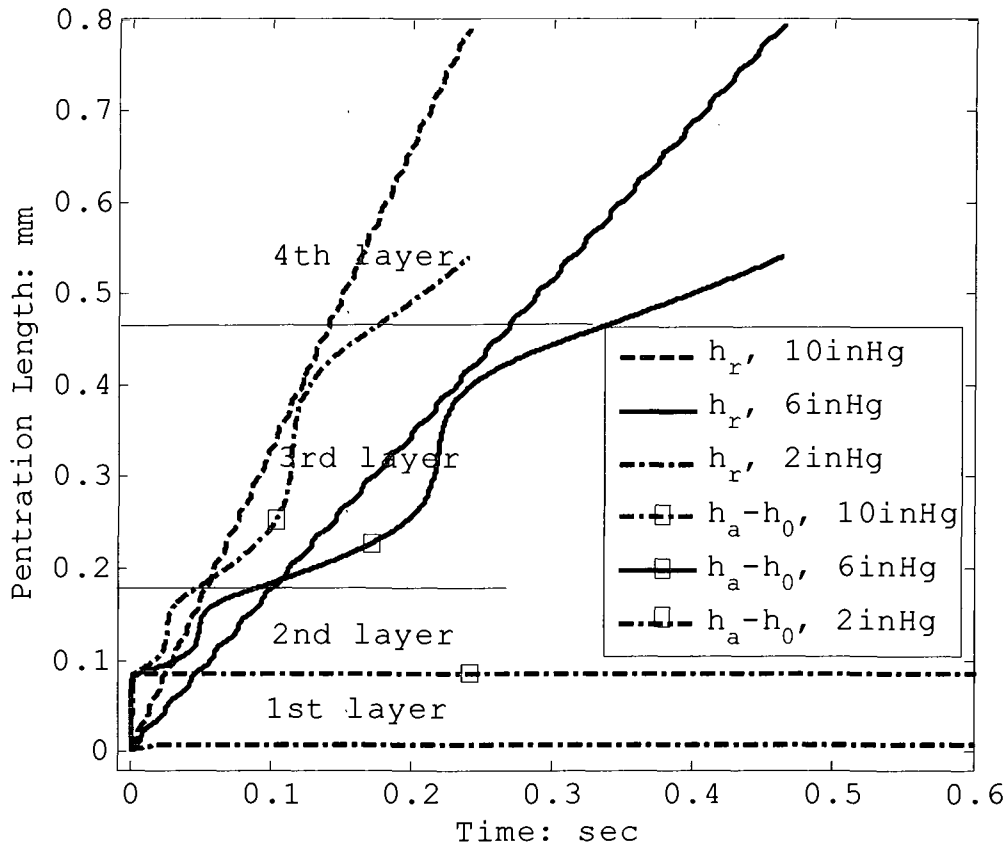


Figure 4.22 The simulated penetration length results under different vacuum pressure for  $v_m=70\text{fpm}$  and  $R_f=10\mu\text{m}$ .

Figure 4.23 presents the effect of pulp fiber pore size on the liquid penetration length in the multi-layer porous medium. The vacuum pressure is maintained at  $P_v = 10$  inHg and the machine speed  $v_m = 70$  fpm. For  $R_f = 10$  and  $20 \mu\text{m}$ , the receding interface penetrates the 0.8mm fiber medium, removing all the water in the pore in 0.24 and 0.269 second, respectively, while the corresponding advancing interface penetrates 0.54 and 0.635 mm located at the fourth layer of the RCP medium. However, the advancing interface for the smaller pore size  $R_f = 4.2 \mu\text{m}$  passes through the first and the second layer and stops somewhere in the third layer. The receding interface penetrates  $0.285 \mu\text{m}$  and about 35.8% of the water in the pore is removed.

Figure 4.23 implies that there is a critical value of the fiber pore size, denoted by  $R_{cr}$ , for each given vacuum pressure. When the pore size is larger than  $R_{cr}$ , it is possible to remove 100% of the water in the pore. When the pore size is smaller than  $R_{cr}$ , the liquid will be driven into an equilibrium state where the vacuum pressure together with the capillary pressure of the advancing interface is counteracted by the capillary

pressure of the receding interface in the small fiber pore, therefore, the water can be only partly removed. The critical pore size  $R_{cr}$  under different vacuum pressures can be obtained through a series of numerical trials and are summarized in Table 4.3.

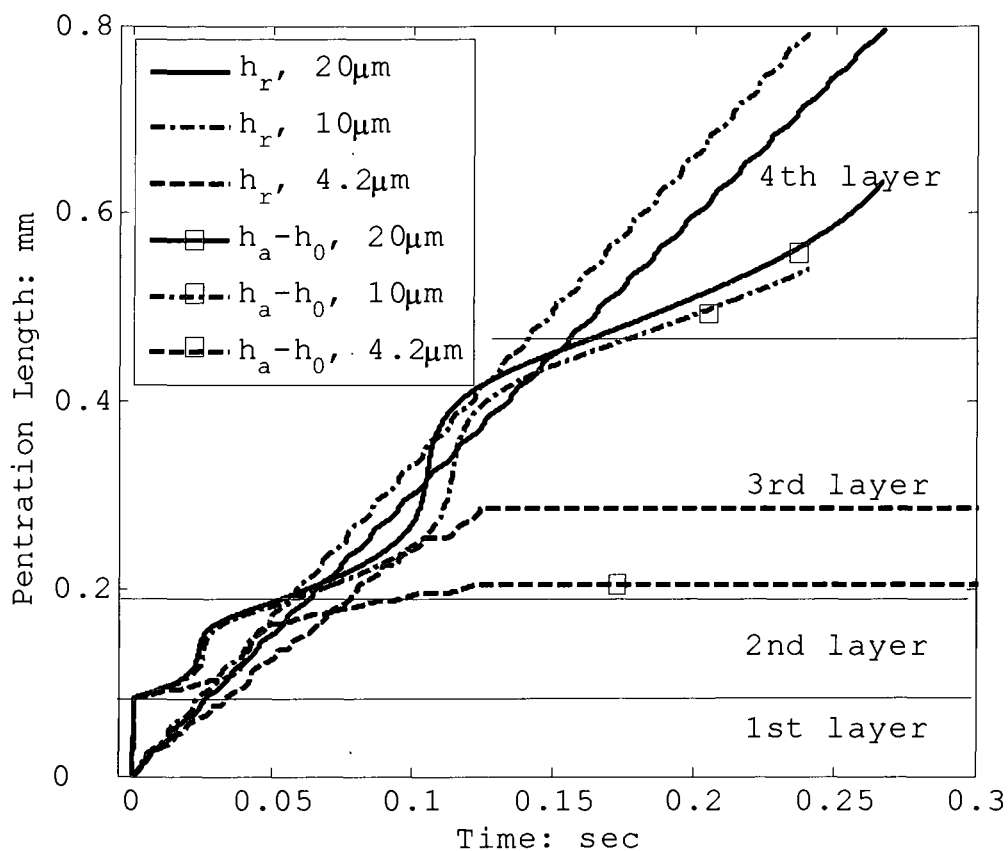


Figure 4.23 The simulated penetration length results for different pulp pore size with  $v_m=70$  fpm and  $P_v=10$  inHg.

Table 4.3 The critical pulp pore size under different vacuum pressure.

$P_v$ (inHg)	2	4	6	8	10
$R_{cr}$ ( $\mu\text{m}$ )	20.81	10.49	7.01	5.27	4.21

According to the experimental observations by the dynamic spiral magnetic resonance imaging, Takahashi et al. (1997) suggested that the actual pore size distribution in the softwood pulp fibers may be approximated by a Gaussian distribution with a mean radius of 4.3  $\mu\text{m}$  and a standard deviation 3  $\mu\text{m}$ . In fact, the radius of the pore can't be a negative value. Therefore, it is more reasonable to describe the pulp pore size distribution by the Weibull distribution. The probability density function of a Weibull random variable, denoted by the pore radius  $R_f$  in the unit of micron, is defined as:

$$P_w(R_f, k_w, \lambda_w) = \begin{cases} \frac{k_w}{\lambda_w} \left( \frac{4.3 \cdot R_f}{\lambda_w E_w} \right)^{k_w-1} e^{-\left(\frac{k_w}{\lambda_w}\right)^{k_w}}, & R_f \geq 0 \\ 0, & R_f < 0 \end{cases} \quad (4.34)$$

where  $k_w > 0$  is the shape parameter and  $\lambda_w$  is the scale parameter of the distribution.  $E_w$  is a mean parameter determined by  $k_w$  and  $\lambda_w$  in the following relation:

$$E_w = \lambda_w \cdot \int_0^{\infty} \xi^{\frac{1}{k_w}} \cdot e^{-\xi} d\xi \quad (4.35)$$

The mean value of  $R_f$  with a Weibull distribution in Equation (4.34) is 4.3  $\mu\text{m}$ .

Figure 4.24 shows the comparison of the Weibull Gaussian distributions of the pore size in the paper web. The pore size is represented by the pore radius  $R_f$ . The Gaussian distribution is calculated with the mean value of 4.3  $\mu\text{m}$  and the standard deviation of 3  $\mu\text{m}$ , while the Weibull distribution is calculated with  $k_w=1.05$  and  $\lambda_w=5$ .

For the given parameters, both the two distributions have the same mean value 4.3  $\mu\text{m}$ . The probability of the small pore size (0.015 ~ 2.6 $\mu\text{m}$ ), and the large pore size (>10.19  $\mu\text{m}$ ) predicted by the Weibull distribution is slightly higher than that by the Gaussian distribution. The probability of the pore size to be larger than 15  $\mu\text{m}$  is 0.02% for the Gaussian distribution and 2.3% for the Weibull distribution. The probability of the pore size to be an irrational negative is up to 7.6% predicted by the Gaussian distribution, but zero by the Weibull distribution.

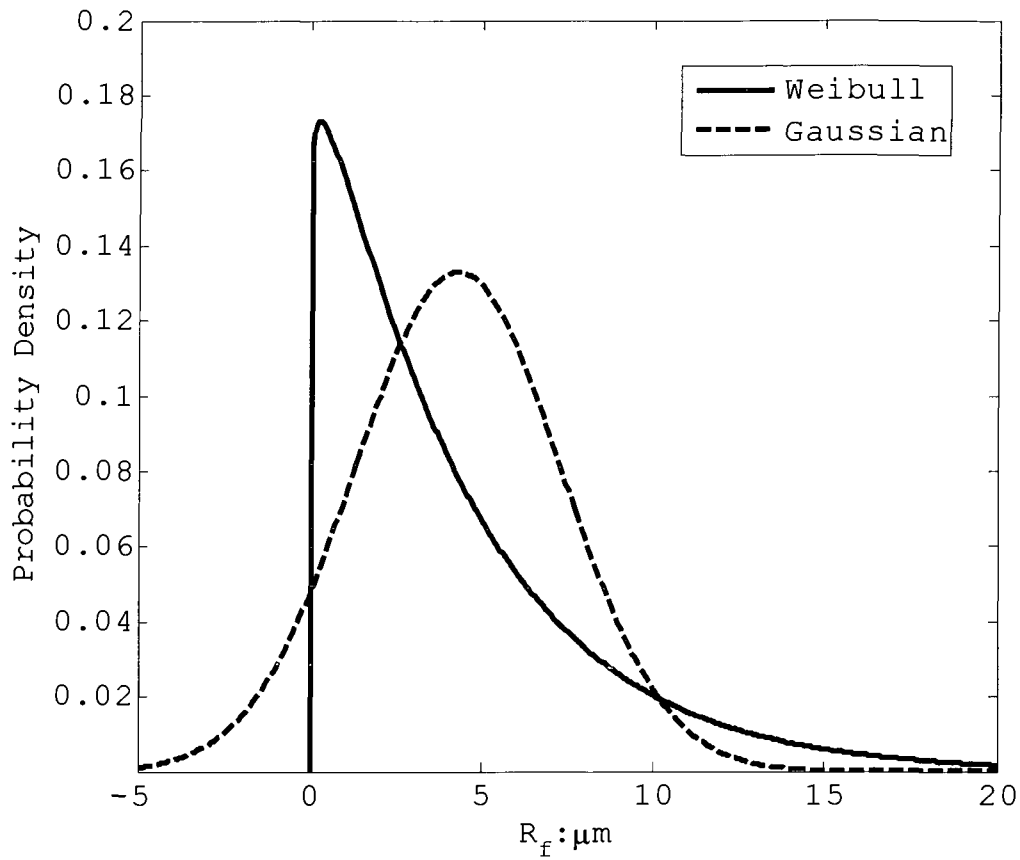


Figure 4.24 Comparison of the Weibull and Gaussian distribution of the pore size in paper web.

The penetration length  $h_r$  of the receding interface during the period of the pulp fiber contacting with the RCP roll surface can be obtained by numerical solving Equation (4.26) or Equation (4.32). Obviously,  $h_r$  is dependent on the vacuum pressure  $P_v$ , the machine speed  $v_m$  and the fiber pore size  $R_f$  besides the geometry of RCP medium, the fluid parameters, the solid-liquid surface

properties and the material properties. The moisture ratio  $\Delta MR$  (kg water/kg fiber) due to the RCP dewatering process can be approximated by:

$$\Delta MR = \frac{\rho \cdot \int_0^{R_f \max} V_{pore}(R_f, h_r) \cdot P_w(R_f, k_w, \lambda_w) dR_f}{BW \cdot \int_0^{R_f \max} A_{total}(R_f, H_0) \cdot P_w(R_f, k_w, \lambda_w) dR_f} \quad (4.36)$$

where  $BW$  is basis weight of the dry solid fiber,  $V_{pore}$  is the void volume in the pore which is previously occupied by the removed water and can be calculated as:

$$V_{pore} = \pi \left( R_f + \frac{D_f}{4} \right)^2 \int_0^{h_r} \left[ 1 + \frac{D_f}{4R_f + D_f} \cos \left( \frac{2\pi z}{D_f} \right) \right]^2 dz \quad (4.37)$$

and  $A_{total}$  represents the total area of the cross section of the pore and the solid fibers that form the pore, which can be approximated by:

$$A_{total} = (2R_f + D_f)^2 \quad (4.38)$$

A typical curve of the variation of the removal water under different vacuum pressure predicted by the above analytical model is given in Figure 4.25. In the calculation,  $BW=110$  Lb/3000 ft<sup>2</sup>, which is the average basis weight of the test samples of the paper web, the pore size distributions is described using Equation (4.34) with  $k_w=1.05$  and  $\lambda_w=5$ . For the slow machine speed from 30 to 70 fpm, the numerical results are not

sensitive to the variation of the machine speed.  $v_m=70$  fpm is used in the calculation in Figure 4.25.

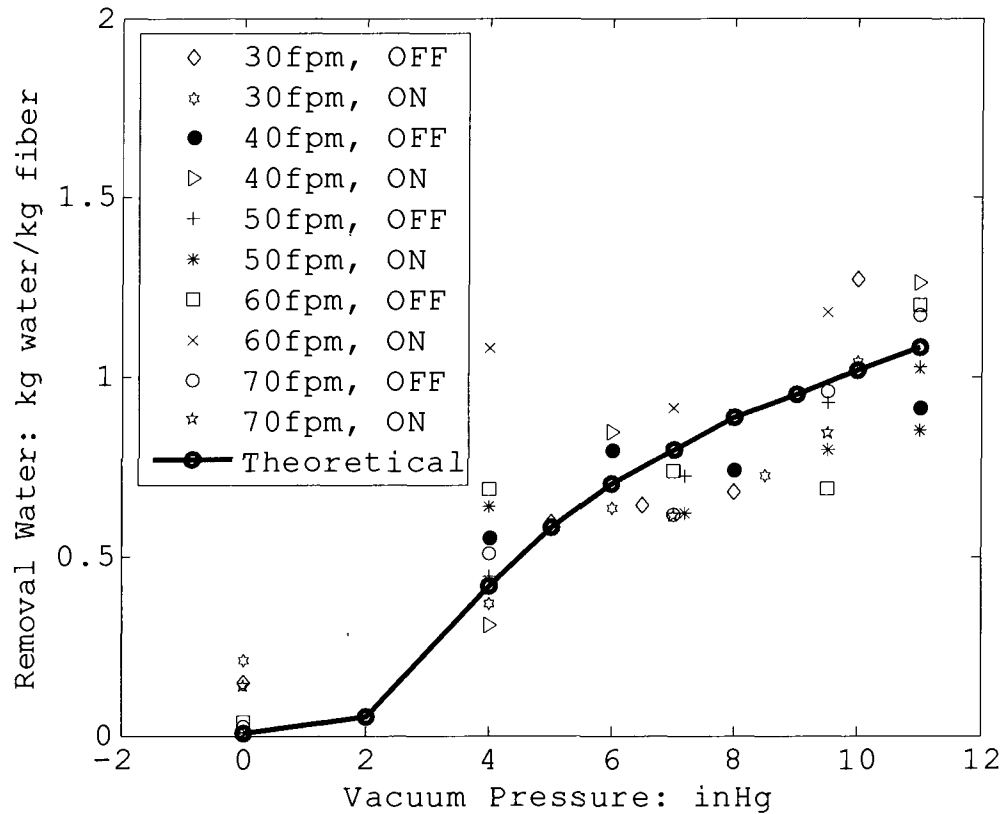


Figure 4.25 Comparison of the theoretical and experiment results of the removal water under different vacuum pressure.

For comparison, the experimental results for  $v_m=30$ , 40, 50, 60 and 70 fpm described in section 4.2 are also presented in Figure 4.24 in which "ON/OFF" means the shower to clean and prewet the RCP surface is on or off. The prewetting effect is considered in the analytical solution in Figure 4.25 by setting a prewetted length of

$H_1/4$  in the initial state. The curve without prewetted length is not shown in Figure 4.25 because it is difficult to differentiate from the prewetted curve.

To focus on the variation of the removal water due to the increase of the applied vacuum pressure underneath the RCP medium, the presented data in Figure 4.25 are obtained by subtracting the amount of the water removed by the compression of the press fabric belt, about 1.5-2.0 kg water/kg fiber, from the total measured removal water in Table 4.1. Although the repeatability of the ten series of experimental data is not quite satisfactory, the increasing trend predicted by the analytical model is qualitatively consistent with the trend shown in the experiment data.

The designed industrial machine speed of the experimental RCP paper machine with a roll diameter of 0.406 meter can be up to 800~900 fpm which is about ten times faster than pilot plant running speed. Although the increased centrifugal force is still small compared to the vacuum suction force and the surface tension force in the micro pores in the medium, the water removal rate may still drop down because the period of the pulp fiber passing the vacuum chamber on the RCP roll is reduced.

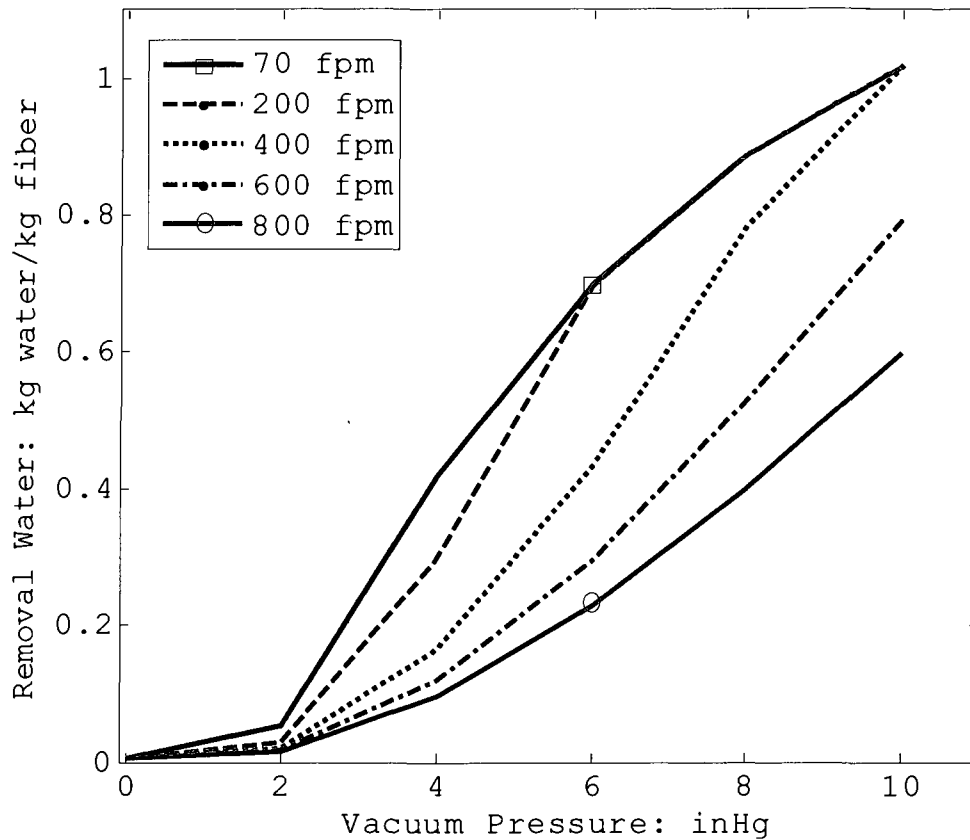


Figure 4.26 The effect of the machine speed on the water remove rate.

Figure 4.26 shows the effect of the machine speed on the water removal rate. When the machine speed increases from 70 fpm to 200 fpm, the water removal rate still keeps at the same level for  $P_v > 6$  inHg, but has a moderate drop for  $P_v < 6$  inHg. When the machine speed increases to 400 fpm, only the water removal rate at  $P_v = 10$  inHg can keep the same level without dropping. When the machine speed increases to 600 fpm and 800 fpm, there is an

evident drop of the water removal rate even for the high vacuum pressure. Figure 4.26 implies that an optimized machine speed can be found for a predetermined vacuum pressure to achieve the fastest water remove rate.

The commercial sized RCP paper machine may have a larger roll with 2 - 3 times the diameter of the small pilot plant RCP roll. The designed machine speed ranges from 3000 fpm to 6000 fpm. The residence time in the vacuum zone may be reduced to several dozen milliseconds. Rather than redo your calculations, indicate that they are for a pilot machine using this RCP roll at 800 fpm. But need to tell reader than large scale machines are faster and perhaps have shorter residence time in the vacuum zone. Using the proposed model, a graph similar to Figure 4.26 can be obtained with the given basis weight, and the pore size distribution of the pulp fibers and the optimized operation parameters can be determined to achieve a high water removal rate.

#### 4.4 Conclusions

An analytical model for simulating the dewatering process in the RCP porous medium is developed in this chapter. The model is based on the general capillary model for complex geometries described in the previous chapters. The production parameters in the paper making process such as the basis weight and pore size distribution in the pulps, the geometry of the multi-layer RCP porous medium, the machine speed and the vacuum pressure are related to the dewatering performance through the proposed model.

An experiment for measuring the flow rate of the liquid passing the RCP medium was carried on the Lab. The observed linearity between the flow rate and the applied suction pressure validated the asymptotic solutions of the flow field in complex geometries derived in chapter 3 and also help us build develop an analytical model to approximate the complicated structure in the porous medium using the simple cosine function.

The effects of the machine speed and vacuum pressure on the dewatering performance of the RCP paper making machine are investigated through a series of pilot plant

RCP experiments. The pilot plant experimental data qualitatively validated the proposed analytical model. The potential of the model to be used as a parametric optimization tool for the industrial porous media design is also discussed in this chapter.

## **CHAPTER 5**

### **CONCLUSIONS AND DISCUSSION**

In this dissertation, the analytical, computational and experimental studies on the dynamic capillary flows in complex geometries have been reported.

(1) Based on the Navier-Stokes equations, a general approach that is capable of modeling the capillary flow in arbitrary irregular geometries with a straight axis of symmetry has been developed. Using this approach, the governing equation to describe the dynamic capillary rise in capillaries with nonuniform elliptical cross-sections is first derived under the assumptions of constant contact angle and parabolic distribution of the axial velocity. Compared with the existing capillary models, the new model includes the full viscous terms and the effects of the fluid inertia. A MATLAB program for numerically solving the derived nonlinear second order differential equation using the Runge-Kutta method was developed. The results for the cases studied, which include capillaries of different wall variations, show that the inertial terms and the viscous terms with the

nonuniformity effects can be underestimated in the existing nonuniform cross section models. For nonuniform capillaries, the capillary rise velocity at the convergent section is faster than that at the divergent section. The capillary interface reaches the equilibrium height at the divergent section for all the cases considered. Due to the fact that the equilibrium height solutions are non-unique for the periodic, sinusoidal capillary case, the inertial effect considered in the proposed model can drive the interface to overshoot the lowest equilibrium location and reach a different equilibrium height. This happens in the numerical calculations for a special sinusoidal tube with  $L=2$  and  $A=0.3$ , but the experimental validation still remains to be explored.

(2) Using the perturbation method, an asymptotic solution of the flow field in nonuniform circular tubes is obtained and is shown to be better than the traditional Hagen-Poiseuille solutions by comparing with the numerical FLUENT results. A new DCA (dynamic contact angle) model, combining with the current velocity-dependent model based on molecular-kinetic theory and empirical time-dependent model based on experiments, is

proposed to describe the dynamic transition process of the gas-liquid interface. The applicable scope of the new DCA model is extended to the entire process from the initial state to the equilibrium state. The capillary flow model is further developed by using the new velocity distribution and the DCA model. The proposed theoretical models are validated by a series of experiments of capillary flow in complex geometries.

(3) The industrial application of the research work was explored by adopting the proposed model to describe the water flow passing through a multi-layer porous medium that is used in Procter & Gamble's dewatering device for paper making industry. The model is based on the general capillary model for complex geometries described in the previous chapters. The production parameters in the paper making process such as the basis weight and pore size distribution in the pulps, the geometry of the multi-layer RCP porous medium, the machine speed, and the vacuum pressure are related to the dewatering performance through the proposed model.

An experiment for measuring the flow rate of the liquid passing the RCP medium was carried out. The observed linearity between the flow rate and the applied

suction pressure validated the asymptotic solutions of the flow field in complex geometries. The mathematical description of the complicated structure in the porous medium using the Cosine function can be found through the porous medium flow rate test.

A series of pilot plant RCP experiments was carried out to investigate the effects of the machine speed and vacuum pressure on the dewatering performance of the RCP paper making machine. The pilot plant experimental data qualitatively validated the proposed analytical model and indicated the potential of the model to be used as a parametric optimization tool for the industrial porous media designing.

## **BIBLIOGRAPHY**

Ahrens FW and Xu H (1999), Effect of pulp drying history on pressing and drying, TAPPI Engineering/Process & Product Quality Conference, Anaheim, California, September 12-16.

Asensio MC (2000), Transport phenomena during drying of deformable, hygroscopic porous media: fundamentals and applications, Doctoral Dissertation, Texas A&M University.

Ayyaswamy PS, Catton I and Edwards DK (1974), Capillary flow in triangular grooves, Journal of Applied Mechanics-Transactions of The ASME, Vol. 41(2), pp: 332-336.

Bico J and Quere D (2002), Rise of liquids and bubbles in angular capillary tubes, Journal of Colloid and Interface Science, Vol. 247(1), pp: 162-166.

Blake TD (1967), Everett D. H. and Haynes J.M., Some Basic Considerations Concerning the Kinetics of Wetting Processes in Capillary Systems. In Wetting, SCI Monography, No. 25, pp:164.

Blake TD, Haynes J. M. (1969), Kinetics of Liquid/Liquid Displacement, Journal of Colloid and Interface Science, Vol. 30(3), pp:421-427.

Blake TD (1993), in: Berg JC (Edition), Wettability, Dekker, New York, pp: 251.

Blake TD, Bracke M and Shikhmurzaev YD (1999), Experimental evidence of nonlocal hydrodynamic influence on the dynamic contact angle, Physics of Fluids, Vol. 11(8), pp: 1995-2007.

Blake TD and Coninck JD (2002), The influence of solid-liquid interactions on dynamic wetting, *Advances in Colloid and Interface Science*, Vol. 96, pp: 21-36.

Blake TD and Shikhmurzaev YD (2002), Dynamic wetting by liquids of different viscosity, *Journal of Colloid and Interface Science*, Vol. 253, pp: 196-202.

Blake TD (2006), The physics of moving wetting lines, *Journal of Colloid and Interface Science*, Vol. 299, pp:1-13.

Brandon S and Marmur A (1996), Simulation of contact angle hysteresis on chemically heterogeneous surfaces, *Journal of Colloid and Interface Science*, Vol. 183, pp: 351-355.

Brittin WE (1946), Liquid rise in a capillary tube, *Journal of Applied Physics*, Vol.17, pp:37-45.

Brochard-Wyart F and deGennes PG (1992), Dynamics of partial wetting, *Advances in Colloid and Interface Science*, Vol. 39, pp: 1-11.

Bruil HG and Van Aartsen JJ (1974), The determination of contact angles of aqueous surfactant solutions on powders. *Colloid and Polymer Science*, Vol. 252(1), pp: 32-38.

Cain JB, Francis DW, Venter RD and Neumann AW (1983), Dynamic Contact Angles on Smooth and Rough Surfaces. *Journal of Colloid and Interface Science*, Vol. 94(1), Page:123-130.

Catton I and Stroes GR (2002), A semi-analytical model to predict the capillary limit of heated inclined triangular capillary grooves, *Journal of Heat Transfer-Transactions of The ASME*, Vol. 124(1), pp: 162-168.

Cazabat AM (1992), Wetting - From Macroscopic to Microscopic Scale, *Advances in Colloid and Interface Science*, Vol. 42, pp: 65-87.

Chen HY, Zhang FZ, Chen T, et al. (2009), Comparative analysis of the dynamic contact angles for two types of superhydrophobic layered double hydroxide film surfaces, *Chemical Engineering Science*, Vol. 64(12), pp: 2957-2962.

Chokshi VN (2007), Experimental measurements and mathematical modeling of the rigid capillary dewatering, Master Thesis, Western Michigan University.

Chuang SC and Thompson HA (1985), Method of and apparatus for removing liquid for webs of porous material, Patent No. US 4,556,450.

Concus P and Finn R (1974a), Capillary free surfaces in absence of gravity, *Acta Mathematica*, Vol. 132(3-4), pp:177-198.

Concus P and Finn R (1974b), Capillary free surfaces in a gravitational-field, *Acta Mathematica*, Vol. 132(3-4), pp:207-223.

Concus P and Finn R (1990), Dichotomous behavior of capillary surfaces in zero gravity, *Microgravity Science and Technology*, Vol. 3(22), pp: 87-92.

Cox RG (1986), The Dynamics of The Spreading of Liquids on A Solid-Surface, 1. Viscous-Flow, *Journal of Fluid Mechanics*, Vol 168, pp:169-194.

Crowl VT and Wooldridge WDS (1967), A Method for the Measurement of Adhesion Tension of Liquids in Contact with Powders, *Wetting*, Society of Chemical Industry, London, pp: 200-212.

Cui ZG, Binks BP and Clint JH (2005), Determination of contact angles on microporous particles using the thin-layer wicking technique, *Langmuir*, Vol. 21, pp: 8319-8325.

Curtis FG and Patrick O (1994), *Applied Numerical Analysis*, Addison-Wesley.

- deGennes PG (1985), Wetting: statics and dynamics, *Reviews of Modern Physics*, Vol. 57(3), pp: 827-863.
- deGennes PG (1990), Dynamics of Wetting - Local Contact Angles, *Journal of Fluid Mechanics*, Vol. 212 pp: 55-63.
- Deiber JA and Schowalter WR (1979), Flow through tubes with sinusoidal axial variations in diameter, Vol. 25(4), pp: 638-645.
- deLazzer A, Langbein D, Dreyer M and Rath HJ (1996), Mean curvature of liquid surfaces in cylindrical containers of arbitrary cross-section, *Microgravity Science and Technology*, Vol. 9(3), pp: 208-219.
- deRuijter MJ, Coninck JD and Oshanin G (1999), Droplet spreading: Partial wetting regime revisited, *Langmuir*, Vol. 15(6), pp: 2209-2216.
- Dettre RH and Johnson Jr. RE (1965), Contact angle hysteresis. IV. Contact angle measurements on heterogeneous surfaces, *The Journal of Physical Chemistry*, Vol. 69(5), pp: 1507-1515.
- Dimitrov DI, Milchev A and Binder K (2007), Capillary rise in nanopores: molecular dynamics evidence for the Lucas-Washburn equation, *Physical Review Letters*, Vol. 99(5), Article number: 054501.
- Dong M, Dullien FAL and Chatzis I (1995), Imbibition of oil in film form over water present in edges of capillaries with an angular cross section, *Journal of Colloid and Interface Science*, Vol. 172, pp: 21-36.
- Dong M and Chatzis I (1995), The imbibitions and flow of a wetting liquid along the corners of a square capillary tube, *Journal of Colloid and Interface Science*, Vol. 172, pp: 278-288.
- Duarte AA, Strier DE and Zanette DH (1996), The rise of a liquid in a capillary tube revisited: A hydrodynamical

approach, American Journal of Physics, Vol. 64(4), pp: 413-418.

Dreyer M, Delgado A and Rath HJ (1993), Fluid motion in capillary vanes under reduced gravity, Microgravity Science and Technology, Vol. 4, pp: 203-210.

Dullien F., Elsayed M., Batra V. (1977), Rate of Capillary Rise in Porous-Media With Nonuniform Pores, Journal of Colloid and Interface Science, Vol. 60, pp : 497.

Dussan VEB and Davis SH (1974), On the motion of a fluid-fluid interface along a solid surface, Journal of Fluid Mechanics, Vol. 65(1), pp: 71-95.

Dussan VEB (1976), The moving contact line: the slip boundary condition, Journal of Fluid Mechanics, Vol. 77, pp: 665-684.

Dussan VEB (1979), On the spreading of liquids on solid surfaces: static and dynamic contact lines, Annual Review of Fluid Mechanics, Vol. 11, pp: 371-400.

Dussan VEB, Rame E and Garoff S (1991), On identifying the appropriate boundary conditions at a moving contact line: an experimental investigation, Journal of Fluid Mechanics, Vol. 230, pp: 97-116.

Eggers J and Evans R (2004), Comment on "dynamic wetting by liquids of different viscosity" by T.D. Blake and Y.D. Shikhmurzaev, Journal of Colloid and Interface Science, Vol. 280, pp: 537-538.

Eick JD, Good RJ and Neumann AW (1975), Thermodynamics of contact angles II. Rough solid surfaces, Journal of Colloid and Interface Science, Vol. 53(2), pp: 235-248.

Einset EO 1996, Capillary infiltration rates into porous media with applications to silcomp processing, JOURNAL OF THE AMERICAN CERAMIC SOCIETY 79 : 333.

Elley DD, and Pepper DC (1946), A Dynamical Determination of Adhesion Tension. Trans. Faraday Soc., Vol. 42, page:697.

Elliott GEP and Riddiford AC (1967), Dynamic contact angles I. the effect of impressed motion, Journal of Colloid and Interface Science, Vol. 23(3), pp: 389-398.

Ensign DE, Knight WR and Trokhan PD (1994), Limiting orifice drying of cellulosic fibrous structures, apparatus therefor, and cellulosic fibrous structures produced thereby, United States Patent, No. 5,274,930.

Ensign DE, Stelljes MG and Trokhan PD (1996), Multiple zone limiting orifice drying of cellulosic fibrous structures, apparatus therefor, and cellulosic fibrous structures produced thereby, United States Patent, No. 5,539,996.

Ensign DE, Dreisig RC, Stelljes MG and Knight WR (2000), Limiting orifice drying medium, apparatus therefore, and cellulosic fibrous structures produced thereby, United States Patent, No. 6,105,276.

Erickson D., Li D. and Park C.B. (2002), Numerical Simulations of Capillary-Driven Flows in Nonuniform Cross-Sectional Capillaries, Journal of Colloid and Interface Science, Vol.250, Page:422-430.

Ershov AP, Zorin ZM, Sobolev VD and Churaev NV (2001), Kinetics of Gas Bubble Motion in a Capillary, Colloid Journal, Vol 63(2), pp. 179-185.

Extrand CW (2003), Contact angles and hysteresis on surfaces with chemically heterogeneous islands, Langmuir, vol.19(9), pp:4017-4021.

Extrand CW (2004), Contact angles and their hysteresis as a measure of liquid-solid adhesion, Langmuir, vol. 20, pp:4017-4021.

Fadeev AY and McCarthy TJ (1999), Trialkylsilane Monolayers Covalently Attached to Silicon Surfaces: Wettability Studies Indicating that Molecular, *Langmuir*, Vol. 15(11), pp. 3759-3766.

Fang Q, Sun M and Huang YZ (2009), Capillary-based microfluidic analysis systems, *Analytical and Bioanalytical Chemistry*, Vol. 393(1), pp: 63-66.

Fisher LR and Lark PD (1979), An experimental study of the Washburn equation for liquid flow in very fine capillaries, *Journal of Colloid and Interface Science*, Vol. 69, pp: 486-492.

Franke TA and Wixforth A (2008), Microfluidics for miniaturized laboratories on a chip, *ChemPhysChem*, Vol. 9, pp: 2140-2156.

Frenkel JI (1946), *Kinetic Theory of Liquids*, Oxford University Press, Oxford.

Glastone S, Laidler KJ, Eyring HJ (1941), *The Theory of Rate Process- The Kinetics of Chemical Reactions, Viscosity, Diffusion and Electrochemical Phenomena*, McGraw-Hill, New York.

Grader L (1986), On the Modeling of the Dynamic Contact Angles. *Colloid and Polimer Science*, Vol. 264, pp: 719-726.

Gribanova EV (1992), Dynamic contact angles: Temperature dependence and the influence of the state of the adsorption film, *Advances in Colloid and Interface Science*, Vol. 39, pp: 235-255.

Good RJ (1973), The rate of penetration of a fluid into a porous body initially devoid of adsorbed material, *Journal of Colloid and Interface Science*, Vol. 42(3), pp: 473-477.

Hamraoui A, Thuresson K, Nylander T and Yaminsky V (2000), Can a dynamic contact angle be understood in

terms of a friction coefficient, *Journal of Colloid and Interface Science*, Vol. 226, pp: 199-204.

Hamraoui A and Nylander T (2002), Analytical approach for the Lucas-Washburn equation, *Journal of Colloid and Interface Science*, Vol. 250, pp: 415-421.

Hansen RS and Miotto M (1957), Relaxation Phenomena and Contact Angle Hysteresis, *Journal of the American Chemical Society*, Vol. 79(7), page: 1765.

Hashimoto T, Shin-ichiro T, Morinishi K and Satofuka N (2008), Numerical simulation of conventional capillary flow and no-flow underfill in flip-chip packaging, *Computers & Fluids*, Vol. 37, pp: 520-523.

Hayes RA and Ralston J (1993), Forced liquid movement on low energy surfaces, *Journal of Colloid and Interface Science*, Vol. 159, pp: 429-438.

Helland JO and Skjæveland SM (2007), Relationship between capillary pressure, saturation, and interfacial area from a model of mixed-wet triangular tubes, *Water Resources Research*, Vol. 43(12), Article No. W12S10.

Hennig A, Grundke K, Frenzel R and Stamm M (2002), Ultrahydrophobic surfaces: Relation between roughness and contact angle hysteresis, *Tenside Surfactants Detergents*, Vol. 39(6), pp: 243-246.

Higuera FJ, Medina A and Linan A (2008), Capillary rise of a liquid between two vertical plates making a small angle, *Physics of Fluids*, Vol. 20, Article No. 102102.

Hoffman RL (1975), A Study of the Advancing Interface. I. Interface Shape in Liquid-Gas System. *J. Colloid Interface Sci.*, Vol. 50, Page:228-241.

Huang CY (2002), The investigation of the capillary flow of underfill materials, *Microelectronics International*, Vol. 19(1), pp: 23-29.

Huh C and Scriven LE (1971), Hydrodynamic model of steady movement of a solid/liquid/fluid contact line, *Journal of Colloid and Interface Science*, Vol. 35(1), pp: 85-101.

Huh C and Mason SG (1977), Steady movement of a liquid meniscus in a capillary tube, *Journal of Fluid Mechanics*, Vol. 81, Issue: Jul 13, pp: 401-419.

Ichikawa Naoki, Hosokawa Kazu, Maeda Ryutaro (2004), Interface motion of capillary-driven flow in rectangular microchannel, *Journal of Colloid and Interface Science*, Vol.280, Page:155-164.

Jia P, Dong MZ, Dai L and Yao J (2008), Slow viscous flow through arbitrary triangular tubes and its application in modelling porous media flows, *Transport in Porous Media*, Vol. 74, pp: 153-167.

Jiang TS, OH SG and Slattery JC (1979), Correlation for dynamic contact angle, *Journal of Colloid and Interface Science*, Vol. 69(1), pp: 74-77.

Joos P, van Remoortere P and Bracke M (1990), The kinetics of wetting in a capillary, *Journal of Colloid and Interface Science*, Vol. 136(1), pp: 189-197.

Jong WR, Kuo TH, Ho SW, Chiu HH and Peng SH (2007), Flows in rectangular microchannels driven by capillary force and gravity, *International Communications in Heat and Mass Transfer*, Vol. 34, Pp:186-196.

Kasivisvanathan SR, Kaloni PN and Rajagopal KR (1991), Flow of a non-newtonian fluid through axisymmetrical pipes of varying cross-sections, *International Journal of Non-linear Mechanics*, Vol. 26(5), pp: 777-792.

Kolb WB and Cerro RL (1993), The motion of long bubbles in tubes of square cross section, *Physics of Fluids A-Fluid Dynamics*, Vol. 5(7), pp: 1549-1557.

Kotorynski WP (1995), Viscous flow in axisymmetric pipes with slow variations, *Computers and Fluids*, Vol. 24(6), pp: 685-717.

Kovcek AR and Radke CJ (1996), Gas bubble snap-off under pressure-driven flow in constricted noncircular capillaries, *Colloids and Surfaces A-Physicochemical and Engineering Aspects*, Vol 117(1-2), pp: 55-76.

Kwok D.Y. and Neumann A.W. (2000), Contact angle interpretation in terms of solid surface tension, *Colloids and Surfaces A: Physicochemical and Engineering Aspects*, Vol. 161, Page:31-48.

Lago M and Araujo M (2001), Threshold pressure in capillaries with polygonal cross section, *Journal of Colloid and Interface Science*, Vol. 243, pp: 219-226.

Lam CNC, Kim N, Hui D, et al. (2001), The effect of liquid properties to contact angle hysteresis, *Colloids and Surfaces A: Physicochemical and Engineering Aspects*, vol. 189, pp:265-278.

Lam CNC, Wu R, Li D, et al. (2002), Study of the advancing and receding contact angles: liquid sorption as a cause of contact angle hysteresis, *Advances in Colloid and Interface Science*, vol. 96, pp:169-191.

Lavi B, Marmur A (2004), The Exponential Power Law: Partial Wetting Kinetics and Dynamic Contact Angles. *Colloids and Surfaces A-Physicochemical and Engineering Aspects*, Vol. 250, Issue 1-3, pp: 409-414.

Lavi B, Marmur A, and Bachmann J (2008), Porous Media Characterization by the Two-Liquid Method: Effect of Dynamic Contact Angle and Inertia. *Langmuir*, Vol. 24, pp:1918-1923.

Lazghab M, Saleh K, Pezron I, et al. (2005), Wettability assessment of finely divided solids, *Powder Technology*, Vol. 157, pp:79-91.

Levine S and Neal GH (1975), Theory of the rate of wetting of a porous medium. Faraday Trans., II, Vol. 71, pp:12.

Levine S, Reed P and Watson EJ (1976), A theory of the rate of rise of a liquid in a capillary, in: Colloid and Interface Science, vol. III: Adsorption, Catalysis, Solid Surfaces, Wetting, Surface Tension, and Water, Edited by Kerker M, Academic Press, New York, pp: 403-419.

Levine S, Reed P and Shutts G (1977), Some aspects of wetting/dewetting of a porous medium, Powder Technology, Vol. 17, pp: 163.

Lockington DA and Parlange JY (2004), A new equation for macroscopic description of capillary rise in porous media, Journal of Colloid and Interface Science, Vol. 278, pp: 404-409.

Ma HB, Peterson GP and Lu XJ (1994), The influence of vapor-liquid interactions on the liquid pressure drop in triangular microgrooves, International Journal of Heat and Mass Transfer, Vol. 37(5), pp: 2211-2219.

Ma HB and Peterson GP (1997a), Laminar friction factor in microscale ducts of irregular cross section, Microscale Thermophysical Engineering, Vol. 1(3), pp: 253-265.

Ma HB and Peterson GP (1997b), Temperature variation and heat transfer in triangular grooves with an evaporating film, Journal of Thermophysics and Heat Transfer, Vol. 11(1), pp: 90-97.

MaCool C (2008), How to reduce printing costs by 17%: A guide to doing well and doing good by printing less, A GreenPrint Technologies White Paper.

Manton MJ (1971), Low Reynolds number flow in slowly varying axisymmetric tubes, Journal of Fluid Mechanics, Vol. 49(3), pp: 451-459.

Mason G and Morrow N (1991), Capillary behavior of a perfectly wetting liquid in irregular triangular tubes, *Journal of Colloid and Interface Science*, Vol. 141(1), pp: 262-274.

Mason G and Morrow N (1994), Effect of contact-angle on capillary displacement curvatures in pore throats formed by spheres , *Journal of Colloid and Interface Science* , vol. 168 (1), pp: 130-141.

Mittelmann HD and Zhu A (1996), Capillary surfaces with different contact angles in a corner, *Microgravity Science and Technology*, Vol. 9(1), pp: 22-27.

Newman S (1968), Kinetics of wetting of surfaces by polymers - capillary flow, *Journal of Colloid and Interface Science*, Vol. 26(2), pp: 209-213.

Ngan CG and Dussan EB (1989), On the dynamics of liquid spreading on solid-surfaces, *Journal of Fluid Mechanics*, Vol. 209, pp: 191-226.

Oliver JF, Huh C and Mason SG (1980), An experimental study of some effects of solid surface roughness on wetting, *Colloids and Surfaces*, Vol. 1, pp: 79-104.

Park S, Venditti RA, Jameel H and Pawlak JJ (2006), Changes in pore size distribution during the drying of cellulose fibers as measured by differential scanning calorimetry, *Carbohydrate Polymers*, Vol. 66, page: 97-103.

Patro D, Saswata B and Vikram J (2007), Flow Kinetics in Porous Ceramics: Understanding with Non-Uniform Capillary Models, *Journal of the American Ceramic Society*, Vol.90(10), Page:3040-3046.

Patro D and Jayaram V (2008), Kinetics of pressureless infiltration of Al-Mg melts into porous Alumina performs, *Metallurgical and Materials Transactions B*, Vol. 39B, pp: 108-115.

Peterson GP and Ma HB (1996a), Analysis of countercurrent liquid-vapor interactions and the effect on the liquid friction factor, *Experimental Thermal and Fluid Science*, Vol. 12(1), pp: 13-24.

Peterson GP and Ma HB (1996b), Theoretical analysis of the maximum heat transport in triangular grooves: A study of idealized micro heat pipes, *Journal of Heat Transfer-Transactions of The ASME*, vol. 118(3), pp: 731-739.

Petrov PG and Petrov JG (1992), A combined molecular-hydrodynamic approach to wetting kinetics, *Langmuir*, Vol. 8, pp: 1762-1767.

Petrov JG, Sedev RV and Petrov PG (1992), Effect of geometry on steady wetting kinetics and critical velocity of film entrainment, *Advances in Colloid and Interface Science*, Vol. 38, pp: 229-269.

Petrov JG, Ralston J, Schneemilch M and Hayes RA (2003), Dynamics of partial wetting and dewetting in well-defined systems, *Journal of Physical Chemistry B*, Vol. 107(7), pp: 1634-1645.

Popescu MN, Ralston J and Sedev R (2008), Capillary rise with velocity-dependent dynamic contact angle, *Langmuir*, vol: 24(21), pp: 12710-12716.

Prevost A, Rolley E and Guthmann C (1999), Thermally activated motion of the contact line of a liquid  $^4\text{He}$  meniscus on a Cesium substrate, *Physical Review Letters*, Vol. 83(2), pp: 348-351.

Ralston J, Popescu M and Sedev R (2008), Dynamics of wetting from an experimental point of view, *Annual Review of Materials Research*, Vol. 38, pp: 23-43.

Ransohoff TC and Radke CJ (1988), Laminar-flow of a wetting liquid along the corners of a predominantly gas-occupied noncircular pore, *Journal of Colloid and Interface Science*, Vol. 121(2), pp:392-401.

Rideal EK (1922), On the Flow of Liquids Under Capillary Pressure. *Phil. Mag.*, Vol 44, pp:1152.

Romero LA and Yost FG (1996), Flow in an open channel capillary, *Journal of Fluid Mechanics*, Vol. 322, pp: 109-129.

Rose W and Heins RW (1962), Moving Interfaces and Contact Angle-Dependency. *Journal of Colloid and Interface Science*, Vol. 17, page 39-48.

Rowlinson JS and Windom B (2002), *Molecular Theory of Capillarity*, Reprint Edition, Published by Courier Dover Publications.

Schneemilch M, Hayes RA, Petrov JG and Ralston J (1998), Dynamic wetting and dewetting of a low-energy surface by pure liquids, *Langmuir*, Vol. 14(24), pp: 7047-7051.

Schwartz LW, and Garoff S (1985), Contact angle hysteresis on heterogeneous surfaces, *Langmuir*, Vol. 1(2), pp: 219-230.

Sedev RV, Petrov JG and Neumann AW (1996), Effect of Swelling of a Polymer Surface on Advancing and Receding Contact Angles, *Journal of Colloid and Interface Science*, Vol. 180, pp: 36-42.

Sharma R., Ross DS (1991), Kinetics of Liquid Penetration into Periodically Constricted Capillaries, *Journal of the Chemical Society-Faraday Transactions*, Vol. 87, pp: 619.

Sharpe MR, Peterson IR and Tatum JP (2002), Wetting kinetics of fluorinated surfaces, *Langmuir*, Vol. 18(9), pp:3549-3554.

Sheng P and Zhou M (1992), Immiscible-fluid displacement: Contact-line dynamics and the velocity-dependent capillary pressure, *Physical Review A*, Vol. 45(8), pp:5694-5708.

Shikhmurzaev YD (1993), The moving contact line on a smooth solid surface, *Int. J. Multiphase Flow*, Vol. 19(4), pp: 589-610.

Shikhmurzaev YD (1994), Mathematical modeling of wetting hydrodynamics, *Fluid Dynamics Research*, Vol. 13, pp: 45-64.

Shikhmurzaev YD (1997), Moving Contact Lines in Liquid/Liquid/Solid Systems. *Journal of Fluid Mechanics*, Vol.334, pp: 211-249.

Sisavath S, Jing XD and Zimmerman RW (2001), Creeping flow through a pipe of varying radius, *Physics of Fluids*, Vol. 13(10), pp: 2762-2772.

Sparrow EM, Lin SH and Lundgren TS (1964), Flow development in the hydrodynamic entrance region of tubes and ducts, *Physics of Fluids*, Vol. 7(3), pp: 338-347.

Stange M, Dreyer ME and Rath HJ (2003), Capillary driven flow in circular cylindrical tubes, *Physics of Fluids*, Vol. 15(9), pp: 2587-2601.

Staples TL, Shaffer DG (2002), Wicking flow in irregular capillaries, *Colloids and Surfaces A-Physicochemical and Engineering Aspects*, Vol. 204, pp : 239-250.

Stelljes MG, Trokhan PD and Ensign DE (2000), Low wet pressure drop limiting orifice drying medium and process of making paper therewith, *United States Patent*, No. 6,021,583.

Stelljes MG, Polat O, Ensign DE, et al. (2004), Method of drying fibrous structures, *Patent No. US 6,746,573 B2*.

Stokes JP, Higgins MJ, Kushnick AP and Bhattacharya S (1990), Harmonic generation as a probe of dissipation at a moving contact line, *Physical Review Letters*, Vol. 65(15), pp: 1885-1888.

Studebaker ML and Snow CW (1955), The Influence of Ultimate Composition Upon the Wettability of Carbon Blacks, Journal of Physical Chemistry, Vol. 59(9), pp: 973-976.

Su SK and Lai CL (2004), Interfacial shear-stress effects on transient capillary wedge flow, Physics of Fluids, Vol. 16(6), pp: 2033-2043.

Tavana H and Neumann AW (2006), On the question of rate-dependence of contact angles, Colloid and Surfaces A: Physicochem. Eng. Aspects, Vol:282, Pages: 256-262.

Tavana H, Jehnichen D, Grundke K, et al. (2007), Contact angle hysteresis on fluoropolymer surfaces, Advances in Colloid and Interface Science, Vol. 134, pp: 236-248.

Trokhan PD, Ensign DE and Stelljes MG (1999), Process of reducing wet pressure drop in a limiting orifice drying medium and a limiting orifice drying medium made thereby, United States Patent, No. 5,912,072.

Turian R. and Kessler F. (2000), Capillary Flow in a Noncircular Tube. AIChE Journal, Vol 46(4), pp:695.

Valmet-Karlstad AB (1999), Internal construction of RCP roll, RCP technical manual.

Van Dyke M (1987), Slow variations in continuum mechanics, Advances in Applied Mechanics, Vol. 25, pp: 1-45.

Vedantam S and Panchagnula VM (2008), Constitutive modeling of contact angle hysteresis, Journal of Colloid and Interface Science, Vol. 321, pp: 393-400.

Verbist G, Weaire D and Kraynik AM (1996), The foam drainage equation, Journal of Physics-Condensed Matter, Vol. 8(21), pp: 3715-3731.

Voinov OV (1976), Hydrodynamics of Wetting, Fluid Dynamics, Vol. 11(5), pp: 714-721.

- Wan JW (2004), Analysis and modeling of underfill flow driven by capillary action in flip-chip packaging, PhD Thesis, University of Saskatchewan.
- Wan JW and Zhang WJ (2005), An analytical model for predicting the underfill flow characteristics in flip-chip encapsulation, IEEE Transactions on Advanced Packaging, Vol. 28(3), pp: 481-487.
- Wan JW, Zhang WJ and Bergstrom (2007), Recent advances in modeling the underfill process in flip-chip packaging, Microelectronics Journal, Vol. 38, pp: 67-75.
- Wan JW, Zhang WJ and Bergstrom DJ (2008), Experimental verification of models for underfill flow driven by capillary forces in flip-chip packaging, Microelectronics Reliability, Vol. 48, pp: 425-430.
- Wang JH, Claesson PM, Parker JL, and Yasuda H (1994), Dynamic contact angles and contact angle hysteresis of plasma polymers, Langmuir, Vol. 10(10), pp:3887-3897.
- Washburn EW (1921), The Dynamics of Capillary Flow, Physical Review, Vol. XVII, No. 3, pp:273-283.
- Watanabe K, Flury M (2008), Capillary Bundle Model of Hydraulic Conductivity for Frozen Soil, Water Resources Research, Vol. 44(12), Article Number: W12402.
- Weislogel MM and Lichter S (1998), Capillary flow in an interior corner, Journal of Fluid Mechanics, Vol. 373, pp: 349-378.
- Weislogel MM (2003), Some analytical tools for fluid management in space: Isothermal capillary flows along interior corners, Adv. Space Res., Vol. 32, pp: 163.
- Wenzel RN (1936), Resistance of solid surfaces to wetting by water, Industrial and Engineering Chemistry, Vol. 28, pp:988-994.

Wenzel RN (1949), Surface roughness and contact angle, *The Journal of Physical Chemistry*, Vol. 53(9), pp: 1466-1467.

Wong H, Morris S and Radke CJ (1992), 3-dimensional menisci in polygonal capillaries, *Journal of Colloid and Interface Science*, Vol. 148(2), pp: 317-336.

Xiao Y, Yang F and Pitchumani R (2006), A generalized analysis of capillary flows in channels, *Journal of colloid and interface science*, Vol. 298, pp: 880-888.

Yang YW (1985), Capillary flow phenomena as related to wettability in porous media, PhD Thesis, University of Wisconsin-Madison.

Yarnold GD and Mason BJ (1949), A theory of the angle of contact, *Proceedings of the Physical Society. Section B*, Vol. 62, pp: 121-125.

Yasuda T and Miyama M (1994), Effect of water immersion on surface configuration of an Ethylene-Vinyl alcohol copolymer, *Langmuir*, Vol.10, pp:583-585.

Young T (1805), An essay on the cohesion of fluids, *Philosophical Transactions of the Royal Society of London*, pp: 65-87.

Young WB (2004), Analysis of capillary flows in non-uniform cross-sectional capillaries, *Colloids and Surfaces A-Physicochemical and Engineering Aspects*, Vol.234, pp:123-128.

Zhou MY and Sheng P (1990), Dynamics of immiscible-fluid displacement in a capillary tube, *Physical Review Letters*, Vol. 64(8), pp: 882-885.